Structural and Thermogravimetric Studies of Alkali Metal Amides and Imides

A thesis submitted for the degree of Doctor of Philosophy to the Division
of Mathematics, Physical and Life Science at the University of Oxford

Rebecca L Lowton
Trinity Term 2009

Inorganic Chemistry Laboratory
Department of Chemistry
University of Oxford
and
Worcester College

RADCLIFFE SCIENCE LIBRARY OXFORD
DEPOSITORY
16 FEB 2010
THESIS

Trinity Term
2009

Rebecca L. Lowton
Worcester College

Structural and Thermogravimetric Studies of Alkali Metal Amides and Imides

A thesis submitted for the degree of Doctor of Philosophy to the Division of Mathematics, Physical and Life Science at the University of Oxford

Abstract

This work presents an in-depth study of the crystal structures and hydrogen sorption potential of the Li – N – H and Li – Na – N – H systems. The structures of the materials have been studied using X-ray and neutron diffraction, Raman spectroscopy and inelastic neutron scattering. The behavior of the materials during heating was studied using variable temperature X-ray diffraction, intelligent gravimetric analysis in conjunction with neutron diffraction, intelligent gravimetric analysis combined with mass spectrometry and differential scanning calorimetry.

The role of cation disorder in the Li – N – H (D) system has been explored, indicating that crystallographic ordering of the Li^+ ions within lithium amide and lithium imide significantly affects the hydrogen sorption properties of the materials. Order-disorder transitions were observed both during hydrogen desorption from ordered $LiNH_2$ and during deuterium adsorption on ordered Li_2ND. Such transitions were not observed in disordered samples of the materials. The intrinsic disorder and the stoichiometry of Li – N – H(D) materials was shown to depend strongly on the techniques used during their synthesis.

Studies regarding the synthesis, crystal chemistry and decomposition properties of the mixed Li / Na amides are presented. Two distinct mixed Li / Na amides of formulae $Li_3Na(NH_2)_4$ and $LiNa_2(NH_2)_3$ were observed in the $LiNH_2$ / $NaNH_2$ phase space. Na was also seen to be soluble in $LiNH_2$, forming sodium-doped $LiNH_2$. $Li_3Na(NH_2)_4$ and Na-doped $LiNH_2$ were found to exhibit significant cation non-stoichiometry, whereas $LiNa_2(NH_2)_3$ was shown to exist as a line phase material.

Thermogravimetric and calorimetric studies of the mixed Li / Na amides suggested that these materials decompose primarily with loss of H_2.

The work described in this thesis was carried out in the Inorganic Chemistry Laboratory at the University of Oxford from October 2005 until July 2009 under the supervision of Professor Peter P Edwards. All of the work presented herein is my own unless otherwise stated and has not been submitted previously for any other degree at this or any other university.

Rebecca L Lowton

July 2009

~ Acknowledgements ~

Thanks must firstly go to my supervisor Peter Edwards for having me as a part of his research group and for giving me such an interesting and exciting project to work on.

Huge thanks also to Martin Jones and Bill David who have provided so much help and guidance during the course of my DPhil. Your input and expertise was so valuable to my work and I am very grateful to you both.

Thanks also to Simon Johnson for helping me to become a practical chemist (even though he's a physicist!), and for helping me to keep everything in perspective. Huge thanks also for your proof reading skills.

Much, much gratitude is due to Marco Sommariva for all of his help with synthesizing $LiND_2$ in the IGA and for all of the late nights he spent with us in the GEM cabin and the ID31 hutch.

Thanks to the members of the Edwards Group as a whole, both past and present, for all of your help, patience, fun and cake over the last few years. Particular mention must go to Catherine for being a lovely Part II student, to Chris for his help with the ball mill and to Kate for helping keep me sane during the write up period, and for not getting irritated with me when the IGA decided it just didn't like me!

I am also very grateful to Timmy Ramirez-Cuesta at ISIS and Andy Fitch and Michaela Bruneli at the ESRF for their help and expertise both during and after beam time.

Thanks also to Phil Chater, Paul Anderson and David Book at Birmingham University for running the Raman measurements for me and to Shige Isobe and Prof Fujii's group at Hiroshima University for coordinating the DSC measurements.

Huge thanks to my friends at OCC who have been such a great support whilst I've been in a panic about getting papers finished, getting samples ready and getting my thesis written. Your thoughts and prayers have been a constant encouragement to me and I thank God for you all.

To my family and friends, both in Bolton and in Oxford, who have given me so much support during my time here. I can't mention you all by name, but you know who you are and I'm so grateful to you.

To my Mum and Dad. Where do I start? I love you both so very much and really couldn't have done any of this without you. Thank you for supporting me so absolutely, encouraging me so continuously and loving me so completely.

Finally, to my Father. You have given me so much and I love you. Thank you for everything.

Great are the works of the LORD;
they are pondered by all who delight in them
Psalm 111 vs 2

~ Contents ~

Chapter One: Introduction

Chapter Two: Experimental Techniques

Chapter Three: A Thermogravimetric and Crystallographic Study of the Li – N – H System.

Chapter Four: The Synthesis and Structural Characterisation of the Mixed Li/Na Amides

Chapter Five: Summary

~ Chapter One ~

Introduction

1.1 A Brief History of Li-N-H Compounds.

The first synthesis of lithium amide ($LiNH_2$) was reported in 1894 by Titherly.[1] Formed by the reaction of molten lithium metal (Li) with gaseous or liquid ammonia (NH_3)[2, 3] $LiNH_2$ is a white solid with a melting point between 373 and 375 °C and a standard enthalpy of formation, ΔH_f, of -176 $kJmol^{-1}$.[4] Since its discovery, $LiNH_2$ has been used extensively in organic chemistry both as a base and an alkylating agent, in the condensation of esters and in de-protonation reactions.[5-8]

$LiNH_2$ was reported to decompose with ammonia loss upon heating to between 300 and 400 °C forming lithium imide (Li_2NH),[9] although more recent studies have noted decomposition at lower temperatures.[10] The disparity in these findings arises due to the low equilibrium vapour pressure of the NH_3-$LiNH_2$ system below 300 °C,[10] which leads to suppression of $LiNH_2$ decomposition if the NH_3 released is not removed from the immediate vicinity of the sample.

Approximately ten years after the work of Titherly,[1] Dafert and Micklauz studied the interaction of lithium nitride (Li_3N) with hydrogen. They found that heating Li_3N under a positive pressure of hydrogen gas led to the formation of a material of empirical formula "Li_3NH_4".[11, 12] This material was further studied, and was ultimately shown to be a 1 : 2 mixture of lithium amide and lithium hydride (LiH).[13, 14] It was not until several years ago – almost a century later – that the hydrogen storage potential of this material was first recognised.[15]

1.2 Hydrogen Storage

The use of hydrogen-powered fuel cells for automotive transportation is widely regarded as one of the most promising solutions to a number of major global concerns, particularly the energetic and economic dependence of society on diminishing oil reserves and the resultant global warming. However, the move towards a hydrogen-based economy is not imminent, as the worldwide introduction of fuel cell vehicles requires a number of scientific and technological breakthroughs, not least in the area of hydrogen storage.

Suitable materials for the storage of hydrogen for automotive applications must satisfy a number of criteria in terms of safety, hydrogen uptake / release conditions and storage capacity. The US Department of Energy (DoE) has summarised these requirements, producing a number of stringent targets to be met by potential storage materials by 2010.[16, 17]

1. High storage capacity: a gravimetric capacity of 2 kWh/kg, (equivalent to 6.5 weight percent (wt%) H_2 in the material, where wt% is defined as the net useful energy / the system mass) and a volumetric capacity of 1.5 kWh/dm^3;
2. Decomposition temperature, T_{dec}, between 60 and 120 °C;
3. Reversibility of the thermal absorption / desorption cycle;
4. Low cost: maximum $4/kWh;
5. Low-toxicity and non-explosive.

A system composed of such a material and a Proton Exchange Membrane (PEM) fuel cell would have a volume, weight and efficiency approximately equivalent to that of a typical petrol-based internal combustion engine.

Several methods for the storage of hydrogen have been considered. These include compression of gaseous H_2 in light weight, high-pressure cylinders, cryogenic storage of liquid H_2, physisorption of H_2 using high surface area materials, and chemisorption of hydrogen in chemical hydrides and complex hydrides.

Research into the field of chemisorption of hydrogen in complex hydrides was for many years dominated by the study of light weight compounds based on the alanate (AlH_4^-)[18, 19] and borohydride (BH_4^-)[20, 21] anions. Whilst showing much promise, the poor reversibility of these systems remains a major obstacle to their use.

$LiNH_2$ was largely ignored in terms of hydrogen storage for a number of years, principally due to its well-documented decomposition with ammonia loss.[9] The material was later brought to the forefront of hydrogen storage research after work, performed by Chen *et al,*[15] revealed that the interaction of $LiNH_2$ with LiH during decomposition suppressed the release of ammonia from the material in favour of the release of hydrogen.

Since this work, the Li – N – H system has proved to be a most promising candidate for hydrogen storage, demonstrating both a high gravimetric storage capacity and facile reversibility.

1.3 The Li – N – H System

The hydrogenation of Li_3N has been shown to be a two-step reversible process as outlined in Equation 1.1, with overall heat of reaction of -161 $kJmol^{-1}$.[11-15]

$$Li_3N + 2H_2 \xleftrightarrow{\text{Step 1}} Li_2NH + LiH + H_2 \xleftrightarrow{\text{Step 2}} LiNH_2 + 2LiH \qquad \text{Equation 1.1}$$

Under a pressure of 300 bar, hydrogenation of Li_3N is accomplished at temperatures of 170-210 °C for Step 1 and 255 °C for Step 2. The maximum theoretical hydrogen storage capacity of the material is 11.5 wt%, although in practice, the value is usually closer to ~10 wt%.[15]

Unfortunately, Step 1 has a low equilibrium pressure of 0.07 bar, and hence conditions of high temperature (320 °C) and low pressure (10^{-5} mbar) are required to facilitate de-hydrogenation of Li_2NH.

These conditions are so far removed from the DoE criteria[16] that the Li – N – H storage system must, for practical purposes, be viewed as being limited to Step 2, involving cycling between lithium imide and lithium amide.

This results in a maximum reversible storage capacity of ~7 wt% below 300 °C (ΔH = - 45 kJ mol^{-1}). The $LiNH_2$ / Li_2NH system, with removal of excess LiH, is presented in Equation 1.2.

$$Li_2NH + H_2 \leftrightarrow LiNH_2 + LiH \qquad \text{Equation 1.2}$$

Li_2NH has been reported to reversibly store around 6.5 wt% hydrogen at temperatures of 255 °C and above.[15] Under dynamic vacuum, the temperature of hydrogen release can be reduced to below 240 °C, although kinetics at this temperature are reported to be comparatively slow.[22]

In order for the Li – N – H system to be viable as a hydrogen store,[16] it will be necessary to reduce the decomposition temperature of lithium amide without compromising the reversibility or storage capacity of the material. Such improvements can only be accomplished if there is a thorough understanding of the chemical and crystallographic processes which occur in the materials during hydrogen sorption.

1.4 The Crystal Chemistry of the Li – N – H System

1.4.1 The Crystal Structure of Lithium Nitride (Li_3N)

Lithium nitride is known to exist in three distinct phases. The α – phase has a hexagonal structure which was first solved in 1935 by Zintl and Brauer[23] and was re-analysed by Juza[24] and Rabenau and Schultz[25] some years later.

The material was indexed to the space group $P6/mmm$ (number 191) with lithium ions occupying the 2c (⅓,⅔,0) and 1b (0,0,½) lattice sites. This forms planar edge-sharing hexagonal Li layers, with each hexagon capped above and below by an additional lithium ion. The nitrogen ions occupy the interstices at the centre of each hexagonal bi-pyramid (the 1a (0,0,0) lattice site) and hence are coordinated by a total of eight lithium ions. The lithium ions within the hexagonal planes are held in a trigonal planar geometry, whilst those capping the hexagons are held in a linear geometry.

The α – phase of Li_3N is stable at room temperature and pressure and is formed *via* the reaction of the elements at high temperature. The material is known to be a fast Li-ion conductor due to the presence of 1-2 % Li vacancies within the structure.[26, 27]

A schematic diagram of α – Li_3N is presented in Figure 1.1, with the atomic positions and lattice parameters summarised in Table 1.1.

Heating the α – polymorph of Li_3N to 300 K at moderate pressures (4.2 kBar) results in transformation into the β – phase which adopts the Na_3As structure.[28, 29] Further pressurisation to between 35 and 45 GPa results in the complete transformation of this phase to the γ – phase, which is isostructural with Li_3Bi.[29]

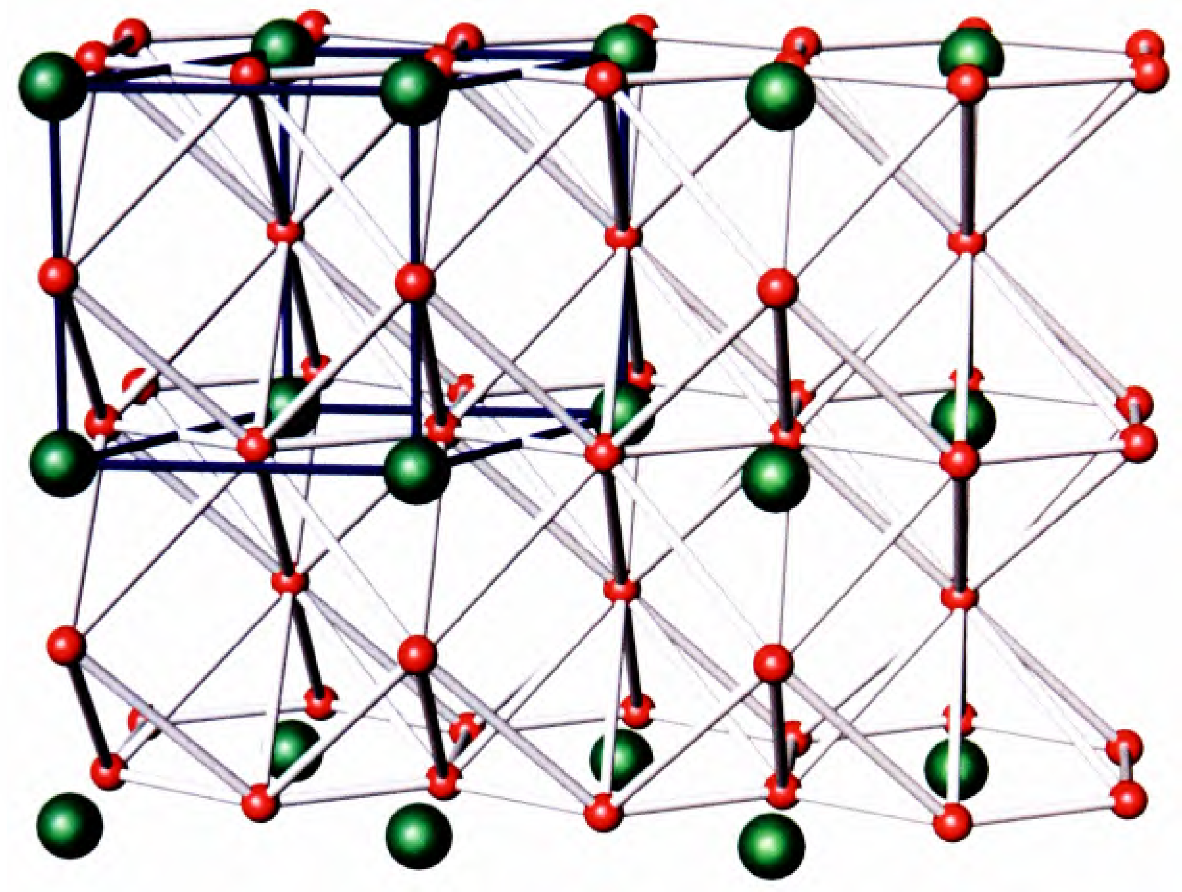

Figure 1.1 : Schematic diagram of the crystal structure of Li_3N (space group $P6/mmm$ (number 191) as calculated by Rabenau and Schulz.[25] Nitrogen is represented by green spheres and Li by red spheres. The Li_3N unit cell is enclosed in the blue box.

α - Li_3N

Atom	Site	*x*	*y*	*z*	Occupancy
N	1a	0	0	0	1
Li 1	1b	0	0	½	1
Li 2	2c	⅓	⅔	0	1

$a = 3.649(1)$ Å, $c = 3.877(1)$ Å

Table 1.1 : Summary of structural parameters for the high temperature phase of Li_3N, space group $P6/mmm$ (number 191)[25]

1.4.2 The Crystal Structure of Lithium Imide (Li_2NH)

The crystal structure of lithium imide was originally solved by Juza in 1951.[30] The material was shown to adopt a cubic anti-fluorite structure belonging to space group $Fm\bar{3}m$ (number 225) with lattice parameter a = 5.047 Å. Li was placed at the 8c (¼,¼,¼) sites, N at the 4a (0,0,0) sites, and H in one quarter of the 32f (x,x,x) sites. More recent experiments utilising synchrotron X-ray powder diffraction[31] and neutron powder diffraction[32] have been performed, resulting in more accurate determination of the H (or D) positions within the crystal structure.

Synchrotron X-ray diffraction studies of Li_2NH were performed by Noritake *et al*[31] and the diffraction data collected were analysed using the Rietveld method.[33] The material was shown to adopt the $Fm\bar{3}m$ space group (number 225) with Li at the 8c (¼,¼,¼) sites, N at the 4a (0,0,0) sites, and H located at either the 32f, 48h, 96j or 96k lattice sites. Comparison of the Li – H interatomic distances calculated for this material with those observed in other lithium – hydrogen compounds (such as $LiNH_2$, LiH, $LiBH_4$ etc.) led to the conclusion that H was most likely to be located at the 48h ($y,y,0$) sites.

A schematic diagram of this structure is presented in Figure 1.2a, with a list of atomic positions and unit cell parameters given in Table 1.2a.

Neutron powder diffraction experiments were performed on a deuterated sample of lithium imide (Li_2ND) by Balogh *et al*,[32] who observed an order – disorder transition at 87 °C. The low temperature phase was indexed to the $Fd\bar{3}m$ space group (number 227), with lattice parameter a = 10.09 – 10.13 Å, approximately double that reported previously.[31] The Li^+ ions were found to fully occupy the 48f (x,⅛,⅛) and 8a (⅛,⅛,⅛) lattice sites and partially occupy the 32e (*x,x,x*) sites, and the $N^{3-}$and D^+ ions were located at the 32e (*x,x,x*) sites.

Two lower energy, fully occupied orthorhombic structures were also suggested from analysis of the diffraction data of the low temperature Li_2ND phase, with space groups *Ima*2 and *Imm*2. Both of these structures were shown to have a unit cell volume close to that calculated during analysis of the diffraction data, with the *Ima*2 structure possessing fewer atomic sites (12) compared to the *Imm*2 structure (17).

The crystal structures of Li_2ND calculated using the $Fd\bar{3}m$ and *Ima*2 space groups are presented in Figures 1.2b and 1.2c, respectively. The atomic positions for these structures are summarised in Tables 1.2b and 1.2c, respectively.

Balough *et al* also indexed the disordered high-temperature phase to the $Fm\bar{3}m$ space group (number 225), with Li^+ and N^{3-} ions located on the 8c (¼,¼,¼) and 4a (0,0,0) sites, respectively, but with the D^+ positions randomised over the 192l (*x,y,z*) sites. This crystal structure is similar to that calculated by Noritake *et al*[31] and presented in Figure 1.2a.

The order-disorder transition of Li_2ND found by Balough *et al*[32] had been observed previously,[34, 35] having been studied by means of solid state ^7Li and ^1H nuclear magnetic resonance (NMR).

This work highlighted that the Li^+ ions and imide (NH^{2-}) groups exhibited a degree of ionic disorder above the transition temperature, whilst below this temperature, the NH^{2-} groups were fully ordered with the N – H bond aligned along the face diagonal of the unit cell.[34]

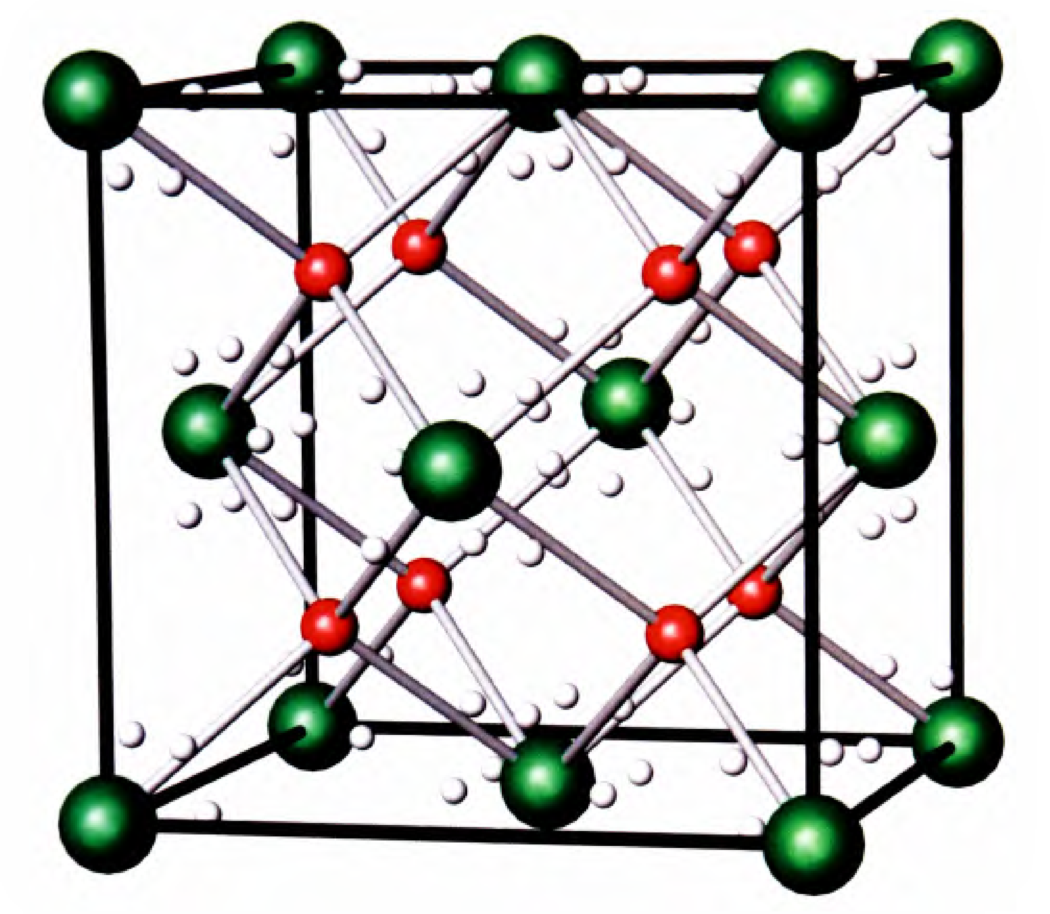

Figure 1.2a : Schematic diagram of the crystal structure of Li_2NH, space group $Fm\bar{3}m$ (number 225), calculated by Noritake et al.[31] N is represented by green spheres, Li by red spheres and H by white spheres.

Li_2NH

Atom	Site	*x*	*y*	*z*	Occupancy
Li	8c	¼	¼	¼	0.95
N	4a	0	0	0	1
H	48h	0.11(2)	0.11(2)	0	0.0833

$a = 5.0742(2)$ Å

Table 1.2a : Summary of structural parameters for the high temperature phase of Li_2NH, space group $Fm\bar{3}m$ (number 225)[31]

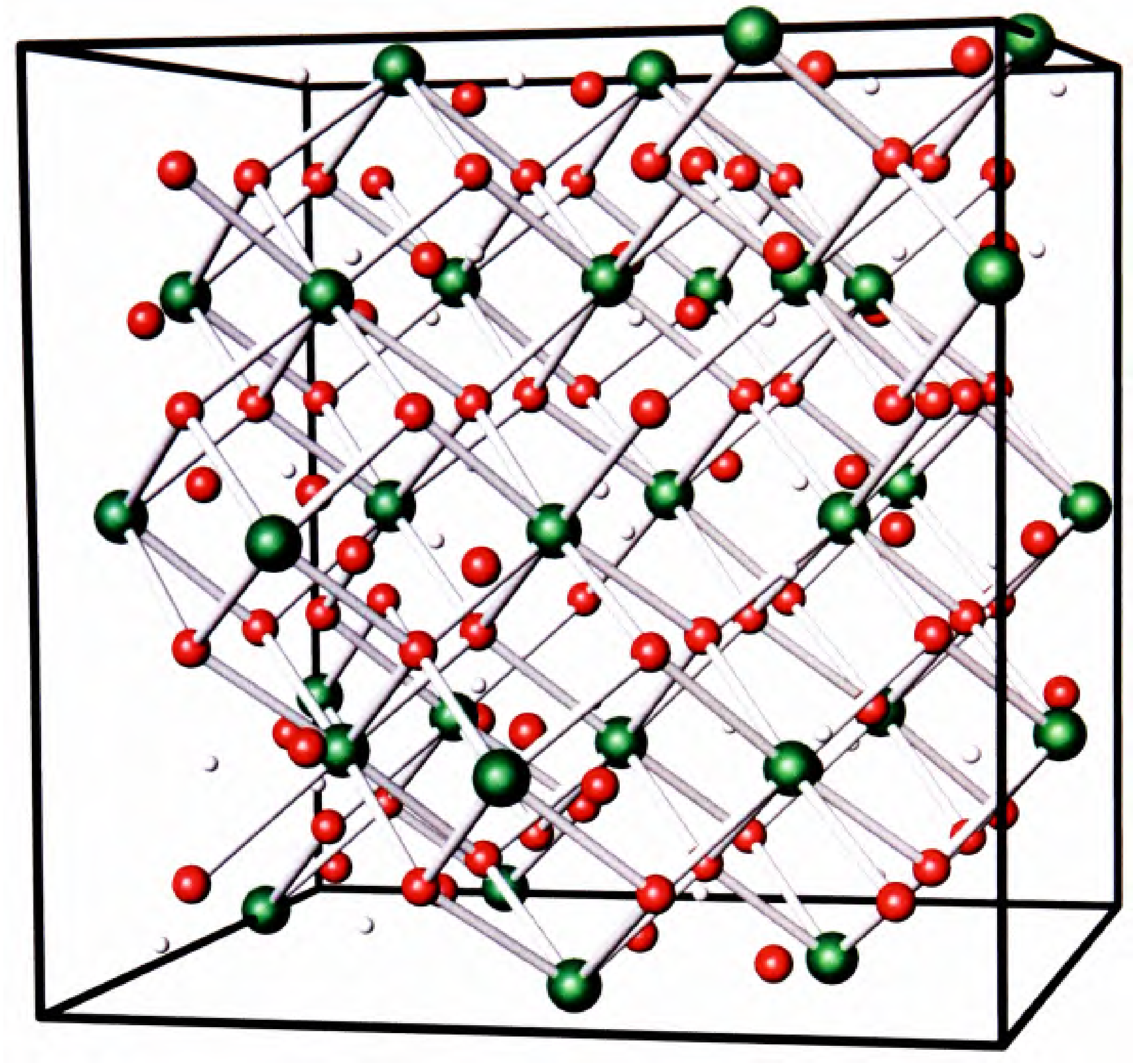

Figure 1.2b : Schematic diagram of the crystal structure of Li_2ND, space group $Fd\bar{3}m$ (number 227), calculated by Balogh *et al.*[32] N is represented by green spheres, Li by red spheres and D by white spheres.

Li_2ND

Atom	Site	*x*	*y*	*z*	Occupancy
Li I	48f	0.3725(3)	⅛	⅛	1
Li 2	8a	⅛	⅛	⅛	1
Li 3	32e	0.0316(8)	0.0316(8)	0.0316(8)	0.252(11)
N	32e	0.2432(1)	0.2432(1)	0.2432(1)	1
D I	32e	0.2846(11)	0.2846(11)	0.2846(11)	1

$a = 10.12988(6)$ Å

Table 1.2b : Summary of structural parameters for the low temperature phase of Li_2ND, space group $Fd\bar{3}m$ (number 227)[32]

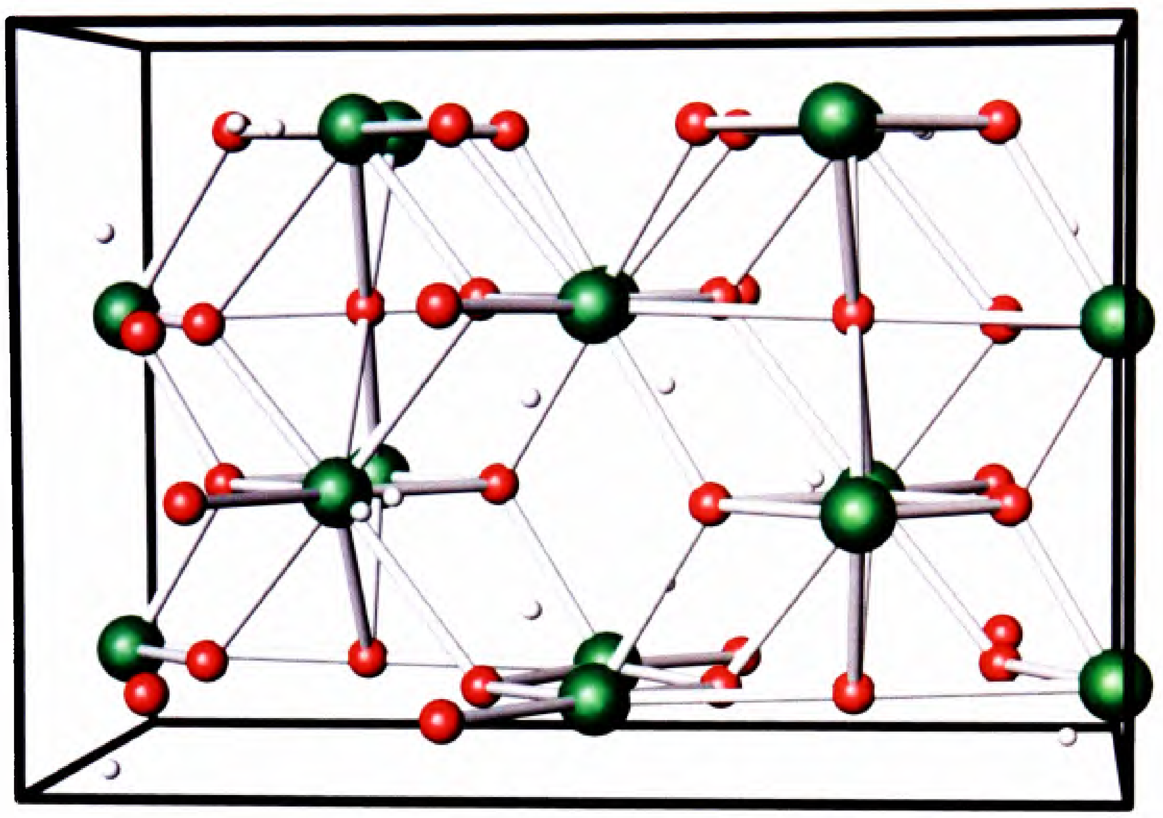

Figure 1.2c : Schematic diagram of the crystal structure of Li_2ND, space group *Ima*2 (number 46), calculated by Balogh *et al.*[32] N is represented by green spheres, Li by red spheres and D by white spheres.

Li_2ND

Atom	Site	*x*	*y*	*z*	Occupancy
Li 1	4b	0.250	0.3826	0.3703	1
Li 2	4b	0.250	0.8765	0.3703	1
Li 3	4b	0.250	0.1058	0.3705	1
Li 4	4b	0.250	0.2498	0.1206	1
Li 5	8c	0.5074	0.1155	0.1372	1
Li 6	8c	0.5073	0.3844	0.1034	1
N 1	4b	0.250	0.0087	0.6101	1
N 2	4b	0.250	0.0089	0.1305	1
N 3	8c	0.4691	0.2405	0.3700	1
D 1	4b	0.250	0.5505	0.2295	1
D 2	4b	0.250	0.5506	0.5114	1
D 3	8c	0.5819	0.1945	0.8700	1

a = 7.118 Å, b = 10.072 Å, c = 7.088 Å

Table 1.2c : Summary of structural parameters for the low temperature phase of Li_2ND, space group *Ima*2 (number 46)[32]

1.4.3 The Crystal Structure of Lithium Amide ($LiNH_2$)

The crystal structure of $LiNH_2$ was partially solved in 1951[30] and was then re-evaluated 21 years later.[36] The structure was indexed to a body-centred tetragonal unit cell belonging to the $I\bar{4}$ space group (number 82) with lattice parameters a = 5.037 Å and c = 10.278 Å.[36] The N^{3-} ions were found to occupy the 8g (x,y,z) sites, forming a distorted cubic close packed anion lattice. The Li^+ ions were found to occupy one half of the tetrahedral interstices at the 2a (0,0,0), 2c (0,½,¼) and 4f (0,½,z) sites and $H^{\delta+}$ ions were placed into two distinct 8g (x,y,z) sites.[36]

Using these atomic positions, the N – H bond distances were calculated at 0.70 Å and 0.76 Å, very much smaller than those reported for monomeric unsolvated $LiNH_2$ (1.022 Å).[37] Density Functional Theory (DFT) calculations also implied that a larger N – H bond length of 1.03 Å would be expected in the material.[38, 39] In light of these studies, additional neutron diffraction data for both $LiNH_2$[40] and $LiND_2$[41] were collected in order to more accurately determine the positions of H (or D) in the material.

The H positions from the original study were reported to be (0.266, 0.149, 0.172) (8g1) and (0.308, 0.359, 0.114) (8g2). The neutron diffraction study of $LiNH_2$ located the H ions at (0.2429, 0.1285, 0.1910) (8g1) and (0.3840, 0.3512, 0.1278) (8g2) and reported N – H bond-lengths of 0.986 Å and 0.942 Å.[40] The neutron diffraction study of $LiND_2$ reported the D positions to be (0.226, 0.1328, 0.1905) (8g1) and (0.394, 0.349, 0.1249) (8g2) with N – D bond lengths of 0.967 Å and 0.978 Å.[41] The H and D positions calculated during these studies were found to be in fairly good agreement, and led to bond lengths more in keeping with those calculated from DFT studies and monomeric $LiNH_2$.

The Li, N and H positions of this structure of $LiNH_2$[40] are summarised in Table 1.3 and a schematic diagram of the unit cell is shown in Figure 1.3.

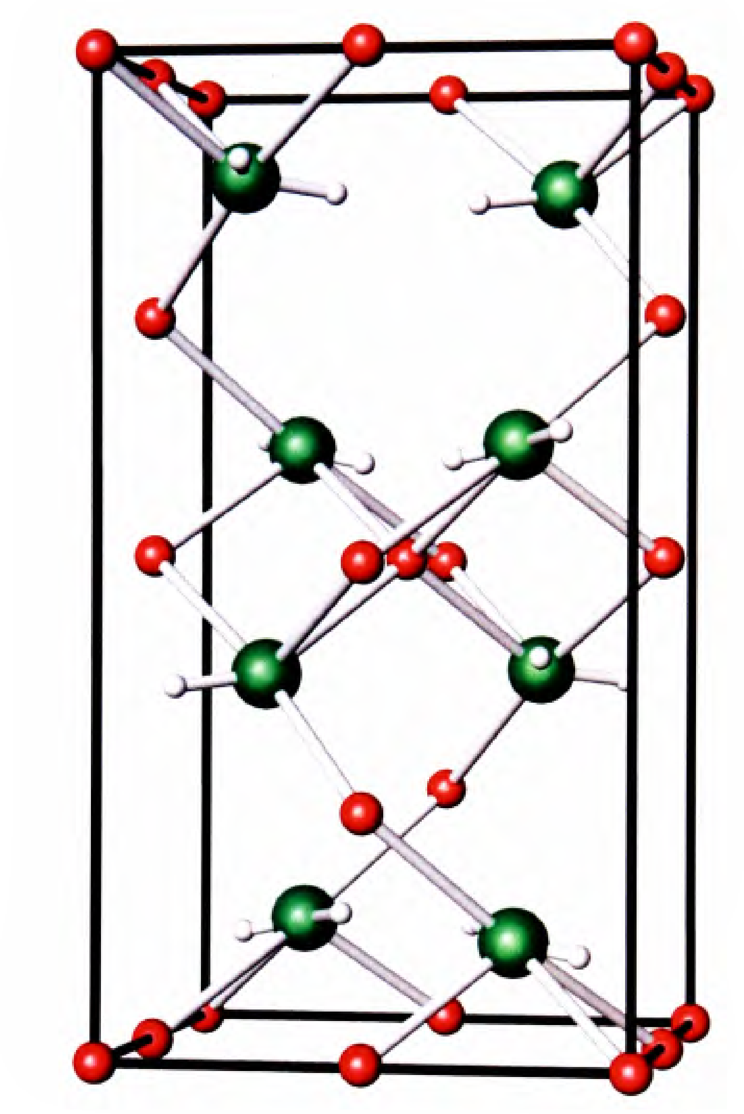

Figure 1.3 : Schematic diagram of the crystal structure of $LiNH_2$, space group $I\bar{4}$ (number 82) calculated by Yang *et al.*[40] N is represented by green spheres, Li by red spheres and H by white spheres.

$LiNH_2$

Atom	Site	*x*	*y*	*z*	Occupancy
Li 1	2a	0	0	0	1
Li 2	4f	0	½	0.00253	1
Li 3	2c	0	½	¼	1
N	8g	0.2286	0.2499	0.1158	1
H 1	8g	0.2429	0.1285	0.1910	1
H 2	8g	0.3840	0.3512	0.1278	1

$a = 5.03442(2)$ Å, $c = 10.25558(5)$ Å

Table 1.3 : Summary of structural parameters for $LiNH_2$, space group $I\bar{4}$ (number 82) as calculated by Yang *et al*[40]

1.4.4 The Crystal Structure of Lithium Hydride (LiH)

The crystal structure of lithium hydride was first solved by X-ray diffraction in 1922 by Bijovet and Karssen.[42] The diffraction pattern was indexed to a cubic unit cell with $Fm\bar{3}m$ space group (number 225) and lattice parameter a = 4.10 Å. The Li^+ ions were located at the 4a (0,0,0) lattice sites with the H^- ions at the 4b (½,½,½) sites, indicating that LiH adopted the rock-salt structure. Figure 1.4 shows the structure of the material, and its atomic positions and lattice parameter are presented in Table 1.4.

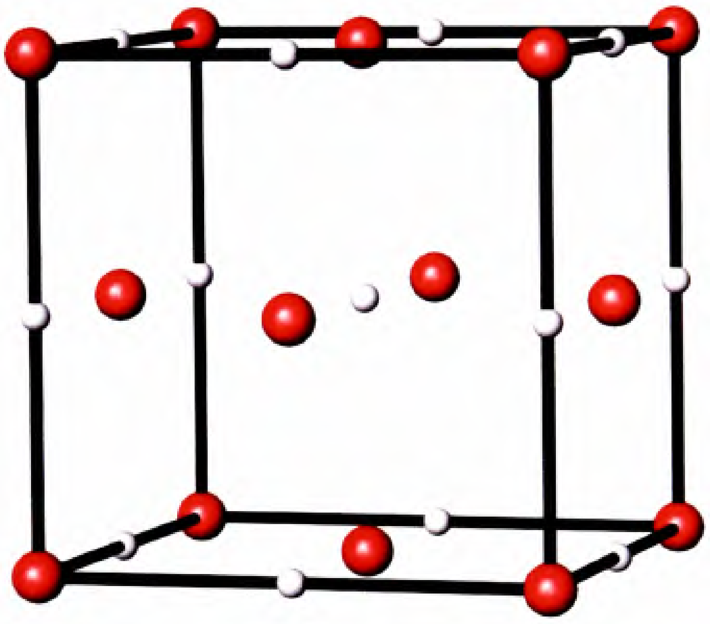

Figure 1.4 : Schematic diagram of the crystal structure of LiH, space group $Fm\bar{3}m$ (number 225) calculated by Bijvoet and Karssen.[42] Li is represented by red spheres and H by white spheres.

LiH

Atom	Site	x	y	z	Occupancy
Li	4a	0	0	0	1
H	4b	½	½	½	1

a = 4.10 Å

Table 1.4 : Summary of structural parameters for LiH, $Fm\bar{3}m$ (number 225) as calculated by Bijvoet and Karssen.[42]

1.4.5 Lithium Nitride Hydride (Li_4NH)

For the sake of completeness it is worth mentioning that in addition to $LiNH_2$ and Li_2NH, Li, N and H can form an additional compound, known as lithium nitride-hydride (Li_4NH). This material contains both the nitride N^{3-} anion and the hydride H^- anion and is formed from the reaction of Li_3N with LiH at 490 °C. Upon heating to 400 °C, Li_4NH decomposes to form Li_2NH and either Li_3N or LiH.[43]

This material, however, is not of principal interest in the hydrogen storage chemistry of the Li – N – H system and will not be referred to further in this work.

1.5 Bonding in the Li – N – H System

In spite of the pyramidal nature of the NH_3 molecule, the $LiNH_2$ monomer has been shown to be planar.[37] The much larger positive charge on the Li^+ ion compared with the H^+ ion leads to stronger coulombic repulsions within the molecule, resulting in a larger Li – N – H bond angle, compared to H – N – H in NH_3.[44] Additionally, overlap of the N lone-pair orbital with the low-lying vacant Li p-orbital is encouraged by back-donation of π-electrons from N to Li, further encouraging the planarity of the $LiNH_2$ unit.[45]

The back-donation of the π-electrons from N to Li also leads to a lower iconicity of $LiNH_2$ than would otherwise be expected, which is reflected in the calculated charge density of Li^+ at +0.458. The Li – N bond can therefore be regarded as predominantly ionic, but with considerable π back-donation from N to Li.

Upon substitution of a Li^+ for a H^+ (occurring during dehydrogenation of $LiNH_2$ to Li_2NH and again to Li_3N), the overlap between the Li p-orbitals and the N lone-pair orbitals is increased, implying that these compounds are very far from being ionic,[46] and that the charge density of the lithium decreases further on transformation of $LiNH_2$ to Li_2NH.

1.6 The Mechanism of $LiNH_2 + LiH \leftrightarrow Li_2NH + H_2$

As mentioned previously (section 1.2), the decomposition properties of $LiNH_2$ alter drastically if decomposition takes place in the presence of LiH. Temperature Programmed Desorption (TPD) studies have shown that the decomposition reaction of pure $LiNH_2$ releases ammonia, with reaction enthalpy (ΔH_r) 83.68 $kJmol^{-1}$, beginning at ~200 °C and peaking at 374°C (the melting point of the material).[47] If mixed with LiH in a 1:1 molar ratio, $LiNH_2$ decomposition occurs predominantly with release of H_2, beginning at a temperature of 170 °C, and peaking at 270 °C, with ΔH_r 45 $kJmol^{-1}$.[43]

In order to fully understand the $LiNH_2$ + LiH hydrogen storage system, it is crucial to determine the mechanism by which lithium amide and lithium hydride interact. It is also necessary to understand how this interaction leads to lower temperature decomposition and why it causes release of hydrogen from the material, as supposed to ammonia.

Two potential mechanisms have been suggested. The first involves the direct solid – solid interaction of $LiNH_2$ with LiH, and the second is mediated by gaseous ammonia.

1.6.1 Solid – Solid Mechanism

The solid – solid mechanism was suggested by Chen *et al*[47] and is based on the direct interaction of a protonic $LiNH_2$ hydrogen with a hydridic LiH hydrogen. This interaction would be further encouraged by the attraction of the partially positive lithium from the hydride and the partially negative nitrogen ion in the amide, leading to the formation of H_2 + Li_2NH as shown overleaf:[47]

$$\begin{array}{ccccccc} \mathrm{Li}^{\delta+} - & \mathrm{HN}^{\delta-} & - \ \mathrm{H}^{\delta+} & & \mathrm{Li-HN} & & \mathrm{H} \\ & \vdots & \vdots & \longrightarrow & | & + & | \\ & \mathrm{Li}^{\delta+} & - \ \mathrm{H}^{\delta-} & & \mathrm{Li} & & \mathrm{H} \end{array} \qquad \text{Equation 1.3}$$

This hypothesis was tested *via* isotopic labelling experiments, in which $LiNH_2$ was reacted with LiD and the gases produced were analysed using TPD. Provided that the decomposition reaction occurred *via* the solid – solid mechanism, the gas produced was anticipated to be HD.

The TPD measurements indicated that the released gas was predominantly H_2, with some HD and D_2, suggesting that the solid – solid mechanism was not correct. This was further confirmed by Fourier Transform Infra-Red (FTIR) measurements of the solid product, which showed that some deuterium was retained in the lithium imide.[47]

1.6.2 Gas-Mediated Mechanism

The second mechanism suggested for the reaction of LiH with $LiNH_2$ was the ammonia-mediated mechanism, based upon the formation of NH_3 from the decomposition of $LiNH_2$ and the subsequent interaction of this gas with LiH.

Hu and Ruckenstein tested this theory by forming two 'two-layer materials' (TLM 1 and 2) out of $LiNH_2$ and LiH in a 1:2 ratio as shown in Figure 1.5.[48] The materials were heated under a continuous flow of helium gas and the out-going gases were analysed using TPD combined with mass spectrometry (TPD-MS). It was found that the carrier gas which passed firstly through the LiH layer contained NH_3, whilst the gas which passed firstly through the $LiNH_2$ layer only contained H_2.

X-ray diffraction (XRD) measurements of TLM 1 after decomposition showed that the LiH layer remained unchanged during the reaction, whilst the $LiNH_2$ layer had been transformed into Li_2NH. The diffraction data from TLM 2 showed that the $LiNH_2$

layer had transformed into Li_2NH during the reaction and the LiH layer had become a mixture of $LiNH_2$ and Li_2NH.[48]

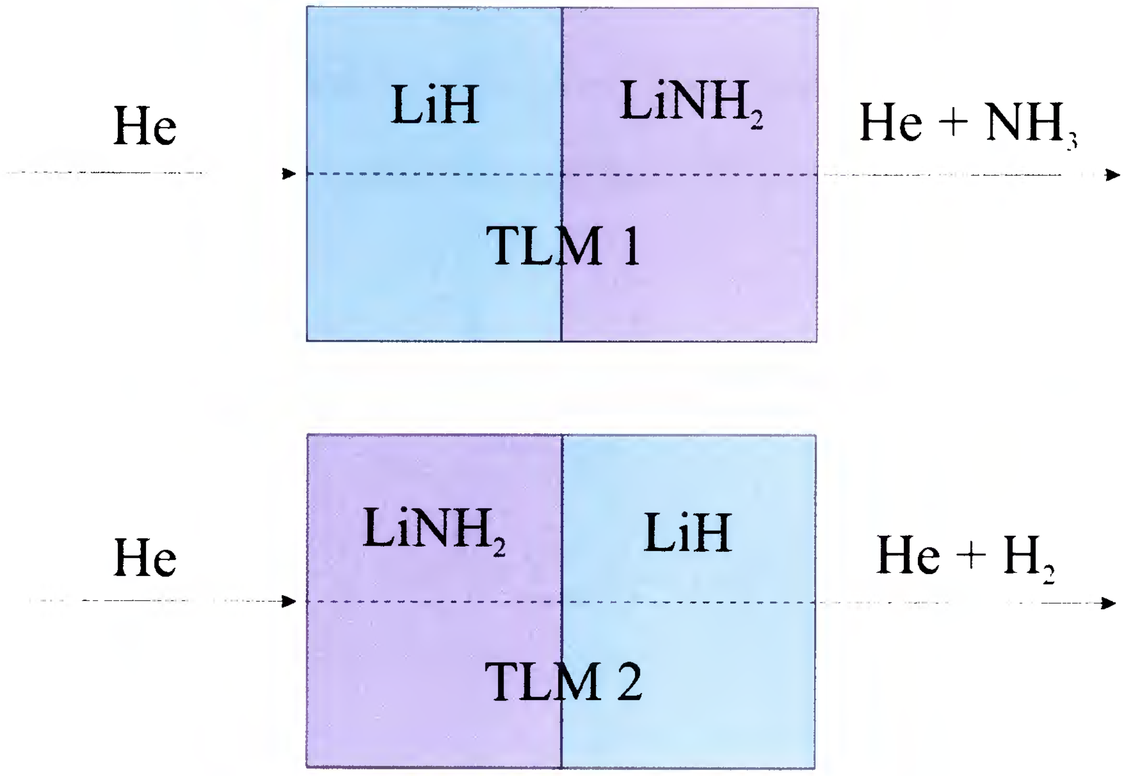

Figure 1.5 : Schematic diagram of the two-layer-materials (TLMs) studied by Hu and Ruckenstein[48]. The outgoing gases were analysed using TPD-MS, and were shown to contain NH_3 for the gas which had passed through TLM 1 and H_2 for the gas which had passed through TLM 2.

These findings led to the suggestion of the following ammonia-mediated two-step reaction mechanism:

$$2LiNH_2 \rightarrow Li_2NH + NH_3$$ Equation 1.4a

$$NH_3 + LiH \rightarrow LiNH_2 + H_2$$ Equation 1.4b

Further experiments on TLM 2 with gas-solid contact times varying from 25 ms – 2.5 ms were undertaken in order to determine the timescale of the reaction between LiH and NH_3. 25 ms contact times resulted in the complete capture of all NH_3, and even contact times as short as 2.5 ms led to the release of only 0.3% of the ammonia formed. These findings imply that the reaction of LiH with ammonia occurs on an ultra-fast timescale, and that the decomposition of $LiNH_2$, (i.e. the generation of ammonia) is the rate determining step of the $LiNH_2$ / LiH decomposition reaction.[48]

An independent study of the reaction of pure lithium hydride with ammonia showed that $LiNH_2$ was indeed formed from the reaction of these two substances.[49]

Additional TPD-MS experiments performed by Ichikawa *et al*[49] have further supported the ammonia-mediated mechanism. The reaction scheme was expanded to include successive amide decompositions and ammonia capture reactions:

$$\begin{aligned}
\mathrm{LiH} + \mathrm{LiNH_2} &\longrightarrow \frac{1}{2}\mathrm{LiH} + \left(\frac{1}{2}\mathrm{LiH} + \frac{1}{2}\mathrm{NH_3}\right) + \frac{1}{2}\mathrm{Li_2NH} \\
&\longrightarrow \frac{1}{2}\mathrm{LiH} + \frac{1}{2}\mathrm{LiNH_2} + \frac{1}{2}\mathrm{Li_2NH} + \frac{1}{2}\mathrm{H_2} \\
&\longrightarrow \frac{1}{2^n}\mathrm{LiH} + \frac{1}{2^n}\mathrm{LiNH_2} + \sum_{k=1}^{n}\frac{1}{2^k}\mathrm{Li_2NH} + \sum_{k=1}^{n}\frac{1}{2^k}\mathrm{H_2} \\
&\longrightarrow \mathrm{Li_2NH} + \mathrm{H_2}
\end{aligned}$$

Equation 1.5

In order to confirm the above mechanism, isotopic labelling experiments were performed which involved reaction of $LiND_2$ with LiH, and $LiNH_2$ with LiD.[50] The relative proportions of H_2, D_2 and HD produced were measured using TPD and thermogravimetry, and were shown to follow the basic rules of probability, thus supporting the ammonia-mediated mechanism.

1.7 Ionic Mobility Within the Li – N – H System.

α-Li_3N is a well-known Li-ion conductor. The ionic conductivity of the material is strongly anisotropic, with diffusion occurring perpendicular to the *c*-axis due to the presence of cationic vacancies within the hexagonal Li-containing planes.[26, 27] These cationic vacancies account for 1-2 % of the lithium sites, and it has been shown that doping the structure with hydrogen improves the ionic conductivity of the material.[51]

Lithium nitride is not the only material in the Li_3N / Li_2NH / $LiNH_2$ system that may demonstrate ionic mobility. Lithium imide is known to adopt the cubic anti-fluorite structure,[30] which is so-called because it is identical to the fluorite structure, (CaF_2) but has the positions of the cations and anions reversed.

Materials adopting the fluorite structure are well known to undergo superionic transitions at elevated temperatures, which result in thermally activated disorder within the materials and increase the anionic mobility between the cubic close-packed cation layers.[52, 53] Similar behaviour has also been observed in materials adopting the anti-fluorite structure, although in these cases the cation is the mobile species.

For example, studies on Li_2O have shown that two distinct cationic migration mechanisms occur within the structure at elevated temperature, which are illustrated in Figure 1.6.

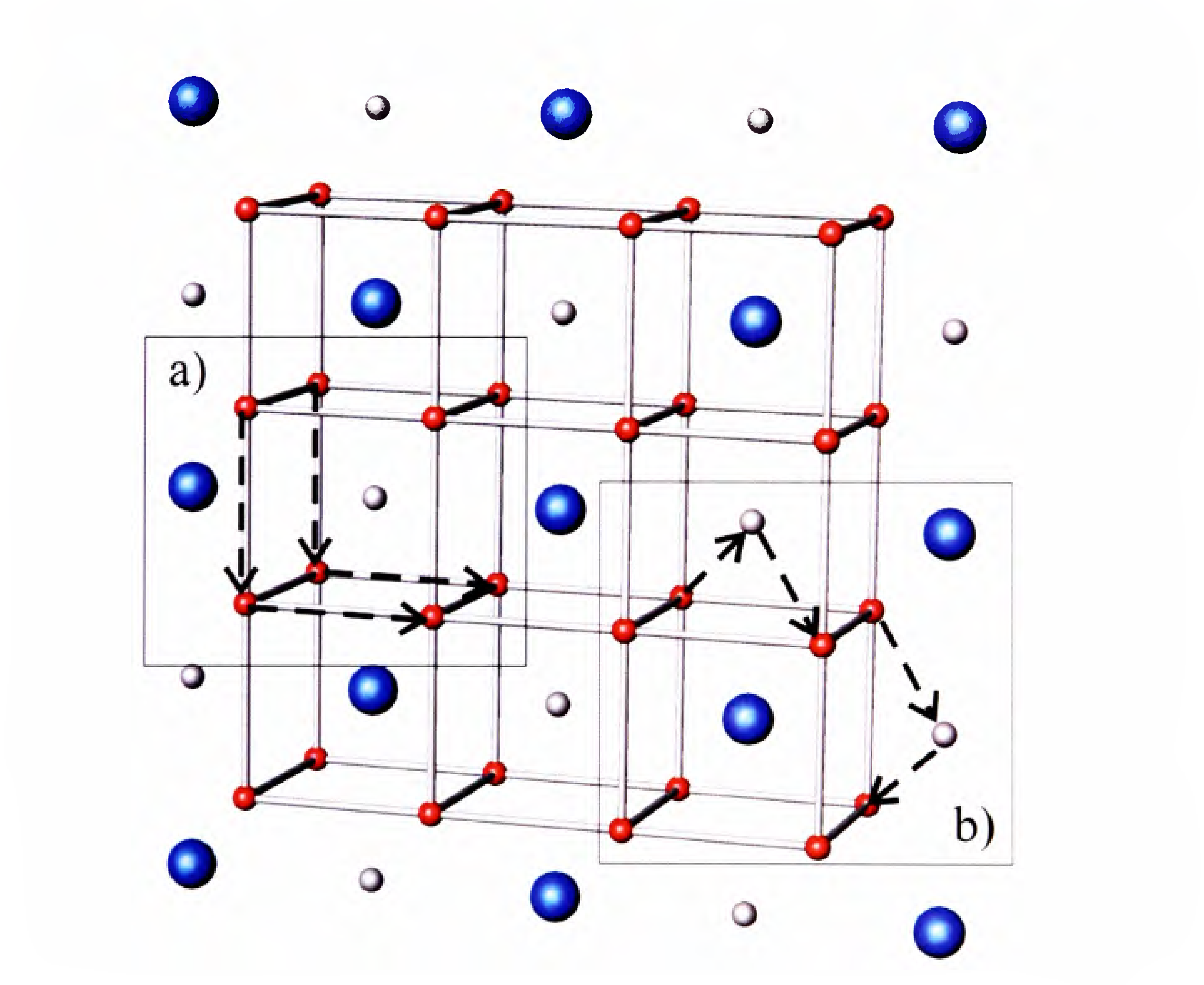

Figure 1.6 : Schematic diagram of Li_2O, highlighting the different mechanisms of ionic migration at elevated temperatures. a) represents tetrahedral – tetrahedral site hopping and b) represents tetrahedral – octahedral site hopping. Li is represented by red spheres, O by blue spheres and the cube centres are represented by grey spheres.

The first migration mechanism (Figure 1.6a) is direct tetrahedral – tetrahedral site-hopping and begins at temperatures around 50% of the melting point of the material. The second mechanism (Figure 1.6b) is tetrahedral – octahedral site-hopping and begins as the temperature of the material reaches approximately 80% of its melting point.[54, 55]

During these ionic migrations, a cation moves from its site in the ordered sub-lattice (forming a vacancy) and lodges itself into a nearby vacant site (becoming an interstitial). The vacancy and interstitial make up what is known as a *Frenkel defect* pair, which is a type of point defect.

Li_2O is topologically identical to Li_2NH, suggesting that such ionic migration mechanisms may also occur in Li_2NH, at appropriate temperatures. Indeed, NMR studies of Li_2NH have confirmed that a transition occurs between the ordered $Fd\bar{3}m$ and disordered $Fm\bar{3}m$ states at a temperature of 80 °C, indicating that the mobility of the Li^+ ions is very much higher above the transition temperature.[35, 56] Additionally, X-ray diffraction studies by Noritake *et al*[57] have shown that, even at room temperature, the occupancy of the Li site is only 0.95, implying the presence of approximately 5% Frenkel defect pairs within the material.

If a (¼, ¼, ¼) translation is applied to the Li_2NH unit cell, (locating the unit cell origin at a lithium ion as opposed to a nitrogen ion), the close relationship of this structure to that of $LiNH_2$ is clear (Figure 1.7).

This figure shows that, upon transformation of Li_2NH into $LiNH_2$, the cubic close packed anions of Li_2NH remain virtually undisturbed, whilst the fractional occupancy of the tetrahedral sites drops from 1 in the imide to ½ in the amide.

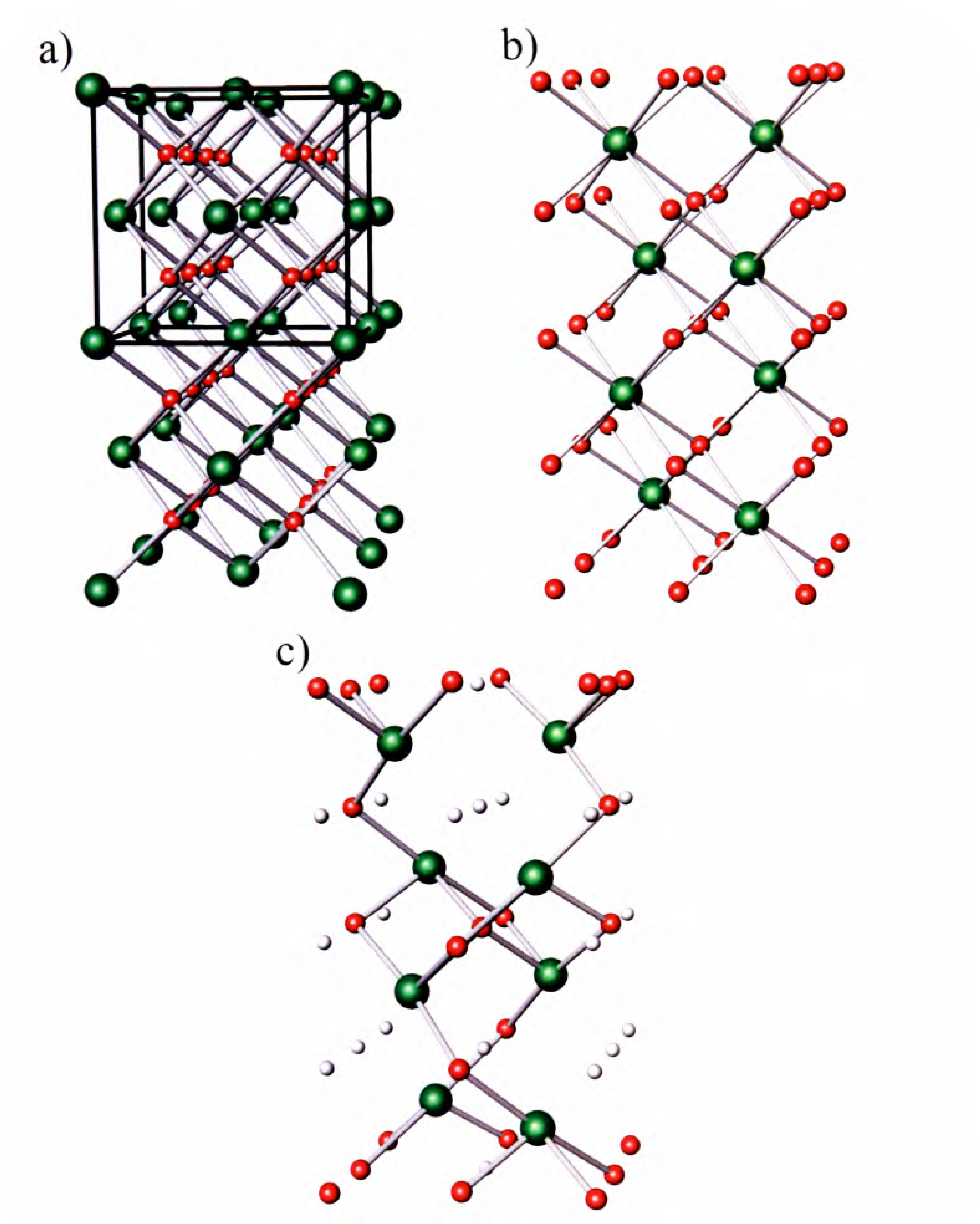

Figure 1.7 : Schematic diagrams of crystal structures of a) Li_2NH, b) Li_2NH after application of a (¼, ¼ ,¼) translation, c) $LiNH_2$. The Li ions are represented by red spheres, N by green spheres and tetrahedral vacancies by white spheres.

$LiNH_2$ can, therefore, essentially be regarded as an (a x a x $2a$) superstructure of Li_2NH, implying that $LiNH_2$ also has the potential to demonstrate ionic mobility between the cubic close-packed anionic layers of the structure. Indeed, several neutron diffraction studies performed on samples of both $LiNH_2$ and $LiND_2$ have shown large displacement parameters for the Li and H(D) positions, implying a significant degree of ionic mobility in the materials even at room temperature.[40, 41] Furthermore, a number of publications report the existence of compositional non-stoichiometry within $LiNH_2$ and Li_2NH, implying the potential of a continuum of materials of formula $Li_{2-x}NH_{1+x}$ ($0 \leq x \leq 1$).[10, 58-60]

1.7.1 Ionic Mobility and Hydrogen Sorption

Given the likelihood that the reaction between LiH and $LiNH_2$ is ammonia-mediated, it is possible that ionic mobility within the $LiNH_2$ and Li_2NH structures plays a significant part in the dehydrogenation / rehydrogentation reactions of the system. The formation and decay of Frenkel defect pairs could possibly be key to the production of NH_3 from $LiNH_2$ and also to the reaction of Li_2NH with H_2 during hydrogen adsorption. A potential mechanism for these steps was outlined in a recent study by David *et al.*[58]

The primary step in the proposed decomposition mechanism is the migration of a Li^+ cation to a nearby tetrahedral or octahedral site, leaving behind a vacancy and forming a Frankel defect pair.

$$LiNH_2 + LiNH_2 \leftrightarrow LiLiNH_2{}^+ + \square NH_2{}^- \qquad \text{Equation 1.6}$$

This Frenkel defect pair can decompose in one of three ways; i) by recombination of the vacancy and interstitial (Equation 1.7a) ii) by a subsequent Li^+

migration to a nearby vacant site (Equation 1.7b) or iii) by expulsion of a proton (Equation 1.7c).

$$\text{i)}\ \ LiLiNH_2{}^{+} + \square NH_2{}^{-} \leftrightarrow LiNH_2 + LiNH_2 \qquad \text{Equation 1.7a}$$

$$\text{ii)}\ \ LiLiNH_2{}^{+} + \square NH_2{}^{-} + LiNH_2 \leftrightarrow LiNH_2 + \square NH_2{}^{-} + LiLiNH_2{}^{+} \qquad \text{Equation 1.7b}$$

$$\text{iii)}\ \ LiLiNH_2{}^{+} + \square NH_2{}^{-} \leftrightarrow \left[Li_2NH + H^{+}\right] + \square NH_2{}^{-} \qquad \text{Equation 1.7c}$$

If the decomposition occurs *via* route iii), the expelled proton will be attracted to the nearby NH_2 ion and the two will combine to form NH_3:

$$Li_2NH + \left[H^{+} + \square NH_2{}^{-}\right] \leftrightarrow Li_2NH + NH_3 \qquad \text{Equation 1.8}$$

If this NH_3 is near to the surface of the grain, it has the potential to leave and subsequently react with lithium hydride to form $LiNH_2 + H_2$.[48]

The re-hydrogenation process can also be discussed in terms of ionic mobility. Migration of a mobile Li^+ ion from Li_2NH to an adjacent lattice site results in the formation of a Frenkel defect pair:

$$Li_2NH \leftrightarrow \square LiNH^{-} + Li^{+} \qquad \text{Equation 1.9}$$

This mobile Li^+ ion may then interact with applied hydrogen gas, resulting in the formation of lithium hydride and producing a proton:

$$Li^{+} + H\text{-}H \leftrightarrow LiH + H^{+} \qquad \text{Equation 1.10}$$

The protonic hydrogen formed would then be attracted towards the negatively charged area surrounding the vacant tetrahedral site, and would then combine with the NH^{2-} ion producing NH_2 :

$$H^{+} + \square LiNH^{-} \leftrightarrow H^{\delta+} - LiN^{\delta-}H \leftrightarrow LiNH_2 \qquad \text{Equation 1.11}$$

1.8 Modifications of the Li – N – H System

It is clear that, though the Li – N – H system has substantial potential as a hydrogen store, the thermodynamics of hydrogen cycling are not compatible with the conditions required for use with PEM fuel cells.[16, 17] Furthermore, ammonia is known to poison PEM fuel cell catalysts and hence, even the small proportion of NH_3 released from the decomposition of $LiNH_2$ + LiH may significantly shorten fuel cells life spans. Therefore, in order to make the Li – N – H system both technologically and economically viable for hydrogen storage, it is necessary not only to modify the materials to ensure favourable kinetics and decomposition temperature, but it is also vital to eliminate ammonia from the evolved gases.

There are two main research pathways which can be taken to address these issues and improve the hydrogen storage properties of the Li – N – H system.

The first of these pathways involves the modification of the system on a micro or nano-scale, which results in more facile ammonia capture due to better contact between LiH and $LiNH_2$ grains and faster gas diffusion through the sample.

The second research pathway involves chemical modification of the system on a crystallographic scale, by altering the unit cell contents through reaction of Li – N – H materials with other substances. The objective of such reactions is to produce materials with lower decomposition temperatures, different ionic mobilities and improved decomposition properties.

A number of studies have been performed following both research pathways. The most successful are summarised in the following sections.

1.8.1 Preparative Routes

Hu and Ruckenstein have performed numerous experiments to investigate how the preparative route influences the hydrogen storage performance of Li_2NH. Usually synthesised *via* the partial decomposition of lithium amide, the alternative methods investigated include those outlined below.

Method i) $2LiNH_2 \xrightarrow{230, 280, 350^\circ C} Li_2NH + NH_3$ [61] Equation 1.12

Method ii) $2Li + 2NH_3 \xrightarrow{200^\circ C} 2LiNH_2 + H_2 \uparrow$ Equation 1.13

$\xrightarrow{200^\circ C} Li_2NH + NH_3$ [62]

Method iii) $LiH + LiNH_2 \xrightarrow{280^\circ C} Li_2NH + H_2$ [61] Equation 1.14

Method iv) $Li_3N + LiNH_2 \xrightarrow{230^\circ C} 2Li_2NH$ [61, 63] Equation 1.15

The Li_2NH formed by the standard method (method i)) had very slow hydrogenation kinetics and reversibly stores only 2wt% H_2 (less than one third the theoretical storage capacity of the material).

Li_2NH formed *via* method ii) exhibited low adsorption kinetics and low storage capacity on the first hydrogenation cycle. Subsequent cycles showed an improvement in both kinetics and storage capacity, however, the maximum storage capacity reached after the 15th cycle was only ~3wt%. The kinetics were believed to have improved during subsequent cycling due to the breakdown of a Li_2O layer surrounding the Li_2NH particles.[62]

Li_2NH formed *via* the reaction of LiH with $LiNH_2$ (method iii)) showed an improvement in hydrogen storage capability over the materials formed by the previous methods. Whilst the kinetics of hydrogen sorption remained slow, the reversible storage capacity of the material was around 4 wt% after 500 minutes absorption time.

Method iv), using between 50 and 28 mol% $LiNH_2$ with Li_3N, formed lithium imide with the fastest hydrogenation kinetics and highest storage capacity. 5.4 wt% H_2 was absorbed in 10 mins and the materials consistently displayed excellent reversible capacity of 6.8 wt % over several cycles.[63] The amide – nitride reaction is believed to occur *via* a two-step ammonia-mediated process[61] analogous to the decomposition process of $LiNH_2$ with LiH.[48]

$2LiNH_2 \rightarrow Li_2NH + NH_3$ Equation 1.16a

$2Li_3N + NH_3 \rightarrow 3Li_2NH$ [61] Equation 1.16b

In this case, Li_3N essentially acts as an ammonia trap, pushing the equilibrium of the reaction to the right and overcoming the problems of low equilibrium pressure associated with lithium amide decomposition.[61] Li_2NH formed *via* this method reportedly out performs lithium imide formed by any other route.

1.8.2 Ball-milling the $LiNH_2$ / LiH Mixture

Studies by Ichikawa *et al*[64] found that mechanically milling a sample of 1:1 $LiNH_2$ + LiH vastly reduced the amount of ammonia desorbed from the mixture, compared to manually ground samples of 1:1 and 1:2 $LiNH_2$ + LiH. This was attributed to the more intimate mixing of the powders, ensuring good contact between $LiNH_2$ and LiH and hence more effective ammonia capture. Furthermore, it was found that the peak temperature of hydrogen desorption from the milled sample was lower than that of the hand-mixed samples. This was also attributed to the nano-scale contact between reactants.

Investigations of pure $LiNH_2$ after ball milling have shown that the onset decomposition temperature can be reduced from 120°C to room temperature.[65] This was attributed to the reduction in particle size, the increase in surface area, and the reduction of the activation energy for decomposition in the milled $LiNH_2$. The study indicated that the rate of the later stage decomposition of $LiNH_2$ is controlled by the rate at which ammonia diffuses through Li_2NH.

1.8.3 Catalysis

Inspired by the effect that catalysis had on the hydrogen storage properties of other complex hydrides[18, 21] a number of studies have been performed to determine whether the inclusion of small amounts of transition metal-based catalysts would also improve the properties of the Li – N – H system.

Ichikawa *et al* studied the effect of doping a ball milled sample of 1:1 $LiNH_2$ + LiH with 1 mol% Ni, Fe, Co and $TiCl_3$.[64] It was found that the mixture containing $TiCl_3$ gave the best hydrogen storage performance, with the sample exhibiting the sharpest desorption curve and producing the largest amount of hydrogen (5.5 wt% in 30 minutes at 200 °C). $TiCl_3$ was seen to reduce the activation energy required for the transformation of LiH + $LiNH_2$ into Li_2NH + H_2 and also completely eliminated NH_3 from the desorbed gas.

Additional work suggests that $TiCl_3$ acts as an agent in the transfer of NH_3 from $LiNH_2$ to LiH on a nanometer scale, through the formation of an ammoniate intermediate.[49]

Other Ti – based catalysts have also been studied including Ti metal and TiO_2, both in the form of micro and nano-particles. Both of these materials reduced the decomposition temperature of the $LiNH_2$ / LiH system only when the catalyst particles were of a nano-scale size. XRD of the decomposed products showed no presence of Ti or TiO_2, implying that a high dispersion of the nano-scale Ti particles is required for effective catalysis.[66]

A number of other catalysts, including Mn, MnO_2 and V_2O_5, were found to improve the decomposition kinetics of pure $LiNH_2$, but were shown to have no effect on the dehydrogenation reaction of $LiNH_2$ with LiH.[67]

1.8.4 Dopants

Based upon the hypothesis that the inclusion of atoms with varying electronegativity may alter the strength of the N – H bond, investigations have been carried out involving doping $LiNH_2$ with other metals. Destabilisation of the N – H bond could potentially result in a reduction of the $LiNH_2$ decomposition temperature. Furthermore, if the dopants used were of a higher oxidation state than Li, charge balancing would cause an increase in the number of vacancies, which would potentially increase the cationic mobility within the material.

Noritake and Orimo found that the inclusion of 10 mol% Mg in $LiNH_2$ reduced the decomposition temperature of $LiNH_2$ by 50 °C.[68, 69] This temperature could be further lowered by increasing the doping level to 30 mol% Mg.[70]

Density Functional Theory (DFT) calculations support the premise that the presence of the more electronegative Mg in $LiNH_2$ does indeed destabilise the N – H bond,[70, 71] and experiments have indicated that the N – H bond lengths in NH_2 groups neighbouring Mg were over 0.01Å greater than those in $LiNH_2$.[71]

Similar studies were performed using potassium (a metal of lower electronegativity than Li) as the dopant. The calculations suggested that K-doped $LiNH_2$ would also display a lower decomposition temperature than pure $LiNH_2$ due to destabilisation of the N – H bond, although the effect would be less pronounced than that observed in the Mg – $LiNH_2$ system.[71]

1.8.5 Complex Li – M – N – H Systems

Given that magnesium hydride, MgH_2, is inherently less stable than LiH, it was proposed that replacing LiH with MgH_2 in the Li – N – H system may reduce the decomposition temperature of $LiNH_2$. It was additionally believed that the use of a 2^+ cation would increase the number of structural defects in the material due to charge balancing effects.[72]

This was indeed found to be the case, with the observation that a mixture of MgH_2 + $2LiNH_2$ reversibly desorbed 4.5 wt% H_2 at 200 °C over nine cycles. The reaction enthalpy of the system was found to be 34 $kJmol^{-1}$, which is ~ 17 $kJmol^{-1}$ lower than that of the $LiNH_2$ / LiH system.[72] X-ray powder diffraction of the product showed no Li_2NH or MgNH and so the following reaction scheme was suggested:

$$2LiNH_2 + MgH_2 \leftrightarrow Li_2Mg(NH)_2 + 2H_2 \qquad \text{Equation 1.17}$$

Further studies of this system reported H_2 – absorption beginning at around 70 °C and peaking at 157 °C and hydrogen release peaking at 166 °C.[73] Interestingly, X-ray powder diffraction of the products after re-hydrogenation showed no $LiNH_2$ or MgH_2 but instead $Mg(NH_2)_2$ + LiH, reflecting the increased thermodynamic stability of $Mg(NH_2)_2$ + 2LiH over $2LiNH_2$ + MgH_2, and suggesting that the reversible reaction is that shown in Equation 1.18:

$$Mg(NH_2)_2 + 2LiH \leftrightarrow Li_2Mg(NH)_2 + 2H_2 \quad ^{73} \qquad \text{Equation 1.18}$$

The identity of the dehydrogenated product as $Li_2Mg(NH_2)_2$ has been supported by additional studies.[74, 75]

An alternative reaction pathway was found upon varying the relative proportions of $Mg(NH_2)_2$ and LiH in the starting material. For instance, Leng *et al*[76] found that the reaction of $3Mg(NH_2)_2$ with 8LiH did not lead to the formation of the mixed Li / Mg imide, but instead formed a mixture of magnesium nitride and lithium imide (Equation 1.19).

In studies by Nakamori *et al,*[77, 78] the hydride to amide ratio was further increased to $3Mg(NH_2)_2$ +12LiH, and the products were shown to be a mixture of the magnesium and lithium nitrides (Equation 1.20).

$$3Mg(NH_2)_2 + 8LiH \leftrightarrow Mg_3N_2 + 4Li_2NH + 8H_2 \quad ^{76} \qquad \text{Equation 1.19}$$

$$3Mg(NH_2)_2 + 12LiH \leftrightarrow Mg_3N_2 + 4Li_3N + 12H_2 \quad ^{77, 78} \qquad \text{Equation 1.20}$$

The 3:8 reaction demonstrated a reversible storage capacity of 7 wt%, with H_2 desorption beginning at 140 °C and peaking at 190 °C. The reverse process has been shown to occur at 200 °C under 30 bar H_2.

The 3:12 reaction had a high gravimetric storage density (9.1 wt%) and peak H_2 desorption temperature of 407 °C. This temperature can be reduced by 140 °C upon ball milling with 1% Ti catalyst. No ammonia was observed during the desorption.[77, 78]

The other main area of research regarding the mixed lithium / metal amides and imides is focused on the Li – Ca – N –H system.[73] By analogy to the Li – Mg – N – H system outlined in Equation 1.17, a mixed Li / Ca imide is formed from the dehydrogenation reaction of a mixture of lithium amide with calcium hydride:[79]

$$2LiNH_2 + CaH_2 \leftrightarrow Li_2Ca(NH)_2 + 2H_2 \qquad \text{Equation 1.21}$$

Although the gravimetric storage density is low (4.3 wt%), the temperatures of hydrogen adsorption (70 °C – 132°C) and desorption (140 °C – 206 °C) are both lower than in the 2:1 $LiNH_2$ + MgH_2 case.[73] Unfortunately higher temperatures and lower pressures are required for the system to liberate an amount of hydrogen approaching the theoretical maximum.

1.8.6 Mixed Anion Systems

Systems involving lithium amide and different lithium-based complex hydrides have shown promising results in terms of decomposition temperature and storage capacity.

$LiNH_2$ has been shown to react with lithium borohydride ($LiBH_4$) to produce the lithium amide-borohydride, $Li_4BH_4(NH_2)_3$. This material is structurally very similar to lithium amide, but decomposes with evolution of H_2 in favour of NH_3.[80]

The mixture of $2LiNH_2$ + $LiBH_4$ was shown to desorb 11 wt% H_2 in the temperature range 100 – 350 °C, forming Li_3BN_2.[81] Unfortunately, the exothermic nature of the dehydrogenation reaction implies that the process may be difficult to reverse under normal conditions.

The lithium amide – lithium alanate ($LiNH_2$ – $LiAlH_4$) system has also been investigated, showing that the transformation of $[AlH_4]^-$ to $[AlH_6]^-$ is comparatively easy if carried out in the presence of $LiNH_2$.

A large amount of hydrogen is released upon ball-milling $2LiNH_2$ with $LiAlH_4$, however, as a consequence of the thermodynamics of the system, re-hydrogenation of the material is very difficult.[82]

$$2LiNH_2 + LiAlH_4 \leftrightarrow Li_3AlN_2 + 4H_2 \qquad \text{Equation 1.22}$$

5.1 wt% hydrogen can, however be reversibly stored in Li_3AlN_2 between 100 and 500 °C. The fully re-hydrogenated state is shown to be composed of AlN, LiH and $LiNH_2$.[83]

$$LiNH_2 + 2LiH + AlN \leftrightarrow Li_3AlN_2 + 2H_2 \qquad \text{Equation 1.23}$$

1.9 Li – Na – N – H Compounds

Although the decomposition properties of mixed cation systems have been studied (section 1.8.5), no research has been performed regarding the hydrogen storage potential of the Li – Na – N – H amides.

In the early 80s, Jacobs and Harbrecht[84] found that the condensation of supercritical ammonia over a mixture of Li and Na metals led to the formation of three distinct mixed Li / Na amide phases. Indexing the X-ray diffraction data of the samples led to the assignment of the space groups and lattice parameters listed in Table 1.5 and identification of the phases as $Li_5Na(NH_2)_6$, $Li_3Na(NH_2)_4$ and $LiNa_2(NH_2)_3$.[84] These materials are calculated to have gravimetric storage densities of 7.9 wt%, 7.5 wt% and 6.0 wt%, respectively.

	$LiNa_2(NH_2)_3$	$Li_3Na(NH_2)_4$	$Li_5Na(NH_2)_6$
a (Å)	6.278(2)	5.072 (4)	5.072(3)
b (Å)	6.278(2)	5.072 (4)	5.072(3)
c (Å)	11.142(4)	11.478(5)	34.36 (1)
Space group	$P4_2/m$	$I\bar{4}$	$I\bar{4}$

Table 1.5 : Lattice parameters and space groups of $LiNa_2(NH_2)_3$, $Li_3Na(NH_2)_4$ and $Li_5Na(NH_2)_6$, determined by Jacobs and Harbrecht from indexing of X-ray diffraction data.[84]

A single crystal of $Li_3Na(NH_2)_4$ was formed, and the refinement of single crystal X-ray diffraction data resulted in the complete solution of the $Li_3Na(NH_2)_4$ crystal structure.[84] The material was found to adopt a structure very similar to that of $LiNH_2$ (section 1.4.3), differing in the replacement of ¼ of the Li^+ ions by Na^+ ions at the 2c (0,½,¼) lattice sites. As in $LiNH_2$, the N ions were shown to occupy the 8g (x,y,z) sites, forming a distorted cubic close packed lattice. The metal ions were located in ½ of the tetrahedral interstices, with Li at the 2a (0,0,0) and 4f (0,½,z) lattice sites, and Na at the 2c (0,½,¼) site. The hydrogen ions were located in two distinct 8g (x,y,z) lattice sites.

A schematic diagram of the structure is presented in Figure 1.8, and the atomic positions and lattice parameters are summarised in Table 1.6. The crystal structures for $Li_5Na(NH_2)_6$ and $LiNa_2(NH_2)_3$ were not solved.

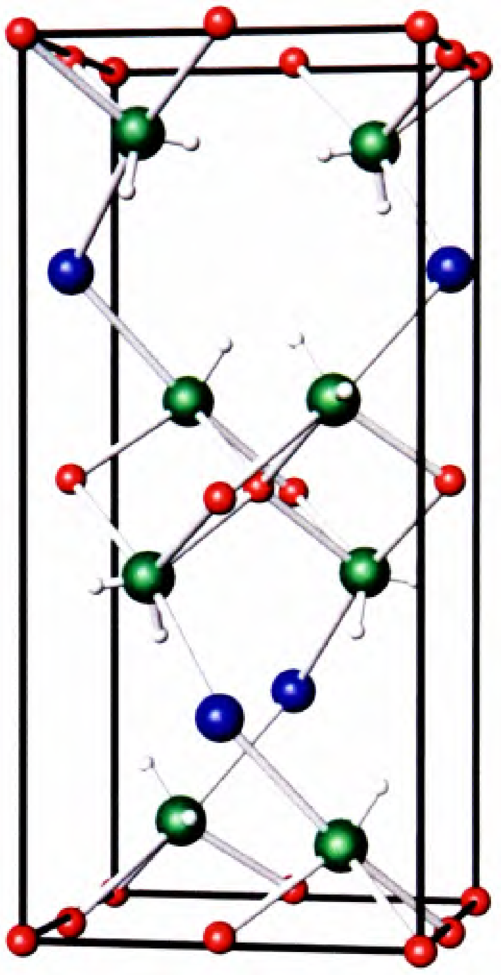

Figure 1.8 : Schematic diagram of the crystal structure of $Li_3Na(NH_2)_4$, space group $I\bar{4}$ (number 82) calculated from single crystal X-ray diffraction data by Jacobs and Harbrecht.[84] Li is represented by red spheres, Na by blue spheres, N by green spheres and H by white spheres.

$Li_3Na(NH_2)_4$

Atom	Site	*x*	*y*	*z*	Occupancy	B_{iso} (Å^2)
Na1	2c	0.0	0.50	0.25	I	0
Li2	2a	0.0	0.0	0.0	I	0
Li3	4f	0.0	0.5	0.0087(5)	1	0
N1	8g	0.2396(4)	0.2380(4)	0.1007(2)	1	0
H1	8g	0.365(5)	0.290(5)	0.110(2)	1	2.0(6)
H2	8g	0.233(7)	0.139(6)	0.168(3)	1	4.9(8)

$a = 5.072(4)$ Å, $c = 11.478(5)$ Å

Table 1.6: Summary of refined structural parameters for $Li_3Na(NH_2)_4$ (space group, $I\bar{4}$ number 82) calculated from single crystal diffraction data.[84]

1.10 Thesis Aims

The work presented in this thesis begins with a detailed thermogravimetric and crystallographic study of the transformations occurring during hydrogen sorption in the Li – N – H system. A number of techniques are used including gravimetric analysis, synchrotron and neutron powder diffraction and variable temperature diffraction. Further work is focused on improving the hydrogen sorption properties of the Li – N – H system through the formation of mixed lithium/sodium amides. Thorough crystallographic analyses of the mixed amides are presented, which are accompanied by crystallographic, calorimetric and thermogravimetric studies of the behaviour of the materials during decomposition.

1.11 References

1. A. W. Titherly, *Journal of the Chemical Society* 1894, 504.
2. E. C. Franklin, *The Nitrogen System of Compounds*, Reinhold, New York, 1935.
3. W. J. Jolly, *Inorganic Chemistry of Nitrogen*, W. A. Benjamin, Inc., New York, 1964.
4. R. J. Mayer, ed., *Lithium, Gmelins Handbuch Der Anorganisgchen Chemie*, System no. 20 edn., Weinghein/Bergstrasse, 1960.
5. I. A. Kaye, *Journal of the American Chemical Society*, 1949, **71**, 2322-2325.
6. I. A. Kaye and I. C. Kogon, *Journal of the American Chemical Society*, 1951, **73**, 5891-5893.
7. C. R. Hauser and J. K. Lindsay, *Journal of the American Chemical Society*, 1955, **73**, 1050.
8. I. Erden, *Handbook of Reagents for Organic Synthesis: Acidic and Basic Reagents*, Wiley, Chichister, 1999.
9. R. Juza and K. Opp, *Zeitschrift fur Anorganische und Allgemeine Chemie*, 1951, **226**, 313 - 324.
10. F. E. Pinkerton, *Journal of Alloys and Compounds*, 2005, **400**, 76 - 82.
11. D. H. Dafert and R. Miklauz, *Monatsh. Chem.*, 1909, **30**, 649.
12. D. H. Dafert and R. Miklauz, *Monatsh. Chem.*, 1910, **31**, 981.
13. O. Ruff and H. Georges, *Berichte der Deutschen Chemischen Gesellschaft*, 1911, **44**, 502.
14. D. H. Dafert and R. Miklauz, *Monatsh. Chem.*, 1912, **33**, 63.
15. P. Chen, Z. T. Xiong, J. Z. Luo, J. Y. Lin and K. L. Tan, *Nature*, 2002, **420**, 302-304.
16. http://www.sc.doe.gov/bes/hydrogen.pdf, Accessed 25.06.09.
17. W. Grochala and P. P. Edwards, *Chemical Reviews*, 2004, **104**, 1283-1315.
18. B. Bogdanovic and M. Schwickardi, *Journal of Alloys and Compounds*, 1997, **253**, 1-9.
19. M. Mamatha, C. Weidenthaler, A. Pommerin, M. Felderhoff and F. Schuth, *Journal of Alloys and Compounds*, 2006, **416**, 303-314.
20. L. Schlapbach and A. Zuttel, *Nature*, 2001, **414**, 353-358.
21. S. I. Orimo, Y. Nakamori, J. R. Eliseo, A. Zuttel and C. M. Jensen, *Chemical Reviews*, 2007, **107**, 4111-4132.
22. G. P. Meisner, F. E. Pinkerton, M. S. Meyer, M. P. Balogh and M. D. Kundrat, *Journal of Alloys and Compounds*, 2005, **404**, 24-26.
23. E. Zintl and G. Brauer, *Zeitschrift fur Elektrochemie und Angewandte Physikalische Chemie*, 1935, **41**, 102.
24. R. Juza, *Fiat Review of German Science*, 1948, **2**, 70.
25. A. Rabenau and H. Schulz, *Journal of the Less-Common Metals*, 1976, **50**, 155-159.

26. U. V. Alpen, A. Rabenau and G. H. Talat, *Applied Physics Letters*, 1977, **30**, 621-623.
27. U. V. Alpen, M. F. Bell and T. Gladden, *Electrochimica Acta*, 1979, **24**, 741-744.
28. M. Mali, J. Roos and D. Brinkmann, *Physical Review B*, 1987, **36**, 3888-3890.
29. H. J. Beister, S. Haag, R. Kniep, K. Strossner and K. Syassen, *Angewandte Chemie - International Edition in English*, 1988, **27**, 1101-1103.
30. R. Juza, *Zeitschrift fur Anorganische und Allgemeine Chemie*, 1951, **266**, 325.
31. T. Noritake, H. Nozaki, M. Aoki, S. Towata, G. Kitahara, Y. Nakamori and S. Orimo, *Journal of Alloys and Compounds*, 2005, **393**, 264-268.
32. M. P. Balogh, C. Y. Jones, J. F. Herbst, J. L. G. Hector and M. Kundrat, *Journal of Alloys and Compounds*, 2006, **420**, 326-336.
33. H. M. Rietveld, *Journal of Applied Crystallography*, 1969, 65-71.
34. P. J. Haigh, R. A. Forman and R. C. Frisch, *Journal of Chemical Physics*, 1966, **45**, 812-&.
35. R. A. Forman, *Journal of Chemical Physics*, 1971, **55**, 1987-&.
36. H. Jacobs and R. Juza, *Zeitschrift fur Anorganische und Allgemeine Chemie*, 1972, **391**, 271-&.
37. D. B. Grotjahn, P. M. Sheridan, I. Al Jihad and L. M. Ziurys, *Journal of the American Chemical Society*, 2001, **123**, 5489-5494.
38. V. Milman and B. Winkler, *Zeitschrift fur Kristallographie*, 2001, **216**, 99-104.
39. K. Miwa, N. Ohba, S. Towata, Y. Nakamori and S. Orimo, *Physical Review B*, 2005, **71**, 1-6.
40. J. B. Yang, X. D. Zhou, Q. Cai, W. J. James and W. B. Yelon, *Applied Physics Letters*, 2006, **88**, 3.
41. M. H. Sorby, Y. Nakamura, H. W. Brinks, T. Ichikawa, S. Hino, H. Fujii and B. C. Hauback, *Journal of Alloys and Compounds*, 2007, **428**, 297-301.
42. J. M. Bijvoet and A. Karssen, *Proceedings of the Koninklijke Nederlandse Academie van Wetenschappen*, 1922, **25**, 27.
43. D. H. Gregory, *Journal of Materials Chemistry*, 2008, **18**, 2321-2330.
44. A. M. Sapse, D. C. Jain and K. R. Ragavachari, *Lithium Chemistry, Wiley: New York*, 1995, 45.
45. E. U. Wurthwein, K. D. Sen, J. A. Pople and P. V. Schleyer, *Inorganic Chemistry*, 1983, **22**, 496-503.
46. A. Hinchliffe and J. C. Dobson, *Theoretica Chimica Acta*, 1975, **38**, 17.
47. P. Chen, Z. T. Xiong, J. Z. Luo, J. Y. Lin and K. L. Tan, *Journal of Physical Chemistry B*, 2003, **107**, 10967-10970.
48. Y. H. Hu and E. Ruckenstein, *Journal of Physical Chemistry A*, 2003, **107**, 9737-9739.
49. T. Ichikawa, N. Hanada, S. Isobe, H. Leng and H. Fujji, *Journal of Physical Chemistry B*, 2004, **108**, 7887 - 7892.
50. S. Isobe, T. Ichikawa, S. Hino and H. Fujii, *Journal of Physical Chemistry B*, 2005, **109**, 14855-14858.
51. M. F. Bell, A. Breitschwerdt and U. Vonalpen, *Materials Research Bulletin*, 1981, **16**, 267-272.
52. W. Hayes and M. T. Hutchings, in *Ionic Solids at High Temperatures Ed. A. M. Stoneham (World Scientific)*, ed. A. M. Stoneham, World Scientific:1989, Editon edn.
53. M. J. Gillian, in *Ionic Solids at High Temperatures Ed. A. M. Stoneham (World Scientific)*, ed. A. M. Stoneham, World Scientific: 1989, Editon edn.
54. T. W. D. Farley, W. Hayes, S. Hull, M. T. Hutchings and M. Vrtis, *Journal of Physics-Condensed Matter*, 1991, **3**, 4761-4781.
55. M. Hayoun, M. Meyer and A. Denieport, *Acta Materialia*, 2005, **53**, 2867-2874.
56. P. J. Haigh, *The Journal of Chemical Physics*, 1966, **45**, 812 - 816.
57. T. Noritake, H. Nozaki, M. Aoki, S. Towata, G. Kitahara, Y. Nakamori and S. Orimo, *Journal of Alloys and Compounds*, 2005, **393**, 264 - 268.
58. W. I. F. David, M. O. Jones, D. H. Gregory, C. M. Jewell, S. R. Johnson, A. Walton and P. P. Edwards, *Journal of the American Chemical Society*, 2007, **129**, 1594 – 1601.
59. A. Huq, J. W. Richardson, E. R. Maxey, D. Chandra and W. M. Chien, *Journal of Physical Chemistry C*, 2007, **111**, 10712-10717.
60. M. O. Jones, W. I. F. David, M. Sommariva, S. R. Johnson, R. M. Ibberson and P. P. Edwards, *In preparation*, 2009.
61. Y. H. Hu and E. Ruckenstein, *Industrial & Engineering Chemistry Research*, 2006, **45**, 4993-4998.
62. Y. H. Hu and E. Ruckenstein, *Industrial & Engineering Chemistry Research*, 2006, **45**, 182-186.
63. Y. H. Hu and E. Ruckenstein, *Industrial & Engineering Chemistry Research*, 2005, **44**, 1510-1513.
64. T. Ichikawa, S. Isobe, N. Hanada and H. Fujii, *Journal of Alloys and Compounds*, 2004, **365**, 271-276.

65. T. Markmaitree, R. M. Ren and L. L. Shaw, *Journal of Physical Chemistry B*, 2006, **110**, 20710-20718.
66. S. Isobe, T. Ichikawa, N. Hanada, H. Y. Leng, M. Fichtner, O. Fuhr and H. Fujii, *Journal of Alloys and Compounds*, 2005, **404**, 439-442.
67. J. H. Yao, C. Shang, K. F. Aguey-Zinsou and Z. X. Guo, *Journal of Alloys and Compounds*, 2007, **432**, 277-282.
68. Y. Nakamori and S. Orimo, *Materials Science and Engineering B*, 2004, **108**, 48-50.
69. Y. Nakamori and S. Orimo, *Journal of Alloys and Compounds*, 2004, **370**, 271-275.
70. S. Orimo, Y. Nakamori, G. Kitahara, K. Miwa, N. Ohba, T. Noritake and S. Towata, *Applied Physics A - Materials Science & Processing*, 2004, **79**, 1765-1767.
71. C. J. Zhang and A. Alavi, *Journal of Physical Chemistry B*, 2006, **110**, 7139-7143.
72. W. F. Luo, *Journal of Alloys and Compounds*, 2004, **381**, 284-287.
73. Z. T. Xiong, G. T. Wu, H. J. Hu and P. Chen, *Advanced Materials*, 2004, **16**, 1522-1525.
74. W. F. Luo and S. Sickafoose, *Journal of Alloys and Compounds*, 2006, **407**, 274-281.
75. Y. Chen, C. Z. Wu, P. Wang and H. M. Cheng, *International Journal of Hydrogen Energy*, 2006, **31**, 1236-1240.
76. H. Leng, T. Ichikawa, S. Hino, N. Hanada, S. Isobe and H. Fujji, *Jounal of Physical Chamistry B*, 2004, **108**, 8763 - 8765.
77. Y. Nakamori, G. Kitahara, K. Miwa, S. Towata and S. Orimo, *Applied Physics A - Materials Science & Processing*, 2005, **80**, 1-3.
78. Y. Nakamori, G. Kitahara, K. Miwa, N. Ohba, T. Noritake, S. Towata and S. Orimo, *Journal of Alloys and Compounds*, 2005, **404**, 396-398.
79. G. T. Wu, Z. T. Xiong, T. Liu, Y. F. Liu, J. J. Hu, P. Chen, Y. P. Feng and A. T. S. Wee, *Inorganic Chemistry*, 2007, **46**, 517-521.
80. P. A. Chater, W. I. F. David, S. R. Johnson, P. P. Edwards and P. A. Anderson, *Chemical Communications*, 2006, 2439-2441.
81. F. E. Pinkerton, G. P. Meisner, M. S. Meyer, M. P. Balogh and M. D. Kundrat, *The Journal of Physical Chemistry B*, 2005, **109**, 6 - 8.
82. Z. T. Xiong, G. T. Wu, J. J. Hu and P. Chen, *Journal of Power Sources*, 2006, **159**, 167-170.
83. P. Chen, Z. T. Xiong, G. T. Wu, Y. F. Liu, J. J. Hu and W. F. Luo, *Scripta Materialia*, 2007, **56**, 817-822.
84. H. Jacobs and B. Harbrecht, *Journal of the Less-Common Metals*, 1982, **85**, 87 - 95.

~ Chapter Two ~

Experimental Techniques

2.1 Crystallography

2.1.1 **Introduction to Crystallography**

The diffraction of X-rays and neutrons by a crystal lattice is one of the most powerful analytical tools used for the structural determination of crystalline materials. Crystalline materials are defined as substances in which the constituent atoms, ions and molecules are packed in a regularly ordered repeating pattern, extending in all three spatial dimensions. The structures of such materials are based upon a *crystal lattice*, which is an infinite array of lattice points in space, each of which is related to other lattice points by translation.

Around each lattice point is located a single atom, or group of atoms, known as the structural *motif.* The motif is the smallest repeating unit in the crystal and is assigned to one of 32 different crystallographic *point groups*, according to its symmetry.

Joining adjacent lattice points with straight lines produces a *unit cell*, which displays the full symmetry of the crystal. The edges of the unit cell are called *unit cell parameters* (or *lattice parameters*) and are labelled a, b and c. The angles between the lattice parameters are denoted α (c/b) β (c/a) and γ (a/b).

There are 14 distinct crystallographic lattice types, referred to as *Bravais lattices,*[1] each of which falls into one of five categories:

i) Primitive (P) - The unit cell is defined by one equivalent point at each corner.

ii) Body centred (I) - In addition to criteria for a primitive cell, there is an equivalent lattice point at the centre of the unit cell.

iii) Face centred (F) - The unit cell has equivalent points at each corner and at the centre of each face.

iv) Rhombohedral (R) - The unit cell has three interaxial equal and acute angles.

v) Centred on a single face (A, B or C) - The unit cell has only one centred face, and is described by the letter not used to describe the face; for example, a unit cell in which the *ab* face is centred is described as *C*.

These five lattice types are then divided up according to the relative lengths of the three lattice parameters a, b and c and unit cell angles α, β and γ, producing the 14 distinct Bravais lattices.

The combination of the symmetry of the 14 Bravais Lattices and the symmetry of the 32 crystallographic point groups leads to a total of 73 different *space groups*. The inclusion of translational symmetry elements (screw axes and glide planes) generates a further 157, leading to a total of 230 different crystallographic space groups.[1]

2.1.2 **Diffraction**

When a periodic array of objects each scatter radiation coherently, constructive interference occurs at specific angles. Since a crystalline material is essentially an ordered periodic array of atoms around lattice points, if irradiated, such materials will behave in the same way as a diffraction grating, with each atom acting as a point source for new beams. Constructive interference between these beams will only occur in certain allowed directions, which are dictated by the separation of the crystal planes in the material. These distances are of the order of a few angstroms (Å) and so radiation of an appropriate energy lies within the X-ray region of the electromagnetic spectrum.

Wave-particle duality suggests that electrons and neutrons of appropriate velocity will interact with crystalline matter in a similar way.

2.1.2.1 X-Ray Diffraction

The oscillating electromagnetic field of X-ray radiation interacts with the oscillating electromagnetic field of electrons in matter, resulting in the coherent scattering of the radiation.

Because crystalline materials consist of a regular three-dimensional array of particles, a great number of different translational relationships exist between the various planes within the materials. A crystal may therefore diffract monochromated radiation in many different directions, with the diffraction angles depending on the various periodic relationships between the atomic planes within the crystal.

The Laue Conditions[2]

The first instance of X-ray diffraction was reported in 1912 by Max von Laue, who stated that constructive interference requires that the path difference between X-rays scattered by different planes is an integer number of wavelengths. Therefore, if the wave-vector of the incident beam is $\boldsymbol{k_i}$ and the wave-vector of the outgoing beam is $\boldsymbol{k_o}$, and $\boldsymbol{k_i} - \boldsymbol{k_o} = \boldsymbol{\Delta k}$ (the scattering vector), Equation 2.1a must be satisfied for constructive interference, where a corresponds to the lattice spacing in the unit cell, θ_i and θ_0 are the incident and outgoing angles of the beam to the horizontal (Figure 2.1) and h is an integer value.

$$\Delta\mathbf{k} = a\sin\theta_i + a\sin\theta_0 = h\lambda \qquad \text{Equation 2.1a}$$

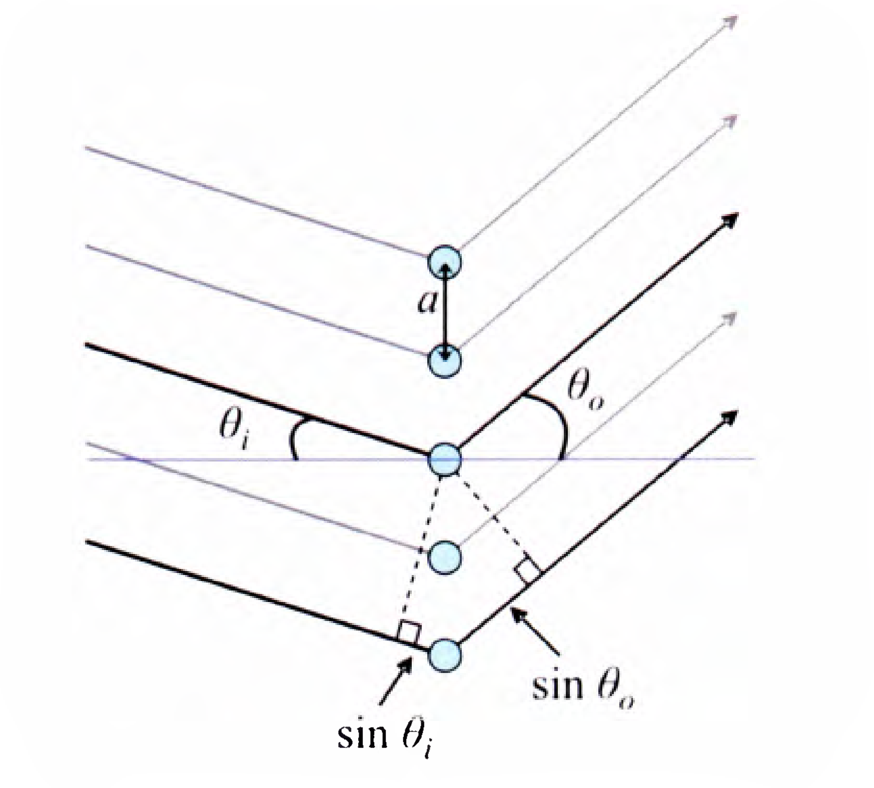

Figure 2.1: Schematic diagram of the Laue Condition for X-ray diffraction in 1 dimension. Similar conditions must also be satisfied in the remaining two dimensions.

This equation and Figure 2.1 only show diffraction occurring within the plane of the paper; however, since a crystal is a three dimensional array of particles, similar conditions for the remaining two directions must also be simultaneously satisfied:

$$\Delta\mathbf{k} = b\sin\sigma_i + b\sin\sigma_0 = k\lambda \qquad \text{Equation 2.1b}$$

$$\Delta\mathbf{k} = c\sin\phi_i + c\sin\phi_0 = l\lambda \qquad \text{Equation 2.1c}$$

These three equations, known as the Laue equations can be simplified to the Bragg equation, which is the universally used basis for X-ray diffraction.

Bragg's Law[3]

Bragg demonstrated that every diffracted beam produced by a crystal in an appropriate orientation can be regarded as if it was reflected from a series of parallel planes passing through the lattice points (Figure 2.2). This draws an analogy between X-ray diffraction and the reflection of light from a plane mirror. The crystal planes, normal, and the incident and the reflected beams are all located within the same plane, and as such, Snell's law states that the angle of incidence is equal to the angle of reflection.

In order to define a set of crystal planes, it is necessary to describe their orientation within the lattice relative to the unit cell. This is achieved through the assignment of three indices *h*, *k* and *l* (known as *Miller indices*) to every plane, such that all planes with a specified *hkl* set will intersect the unit cell at *a/h*, *b/k* and *c/l*.

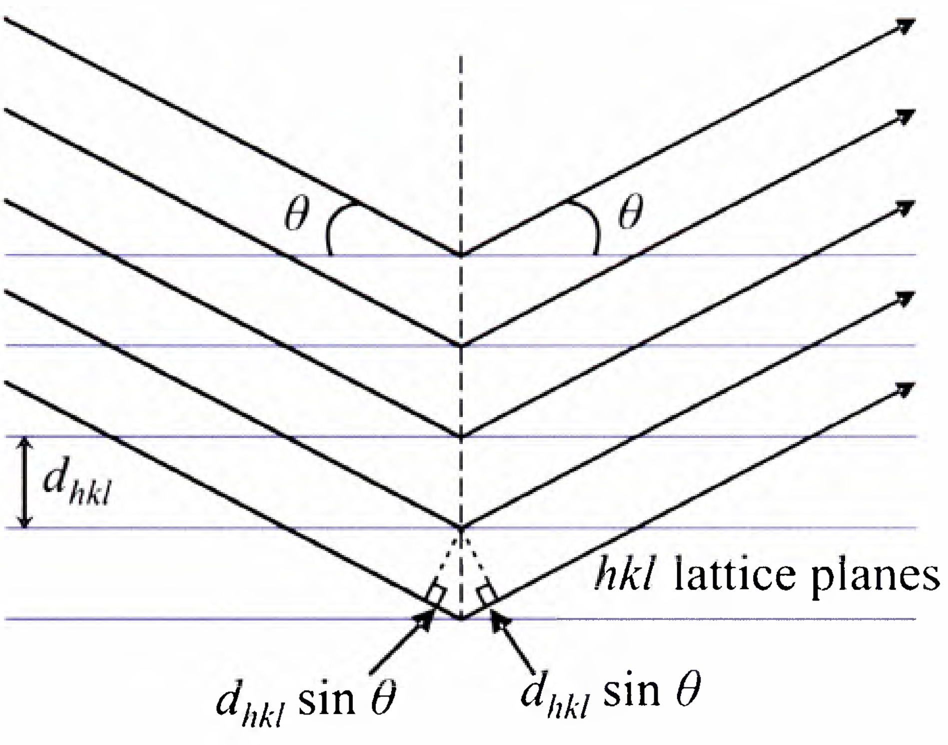

Figure 2.2: Schematic diagram of the Bragg condition for X-Ray diffraction.

Each *hkl* plane is separated by a distance d_{hkl}, and constructive interference between diffracted waves is only observed when the path difference of the incident waves is equal to an integer number of wavelengths.[2] According to Figure 2.2 the path difference between the beams reflecting from two adjacent planes is $2d_{hkl}\sin\theta$. Therefore, the condition required for the constructive interference of the X-rays is:

$$2d_{hkl}\sin\theta = n\lambda \qquad \text{Equation 2.2a}$$

where *n* is an integer. In practice, *n* can be set to 1[4] and so the Bragg equation becomes:

$$\lambda = 2d_{hkl}\sin\theta \qquad \text{Equation 2.2b}$$

Reciprocal Space

Whilst Bragg's law gives us a relatively straight-forward visual model of the processes occurring during diffraction, the most useful method for describing diffraction phenomena involves the discussion of the *reciprocal lattice* as developed by Ewald.[5] The limitation of the Bragg equation is that it restricts the analysis of data from a three-dimensional crystal into only two-dimensions. This problem can be solved by representing the lattice planes of the *real lattice* as *reciprocal lattice points,* such that the d_{hkl} plane is represented in the reciprocal lattice as a point at a distance of d_{hkl}^* from the origin:

$$d^*_{hkl} = 1/d_{hkl} \qquad \text{Equation 2.3}$$

The units are reciprocal angstroms (Å^{-1}) and the space is referred to as *reciprocal space*. The unit cell parameters of this lattice are referred to as a^*, b^* and c^* and the reciprocal of the angles α, β and γ as α^*, β^* and γ^* (where the reciprocal of an angle is defined as the compliment, i.e. 180° – the real-space angle).

This simplifies matters somewhat, as a set of *hkl* Bragg planes in the real lattice is represented by a vector in the reciprocal lattice which can be resolved into its components:

$$\mathbf{d}^*_{hkl} = ha^* + kb^* + lc^* \qquad \text{Equation 2.4}$$

The Ewald Sphere

The real application of the reciprocal lattice comes when we consider how an incident beam interacts with a crystal, (Figure 2.3). If an incident X-ray beam (labelled IO in Figure 2.3) interacts with a crystal at a point C (Figure 2.3), it will be diffracted. Diffraction will only occur towards a particular point (labelled A), if that point coincides with a reciprocal lattice point, d_{hkl}^*.

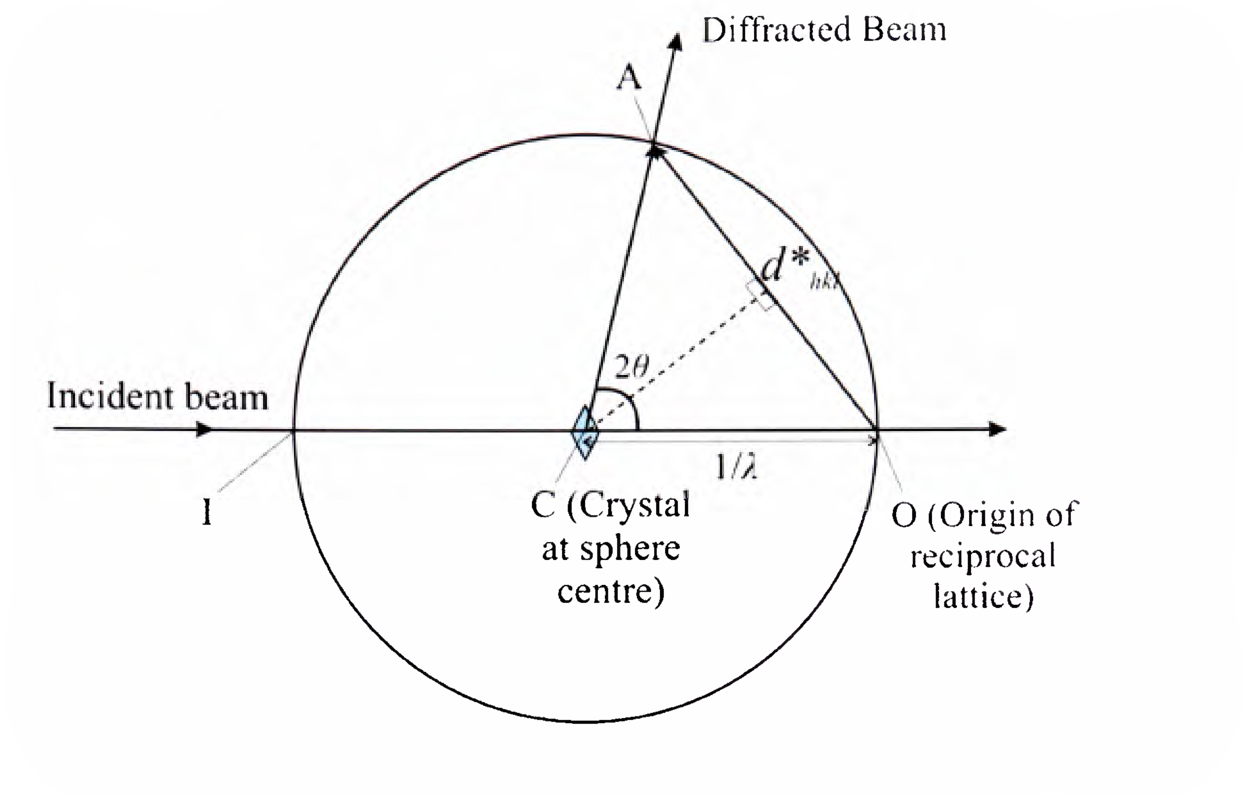

Figure 2.3: A planar section of the Ewald reflecting sphere

This will occur only when Bragg's law is satisfied in reciprocal space (Equation 2.5a). Braggs Law (Equation 2.2b) can be rearranged into Equation 2.5b.

$$\mathrm{OA}=\mathbf{d}^*_{hkl} = {}^{1}\!/_{d_{hkl}} = 2\mathrm{CO}\sin\theta = \mathrm{IO}\sin\theta \qquad \text{Equation 2.5a}$$

$$\frac{1}{d_{hkl}} = \frac{2\sin\theta}{\lambda} \qquad \text{Equation 2.5b}$$

Comparison of Equations 2.5a and 2.5b leads to Equation 2.5c, which shows that Bragg's law in reciprocal space is met only when reciprocal lattice points lie on the surface of a sphere centred at the crystal and with radius 1/ λ. This is known as the Ewald sphere.

$$\mathrm{IO} = {}^{2}\!/_{\lambda} \qquad \text{Equation 2.5c}$$

Given that the reciprocal lattice is directly related to the real lattice, rotation of a crystal in the real lattice will lead to an equal rotation in the reciprocal lattice. If the crystal is rotated, each point of the reciprocal lattice up to a distance of 2/λ from the origin will intersect the sphere of reflection.

The Intensities of Bragg Reflections

X-ray diffraction measures the intensity, I, of diffraction peaks (or *Bragg reflections*) as a function of the angle between the incident and diffracted beams, 2θ, at a constant wavelength, λ. The relative intensities of the peaks in a diffraction pattern and the arrangement of atoms in the crystal are related to each other by a *Fourier Transformation*; that is, the diffraction pattern of a crystal is the Fourier transform of the electron density within the crystal (and vice versa).

The intensity of a diffracted beam is given by Equation 2.6,[6] where ψ_{hkl} is the wavefunction of the beam scattered by the *hkl* plane, L is the Lorentz polarisation factor, p is the polarisation correction, F_{hkl} is the structure factor and s is a scale factor (which takes into account the constants of the experimental system, the multiplicity of the *hkl* reflection, the volume fraction of the material within the sample and the volume of the unit cell).

$$I_{hkl} = |\psi_{hkl}|^2 = sLp|F_{hkl}|^2 \qquad \text{Equation 2.6}$$

The structure factor, F_{hkl}, is the dominating term in the equation. It is a complex number describing the way in which an incident beam is scattered by atoms in a unit cell. It takes into account the relative scattering powers and positions of all the atoms present and is calculated according to Equation 2.7, or (equivalently) Equation 2.8.[6] In these equations, $f_n(\theta)$ is the scattering factor and x_n, y_n and z_n are the fractional coordinates of atom n.

$$F_{hkl} = \sum_{n=1}^{N} f_n(\theta)\exp\left[2\pi i\left(hx_n + ky_n + lz_n\right)\right] \qquad \text{Equation 2.7}$$

$$\begin{aligned} F_{hkl} = &\sum_{n=1}^{N} f_n(\theta)\left[\cos 2\pi\left(hx_n + ky_n + lz_n\right)\right] \\ &+ i\sum_{n=1}^{N} f_n(\theta)\left[\sin 2\pi\left(hx_n + ky_n + lz_n\right)\right] \end{aligned} \qquad \text{Equation 2.8}$$

If the crystal structure of the diffracting material is centro-symmetric (I.E. the same atom is present at x, y, z and $-x$, $-y$, $-z$) the imaginary part of the structure factor reduces to zero (since $\sin x = -\sin x$) and hence the structure factor can be described by Equation 2.9.

$$F_{hkl} = \sum_{n=1}^{N} f_n(\theta)\left[\cos 2\pi\left(hx_n + ky_n + lz_n\right)\right] \qquad \text{Equation 2.9}$$

The equations used to calculate the structure factor indicate that the intensities of X-ray reflections depend upon the atomic location, the thermal motion of the atoms within the material (through the scattering factor $f_n(\theta)$) and the site occupancies within the structure. During the collection of diffraction data, much of this information is lost; it is only by modelling the intensities of the various diffraction peaks that such information can be recovered.

Upon recovery, the data undergo a reverse Fourier transformation to give the electron distribution of the sample, from which the atomic make-up of the material can be determined.

2.1.2.2 X-ray Powder Diffraction (XRPD).

The diffraction discussed up until now has assumed that the diffracting materials were single crystals. Whilst single crystal materials can indeed be formed, it is well known that the majority of materials are polycrystalline (powders), composed from millions of tiny crystallites.

The great number of crystallites in such materials means that a polycrystalline sample will contain powder grains orientated in all directions. As such, some crystallites in the powder will be fortuitously orientated at the Bragg angle to the incident radiation for each *hkl* lattice plane. This means that during X-ray powder diffraction (XRPD) measurements, all sets of *hkl* planes will be irradiated simultaneously at every angle of the incident beam.

In terms of the Ewald sphere, the scattering vectors are no longer found to lie at discrete reciprocal lattice points, but instead are found on the surface of spheres with radii d_{hkl}^*, as shown in Figure 2.4.

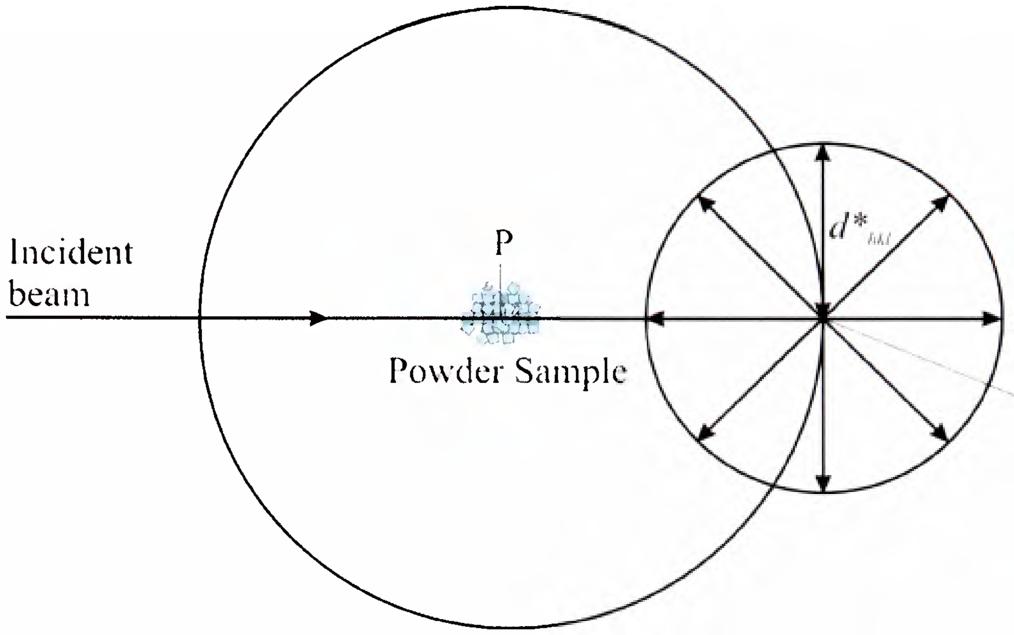

Figure 2.4: A slice taken through the Ewald reflecting sphere in X-ray powder diffraction

Constructive interference occurs only when the scattering vectors lie at the intersection of the Ewald sphere and a series of concentric spheres located at the origin of the reciprocal lattice.[1] The points of intersection form a number of concentric circles which, when joined to the crystal origin, form a series of concentric cones of varying intensity, known as *Debye-Scherrer cones* (Figure 2.5). These patterns are projected onto a 2D detector, and therefore appear as a series of concentric circles.[1]

It is important to note that, due to the two-dimensional nature of the detector, lattice planes of equivalent d-spacing but different *hkl* values appear at the same value of 2θ and hence cannot be resolved. In addition, diffraction peaks have a finite width, and therefore peak overlap often occurs for planes of similar scattering angle.[1]

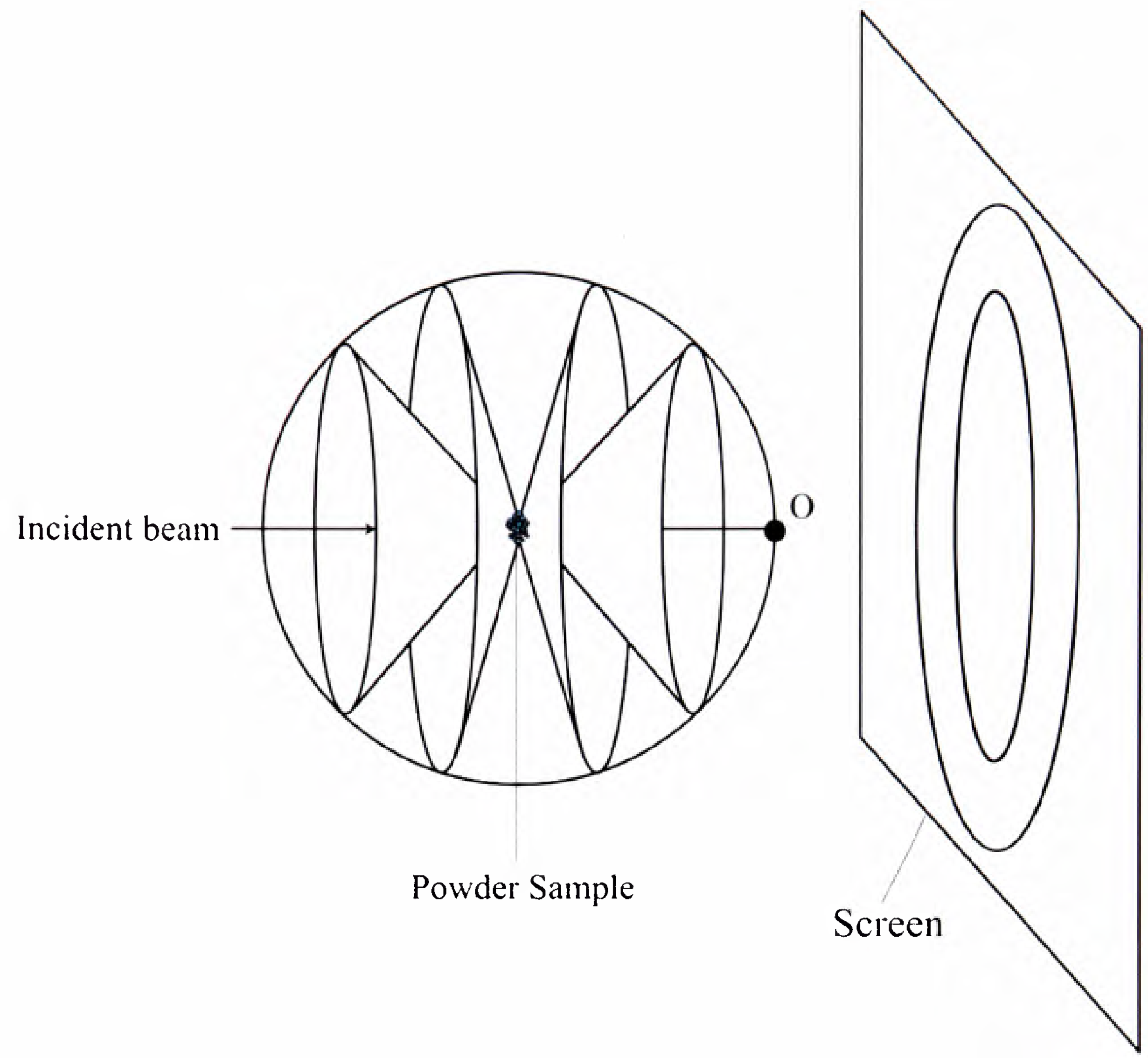

Figure 2.5: Schematic diagram of Debye-Scherer cones in X-ray powder diffraction

This leads to difficulty in the assignment of absolute intensities for reflections and hence, gaining complete structure solution from X-ray powder diffraction data is very difficult.

Until recently, structure solution from X-ray diffraction could only be achieved using single crystal measurements, however, the collection of high resolution data using high intensity synchrotron beams has led to increased "*ab inito*" structure solution from powder diffraction data.

Where a reasonable structure model is known, *refinement* of this model is possible through the comparison of a calculated model with experimental diffraction data. The crystal structure of the material studied can be established by minimising the difference between the calculated model and the diffraction data using one of several refinement techniques, which are discussed in more depth later (section 2.1.4.).[7]

X-ray powder diffraction data is also widely used as a fingerprinting technique to assess the compositional purity of samples. This can be achieved by comparison of experimental data with known diffraction patterns of various compounds which are collected together in crystallographic databases.[8]

2.1.2.3 Laboratory Equipment

PANalytical X'Pert Diffractometer

X-ray diffraction measurements for samples studied during this thesis were carried out regularly on a PANalytical X'Pert diffractometer. X-rays were produced through the acceleration of electrons from a 40mA filament tube through a potential voltage of 45kV towards a copper (Cu) anode. The accelerated electrons provide the energy required for ionisation of a core Cu 1s electron. An electron from a higher energy orbital then falls, resulting in the emission of X-ray radiation. Two electron transitions are possible at the Cu anode. These are the 2p to 1s (K_α) and the 3p to 1s (K_β) transitions, the first of which (K_α) occurs most frequently. The radiation emitted from this transition is therefore selected for use. Given that there are two populated spin states of a 2p electron ($^2P_{3/2}$ and $^2P_{1/2}$) the transition from 2p to 1s is a doublet, $K_{\alpha1}$ / $K_{\alpha2}$, with wavelengths 1.54051 and 1.54433 Å, respectively. The probability of transition from the $^2P_{3/2}$ state is twice that of the $^2P_{1/2}$ state and hence $K_{\alpha1}$ is isolated from $K_{\alpha2}$ and K_β radiation by a monochromator (a cut Ge (111) crystal) placed in the path of the beam.

The diffractometer operates in Bragg-Brentano geometry from a fixed X-ray source with the detector set on the 2θ axis. The divergence slit is automatically adjusted in order to maintain a fixed sample irradiation area throughout the scan.

For measurement, samples were finely ground in the glove box and mounted onto a greased glass slide. The slide was then inserted into an airtight sample holder and transferred to the diffractometer. Measurements were carried out between 2θ = 10° and 70° using a step-size of 0.008°.

Synchrotron X-ray Powder Diffraction and the ID31 Beamline at the European Synchrotron Radiation Facility[9]

High-resolution X-ray powder diffraction data were collected on many samples using the ID31 beamline at the European Synchrotron Radiation Facility (ESRF) in Grenoble, France.

Synchrotron radiation is characterised by its high-intensity, which is many magnitudes greater than that achieved using conventional X-ray tubes. Synchrotron radiation is generated from the acceleration of charged particles around a ring at relativistic velocities.

At the ESRF, electrons are accelerated to high speeds to achieve a final energy in the GeV range. These electrons are stored under ultrahigh vacuum ($<1.33 \times 10^{-13}$ Bar) on a closed loop to minimise collision, and are forced to circle the loop by strong magnetic fields. The change of direction (and hence acceleration) of the electrons leads to the emission of X-ray radiation at frequencies in the keV region, which is variable depending on the velocity of the electrons. The X-rays are emitted tangentially to the electron's circular orbit and are polarised in the direction perpendicular to the magnetic field.

Despite the ultrahigh vacuum, the number of electrons in the ring (and hence the flux of the radiation produced) decreases with time due to collisions between electrons and other particles and electron-electron events which occur in the ring. To negate this effect, a large number of "electron bunches" are injected into the ring every 24 hours.

The radiation received at an experimental station consists of a series of pulses. Every pulse of radiation has a duration of the order of a nanosecond (several orders of magnitude less than the time resolution achieved in the experiment) and hence the mean intensity of the beam can be considered to be constant with time.

The ID31 beamline operates at an energy range of between 5 and 60 keV. The diffraction data presented during this thesis were collected using a wavelength of around 0.8 Å and a step-size of 0.003°. The wavelength is selected by rotation of a water-cooled double crystal Si (111) monochromator. A bank of nine scintillation detectors, each spaced ~2° apart, measure the diffracted intensity as a function of 2θ, with each detector preceded by a Ge (111) crystal analyser. The nine crystals are mounted on a single rotation stage so that only a single adjustment is necessary when changing the wavelength.

The diffractometer was operated in Debye-Scherrer transmission geometry. Samples were loaded into borosilicate glass capillary tubes (diameter 0.8 mm – 1.1 mm) within a N_2 atmosphere glove bag. The capillaries were then fitted with a glass rod and temporarily sealed using vacuum grease. After removal from the glove bag, the capillaries were sealed permanently using a gas-oxygen flame. The capillaries were rotated in the beam during data collection in order to give a good powder average.

The high intensity of the incident synchrotron radiation is such that the acquisition time required to collect diffraction patterns is very short. Typically, only 10 - 15 minutes are required to collect data of refinable quality with typical peak intensities of order of 10^4 counts.

The short time required for data collection means that synchrotron radiation can be easily used for screening large numbers of samples in a comparatively short space of time. The ID31 beamline is set up in such a way as to allow a total of 50 different sample capillaries to be loaded onto a disc, which, when used in conjunction with a robot arm, permits the automated collection of high-quality data from a large number of samples (Figure 2.6).

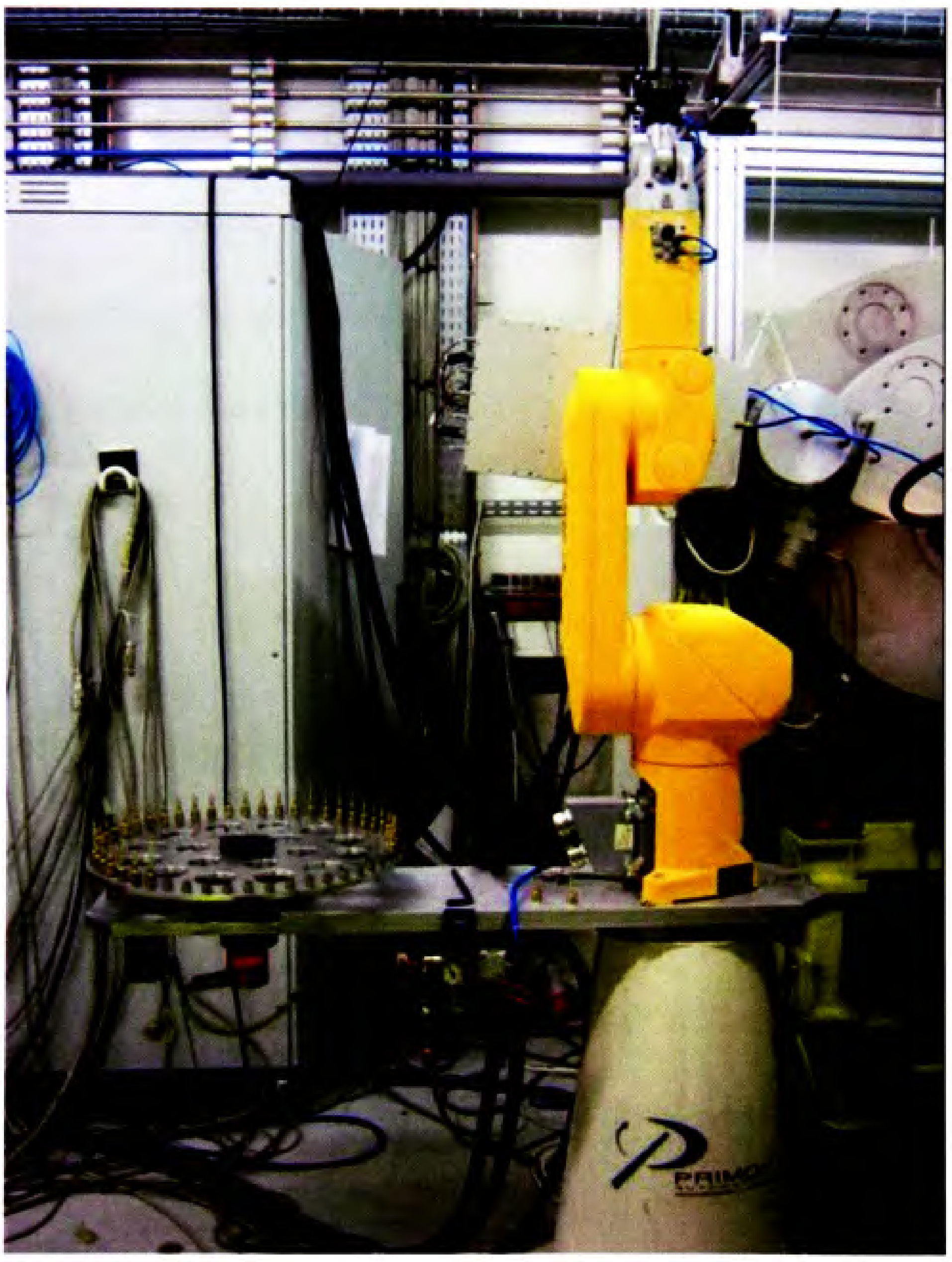

Figure 2.6: Sample loading disc and robot arm used at the ID31 beamline, ESRF, Grenoble.

The short time required for data collection also suggests the possibility of *in-situ* diffraction studies for reactions in the synchrotron beam. The diffractometer can be fitted with a cryostream or heater and hence can be used to study crystallographic changes over a wide range of temperatures.

2.1.2.4 Limitations of X-ray Powder Diffraction

X-ray diffraction unfortunately has a number of limitations, which means that it is not a universally appropriate technique for all crystalline materials.

The first and greatest of these limitations is the dependence of the diffraction intensity on the square of the structure factor (*F(hkl)*) of the atoms.

As introduced in Equation 2.9, *F(hkl)* is related to the sum of the scattering factors, *f(θ)*, of all of the atoms in the unit cell. The scattering factor of a specific atom is calculated by summing the contributions from all electrons in the atom, as outlined in Equation 2.10, where *e* is the charge of an electron, *m* is the electron mass and *c* is the speed of light in free space.[1]

$$f(\theta) = \frac{1}{2}(1+\cos 2\theta)\frac{e^2}{mc^2}\int \psi\psi^* \exp\,(ikr)\,\mathrm{dT} \qquad \text{Equation 2.10}$$

F(hkl) therefore has a significant dependence on atomic number (*Z*), and hence the intensity of the diffraction data, I, depends upon the square of *Z*. There are three important consequences of this dependence. Firstly, it is not possible to distinguish between atoms of similar atomic number by X-ray diffraction. Secondly, the diffraction pattern of a material containing both heavy and light atoms will be dominated by scattering from heavy atoms (high *Z*) and information regarding light atoms (low *Z*) will be difficult to extract. Thirdly, with only one electron, hydrogen cannot be observed using X-ray diffraction.

Equation 2.10 also shows that the scattering factor ($f(\theta)$) has a dependence on 2θ, and decreases with increasing θ. This decrease arises because the destructive interference between the scattered waves from different parts of the electron distribution increases with θ. This means that most data collected at high angle ($2\theta > 70°$) is generally not suitable for use. Furthermore, the atomic scattering factor *f(θ)* applies only to stationary atoms, and atoms are known to vibrate. This vibration smears out the electron density, increasing the size of the electron cloud and leading to a drop in intensity with increasing θ.

In light of these limitations, X-ray diffraction is often supplemented by other techniques.

2.1.3 Neutron Powder Diffraction

Neutrons of appropriate energy can also be of a suitable wavelength to interact with atoms. Unlike X-ray diffraction where the incident radiation interacts with (and is diffracted by) the electrons of an atom, neutrons interact with the nucleus and hence there is no systematic dependence of neutron scattering factor on the atomic number, Z.

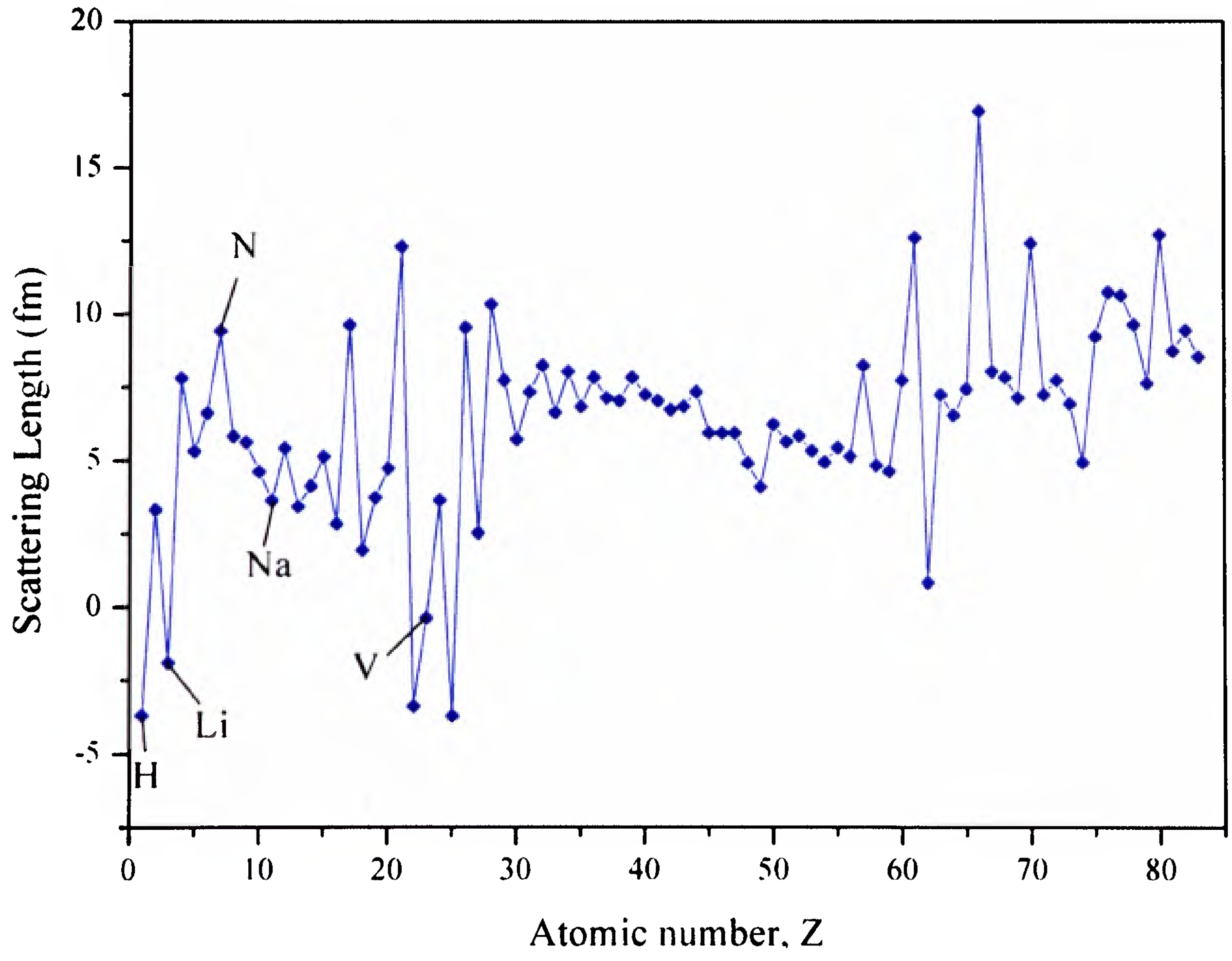

Figure 2.7 : Variation of coherent neutron scattering cross section with atomic number across the Periodic Table. Labelled elements are those studied in this work.

This makes neutron diffraction an extremely powerful technique for locating light atoms which are poor X-ray scatterers (particularly hydrogen), and for differentiating between isoelectronic (or almost isoelectronic) atoms within a material. Figure 2.7 presents the variation of the scattering length of atoms across the Periodic Table.[10]

The scattering of neutrons by atoms can occur in both a coherent and an incoherent way. *Coherent scattering* occurs when the scattered waves from different nuclei of the same atom-type interfere constructively. *Incoherent scattering* occurs when the isotopic order of the sample destroys local order, thus reducing interference between the scattered waves. Whether neutrons interact coherently or incoherently with a sample depends on the natural isotopic and spin-mixture of the sample, and all atoms have both a coherent and an incoherent neutron scattering cross section.[11]

Neutron diffraction is concerned with the coherent scattering of neutrons, and hence nuclei with a high incoherent scattering cross section are not suitable for neutron diffraction studies. Fortunately, because neutrons interact with, and are scattered by, the nucleus of an atom, different isotopes of the same element interact with neutrons in a different way. For example, hydrogen (^{1}H) has a high incoherent scattering cross section and a low coherent scattering cross section, and as such, is a poor nucleus for neutron diffraction. Deuterium (^{2}H or D), however, has a low incoherent scattering cross section and a high coherent scattering cross section, and is therefore a very good nucleus for neutron diffraction. As such, neutron diffraction experiments often involve the study of isotopically enriched samples.

Neutron diffraction has a number of other advantages over X-ray diffraction. Firstly, the wavelength of the incident neutron beam is several orders of magnitude greater than the size of the nucleus with which it interacts, meaning that radiation scattered from different parts of a nucleus does not have any significant difference in path length. The atomic scattering factor therefore shows no angular dependence and useful data can therefore be collected angles as high as 180° (*cf* $2\theta < 70°$ in X-ray diffraction).

Additionally, the uncharged nature of neutrons means that penetration into materials is great, resulting in the acquisition of data from the bulk of the materials studied, rather than from the surface. An added advantage of high neutron penetration is the ability to perform variable temperature measurements, since bulky furnaces and cryostats are more easily penetrated by neutrons than by X-rays.

Unfortunately, neutron diffraction is not without some disadvantages. Neutrons are much harder to produce than X-rays, meaning that neutron facilities are very expensive to run, and hence much less common than X-ray facilities. Neutrons also have a weaker interaction with matter than X-rays, which, coupled with the lower intensity of neutron sources compared to X-ray sources, means that large sample sizes (around 2g) and long collection times (~ 1 hour) are required to ensure a good signal-to-noise ratio (*cf* 20 mg of sample and 15 minutes collection time required for synchrotron X-ray diffraction). Finally, the high intensity of X-ray sources can be sacrificed in favour of high resolution and X-ray diffraction can therefore be capable of measuring very small structural distortions. Such compensation is not possible in neutron diffraction and as such, small structural distortions can often not be resolved from neutron studies.

2.1.3.1 ISIS Pulsed Neutron Facility

The neutron powder diffraction data presented during this thesis were collected using the GEneral Materials diffractometer (GEM) at the ISIS pulsed neutron source.

The neutrons at ISIS are produced *via spallation.* Spallation is the process by which a heavy metal target (tungsten in this case) is bombarded with pulses of high-energy protons which disrupt the atomic nuclei of the target, resulting in the expulsion of neutrons. These neutrons are then *moderated* (slowed) and *collimated* for use in *time-of-flight* (t-o-f) measurements.[12]

During measurement, the sample is irradiated with the neutron beam in regular pulses. The neutrons travel a known distance, *L,* from the source to sample, and then to a fixed detector which records the arrival time of the neutrons, or their time-of-flight (*t*). According to the de Broglie relationship, the neutron's wavelength is related to its momentum. The d-spacing of the *hkl* planes can therefore be calculated by combining the de-Broglie relationship with Bragg's law as shown in Equation 2.11, where *m* is the neutron mass and *h* is Plank's constant.

$$n\lambda = \frac{nh}{mv} = \frac{nht}{mL} = 2d_{hkl}\sin\theta \qquad \text{Equation 2.11}$$

Substitution of the values for *m* and *n* gives

$$t = 505.56Ld_{hkl}\sin\theta \qquad \text{Equation 2.12}$$

The t-o-f technique allows an entire diffraction pattern to be measured by a single detector, however, to reduce measurement time, t-o-f diffractometers have a large number of detectors arranged in a series of different "*banks*", each with its own characteristic resolution, d-spacing and count rate.

The GEneral Materials Diffractometer (GEM).

The GEneral Materials diffractometer (GEM) is designed to be a high-intensity, good-resolution machine, particularly suitable for structural studies of both crystalline powders and disordered materials.

The length of the evacuated primary flight path from moderator to sample is relatively long at 17 m, which leads to high resolution of up to Δd/d = 2-3 x 10^{-3} in backscattering and Δd/d = 5 x 10^{-3} at the 90° detector bank, constant at all d-spacing values. The detector array on GEM has a very large area of 7.270 m^2 and a large range in scattering angles from 1.2° – 117.4°. Slits are used in order to minimise interaction of the neutron beam with anything other than the sample. Figure 2.8 is a schematic diagram of the layout of GEM.[13]

The neutron diffraction data presented in this thesis were measured from powdered, deuterated samples, which were loaded in vanadium cans of diameter 8 mm.

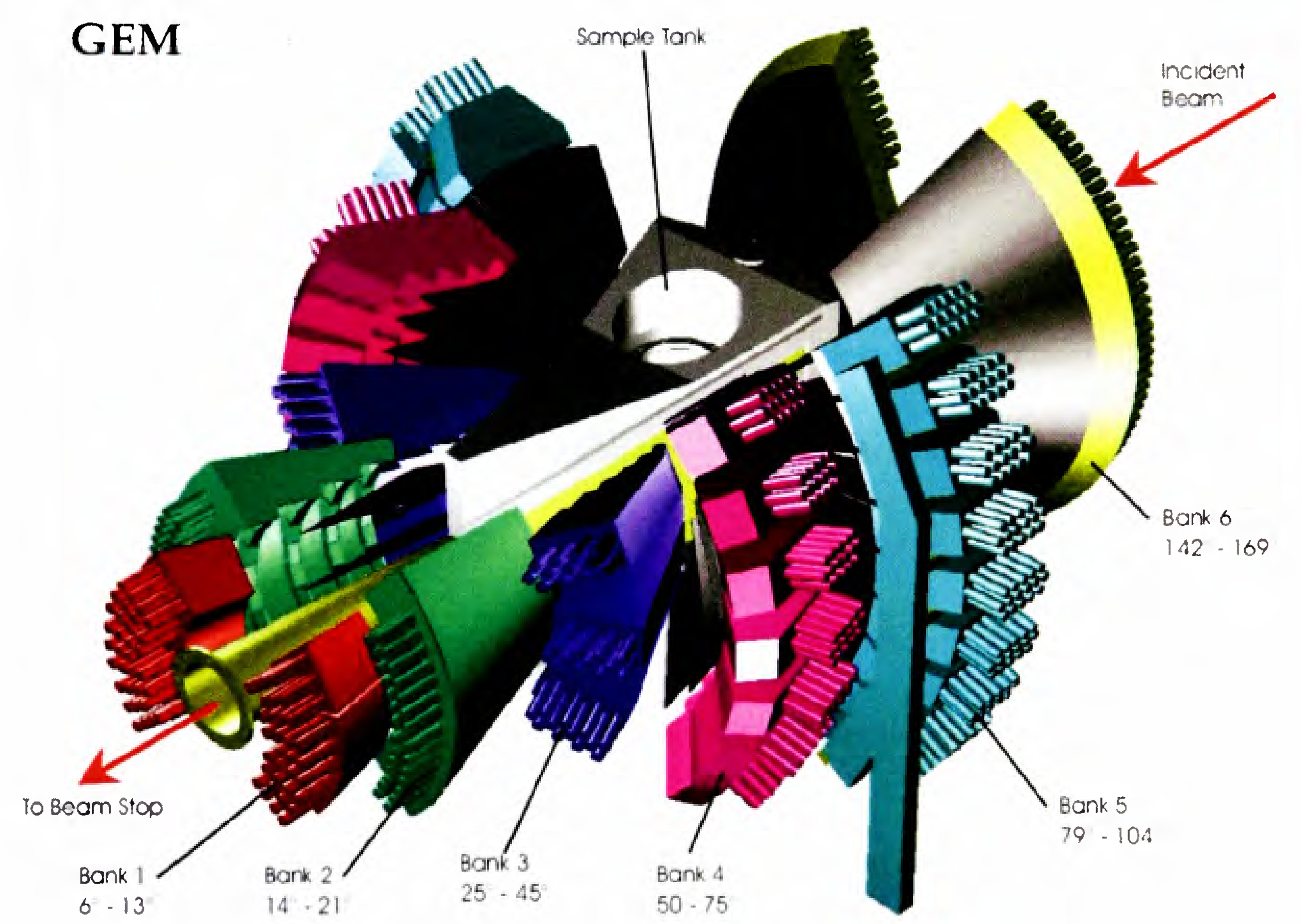

Figure 2.8: Schematic diagram of the GEneral Materials diffractometer (GEM) at the ISIS pulsed neutron facility. [13]

2.1.4 The Rietveld Profile Refinement Technique

A powder diffraction pattern (X-ray, neutron or otherwise) consists of a series of peaks, often with reflections from many Bragg planes contributing to the intensity of the data at any given point. Prior to the development of the Rietveld method, powder diffraction data were modelled using software which had originally been developed for the analysis of single crystal diffraction data. The software was re-written in order to account for overlapping *hkl* reflections, however, refinement of powder diffraction data using these methods met with only limited success.

The development of the Rietveld method[14] in the late 1960s resulted in a huge advancement in the quantitative analysis of powder diffraction data. Rather than attempting to assign each diffraction peak to several Bragg reflections, Hugo Rietveld coined a least-squares refinement method, which involves the treatment of each individual point of the diffraction data, thus allowing for the treatment of overlapping reflections. An initial structural model providing space group, lattice parameters and atomic coordinates is required and the analysis involves the continuous minimisation of the difference between this model (the *calculated*) and the collected data (the *observed).*

The intensity of the model at point i ($y_{i(calcd)}$) is calculated according to Equation 2.13, where s is a scaling factor, K represents the Miller indices *hkl*, L_K is the Lorentz polarisation factor, F_K is the structure factor, ϕ is the peak profile function, P_K is the preferred orientation function, A is the absorption factor and $y_{i(background)}$ is the background intensity at point i, which is modelled using high-order polynomials.

$$y_{i(calcd)} = s\sum_K L_K \mid F_K \mid^2 \phi(2\theta_i - 2\theta_k)P_K A - y_{i(background)} \qquad \text{Equation 2.13}$$

These calculated intensities are then compared to the measured intensities in the diffraction data *via* calculation of the residual, S_y. The ultimate aim of the Rietveld refinement method is to minimise S_y by providing the best fit to all y_i simultaneously.

S_y is given by Equation 2.14 where w_i is the weighting factor for point i and $y_{i(obs)}$ is the observed intensity for point i:

$$S_y = \sum_{i=1}^{n} w_i \left[y_{i(obs)} - y_{i(calcd)} \right]^2 \qquad \text{Equation 2.14}$$

Each of the parameters listed in Equation 2.13, in addition to those specific to the model, can be refined in order to gain the best fit to the collected data. The order in which the parameters are refined may be crucial to the success of the refinement.

Firstly, a close match to the measured peak positions must be obtained through refinement of lattice parameters, zero point correction, background pattern and scale factors. Upon achieving satisfactory values for these parameters, parameters influencing the peak intensities, such as the atomic positions, thermal displacement parameters and site occupancies, can then be introduced into the refinement, along with the profile function and the absorption factor.

The quality of the refinement is examined throughout the process both visually through comparison of the calculated, observed and difference plots, and numerically by the calculation of statistical parameters (*R values*). These *R* values are split into three types, namely the profile *R* value, R_p, the weighted profile *R* value (R_{wp}) and the expected *R* value (R_{exp}), which are calculated according to Equations 2.15, 2.16 and 2.17, respectively, where N_o is the number of observables and N_v is the number of refined parameters.

$$R_p = \frac{\sum \left| y_i - y_{i(calcd)} \right|}{\sum y_i} \qquad \text{Equation 2.15}$$

$$R_{wp} = \left[\frac{\sum w_i \left(y_i - y_{i(calcd)} \right)^2}{\sum w_i y_i^2} \right]^{\frac{1}{2}} = \left[\frac{S_y}{\sum w_i y_i^2} \right]^{\frac{1}{2}} \qquad \text{Equation 2.16}$$

$$R_{\exp} = \left[\frac{N_o - N_v}{\sum w_i y_i^2} \right]^{\frac{1}{2}} \qquad \text{Equation 2.17}$$

The final R_{wp} should approach the statistically expected R_{exp}. The deviation between these R values is expressed in terms of their ratio R_{wp} / R_{exp} and is referred to as the "goodness of fit" or χ factor.

$$\chi^2 = \frac{\sum w_i (y_i - y_{i(calcd)})^2}{N_o - N_v} = \frac{S_y}{N_o - N_v} \qquad \text{Equation 2.18}$$

Generally, the better the match between the data and the model, the closer the goodness of fit is to 1. Typical values for goodness of fit for Rietveld analysis of diffraction data are < 2.5, although visual inspection of the difference profile ($y_{obs} - y_{calcd}$) is also important in the determination of the match between the data and the model.

2.1.4.1 Refinement Software and Techniques

The structural refinements presented throughout this thesis were performed using the Rietveld method[14] (unless otherwise stated) and the TOPAS Academic software suite.[15]

Such refinements commenced with the modelling of the background data using high order polynomials. Upon attaining a good fit to the background, crystallographic models for the suspected phases (obtained from the Inorganic Crystal Structure Database (ICSD))[8] were included one by one. In order to obtain the best match between the peak positions of the model and the data, the lattice parameters and scale factors of the phases would be refined, as well as the zero-point error (X-ray diffraction only). The peak profile of each phase would then be refined to obtain the best match between the peak shapes of the data and the model. Finally, factors influencing the relative intensities of the Bragg reflections (the atomic thermal parameters, lattice site occupancies and atomic positions) would be refined.

The Rietveld process adjusts these refinable parameters using a least squares procedure in order to minimise the residual between the model and the data. This is a mathematical method which does not account for any correlation between the refined parameters. It is therefore necessary to exercise caution in the refinement of, for example, atomic thermal parameters (which model a smearing of the electron density) and lattice site occupancies (which assume that the electron density is concentrated at the atomic site), in order to ensure that correlation does not influence the refined values of these parameters.

Any deviations from the general method described above are outlined in more depth during the relevant discussion sections.

2.1.4.2 Rietveld Analysis of Multiple Data Sets – Batch Refinements

TOPAS Academic has a facility with which to perform *batch refinements.* These refinements work on the principal that the data from the $n+1^{\text{th}}$ diffraction pattern is likely to closely resemble that of the n^{th} pattern. This implies that the refined model obtained from Rietveld analysis of the n^{th} data set would provide a good starting model for Rietveld analysis of the $n+1^{\text{th}}$ data set; each successive data set in the batch is therefore refined using a starting model obtained from Rietveld analysis of the previous data set.

A start-point for the batch refinement must obviously be established, which involves the refinement of a single data-set, as outlined above, to produce a seed file. If the data set studied involves a number of phase changes etc, several seed files may be required at a number of specific points throughout the batch refinement.

To illustrate, a sample batch file involving the first two data-sets of a variable temperature study of $Li_{1-z}Na_zNH_2$ is replicated overleaf.

This explanation is colour coded for the sake of clarity.

```
cd C:\File_containing_refinement_software
```
(takes us to the refinement software)

```
tc "C:\File_containing_data_to_be_refined"\seed_file_name "macro   XYG{n.xye}" "
```
(transfers data to be refined to software, applies seed input file to n^{th} data set)

```
cd "C:\ File_containing_data_to_be_refined"\"
```
(takes us to the file containing the data)

```
copy seed_file_name.out n.inp
```
(copies the output file from the refinement, re-naming it as the n^{th} input file)

```
copy seed_file_name.out seed_file_name.inp
```
(copies the output file and uses it to replace the seed input file; this is the input file used as the starting model for the next refinement.)

```
cd C:\TOPASa
tc "C:\TOPASa\Li1-zNaz"\Li1-x "macro XYG{Li(1-z)Naz_VT_1.xye}" "
cd "C:\TOPASa\Li1-zNaz"
copy Li1-z.out Li(1-z)Naz_VT_1.inp
copy Li1-z.out Li1-z.inp

cd C:\TOPASa
tc "C:\TOPASa\Li1-zNaz"\Li1-x "macro XYG{Li(1-z)Naz_VT_2.xye}" "
cd "C:\TOPASa\Li1-zNaz"
copy Li1-z.out Li(1-z)Naz_VT_2.inp
copy Li1-z.out Li1-z.inp
```

Batch refinements continue from data set to data set automatically unless the refinement is interrupted. As such, all of the allowed parameters for all of the phases included in the seed file are refined simultaneously, which means that the refined parameters obtained from batch analysis may not be as reliable as those obtained from the refinement of individual data sets (section 2.1.4.1). Generally speaking, the batch refinements performed during the course of this thesis included refinement of the background data (using high order polynomials), zero-point error (X-ray data only), scale factors and lattice parameters, peak profiles and atomic thermal factors. During the batch refinement of neutron diffraction data, the data collected at banks 4 and 5 were refined simultaneously to ensure that the calculated parameters were as accurate as possible. Any deviations from this general method (for example, the refinement of site occupancies etc) are highlighted in the relevant discussion sections.

The final values of the refined parameters for each data set can be collected in an output file, which allows us to monitor crystallographic changes occurring within the sample throughout the data collection.

Batch refinements are used as a means of greatly reducing the amount of time required for the refinement of vast numbers of subsequent data sets. They are particularly useful for the refinement of solid solutions with the same crystal structure but changing lattice constants, or for analysing data collected during variable temperature X-ray or neutron diffraction measurements.

2.2 Gravimetric Analysis

Gravimetric Analysis is the process by which the mass of a sample is monitored as a function of time. The gravimetric analysis measurements presented in this thesis were performed using Intelligent Gravimetric Analysis (IGA), where changes in sample mass were measured under varying conditions of pressure and / or temperature. This technique was used both in isolation and combined with two additional techniques, the first being mass spectrometry and the second being neutron diffraction.

2.2.1 **Intelligent Gravimetric Analysis with Mass Spectrometry**

The intelligent gravimetric analysis with mass spectrometry (IGA-MS) equipment used consists of a high-temperature, high pressure stainless steel reaction vessel, an associated vacuum/gas cabinet, and a dynamic sampling mass spectrometer (DSMS). The system can be fitted with an inert sample loader which can be filled with N_2 to ensure that contact between the sample and atmosphere is minimised during sample loading and unloading.

The cylindrical reaction vessel houses a stainless steel sample holder, a platinum resistance thermocouple (accurate to ± 0.2 °C) and a gas inlet/outlet tube. The reaction vessel can be used at pressures between 10^{-6} mbar and 20 bar and temperatures between -5 and 500 °C. The sample holder consists of a small stainless steel mesh bucket (0.07 – 0.09g) which is suspended from a microbalance (accurate to ± 0.1μg) by means of a gold chain and a stainless steel connector.

The temperature of the reaction vessel can be controlled by means of a water bath for temperatures between -5 and 80 °C (typical heating rate 1 °C/min) or a furnace for temperatures between 80 and 500 °C (typical heating rate 2 °C/min).

Experiments can be performed either in a sealed system or under a continuous flow of helium gas. For measurements performed under flowing gas, a small proportion of the outgoing gas can be diverted towards the mass spectrometer by way of a 10 bar capillary tube. The mass spectrometer is of model HAL 201, type 124100 and is fitted with a dual Faraday/Electron Multiplier detector. It is sensitive to a mass range of 200 atomic mass units (AMU) and has a detection limit range of 0.1 to 1 ppm, subject to spectral interference. The spectrometer is capable of recording the partial pressures of up to five gases of different molecular mass.

Buoyancy effects due both to the different temperatures and volumes of the sample and counterweight are controlled and corrected through software calculation. The software has provision for non-ideal gas behaviour through use of van der Waal's constants and compressibility tables.

For a typical experiment, around 70 – 90 mg of sample was loaded into the stainless steel mesh bucket within the glove box. This bucket was placed into the transport cell, which was then inserted into the inert sample loader. The sample loader was flushed with nitrogen gas for 30 minutes before the transport cell was opened and the sample bucket placed onto the stainless steel wire. The reaction vessel was then raised and sealed with a copper gasket. After the measurement, the sample was removed using the inert sample loader under nitrogen and returned to the glove box.

Measurements of the sample mass, temperature and pressure and the partial pressures of the evolved gases were taken every 12.5 seconds and plotted as a function of time.

2.2.2 Intelligent Gravimetric Analysis with Neutron Diffraction

As outlined in section 2.1.3, neutrons have a very high penetration and can therefore pass through bulky cryostats and heaters much more easily in comparison with X-rays. A collaboration between the ISIS Facility, Oxford University and Hiden has exploited this property through the design and commissioning of an intelligent gravimetric analyser (IGA) which can be used in conjunction with the GEM neutron diffractometer at the ISIS facility.

The technique, known as Intelligent Gravimetric Analysis with Neutron Diffraction (IGA^n), allows the simultaneous collection of thermogravimetric measurements and neutron diffraction data. The thermogravimetric data collected during experiments allows one to monitor the variation of the sample mass in response to changes in the pressure and temperature of the sample. The combination of these data with the corresponding neutron diffraction data not only gives a full indication of the crystallographic phase changes which occur during the experiment, but will also potentially allow the full characterization of reaction intermediates and non-stoichiometric transformations.

The intelligent gravimetric analyser used for these experiments is identical to that described in section 2.2.1 in most respects. The main ways in with the IGA^n differs from the IGA described previously are summarised below.

1) The sample holder used in the IGA^n is a thin quartz receptacle (0.8-1.0 g) which is suspended from the microbalance by a gold chain with a tungsten connector.

2) The IGA^n reaction vessel is fitted with a standard Tomkinson flange.

3) Instead of a removable sample loader, the IGA^n is housed in a custom built Argon-filled glove box in order to minimise the likelihood of aerial oxidation and isotope exchange during sample loading. After loading, the IGA^n is craned out of the glove box and into the diffractometer.

4) The temperature of the IGA^n is varied using two band heating elements which are located inside the reaction vessel above and below the sample. The heaters are positioned to ensure minimum interaction with the neutron beam.

To load the apparatus, weighed amounts (0.1-1.0 g) of a thoroughly ground sample were loaded into the quartz sample holder in an Ar filled glove box, which was then transferred to the IGA^n glove box using an airtight Kilner® jar. The sample holder was then loaded on to the tungsten hang down wire, and the IGA^n reactor vessel was sealed to the Tomkinson flange. The set-up was then craned out of the glove-box and into the GEM diffraction chamber, where it was screwed into place.

Neutron diffraction data were collected from the sample every 2.52 minutes during the experiments and thermogravimetric data were recorded approximately every 5 seconds. The measured mass is accurate to ± 0.0001 mg and the measured temperature and pressure are accurate to ± 0.001 °C, ± 0.01 mbar, respectively.

2.2.3 **Intelligent Gravimetric Analysis**

The IGA^n outlined in Section 2.2.2 could also be used off-line as a standard IGA for experiments involving the absorption of gases (section 2.6.2.1).

2.3 Vibrational Spectroscopy

Vibrational spectroscopy has been extensively used by inorganic chemists due to its very wide applicability; every molecular or covalently bonded material will have some type of vibrational spectrum, and data can be easily collected from solids, liquids and gases.

If we consider a molecule to be composed of massive particles (atoms) joined by virtually mass-less connections (bonding electrons), the molecule can be described as a *simple harmonic oscillator* and the motion of the atoms can be calculated classically using Newton's laws of motion:[16]

$$F(x) = -kx \qquad \text{Equation 2.20a}$$

$$V(x) = \frac{1}{2}kx^2 \qquad \text{Equation 2.20b}$$

Assuming the system obeys Hooke's law (Equations 2.20a and 2.20b where *F(x)* is the force experienced by the particle, *V* is the potential energy of the vibrations, *k* is the force constant and *x* is the displacement from equilibrium) the characteristic *normal vibrations* of the molecule will have a frequency calculated according to Equation 2.21 (where k_i is the force constant and μ_i is the reduced mass for the vibration):

$$\omega_i = \sqrt{\frac{k_i}{\mu_i}} \qquad \text{Equation 2.21}$$

However, given that we are working on the atomic scale, the quantization of energy must be taken into account. The quantized energy of a normal vibration is given by Equation 2.22, where υ is the vibrational quantum number, $\hbar$ is Plank's constant divided by 2π and the ½ corresponds to the vibrational zero-point energy of the system:

$$E_\upsilon = \hbar\omega\left(\upsilon + \tfrac{1}{2}\right) \qquad \text{Equation 2.22}$$

A molecule containing N atoms will have $3N$ degrees of freedom. Of these, three degrees of freedom will be translational, and three will be rotational (two if the molecule is linear), which leaves $3N$-6 vibrational degrees of freedom (or $3N$-5 for a linear molecule).[16]

Unfortunately, the picture is not as simple as that outlined as very few systems can be accurately described as simple harmonic oscillators. *Anharmonicity* occurs because the potential energy of a molecular vibration cannot increase without limit and it must approach a finite value, corresponding to the dissociation energy of the system.

The anharmonicity of an oscillating system can be accounted for by representing the variation of potential energy with displacement as a power series in $(\upsilon + \frac{1}{2})$:

$$E_{\upsilon}^{general} = \hbar\left[\omega_e\left(\upsilon + \tfrac{1}{2}\right) - x_e\left(\upsilon + \tfrac{1}{2}\right)^2 - y_e\left(\upsilon + \tfrac{1}{2}\right)^3 - \ldots\right] \qquad \text{Equation 2.23}$$

This power series can be simplified to include just the first two terms, which gives a reasonable approximation to the anharmonic oscillator, known as the *Morse oscillator*:

$$E_{\upsilon}^{Morse} = \hbar\left[\omega_e\left(\upsilon + \tfrac{1}{2}\right) - x_e\left(\upsilon + \tfrac{1}{2}\right)^2\right] \qquad \text{Equation 2.24}$$

A molecule can be excited from its ground vibrational state to an excited vibrational state through interaction with radiation or particles of appropriate wavelength (such as neutrons). As such, vibrational spectroscopy allows us to collect valuable data about the vibrational modes of a molecule, and can therefore be highly useful in structural determination and finger printing.

2.3.1 Raman Spectroscopy

During the interaction of radiation with a molecule, the radiation will be scattered in either an *elastic* or an *inelastic* manner. *Elastic scattering* occurs when no energy or momentum is transferred between the radiation and the molecule. *Inelastic scattering* is the term given when momentum or energy is transferred between the radiation and the molecule during the scattering process.

The inelastic scattering of photons by molecules is known as Raman scattering, named after C. V. Raman, who first observed the phenomenon in 1928.[17] Raman scattering does not involve the direct or resonant absorption of radiation, and occurs only in molecules which exhibit a change of polarizibility during a molecular vibration.

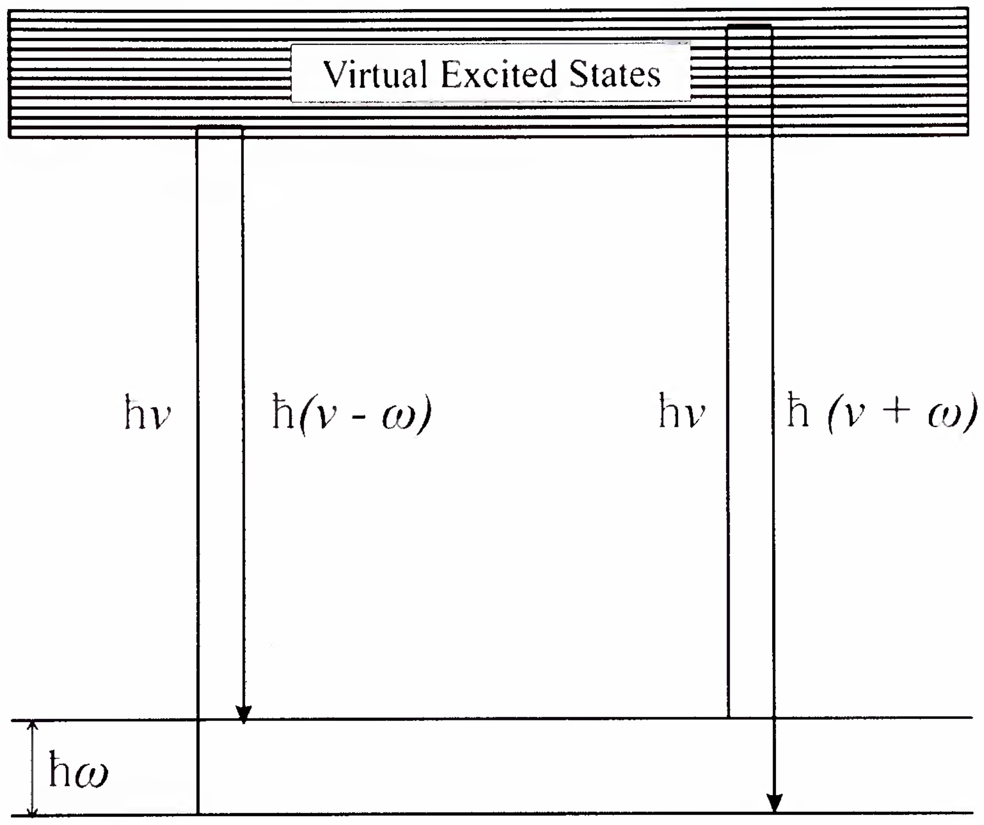

Figure 2.9: Schematic diagram of the energy levels involved during Raman scattering

Irradiation of a molecule with monochromatic (laser) light of frequency ν may result in the polarization of the electron cloud. This arises due to the interaction of the molecule with the oscillating electric vector of the incident radiation. Such an interaction may result in the absorption of an incident photon, causing the excitation of a vibrational state from frequency ω up to a "virtual state" of frequency $(\nu \pm \omega)$. The lifetime of this virtual state can be considered sufficiently short that decay is instant, occurring with the release of a photon of frequency $(\nu \mp \omega)$ as illustrated in Figure 2.9.

The principle of the conservation of energy requires that a change in the vibrational energy of the molecule must occur during an inelastic collision. The separation of adjacent energy levels ($\hbar\omega$) can therefore be calculated by measuring the energy of the scattered photon.

The frequencies of these separations are recorded as shifts from the incident frequencies. Those appearing below the exciting frequency are known as the Stokes frequencies, and those above the exciting frequency, the anti-Stokes frequencies. Notice that the frequency displacement for both the Stokes and anti-Stokes lines from the exciting frequency is ω, which is the characteristic frequency of a particular vibrational mode. The Stokes lines are more intense than the anti-Stokes lines, as the population of the molecular energy levels follows a Boltzmann distribution (meaning that most molecules are in their ground vibrational level at room temperature). Stokes lines are therefore measured with a much better signal-to-noise ratio.[18]

Unfortunately, the vast majority of collisions observed during sample irradiation are elastic, and therefore, much of the radiation is scattered without change of frequency (*Rayleigh scattering*).

The observed Raman shift is independent of the exciting frequency chosen (as it is a difference measurement rather than an absolute measurement) and hence various light sources can be used. Generally, it is the right – angle scattering of intense, monochromatic laser-light which is measured during an experiment.

Raman experiments outlined in this thesis were performed at Birmingham University, using a Renishaw inVia Raman microscope with a spectral range of 4500 cm^{-1} – 100 cm^{-1}, using a 633 nm HeNe laser through an 1800 grating.

2.3.2 Inelastic Neutron Scattering

As outlined in section 2.3.1, radiation can interact with matter in either an elastic or an inelastic manner, depending on whether or not momentum is transferred during the scattering process. This is also true for neutrons.

Having interacted with matter, scattered neutrons can then interact with other scattered neutrons in either a coherent or an incoherent manner, depending on the isotopic and spin ordering of the sample (section 2.1.3). Inelastic Neutron Scattering (INS)[19] is concerned with the *inelastic* scattering of neutrons from *incoherent* systems.

A form of vibrational spectroscopy, inelastic neutron scattering occurs when the collision of a neutron with a molecule results in the transfer of a quantum of vibrational energy of specific frequency from the neutron to the molecule.

Practically speaking, a beam of neutrons of known velocity is passed through a sample and the distribution of velocities of the out-going neutrons is analysed, resulting in a vibrational spectrum, in the form of a spectrum of energy losses.

Considering more closely the momentum and energy transfer which occurs during INS, we can write:

$$E = \hbar\omega = \tilde{\nu}hc = \frac{m_n |v|^2}{2} \qquad \text{Equation 2.25a}$$

$$E = \frac{\hbar |k|^2}{2m_n} \qquad \text{Equation 2.25b}$$

where E is the neutron energy, $\hbar$ is Plank's constant (h) divided by 2π, ω is the angular frequency, $\tilde{\nu}$ is the wavenumber, c the speed of light, m_n the mass of a neutron, v the neutron velocity and k the momentum of the neutron.

The transfer of momentum is frequently ignored in vibrational spectroscopy because the mass of a photon is negligible. This is not the case in neutron scattering, where the change of direction and/or energy of the neutron during collision indicates a transfer of momentum. This momentum transfer is treated classically, as shown in Figure 2.10.

Two sides of the vector triangle are found from the incident and final neutron momenta ($\boldsymbol{k}_i$ and $\boldsymbol{k}_f$, respectively). The third side is the neutron momentum transfer vector, $\boldsymbol{Q}$, and is determined using the cosine rule.

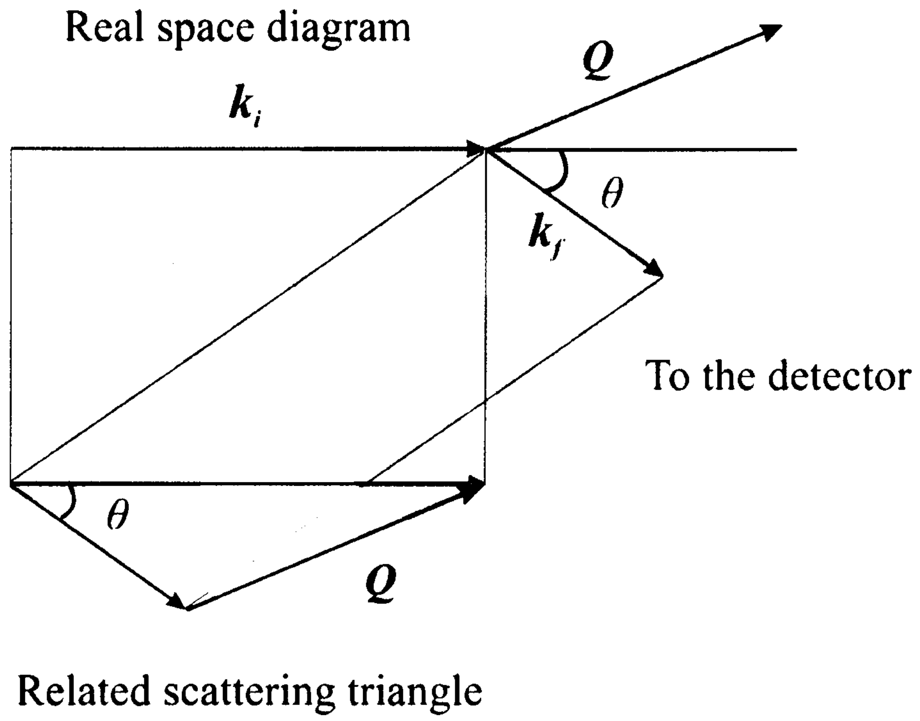

Figure 2.10 : Schematic diagram showing transfer of momentum during an inelastic neutron scattering collision

An inelastic neutron scattering spectrometer consists of a single detector of area A held at a distance d_f from the sample and angle θ from the incident neutron beam. d_f and θ are defined as the polar coordinates of the system and the solid angle $d\Omega$ (subtended by an angular element $d\theta$) is $2\pi \sin\theta \, d\theta$. The energy spectrum of the sample is scanned and the number of neutrons reaching the detector is recorded per second (the final flux, J_i). J_i is then normalised to the number of incident neutrons reaching the sample per second (the incident flux, J_f). The strength of the sample's response is therefore a function of energy, E and solid angle $d\Omega$.[19]

The observable is the rate of change of the cross section, σ, with respect to the final energy, E_f and the solid angle dΩ. This is the double differential scattering cross section $\frac{\mathrm{d}^2\sigma}{\mathrm{d}E_f\,\mathrm{d}\Omega}$ where $\mathrm{d}\Omega = \frac{A}{d_f^2}$.[19]

This double differential is employed in the *Scattering Law* (Equation 2.26) which relates the momentum transfer vector, $\boldsymbol{Q}$, and the wavenumber, ω, to the observable intensities:[19]

$$S(\boldsymbol{Q},\omega)_l = \frac{4\pi}{\sigma_l}\frac{\boldsymbol{k}_i}{\boldsymbol{k}_f}\left(\frac{\mathrm{d}^2\sigma}{\mathrm{d}E_f\mathrm{d}\Omega}\right)_l \qquad \text{Equation 2.26}$$

σ_l is the scattering cross section of atom l and $\boldsymbol{k}_i$ and $\boldsymbol{k}_f$ are the momenta of the incident and final neutrons, respectively.

For a single molecule containing N atoms, the scattering law becomes:[19]

$$S^{\bullet}(\mathbf{Q},\omega)_{total} = y\sum_{l=1}^{N} S(\mathbf{Q},\omega)_l\sigma_l \qquad \text{Equation 2.27a}$$

For a powder, the powder averaged scattering law is given by:[19]

$$S(\mathbf{Q},\omega)_{powder} = \frac{1}{4\pi}\int S(\mathbf{Q},\omega)\mathrm{d}\mathbf{Q} \qquad \text{Equation 2.27b}$$

INS possesses several advantages over other forms of vibrational spectroscopy. Firstly, INS spectra can be readily and accurately modelled using molecular dynamics software. The intensities measured during an experiment can be straightforwardly related to the atomic displacements of the scattering atoms.

The technique is also sensitive to the vibrations of hydrogen atoms within the sample, arising from the fact that hydrogen has a uniquely high incoherent scattering cross section.[11] Conversely, optical techniques tend to be more sensitive to vibrations involving heavier atoms, due to the larger number of electrons.

INS is also not subject to the selection rules necessary for induced optical excitations, meaning that, in principle, all molecular vibrations are INS active and measurable.

Photons have only a low penetration and hence, optical techniques can not be used to gain information regarding the bulk of a sample. The penetration of neutrons is sufficiently high that they can pass readily through the walls of containment vessels and into the bulk of the sample, thus providing valuable information regarding the bulk properties of the materials studied.

INS also has a uniquely wide spectral range, covering the entire molecular vibrational range of interest (16 – 4000cm^{-1}). The range below 400 cm^{-1} obtained from INS spectroscopy is especially valuable as this range is notoriously difficult to observe using optical spectroscopy.

The disadvantages of the use of this technique are much the same as those outlined for neutron powder diffraction in section 2.1.3, namely the expense of using a neutron source and the long experimental times required to collect sufficient data.

The TOSCA Spectrometer

The inelastic neutron scattering data presented in this work were collected using the TOSCA spectrometer at the ISIS pulsed neutron facility at the Rutherford Appleton Laboratory.

TOSCA is an indirect geometry time-of-flight (t-o-f) spectrometer with optimal energy range 0 – 4000 cm^{-1} (0 – 500 meV), and best results below 2000 cm^{-1} (250 meV). A t-o-f technique is used for energy analysis of the scattered neutrons.[20]

The flight path to TOSCA is 17 m in length, which results in good spectral resolution. A tailcutter is included on the leading edge to remove low energy neutrons that would otherwise result in frame overlap.

A diagram of the TOSCA spectrometer is presented in Figure 2.11.[21]

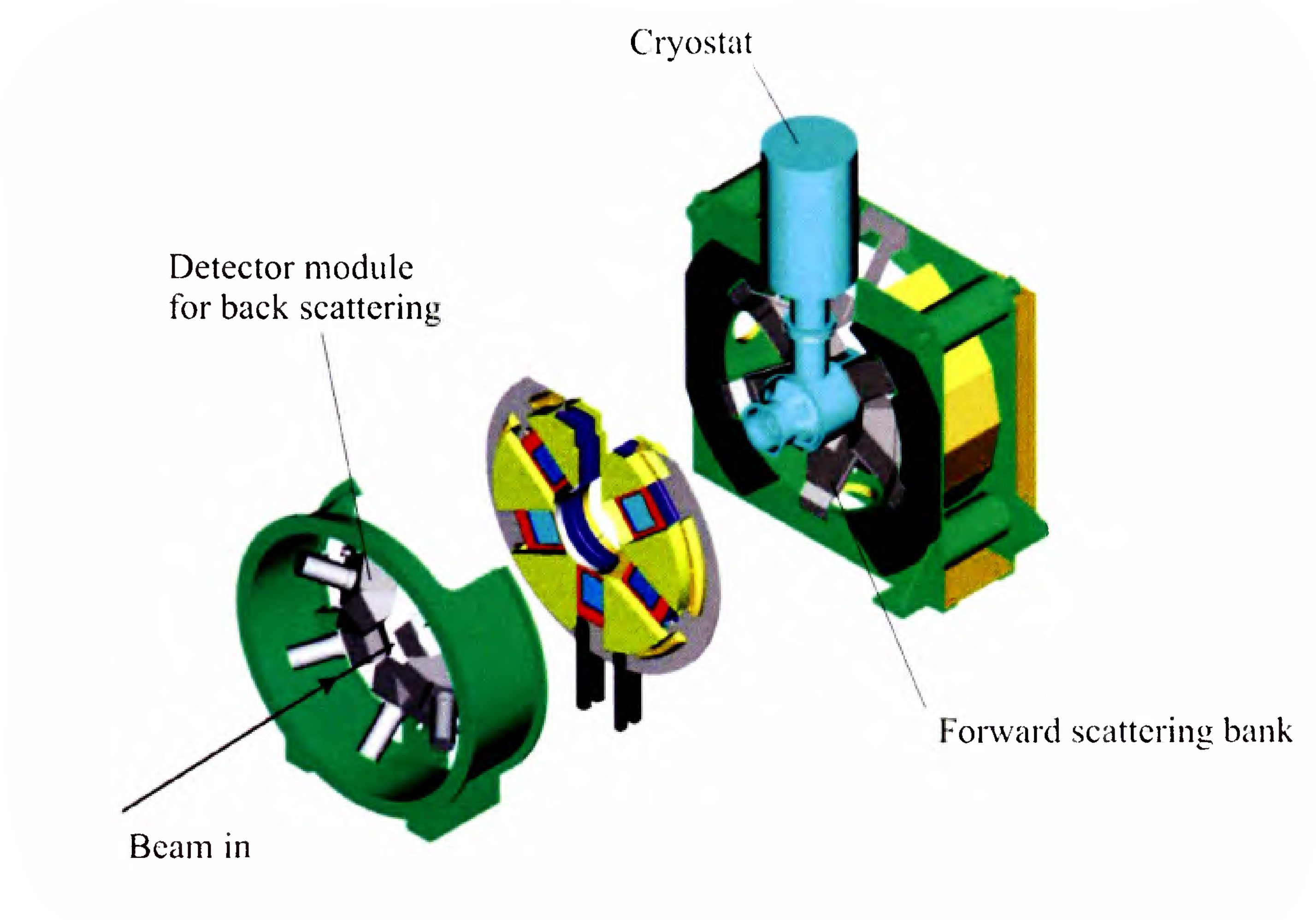

Figure 2.11: Schematic diagram of the TOSCA inelastic neutron spectrometer at the ISIS pulsed neutron facility.[21]

2.3.2.1 Modelling of INS Data Using Castep

The data collected from INS studies were modelled using the Castep[22] software package in conjunction with Materials Studio.[23] Castep is a first principles quantum mechanical code which uses density functional theory[24] to perform electronic structure calculations.

For the data presented in this thesis, Castep was used to calculate the optimum geometry of materials *via* the imposition of $P1$ symmetry on the crystal structures.

Phonon density of states calculations were then performed on the optimised structures, which allowed the molecular vibrations of the materials to be simulated and a theoretical spectrum to be calculated. Comparison of the calculated spectrum with the observed spectrum gives an indication of the accuracy of the geometrically optimised structure.

2.4 Differential Scanning Calorimetery

Differential scanning calorimetery (DSC) is a technique by which the heat flow between a sample and its surroundings can be measured as a function of temperature and time. The technique can be used to gather information about exothermic and endothermic processes, including decomposition, phase transitions, structural transitions and all other processes which involve heat exchange between a sample and its surroundings.

The DSC data presented in this thesis were collected using a Q10 PDSC TA Instruments calorimeter at Hiroshima University. The DSC was installed in an argon-filled glove box in order to prevent aerial oxidation of the sample. The recorded sample temperature and heat flow were accurate to ± 0.0001 °C and 0.00001 mW, respectively.

Samples of ~10 mg were loaded into aluminium sample pans which were sealed with aluminium caps and loaded into the DSC apparatus. The samples were heated under a flow of Ar gas to a temperature of 400 °C at a rate of 5 °C/min. Measurements of the sample temperature and heat flow were taken approximately every 0.5 seconds. The heat-exchange events observed were then integrated with respect to time in order to calculate the enthalpy change associated with each heat-transfer event.

2.5 Synthetic Techniques

2.5.1 **Source and Purities of Starting Materials**

$LiNH_2$ (95 %, Aldrich), Li_3N (80 mesh, Aldrich), LiH (95%, Aldrich), LiD (98 atom%, Aldrich), NaH (95%, Aldrich), $NaNH_2$ (90%, Aldrich), $NH_3(g)$ anhydrous BOC Special Gases / CK Gasses, $ND_3(g)$ anhydrous, 99.99% atom purity BOC Special Gases / CK Gasses.

2.5.2 **Argon-filled Glove Box**

The majority of the materials used and produced during the course of this research were both air and moisture sensitive. All materials were therefore stored and handled under an inert atmosphere inside an argon-filled glove box.

The gas within the glove box was continually circulated through a pair of columns containing molecular sieves and a copper-based catalyst. These columns acted to remove O_2 and H_2O from the gas and maintain the levels of these contaminants at <0.1ppm. The integrity of the glove box atmosphere was maintained on a daily basis by the drying of all glassware in an oven and the thorough pump-purging of the ports before use.

2.5.3 **Synthetic Techniques**

Syntheses were performed using traditional ambient and low pressure solid-state techniques. These techniques commenced with the weighing of appropriate quantities of reactant materials, followed by thorough grinding of the reaction mixtures using an agate pestle and mortar.

The powders formed were packed into alumina crucibles which were then placed into quartz tubes. The alumina crucibles were necessary in order to prevent contact and possible reaction of the powders with the quartz. Alumina was the choice material for the crucibles due to its relative inertness to most ceramic materials.

Having placed the packed crucibles into the quartz tubes, the tubes were capped with a Swagelock fitting and connected to either a single, double or triple Young's tap, depending upon the reaction conditions to be used (sections 2.5.3.1 – 2.5.3.3). The Swagelock fittings and Young's taps formed an air-tight seal with the quartz, ensuring that the reactants were in a sealed environment under argon gas. The reaction set-up could then be removed from the glove box without risking aerial oxidation of the reaction mixtures.

The synthesis conditions used during this research mostly fall into three main categories: sealed evacuated tube synthesis, synthesis under flowing gas and synthesis under moderate pressure. These three techniques are outlined below. Any alternative synthetic techniques used are outlined in the relevant experimental sections (section 2.6).

2.5.3.1 Sealed Evacuated Tube Synthesis

If a reaction was performed in a sealed evacuated tube, a loaded quartz tube was capped *via* a Swagelock fitting with a single Young's tap (Figure 2.12). Having closed the Young's tap, the tube was removed from the glove box and connected to a vacuum line, where it was evacuated to pressures of the order of 10^{-4} mbar for a number of hours. The tube was then sealed using an oxygen-methane gas torch, placed into a muffle furnace and heated to the reaction temperature at a rate of 1 °C per minute. After the reaction, the tube was allowed to cool to room temperature inside the furnace, and was then scored and cracked inside the glove box. The reaction product was then removed from the alumina crucible and stored inside the glove box in a sealed container.

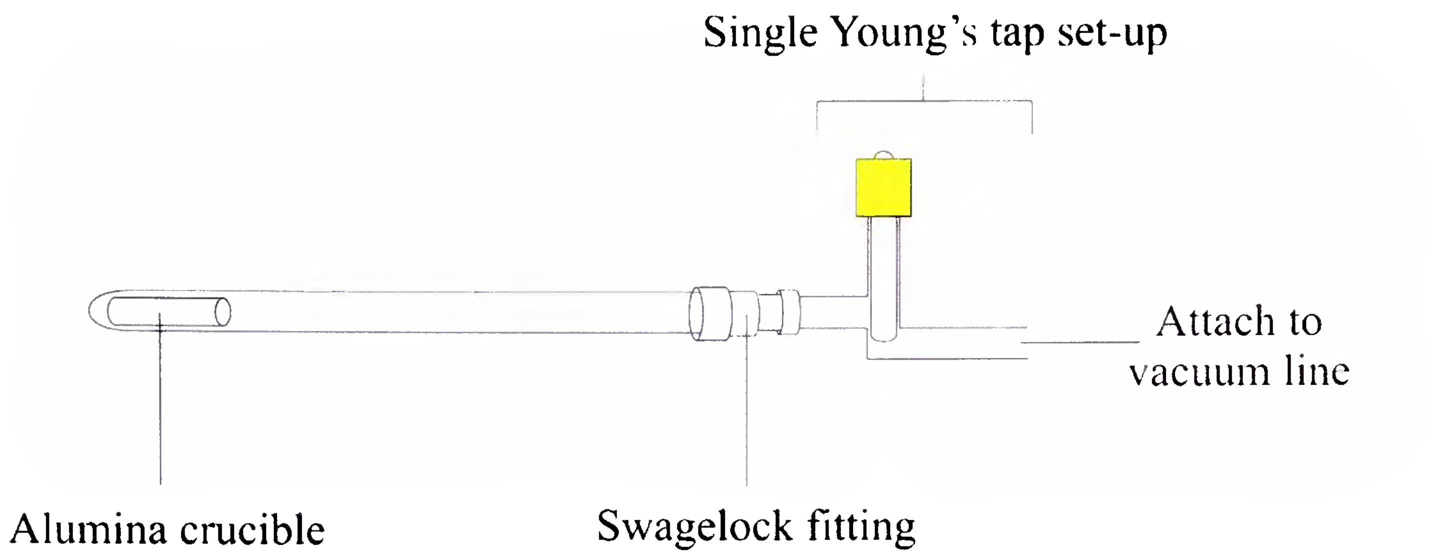

Figure 2.12 : Schematic diagram of the experimental set-up used to make a sealed evacuated tube. The single Young's tap fitting was attached to the vacuum line and the tube was evacuated for several hours. The evacuated tube was then sealed using an oxygen-methane torch and placed into a muffle furnace.

2.5.3.2 Flowing Gas Synthesis

A number of the materials studied were synthesised under a positive pressure of flowing Ar. In such cases, a loaded quartz tube was capped *via* a Swagelock fitting using either double or triple Young's taps (Figure 2.13). Having closed the Young's taps, the quartz tube was removed from the glove box and taken to a tube furnace. The Young's taps would then be attached to an Ar cylinder and a gas outlet via a network of PVC tubing and gas bubblers, which had previously been flushed with Ar for five minutes to remove oxygen. The Young's taps were then opened and the flow-rate was reduced until a slow, steady stream of bubbles was observed in the inlet and outlet bubblers. Incoming gas was passed through concentrated sulphuric acid (H_2SO_4) to ensure the removal of all water from the gas, and outgoing gas was bubbled through paraffin oil to ensure there was no possibility of aerial suck-back (Figure 2.13).

The quartz tube was then fed into the centre of the tube furnace and heated to the reaction temperature at a rate of 1 °C per minute. After the reaction, the flow of gas continued until the sample had cooled to room temperature. The Young's taps were then closed, detached from the PVC tubing and the quartz tube was removed from the furnace. The quartz tube was then evacuated to 10^{-4} mbar on a vacuum line and taken into the glove box, where the sample was removed from the crucible and stored in a sealed container.

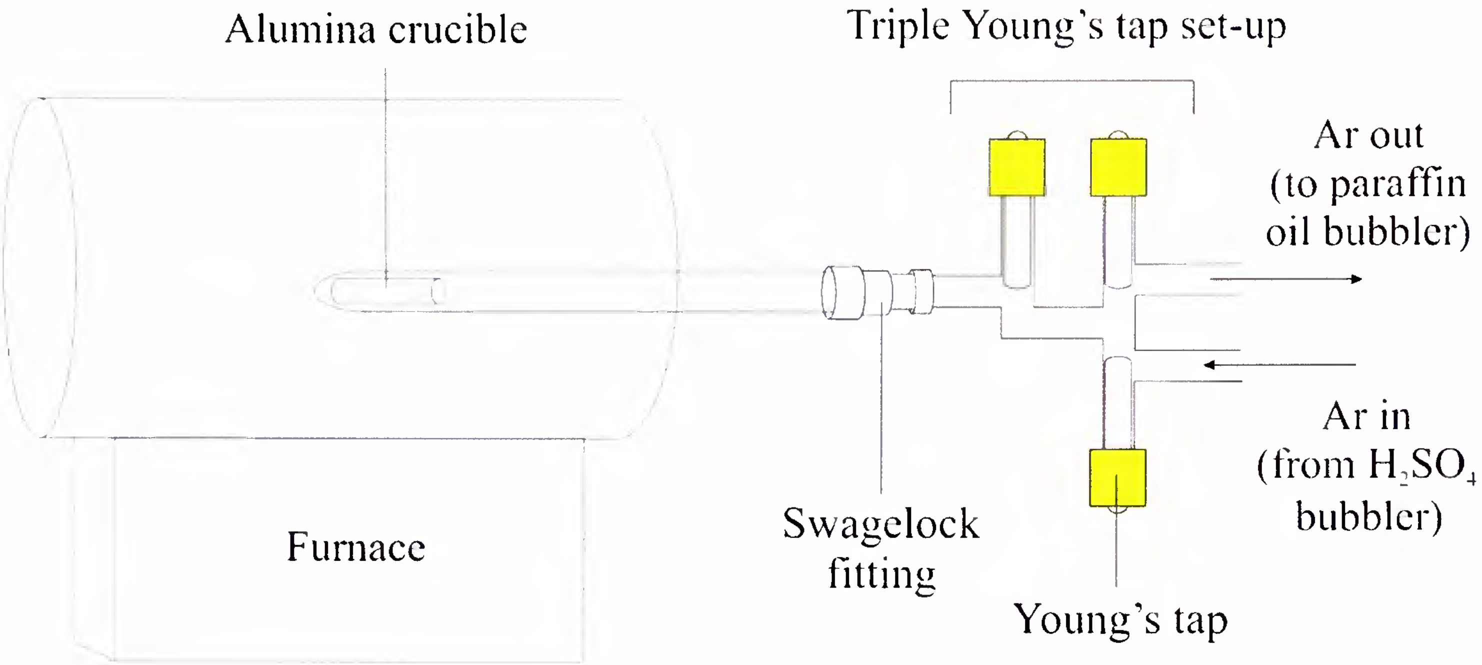

Figure 2.13 : Schematic diagram of the experimental set-up used for reactions performed under flowing gas.

2.5.3.3 Synthesis Under Moderate Pressure

Some syntheses required the starting materials to be reacted under a static pressure of gaseous ammonia. In such cases, the reactants were prepared in the glove box as outlined previously and then placed into an alumina crucible. The crucible was loaded into a glass tube which was fitted with a ground glass "cone" joint. The cone joint was smeared with vacuum grease and then attached to a ground glass "socket" joint which was fitted with a single Young's tap (Figure 2.14). This cone-socket connection was clipped using a "quick fit" joint clip, in order to ensure the integrity of the seal, and the Young's tap was closed. The sealed reaction vessel was then removed from the glove box and evacuated to 10^{-4} mbar for several hours on the vacuum line.

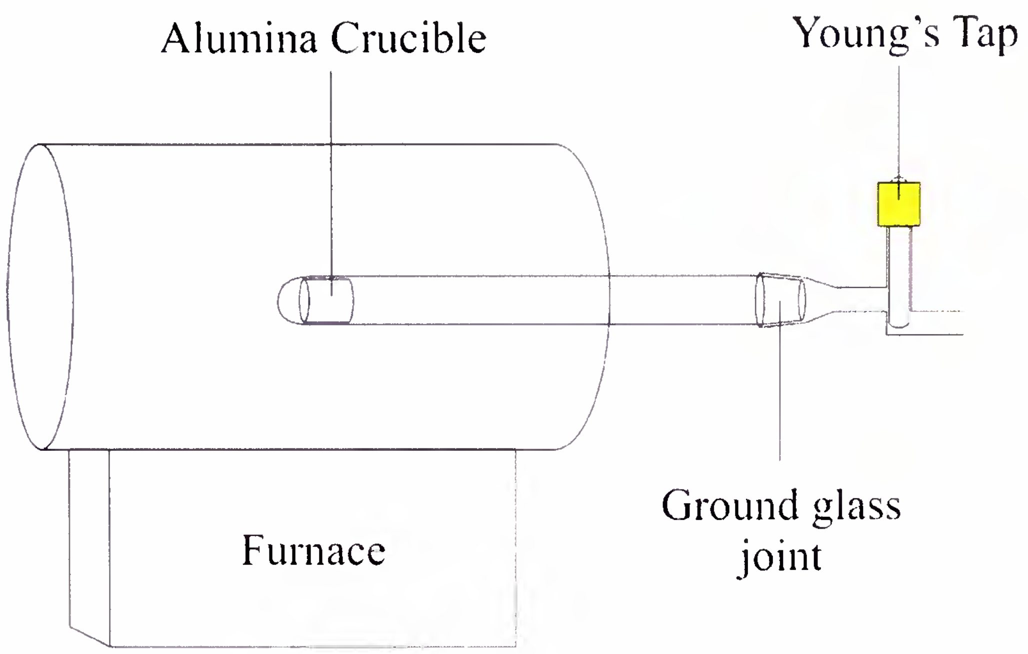

Figure 2.14 : Schematic diagram of the experimental set-up used for synthesis reactions performed under a moderate pressure of gas.

The vessel was then connected to a stainless steel ammonia line and the connecting valve was evacuated. The Young's tap was then opened and the reaction vessel charged to a specified pressure of ammonia, which was measured using a pressure gauge. The Young's tap was then closed and the vessel heated in a tube furnace at a rate of 1 °C per minute to the target temperature (Figure 2.14). After the reaction, the tube was allowed to cool to room temperature in the furnace, and was then flushed with Ar, evacuated to 10^{-4} bar, and taken into the glove box. The sample was then re-ground and the process repeated a number of times until ammoniation was complete (as determined by X-ray diffraction of the product).

2.6 Overview of Synthesis Reactions

2.6.1 **Li – N – H Compounds**

2.6.1.1 Li_2NH

Li_2NH was synthesised *via* two different synthetic pathways. The first method consisted of the 1:1 reaction of $LiNH_2$ with LiH[25] at 400 °C, and the second method involved the reaction of a 1:1 mixture of $LiNH_2$ with Li_3N[25] at 300°C. Both reactions were performed under flowing Ar gas for 24 hours, according to the general synthetic procedure outlined in section 2.5.3.2.

2.6.2 **Li – N – D Compounds**

2.6.2.1 $LiND_2$

$LiND_2$ was synthesised for neutron diffraction experiments. Two distinct methods were used.

The first $LiND_2$ sample was synthesised *via* the reaction of LiD with $ND_3(g)$, according to the general procedure outlined in section 2.5.3.3. The evacuated reaction vessel was charged to 0.8bar with ND_3 at room temperature, sealed and then heated to 200°C for 12 hours. The sample was re-ground in the glove box, and the reaction process repeated until X-ray diffraction data indicated that <5 mass% unreacted LiD remained in the sample.

The second synthetic technique utilised the Intelligent Gravimetric Analyser (IGA, section 2.2.3). Li_3N was hand-ground in the glove box and loaded into a quartz bucket which was transferred under inert atmosphere to the IGA. The reaction vessel was charged to a pressure of 3 bar with ND_3 and the sample was then heated to 250 °C. These conditions of temperature and pressure were maintained until no further mass change was observed in the thermogravimetric data.

2.6.2.2 Li_2ND

Li_2ND was synthesised *via* the reaction of Li_3N with $LiND_2$ at 300 °C under flowing Ar gas for 24 hours, according to the general procedure outlined in section 2.5.3.2. The $LiND_2$ used during this synthesis was formed *via* the reaction of Li_3N with ND_3 in the IGA as outlined in section 2.6.2.1.

2.6.2.3 Ball milled Li_2ND + LiD

Li_2ND was synthesised as outlined in section 2.6.2.2 and was then milled in a 1:1 molar ratio with LiD in a planetary (rotating) ball mill (model Retsch PM100) under an argon atmosphere.

Twelve 20 mm tungten carbide (WC) milling balls were loaded into a WC milling bowl of volume 250 ml. The milling bowl was taken into the glove box and 6g of pre-ground 1:1 Li_2ND + LiD mixture was loaded into the bowl. The bowl was then sealed to a WC lid *via* a rubber o-ring, removed from the glove box and taken to the ball mill.

The sample was milled at a rate of 350 rpm for a total of three hours. Milling was paused at intervals of 15 minutes in order to dissipate the heat generated by the friction of the milling process. The direction of milling was reversed after each pause.

2.6.3 Na – N – D Compounds

2.6.3.1 $NaND_2$

$NaND_2$ was synthesised *via* two different methods. The first method involved the reaction of NaH with ND_3(g), according to the method outlined in section 2.5.3.3. The evacuated reaction vessel was charged to 0.8bar ND_3 at room temperature, sealed and then heated to 200°C for 12 hours. The sample was re-ground in the glove box, and the reaction process repeated a number of times, until X-ray diffraction data indicated that the proportion of NaH remaining in the sample was less than 5 mass%.

The second synthesis utilised the Intelligent Gravimetric Analyser (IGA) apparatus (section 2.2.3). NaH was hand-ground in the glove box and loaded into a quartz bucket, which was transferred under inert atmosphere to IGA. The reaction vessel was charged to a pressure of 3 bar with ND_3 and the sample was then heated to

200 °C. These conditions of temperature and pressure were maintained until no further mass change was observed in the thermogravimetric data.

2.6.4 Li – Na – N – H

2.6.4.1 $(LiNH_2)_x(NaNH_2)_{1-x}$

Reactions of $(LiNH_2)_x(NaNH_2)_{1-x}$, (where $x = n/12$, $n = 0,1,2.....12$) were performed in sealed evacuated tubes according to the general method outlined in section 2.5.3.1. The tubes were heated to 200°C in a muffle furnace for 12 hours and then allowed to cool to room temperature. To study the effect of annealing, subsequent reactions were performed, where the products of the $x = n/12$ $(LiNH_2)_x(NaNH_2)_{1-x}$ reactions were re-ground after the initial firing at 200 °C and then re-heated in sealed evacuated tubes for a further 12 hours at 100 °C.

2.6.4.2 $(LiNH_2)_v(NaNH_2)_{1-v}$,

Reactions of $(LiNH_2)_v(NaNH_2)_{1-v}$ were performed for values of v from 0.90 – 1.00 in steps of 0.01. These reactions were performed both in sealed evacuated tubes according to the method outlined in section 2.5.3.1, and under flowing Ar according to section 2.5.3.2. In both cases, the reactants were heated to 200°C and the temperature maintained for 12 hours.

2.6.4.3 $(Li_2NH)_x(NaNH_2)_{1-x}$

Li_2NH was formed from the reaction of LiH with $LiNH_2$ under flowing argon as outlined in Section 2.6.1.1.

Mixtures of Li_2NH and $NaNH_2$ ($(Li_2NH)_x(NaNH_2)_{(1-x)}$, where $x = n/12$, $n = 0,1,2.....12$) were heated to 200 °C for 12 hours in sealed evacuated tubes, according to the method described in section 2.5.3.1.

2.6.4.4 $Li_3Na(NH_2)_4$

A number of compositions of $LiNH_2$ + $NaNH_2$ with a ratio of ~ 3:1 were reacted under flowing Ar according to the general method outlined in section 2.5.3.2. The mixtures were heated in the tube furnace for 12 hours at 200 °C and then allowed to cool under flowing gas to room temperature. The material of highest $Li_3Na(NH_2)_4$ purity was synthesised from a 74 : 26 mixture of $LiNH_2$ and $NaNH_2$.

A sample thus formed was washed with t-butyl amine under inert atmosphere using Schlenk techniques. The powder was dissolved in t-butyl amine and the solution filtered through a cannula into a clean Schlenk flask. The t-butyl amine was then removed under vacuum at room temperature, leaving behind the crystalline product.

2.6.4.5 $LiNa_2(NH_2)_3$

A number of compositions of $LiNH_2$ + $NaNH_2$ with a ratio of ~ 1:2 were reacted under flowing Ar, according to the general method outlined in section 2.5.3.2. The mixtures were heated in the tube furnace for 12 hours at 200 °C, and then allowed to cool under flowing gas to room temperature. The products formed were studied by X-ray diffraction, and the material of highest $LiNa_2(NH_2)_3$ purity was formed from a 38 : 62 mixture of $LiNH_2$ and $NaNH_2$.

A sample thus formed was washed with t-butyl amine under inert atmosphere using Schlenk techniques. The powder was dissolved in t-butyl amine and the solution filtered through a cannula into a clean Schlenk flask. The t-butyl amine was then removed under vacuum at room temperature, leaving behind the crystalline product.

2.6.5 Li – Na – N – D

2.6.5.1 $Li_3Na(ND_2)_4$

$Li_3Na(ND_2)_4$ was synthesised from a 3 : 1 reaction of $LiND_2$ with $NaND_2$ under flowing Ar, as outlined in section 2.5.3.2. The mixture was heated in the tube furnace for 12 hours at 200°C and allowed to cool to room temperature under flowing Ar in the furnace.

The $LiND_2$ used during this reaction was formed in the IGA from the reaction of Li_3N with ND_3, as outlined in section 2.6.2.1. The $NaND_2$ used was also synthesised in the IGA, *via* the reaction of NaH with ND_3, according to the process outlined in section 2.6.3.1.

2.6.5.2 $LiNa_2(ND_2)_3$

$LiNa_2(ND_2)_3$ was synthesised from the 1 : 2 reaction of $LiND_2$ with $NaND_2$ under flowing Ar according to the general procedure outlined in section 2.5.3.2. The reaction mixture was heated to 200°C for 12 hours and allowed to cool to room temperature under flowing Ar in the furnace.

The $LiND_2$ and $NaND_2$ precursors used during this reaction were synthesised from LiD and NaH, respectively, under a static pressure of ND_3, as described in sections 2.6.2.1 and 2.6.3.1.

2.6.5.3 $Li_{1-z}Na_zND_2$

$Li_{1-z}Na_zND_2$ was synthesised from a 95 : 5 reaction of $LiND_2$ with $NaND_2$ in a sealed evacuated tube, as outlined in section 2.5.3.1. The mixture was heated in the muffle furnace for 12 hours at 200°C and allowed remained in the furnace during cooling.

The $LiND_2$ used during this reaction was synthesised in the IGA from the reaction of Li_3N with ND_3, as outlined in section 2.6.2.1. The $NaND_2$ used was also synthesised in the IGA, *via* the reaction of NaH with ND_3, according to the process outlined in section 2.6.3.1.

2.7 References

1. R. Jenkins and R. L. Snyder, *Introduction to X-ray Powder Diffractometry*, Wiley Interscience, 1996.
2. C. Kittel, *Introduction to Solid State Physics*, John Wiley & Sons, New York, 1976.
3. W. L. Bragg, *Proceedings of the Cambridge Philosophical Society*, 1912, 17.
4. A. R. West, *Solid State Chemistry and it's Applications*, John Wiley and Sons Ltd, 1985.
5. P. P. Ewald, *Annalen der Physik (Berlin, Germany)*, 1918, 519.
6. A. K. Cheetham and P. Day, *Solid State Chemistry Techniques*, Clarendon Press, Oxford, 1978.
7. W. I. F. David, K. Shankland, L. B. McCusker and C. Baerlocher, *Structure Determination from Powder Diffraction Data*, Oxford Science Publications, 2002.
8. http://icsdweb.fiz-karlsruhe.de/, Accessed 25.06.09.
9. http://www.esrf.eu/UsersAndScience/Experiments/StructMaterials/ID31, Accessed 25.06.09.
10. *International Tables for Crystallography*, 3 edn., 2004.
11. V. F. Sears, *Neutron News*, 1992, **3**, 29 - 37.
12. A. R. West, *Basic Solid State Chemistry*, John Wiley and Sons, Ltd, 1999.
13. http://www.isis.rl.ac.uk/disordered/gem/gem_home.htm, Accessed 25.06.09.
14. H. M. Rietveld, *Journal of Applied Crystallography*, 1969, 65-71.
15. A. Coelho, *TOPAS, General Profile and Structure Analysis Software for Powder Diffraction Data, version 4.0, Bruker AXS, Karlsruhe, Germany, 2004; http://members.optusnet.com.au/_alancoelho*, 1992-2004.
16. P. W. Atkins, *Physical Chemistry*, 6th edn., Oxford University Press, 1978.
17. C. V. Raman, *Nature*, 1928.
18. E. A. V. Ebsworth, D. W. H. Rankin and S. Cadock, *Structural Methods in Inorganic Chemistry*, 2nd edn., Blackwells Scientific Publications, 1987.
19. P. C. H. Mitchell, S. F. Parker, A. J. Ramirez-Cuesta and J. Tomkinson, *Vibrational Spectroscopy with Neutrons*, World Scientific.
20. http://www.isis.rl.ac.uk/molecularSpectroscopy/tosca/index.htm., Accessed 27.06.09.
21. http://www.isis.rl.ac.uk/imageArchive/pages/isis2000tosca.htm, Accessed 26.06.09.
22. S. J. Clark, M. D. Segall, C. J. Pickard, P. J. Hasnip, M. J. Probert, K. Refson and M. C. Payne, *Z. Kristall.*, 2005, **220**, 567-570.
23. Accelrys Software Inc, Editon edn., 2001 - 1009.
24. W. Kohn, A. D. Becke and R. G. Parr, *Journal of Physical Chemistry*, 1996, **100**, 12974-12980.
25. Y. H. Hu and E. Ruckenstein, *Industrial & Engineering Chemistry Research*, 2006, **45**, 4993-4998.

~ Chapter Three ~

A Thermogravimetric and Crystallographic Study of the Li – N – H System.

3.1 Introduction and Scope of Chapter

$LiNH_2$ is widely regarded as a most promising material for hydrogen storage due to it's high hydrogen content and the reversibility of the $LiNH_2$ + LiH – Li_2NH + H_2 system.[1-6]

Much research has been dedicated to this system and the crystal structures of the stoichiometric amide and imide phases are well characterised.[7-9] The crystallographic changes that occur during hydrogen sorption processes, however, remain largely unstudied, although there is evidence to suggest that the transformation between Li_2NH + H_2 and $LiNH_2$ + LiH may occur *via* a continuous series of non-stoichiometric intermediates of composition $Li_{2-x}NH_{1+x}$ ($0 \leq x \leq 1$).[10] Time resolved variable temperature diffraction studies are necessary to provide further information regarding the crystallographic transformations which occur during hydrogen sorption of the Li – N – H system.

The following chapter presents a detailed thermogravimetric and crystallographic study of the $LiNH_2$ / Li_2NH system. Presented first are the results from combined intelligent gravimetric analysis with mass spectrometry (IGA-MS, section 2.2.1) experiments of $LiNH_2$ and 1:1 $LiNH_2$ + LiH. These studies are followed by room temperature and variable temperature diffraction studies of various Li – N – H(D) materials. The synchrotron diffraction data presented were collected using the ID31 beam line at the European Synchrotron Radiation Facility (ESRF, section 2.1.2.3) and room temperature neutron diffraction data were collected using the GEneral Materials diffractometer (GEM) at the ISIS pulsed neutron facility (section 2.1.3.1). Variable temperature neutron diffraction measurements were performed using the GEM diffractometer in conjunction with the intelligent gravimetric analysis combined with neutron diffraction (IGA^n) apparatus (section 2.2.2).

3.2 Thermogravimetric Study of the Li – N – H System Using Intelligent Gravimetric Analysis with Mass Spectrometry.

Combined intelligent gravimetric analysis and mass spectrometry (IGA-MS) studies were performed on samples of $LiNH_2$ and 1:1 $LiNH_2$ + LiH in order to confirm the results reported previously.[1, 11] Samples of $LiNH_2$ and 1:1 $LiNH_2$ + LiH ($LiNH_2$ and LiH both Aldrich, 95% purity) were intimately ground under inert atmosphere, loaded into a stainless steel mesh bucket and then transferred under inert atmosphere to the intelligent gravimetric analyser (IGA) (section 2.2.1). The samples were then heated under a flow of 1 bar He to 400 °C at a rate of 2 °C per minute, and this temperature was maintained for 12 hours. The outgoing gases were sampled by a dynamic sampling mass spectrometer in order to measure the partial pressures of NH_3 and H_2 emitted from the samples (section 2.2.1). The spectrometer was set in flow mode and scanned for molecules 17 and 2 atomic mass units (AMU), corresponding to NH_3 and H_2, respectively.

3.2.1 A Thermogravimetric Study of $LiNH_2$

The thermogravimetric data for the decomposition of $LiNH_2$, measured using the IGA-MS apparatus (section 2.2.1), are presented in Figure 3.1a. As the temperature of the system increased from room temperature up to 269 °C, the mass of the sample was observed to decrease slowly, resulting in a mass loss of 1.8 mass%. This decrease in mass was attributed to the desorption of physisorbed gases from the surface of the powder grains. Upon reaching a temperature of 269 °C, a rapid decrease in sample mass was observed, with a total of 33 mass% lost during this process.

Differentiation of the thermogravimetric data (insert of Figure 3.1b) suggests that this mass loss occurred in two steps, with the rate of mass loss increasing as the sample temperature reached 400 °C.

The peak desorption temperature for $LiNH_2$ reported in the literature is below 400 °C,[12] indicating that $LiNH_2$ decomposition was suppressed during this study. The difference in the peak desorption temperatures observed in the present work and that reported previously[12] can be attributed to the relatively large sample size of ~90 mg used in our experiments. In samples of this size, NH_3 may be easily trapped within grains of $LiNH_2$, resulting in a local concentration of NH_3 greater than or equal to the equilibrium vapour pressure of the NH_3-$LiNH_2$ system. This local concentration of NH_3 would act to suppress decomposition of $LiNH_2$, as outlined in section 1.1.[11] It is only when a higher temperature is reached (with an equivalently higher vapour pressure of NH_3) that the decomposition reaction continues.[11]

The mass spectrometry data, showing the partial pressures of NH_3 (17 AMU) and H_2 (2 AMU) evolved from the sample as a function of time, are presented in Figure 3.1b. It is clear from this data that the observed mass loss was primarily due to the production of ammonia, with a small proportion of H_2 also formed (probably from the decomposition of NH_3 into H_2 + N_2). Integration of the NH_3 and H_2 mass spectrometry traces suggest that the molar ratio of NH_3 : H_2 released during the study was approximately 3:1.

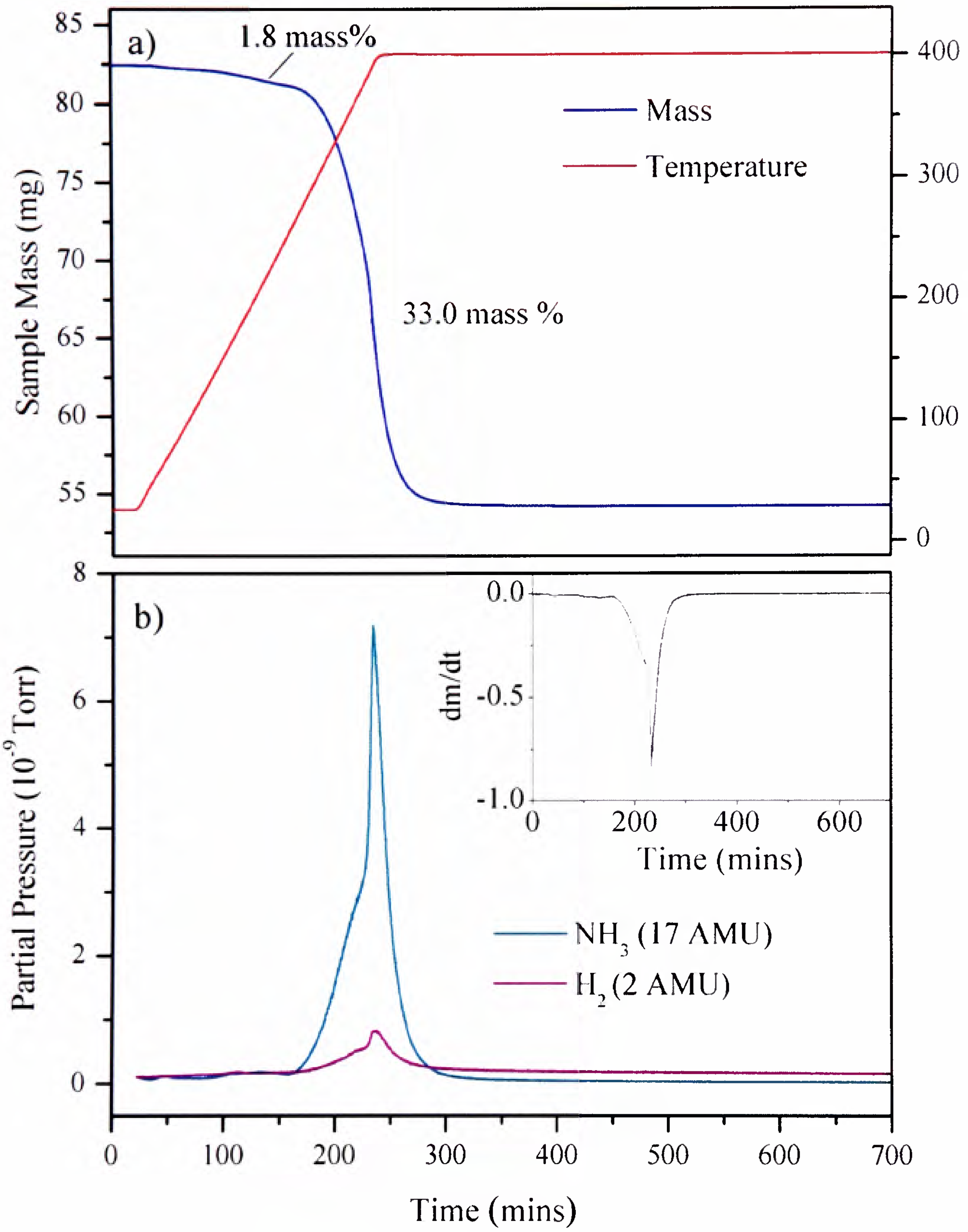

Figure 3.1a and b : a) Thermogravimetric data of $LiNH_2$, collected using intelligent gravimetric analysis with heating rate 2 °C/min and target temperature 400 °C. The red line represents the temperature of the sample and the blue line the sample mass. b) Partial pressures of NH_3 (turquoise line) and H_2 (purple line), recorded during thermogravimetric study of $LiNH_2$ using *in-situ* mass spectrometry. Insert: differential of sample mass (m) with respect to time (t).

The total mass loss from the $LiNH_2$ sample was 35 mass%, which is in good agreement with the theoretical mass loss of 37 mass%, which would be expected for the decomposition reaction outlined in Equation 3.1.

$$2LiNH_2 \longrightarrow Li_2NH + NH_3 \qquad \text{Equation 3.1}$$

The 2 mass% discrepancy between the theoretical and experimental mass losses was thought to arise from the evolution of H_2.

3.2.2 A Thermogravimetric Study of $LiNH_2$ + LiH

The thermogravimetric data for the decomposition of the 1:1 mixture of $LiNH_2$ + LiH are presented in Figure 3.2a.

As expected, the decrease in the mass observed for this sample (12.5 mass%) was much lower than that observed for pure $LiNH_2$ (35 mass%). A small mass loss of 0.5 mass% was observed at the outset of the experiment, which was attributed to the desorption of physisorbed gas from the sample. A steep loss of 12 mass% commenced as the sample reached 194 °C, which is some 75 °C below the first major mass loss observed from pure $LiNH_2$ (section 3.2.1). These findings are consistent with the observations of Ichkawa *et al*, that mixtures of 1:1 $LiNH_2$ + LiH commence decomposition at a lower temperature than pure $LiNH_2$. [3]

The partial pressures of NH_3 and H_2 released during this study and recorded by mass spectrometry are presented in Figure 3.2b. The presence of LiH in the reaction mixture greatly reduced the amount of NH_3 desorbed from the sample (compared to pure $LiNH_2$ in section 3.2.1), resulting in the formation of H_2.

The partial pressure of H_2 (2 AMU), recorded during decomposition of the $LiNH_2$ / LiH mixture, consists of two main desorption features which peak at 307 °C and 380 °C, and have an integrated ratio of 2 : 1. The first feature has a shoulder at 170 minutes (temperature 274 °C), implying that this feature is a composite of two desorption processes. The mass spectrometry data for NH_3 (AMU 17) consisted of a broad peak with onset temperature 240 °C, and peak temperature at 372°C (the melting point of pure $LiNH_2$).

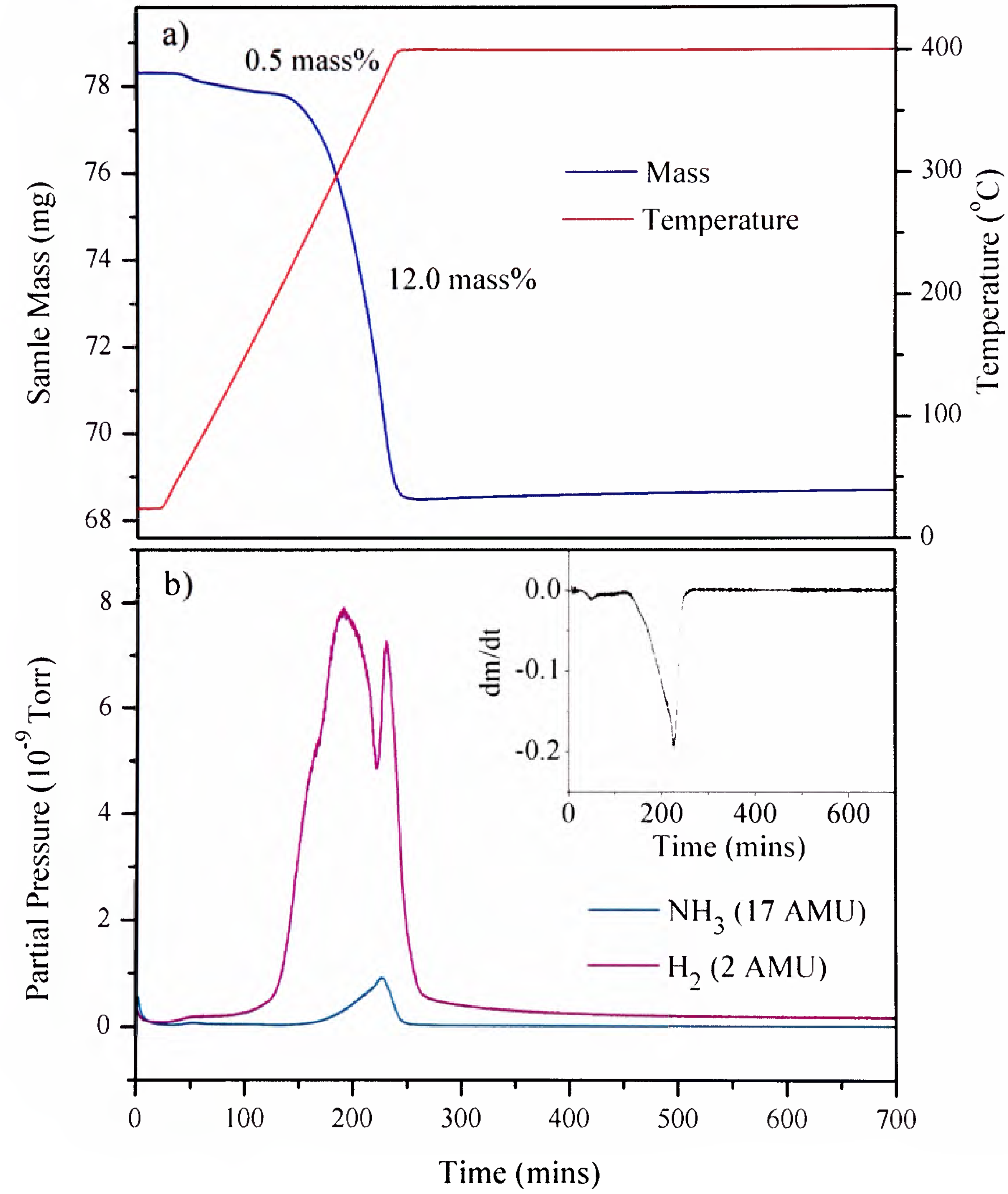

Figure 3.2a and b : a) Thermogravimetric data of 1:1 $LiNH_2$ + LiH, collected using intelligent gravimetric analysis with heating rate 2 °C/min and target temperature 400 °C. The red line represents the temperature of the sample and the blue line the sample mass. b) Partial pressures of NH_3 (turquoise line) and H_2 (purple line), recorded during the decomposition of 1:1 $LiNH_2$ + LiH using *in-situ* mass spectrometry. Insert: differential of sample mass (m) with respect to time (t).

The derivative of the gravimetric data (insert of Figure 3.2b) implies that the first H_2-releasing step (corresponding to the shoulder on the H_2 partial pressure trace at t = 170 minutes, temperature 274 °C) had the slowest rate of mass change, compared to the other H_2-releasing processes. The rate of mass loss increased as the decomposition reaction progressed to the second H_2-releasing step (T = 307 °C, t = 190 minutes), and peaked during the third H_2-releasing step (T = 380 °C, t = 230 minutes), which also coincided with the peak ammonia desorption.

Integration of the entire mass spectrometry profiles for H_2 and NH_3 gave a ratio of 17 H_2 molecules released per molecule of NH_3, with the implication that the major reaction that occurred during the experiment was hydrogen-releasing. These findings agree with previous studies reported in the literature, indicating that decomposition of the sample studied occurred according to Equation 3.2:[1-6]

$$LiNH_2 + LiH \longleftrightarrow Li_2NH + H_2 \qquad \text{Equation 3.2}$$

The mass loss anticipated from Equation 3.2 is 7 mass%, which is 5.5 mass% lower than that observed experimentally. The release of 1 mole of NH_3 for every 17 moles of H_2 accounts for 3.5 mass% of the discrepancy, and desorption of physisorbed gases prior to decomposition accounts for a further 0.5 mass%.

The remaining 1.5 mass% loss observed experimentally remains unaccounted for.

As outlined in Chapter One, the reaction of $LiNH_2$ with LiH to form $Li_2NH + H_2$ is believed to occur via the two step ammonia-mediated reaction outlined below:[3, 13, 14]

$$2LiNH_2 \rightarrow Li_2NH + NH_3 \qquad \text{Equation 3.3a}$$

$$NH_3 + LiH \rightarrow LiNH_2 + H_2 \qquad \text{Equation 3.3b}$$

Both the observed partial pressure of ammonia and the total mass lost during decomposition suggest that ammonia-capture (according to Equation 3.3b) was not 100 % effective during this experiment. This will have arisen due to the decreasing concentration of LiH in the sample during the decomposition, since $LiNH_2$ and LiH must be found in close contact for the NH_3 released to be captured. In ground samples such as this one, the probability of this drops with decreasing LiH-content, thus increasing the likelihood of ammonia release.

3.3 Room-Temperature Synchrotron X-ray Diffraction Studies of the Li – N – H System

3.3.1 Synchrotron X-ray Diffraction Study of Li_3N

Diffraction data from a sample of Li_3N (Aldrich, 99% purity) was collected in order to determine the purity of the material used during subsequent experiments. The sample was thoroughly ground and packed into a 1.0 mm diameter capillary tube under N_2 atmosphere. The tube was sealed and mounted onto the ID31 diffractometer at the ESRF (section 2.1.2.3) and diffraction data were collected using a wavelength of 0.8000 Å and a step-size of 0.003°. Rietveld analysis[15] (section 2.1.4) of the diffraction data was performed according to the general method outlined in section 2.1.4.1 using the TOPAS Academic software suite.[16] The diffraction data and the refined model are presented in Figure 3.3.

Refined scale factors, generated from Rietveld analysis[15] of the diffraction data, indicated that Li_3N as purchased was a mixture of α- and β-Li_3N (96 mass%) with minority phases Li_2O and LiOH. The Li_3N present was 86 mass% α-phase and 14 mass% β-phase.

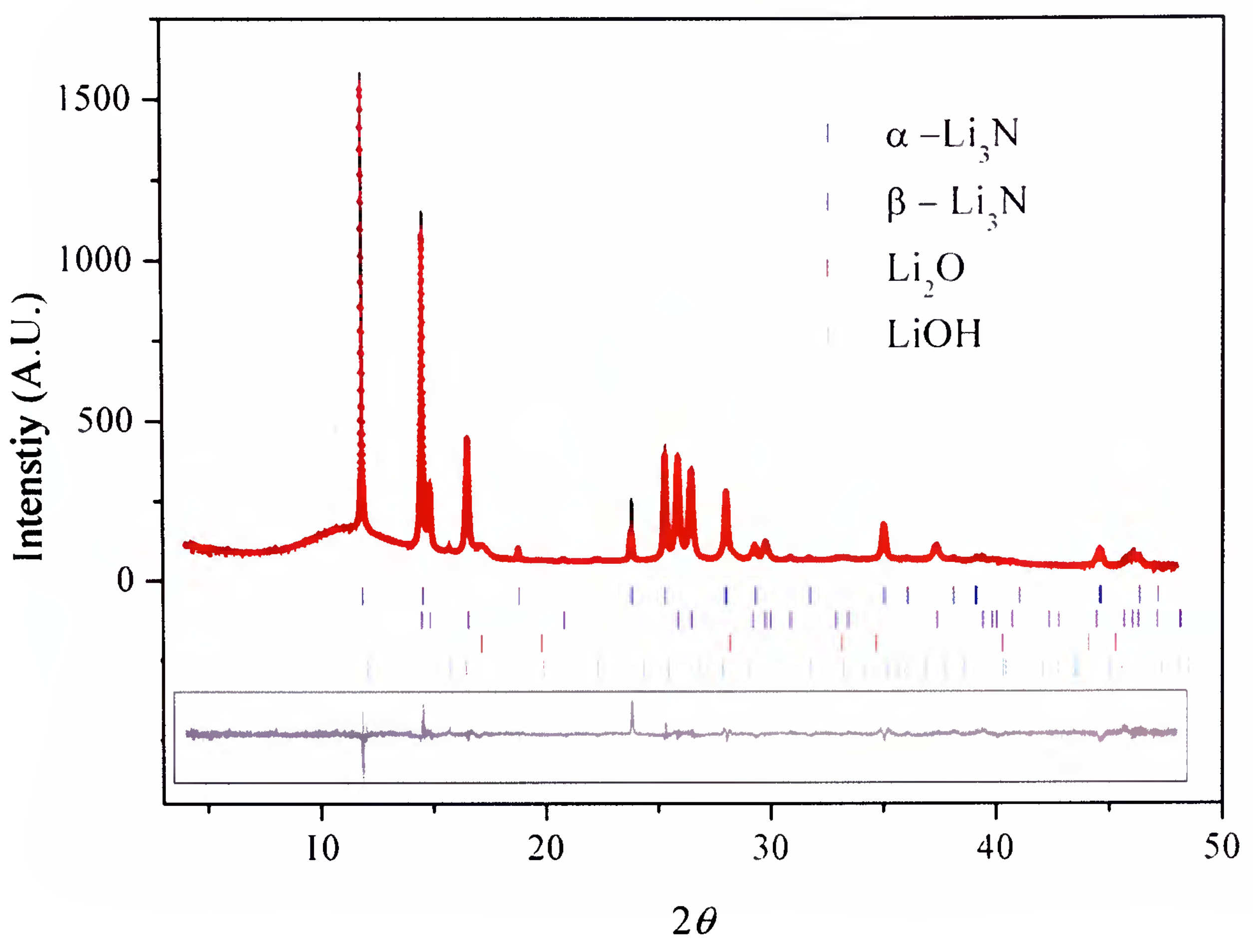

Figure 3.3 : Observed (solid line), calculated (red dots), and difference plots (y_{obsd} - y_{calcd}, solid line in box) for the structure refinement of Li_3N from X-ray synchrotron diffraction data collected at λ = 0.8000 Å and with a step size of 0.003 Å. The Bragg peak positions for α-Li_3N, β-Li_3N, Li_2O and LiOH Li_2NH are shown by the vertical tick marks. R_{wp} 6.043, R_{exp} 3.552, goodness of fit 1.716

3.3.2 Synchrotron X-ray Diffraction Study of Li_2NH

A sample of Li_2NH was synthesised *via* the reaction of $LiNH_2$ with Li_3N under flowing Ar at 300 °C (section 2.6.1.1). Diffraction data for the Li_2NH formed was collected in a sealed capillary tube as described previously (section 2.1.2.3) with X-ray radiation of wavelength of 0.8000 Å and a step-size of 0.003°. These data are presented in Figure 3.4

The data were analysed using the Rietveld method[15] (section 2.1.4) utilising TOPAS Academic fitting software[16] according to the general refinement procedure outlined in section 2.1.4.1. Refined scale factors indicated that Li_2NH was the majority phase present, accounting for 90.5 mass% of the material. Impurity phases were identified as un-reacted $LiNH_2$ (4.5 mass%) and Li_3N (0.8 mass%) together with Li_2O (4.2 mass%). The vast majority (99.4 mass%) of the Li_2NH in this sample adopted the cubic anti-fluorite $Fm\bar{3}m$ structure. The remaining 0.6 mass% adopted the $Fd\bar{3}m$ structure.

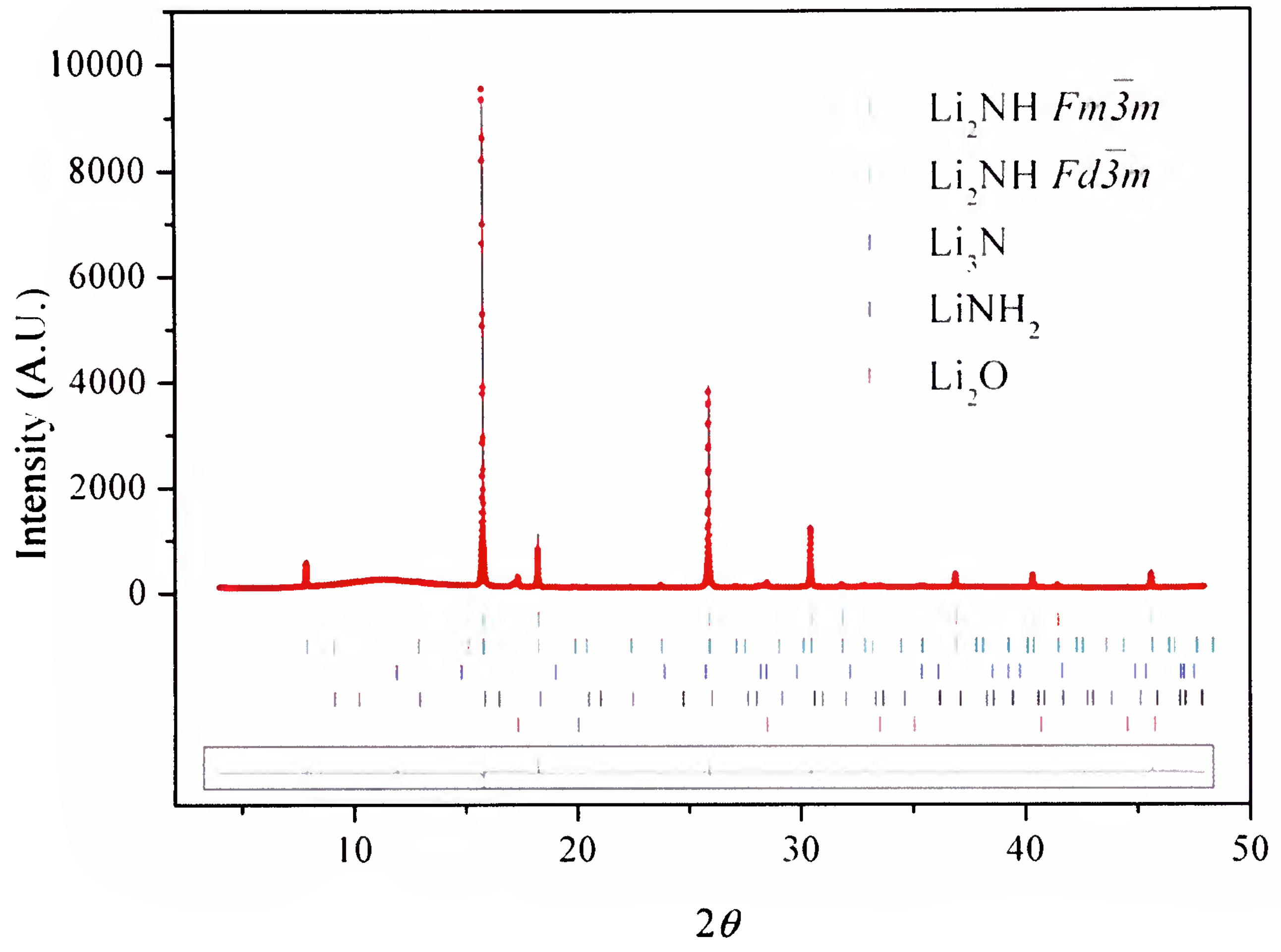

Figure 3.4 : Observed (solid line), calculated (red dots), and difference plots (y_{obsd} - y_{calcd}, solid line in box) for the structure refinement of Li_2NH from X-ray synchrotron diffraction data collected at λ = 0.8000 Å and with a step size of 0.003 Å. The Bragg peak positions for Li_2NH and two phases of Li_2O are shown by the vertical tick marks. R_{wp} 6.589, R_{exp} 2.988, goodness of fit 2.205

As outlined in section 1.4.2, the $Fd\bar{3}m$ structure is usually the preferred structure of Li_2NH at temperatures below 87 °C.[8] The presence of the $Fm\bar{3}m$ structure during these room temperature measurements implies that the cooling rate of the sample was too fast to allow transformation of the $Fm\bar{3}m$ phase into the $Fd\bar{3}m$ phase.

A schematic diagram of the $Fm\bar{3}m$ structure of Li_2NH, and a table listing the unit cell parameters and atomic positions of the atoms has been presented previously in section 1.4.2. The refined lattice parameter for the Li_2NH studied here was a = 5.07122(3) Å, which is in good agreement with that reported previously for Li_2NH.[7, 8]

3.3.3 Synchrotron X-ray Diffraction Study of $LiNH_2$

The synchrotron X-ray diffraction data of an as-found sample of $LiNH_2$ (Sigma Aldrich, 95% pure) were collected using the ID31 beamline at the ESRF (section 2.1.2.3) with wavelength of 0.7988 Å and a step-size of 0.003°. Rietveld analysis[15] of the data was performed according to the general method outlined in section 2.1.4.1 using the TOPAS Academic software suite.[16] The collected data and refined model are presented in Figure 3.5 and the refined structural and thermal parameters calculated for $LiNH_2$ are summarised in Table 3.1.

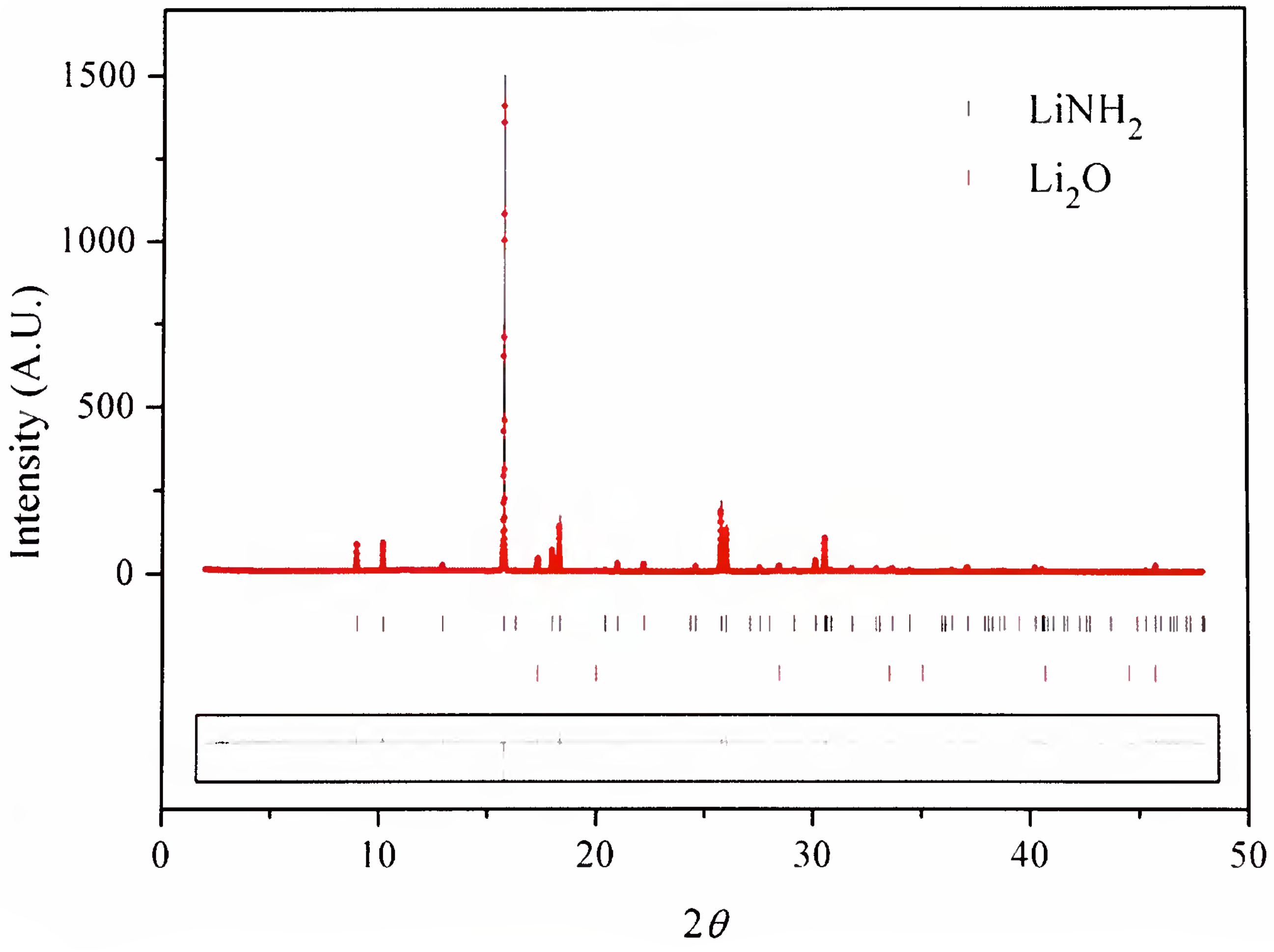

Figure 3.5 : Observed (solid line), calculated (red dots), and difference plots (y_{obsd} - y_{calcd}, solid line in box) for the structure refinement of $LiNH_2$ (Aldrich 95%) from X-ray synchrotron diffraction data collected at λ = 0.7998 Å and with a step size of 0.003 Å. The Bragg peak positions for $LiNH_2$ and Li_2O are shown by the vertical tick marks. R_{wp} 8.340, R_{exp} 4.451, goodness of fit 1.874

Rietveld modelling of the atomic site occupancies found no significant deviation in Li or H content and as such, the $LiNH_2$ sample was concluded to be fully stoichiometric. Refined scale factors suggested that the sample was majority phase $LiNH_2$ (95 mass%) together with impurity Li_2O (5 mass%).

$LiNH_2$

Atom	Site	*x*	*y*	*z*	Occupancy	B
Li 1	2a	0	0	0	1	2.67(5)
Li 2	4f	0	½	0.0041(6)	1	2.67(5)
Li 3	2c	0	½	¼	1	2.67(5)
N	8g	0.2269(3)	0.249 (1)	0.1143(1)	1	1.44(4)
H 1	8g	0.2429	0.1285	0.1019	1	2.0534
H 2	8g	0.3840	0.3512	0.1278	1	2.0534

$a = 5.03760(2)$ Å, $c = 10.26472(6)$ Å

Table 3.1 : Summary of structural parameters for $LiNH_2$, space group $I\bar{4}$ (number 82)

3.4 In Situ Diffraction 1 : Variable Temperature Synchrotron X-ray Diffraction Studies of $LiNH_2$ and $LiND_2$

In order to gain a crystallographic overview of the processes occurring during the decomposition of lithium amide, variable temperature synchrotron X-ray diffraction experiments were performed on samples of $LiNH_2$ and $LiND_2$.

The samples were ground under inert atmosphere and packed into silica glass capillary tubes. These tubes were sealed and mounted onto the ID31 beamline at the ESRF, which was fitted with a blower furnace (section 2.1.2.3). The samples were then heated to 350 °C in steps of 5 or 10 °C and allowed to equilibrate for one minute at each temperature, prior to data collection. Diffraction data (wavelength of 0.7998 Å and a step-size of 0.003°) were then collected over a 2θ range of 8 – 32° for a period of three minutes at each temperature.

The diffraction data collected during these studies are presented in *surface plots*. Surface plots are formed by stacking successive diffraction patterns, one behind the other, and viewing the stack from above. The lines observed correspond to the positions of the Bragg peaks at each point during the experiment. The colour of the various lines is indicative of the relative intensities of the Bragg peaks and variation of these colours often indicates changes in the relative proportions of the phases present. Deviation in the gradient of the lines from the vertical is indicative of variations in the lattice parameters of the phases. The appearance and disappearance of lines is consistent with formation and loss of crystalline phases, respectively, whilst splitting or convergence of lines can be indicative of phase transformations.

Surface plots provide a very convenient way of viewing the crystallographic progress of a reaction, however, information regarding the crystal structures of the materials present cannot be obtained from the study of such diagrams. As such, values of lattice parameters, site occupancies and scale factors etc must be obtained from Rietveld analysis[15] of each individual data set (section 2.4.1).

Analysis of data from variable temperature experiments such as these would be an extremely time consuming process. However, if the crystallographic variation between subsequent data sets is small, refinement of a large number of data sets can be performed with relative ease by utilising the batch facility included in many refinement packages.

These techniques use the refined model from a previous diffraction pattern as the starting model for the next diffraction pattern. The TOPAS Academic software suite[16] includes such a facility, which is outlined in more depth in section 2.1.4.2.

3.4.1 Variable Temperature Synchrotron X-ray Diffraction Study of $LiNH_2$

A sample of $LiNH_2$ (Aldrich, 95%) was thoroughly ground and packed under inert conditions into a 1.0mm glass capillary. The capillary was sealed and mounted onto the ID31 diffractometer at the ESRF, which was fitted with a blower heater (section 2.1.2.3). The $LiNH_2$ sample was heated at a rate of 10 °C/min to 305 °C and then at 5 °C/min to 350 °C and diffraction data collected as outlined in section 3.4. A surface plot of the data collected is presented in Figure 3.6.

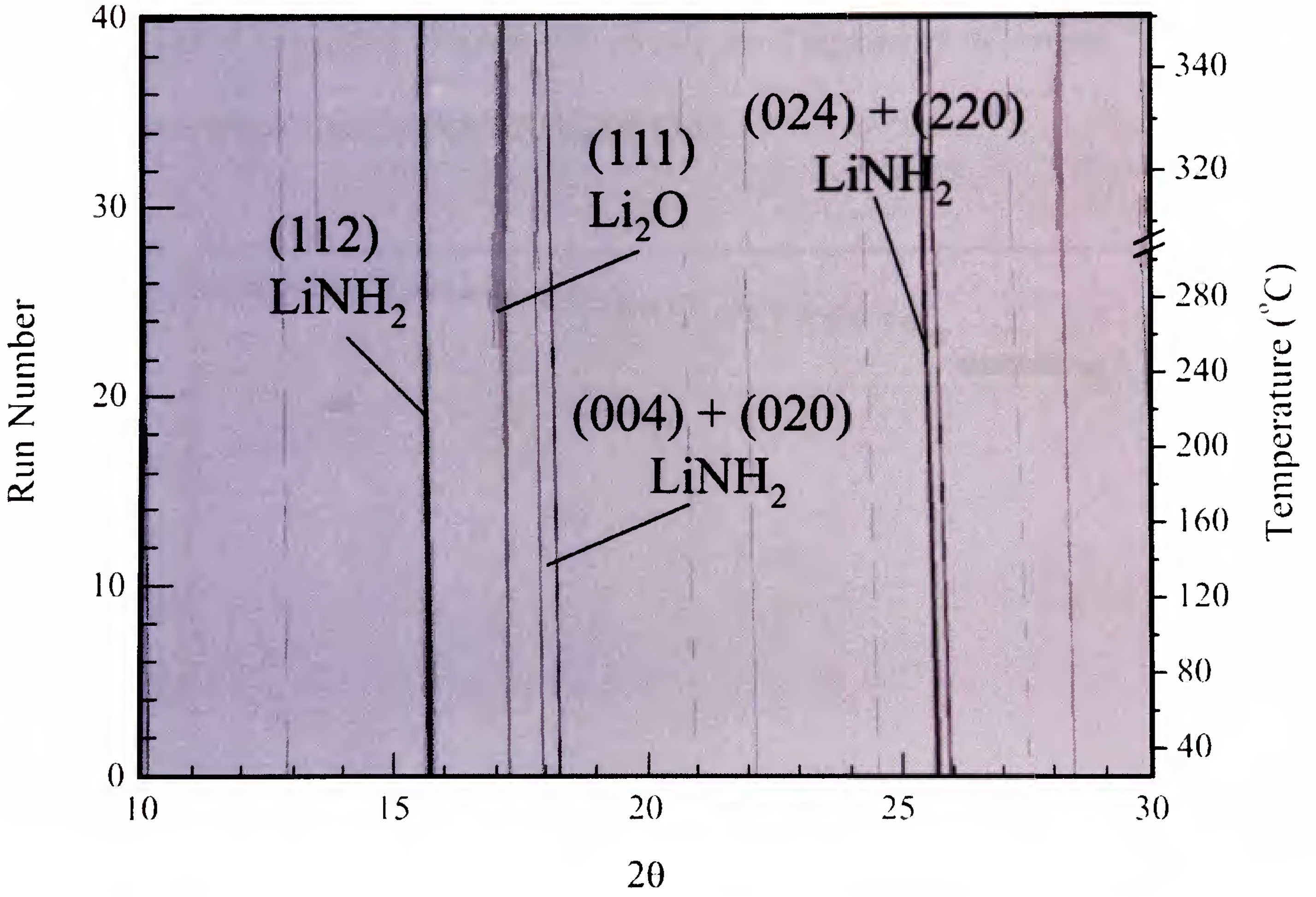

Figure 3.6 : Surface plot of synchrotron X-ray diffraction data collected during the heating of $LiNH_2$ (Aldrich, 95% purity) to 350 °C in a sealed glass capillary tube. Lines corresponding to Bragg reflections of the various phases are indexed

The negative gradient of the lines in the surface plot is indicative of a shift in the positions of the Bragg reflections to lower 2θ values during the experiment. This is consistent with thermal expansion of the lattice parameters. The Bragg reflections corresponding to Li_2O (2θ = 17.2 and 28.4) were observed to broaden and increase in intensity during the course of the reaction, however, other than a shift to a lower 2θ value, little variation was observed in the Bragg reflections of $LiNH_2$ (2θ = 15.5, 17.9, 18.2, 25.7, 25.9).

The diffraction data were refined using the Rietveld method,[15] implementing the batch refinement capabilities of the TOPAS Academic software suite[16] according to the method outlined in section 2.1.4.2. A full summary of the refined structural parameters is presented in Appendix A1.1.

Prior to heating, the majority phase of the sample was $LiNH_2$ (88 mass%) with minority Li_2O (12 mass%). Figure 3.7a shows the temperature dependent variation of the calculated phase fractions of $LiNH_2$ and Li_2O.

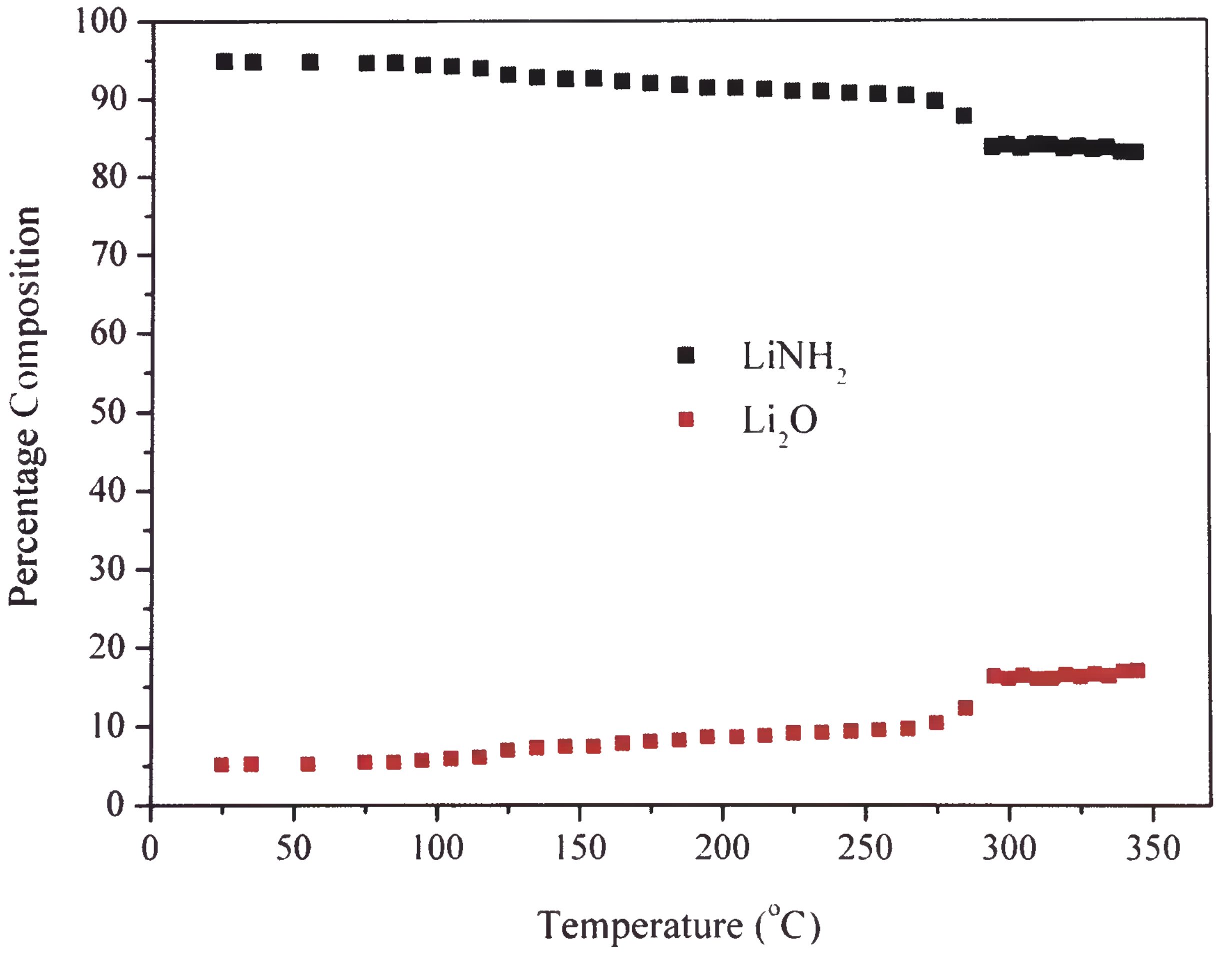

Figure 3.7a : Temperature dependent variation of refined $LiNH_2$ and Li_2O phase fractions, calculated from Rietveld analysis of synchrotron diffraction data (*via* batch refinement) collected during the heating of $LiNH_2$ to 350 °C. Mean errors $LiNH_2$ ± 0.2, Li_2O ± 0.2. Error bars smaller than data markers.

The figure indicates that the phase fraction of Li_2O increased steadily as the sample temperature rose from 25 °C to 295 °C. A corresponding decrease was observed in the $LiNH_2$ phase fraction, suggesting that the increasing Li_2O content arose due to the interaction of $LiNH_2$ with oxygen. The scale factors of $LiNH_2$ and Li_2O became constant as the temperature of the system increased above 295°C. This was presumably due to the utilisation of all oxygen present, implying that the oxygen was derived from the silica (SiO_2) walls of the capillary tube.

The temperature dependent variation of the $LiNH_2$ lattice parameters, *c/a* ratio, $LiNH_2$ unit cell volume and Li site occupancies are presented in Figures 3.7b, c, d and e, respectively.

The unit cell parameters of $LiNH_2$ (Figure 3.7b) increased almost linearly with temperature up to 295 °C. Upon reaching 295 °C, a sudden decrease was observed in the length of the *c*-lattice parameter, which was accompanied by a small increase in the length of the *a*-parameter. This resulted in an overall decrease in the unit cell volume (Figure 3.7d) and was attributed to a first order transition in the lattice parameters.

This transition coincided with an increase in the cation disorder of $LiNH_2$, as evidenced by variations in the Li-occupancy of the 2c (0,½,¼) and 2d (½,0,¼) sites (Figure 3.7e)). A decrease in the 2c site occupancy was accompanied by a corresponding increase in the 2d site occupancy, suggesting Li^+ ion migration from the 2c – 2d sites. The 2a (0,0,0) and 4f (0,½,*z*) sites remained fully occupied throughout the course of the experiment (Figure 3.7e)).

Decomposition of the sample to form Li_2NH was not observed, even though the sample-temperature increased beyond the usual decomposition point of $LiNH_2$. Given the sealed, pressurised conditions used during this study, it is likely that the low equilibrium vapour pressure of the $LiNH_2$-NH_3 system[11] was reached very early in the experiment. Suppression of the decomposition of $LiNH_2$ during this experiment was, therefore, not surprising.

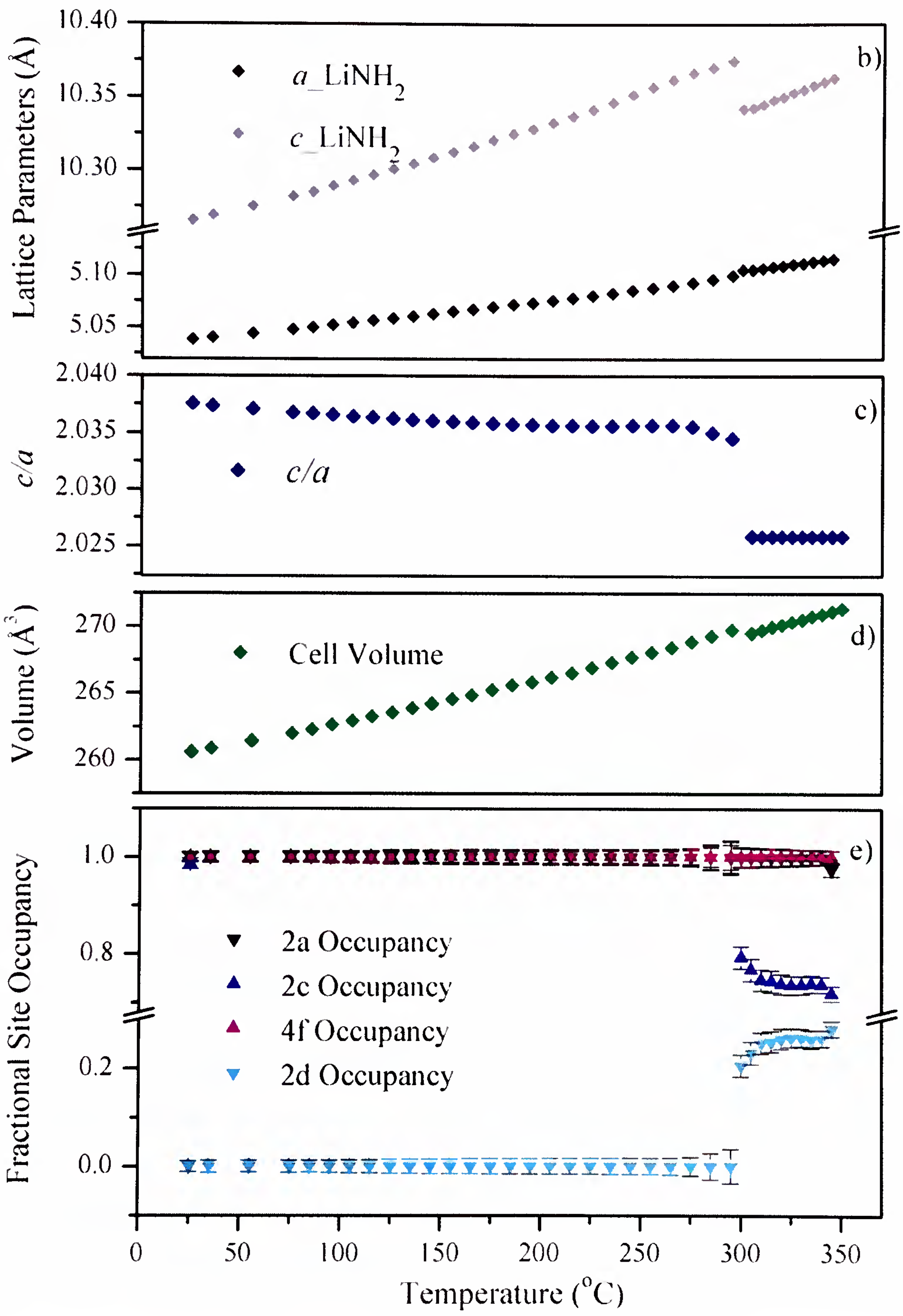

Figure 3.7 b, c, d and e: Temperature dependent variation of b) refined $LiNH_2$ lattice parameters, c) *c/a* ratio, d) unit cell volume and e) refined Li 2a (0,0,0),2c (0,½,¼), 2d (½,0,¼) and 4f (0,½,*z*) site occupancies of $LiNH_2$, calculated from Rietveld analysis of synchrotron diffraction data (*via* batch refinement) collected during the heating of $LiNH_2$ to 350 °C. Mean errors *a*_$LiNH_2$ ± 0.00003, *c*_$LiNH_2$ ± 0.00007, 2a occupancy ± 0.015, 2c occupancy ± 0.016, 4f occupancy ± 0.013, 2d occupancy ± 0.016. Error bars only shown if larger than data markers.

3.4.3 Variable Temperature Synchrotron X-ray Diffraction Study of $LiND_2$

A sample of $LiND_2$ was synthesised *via* the reaction of Li_3N (Aldrich, 99% purity) with ND_3 (BOC special gases) in the IGA according to the process outlined in section 2.6.2.1. The material formed was ground and packed under an inert atmosphere into a 1.0 mm capillary tube which was sealed and mounted onto the ID31 diffractometer at the ESRF (section 2.1.2.3). The diffractometer was fitted with a blower heater and the sample was heated to 355 °C in intervals of 10 °C, with diffraction data collected at each set point as outlined in section 3.4. A surface plot (section 3.4) of this data is presented in Figure 3.8.

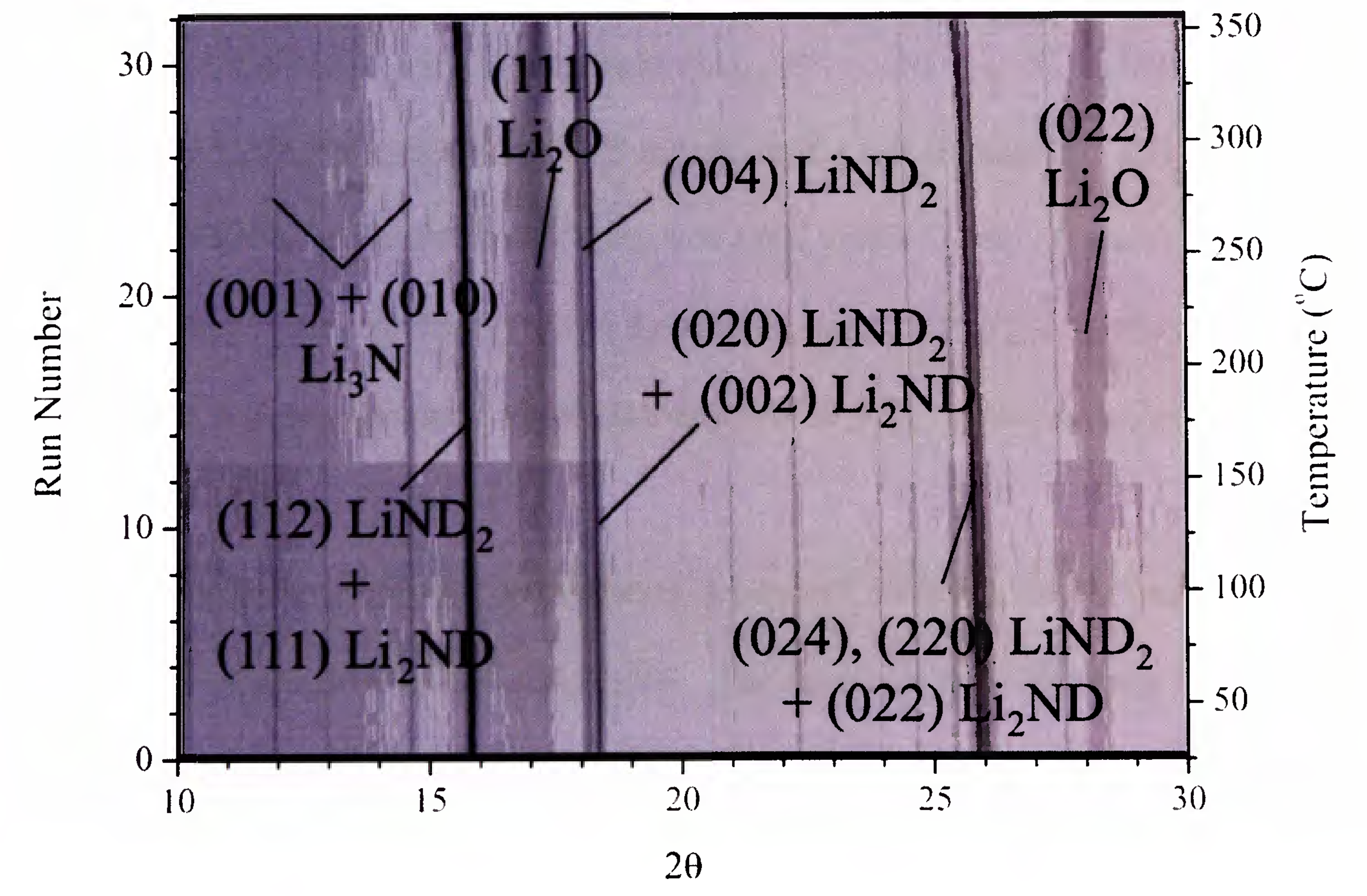

Figure 3.8 : Surface plot of synchrotron X-ray diffraction data collected during the heating of $LiND_2$ (synthesised from Li_3N +ND_3) to 355 °C in a sealed glass capillary tube. Lines corresponding to Bragg reflections of the various phases are indexed.

The negative gradient of the lines observed indicates a shift in the Bragg peaks to lower 2*θ* value with increasing temperature. This is consistent with thermal expansion of the phases present. The lines corresponding to Li_2O (2θ = 17.2 and 28.4) were seen to broaden and increase in intensity during the course of the experiment. The Bragg peaks at 2*θ* = 12 and 14.5 (indexed to Li_3N) decreased in intensity and ultimately vanish as the sample temperature increased beyond 255 °C. Other than shifting to lower 2*θ* values, little variation could be observed in the remaining Bragg peaks from this figure.

Rietveld analysis[15] of the variable temperature $LiND_2$ diffraction data was performed using the batch facility of TOPAS Academic refinement software[16] as outlined in section 2.4.1.2. Refinement of the diffraction data collected at room temperature indicated that the majority phase of the sample was $LiND_2$ (79 mass%), which appeared to be Li-rich, with stoichiometry $Li_{1.12(1)}ND_{1.88(1)}$. The impurity phases present were Li_2ND (8 mass%), Li_3N (5 mass%) and Li_2O (8 mass%). The presence of Li_3N in the sample implied that the reaction of Li_3N with ND_3 did not reach completion, and the presence of 8 mass% Li_2ND in the sample suggests that the synthesis of $LiND_2$ from $Li_3N + ND_3$ may proceed *via* the formation of Li_2ND, or that some Li_3N may have reacted with $LiND_2$ to form Li_2ND.

Figure 3.9a shows the temperature-dependent variation of the refined phase-fractions of $LiND_2$, Li_2O, Li_3N and Li_2ND. The figure shows a decrease in the phase fraction of $LiND_2$ up to a temperature of 185 °C. A corresponding increase was observed in the phase fraction of Li_2O, indicating that $LiND_2$ reacted with oxygen to form Li_2O. The phase-fraction of Li_2O became constant between temperatures of 185 °C and 295 °C, indicating that all of the $LiND_2$ in contact with oxygen had converted to

Li_2O, and suggesting that the oxygen present had been derived from the silica capillary tube. Above 295 °C, a slight decrease was observed in the Li_2O phase fraction.

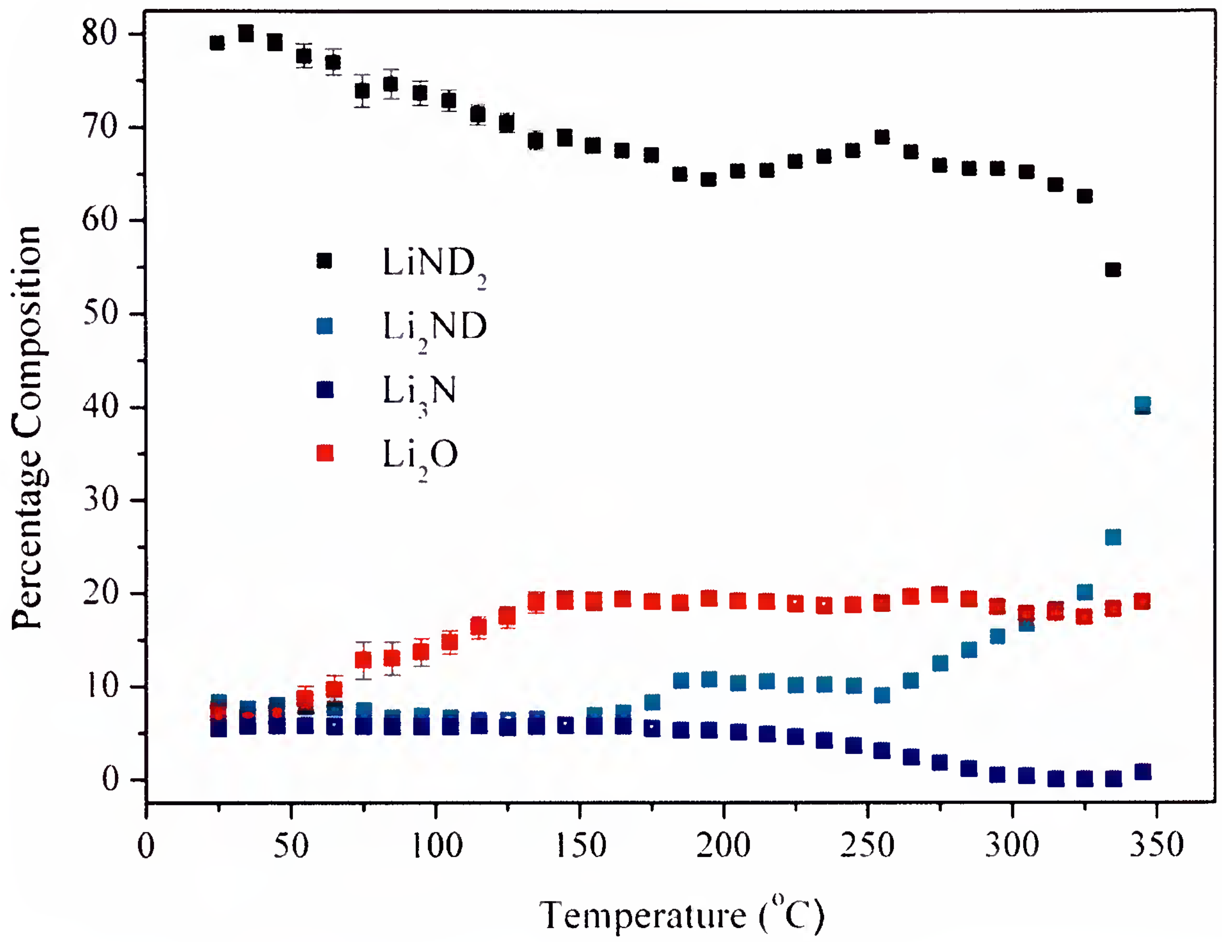

Figure 3.9a : Temperature dependent variation of refined $LiND_2$, Li_3N, Li_2ND and Li_2O phase fractions, calculated from Rietveld analysis of synchrotron diffraction data (*via* batch refinement) collected during the heating of $LiND_2$ to 350 °C. Mean errors, $LiND_2 \pm 0.9$, $Li_2ND \pm 0.3$, $Li_3N \pm 0.3$ and $Li_2O \pm 0.1$. Errors only shown if larger than data markers.

Upon reaching a temperature of 245 °C, the phase fraction of Li_2ND increased and corresponding decreases were observed in the $LiND_2$ and Li_3N fractions. This suggests that some $LiND_2$ reacted with the Li_3N impurity, forming Li_2ND as outlined in Equation 3.4.

$$Li_3N + LiND_2 \longrightarrow 2\,Li_2ND \qquad \text{Equation 3.4}$$

Upon reaching a temperature of 325 °C, the phase fraction of $LiND_2$ decreased very sharply, and a corresponding increase was observed in the phase fraction of Li_2ND. No Li_3N impurity was present in the sample at this point, suggesting that this crystallographic change resulted from the decomposition of $LiND_2$ with loss of ND_3, according to Equation 3.5.

$$2\,LiND_2 \longrightarrow Li_2ND + ND_3 \qquad \text{Equation 3.5}$$

Figures 3.9b, c, d and e present the temperature dependent variation of the $LiND_2$ lattice parameters, *c/a* ratio, unit cell volume and Li – site occupancies, respectively.

It is clear that the unit cell parameters and unit cell volume of $LiND_2$ increased virtually linearly with temperature throughout the experiment (Figure 3.9b, c and d). No first order transition in lattice parameters was observed for $LiND_2$, which contrasts with the behaviour of $LiNH_2$ observed under similar conditions (section 3.4.1).

The room temperature stoichiometry of the $LiND_2$ sample was calculated at $Li_{1.12(1)}ND_{1.88(1)}$ using the refined Li occupancies of the 2a (0,0,0), 2c (0,½,¼), 4f (0,½,*z*), 2d (½,0,¼) and 4e (0,0,0.275) sites and assuming a charge-neutral material ($Li_{1+x}ND_{2-x}$). The Li-occupancies of the 2a, 2c, 4f, 2d and 4e sites were then refined as a function of temperature (Figure 3.9e).

A slight increase was observed in the occupancies of the 2c (0,½,¼), 4f (0,½,*z*), and 4e (0,0,0.275) lattice sites when the temperature of the sample reached 185 °C. Increasing the temperature further to 245 °C resulted in a decrease in the occupancy of the 2c and 4e sites, which coincided with the formation of Li_2ND from $LiND_2$ + Li_3N. The 2a (0,0,0) lattice site remained fully occupied up to a temperature of 315 °C.

As the temperature of the sample reached 325 °C, the occupancy of all Li lattice sites decreased. This coincided with the decomposition of $LiND_2$ to form Li_2ND, as indicated by the phase fraction values presented in Figure 3.9a. This suggests that the $LiND_2$ remaining after partial decomposition of the material into Li_2ND is of lower Li-content than that present prior to decomposition.

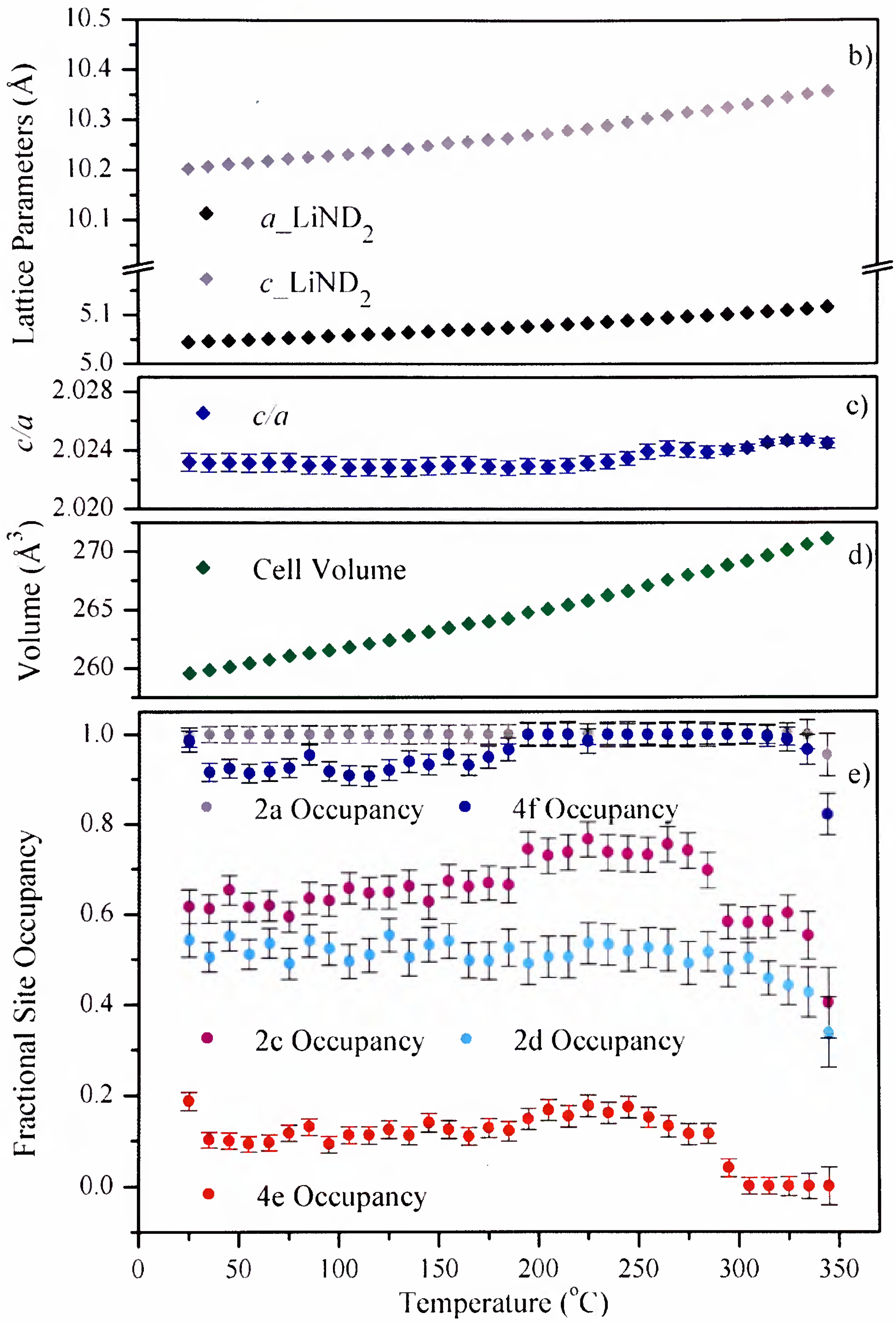

Figure 3.9 b, c, d and e: Temperature dependent variation of b) refined $LiND_2$ lattice parameters, c) *c/a* ratio, d) unit cell volume and e) refined Li occupancies of the 2a (0,0,0), 2c (0,½,¼), 2d (½,0,¼), 4f (0,½,*z*) and 4e (0,0,*z*) sites of $LiND_2$, calculated from Rietveld analysis of synchrotron diffraction data (*via* batch refinement) collected during the heating of $LiND_2$ to 350 °C. Mean errors, *a*_$LiND_2$ ± 0.00015, *c*_$LiND_2$ ± 0.0003, 2a occupancy ± 0.02, 2c occupancy ± 0.03, 2d occupancy ± 0.04, 4f occupancy ± 0.02 and 4e occupancy ± 0.02. Error bars only shown if larger than data markers.

These observations imply that the cation disorder of $LiND_2$ increases with increasing temperature, suggesting that disorder of the Li^+ sub-lattice (and perhaps motion of the Li^+ ions from site to site) may be an important factor in the transformation of $LiND_2$ into Li_2ND. Occupancies of the D sites could not be tracked due to the *Z*-dependence of X-ray intensity (section 2.1.2.1) and hence, the relative order of the D atoms may also play a significant role in the transformation of $LiND_2$ into Li_2ND.

A full summary of the refined structural parameters is presented in Appendix A.1.1.

3.4.4 Comparison of Variable Temperature Synchrotron X-ray Diffraction Data of $LiNH_2$ and $LiND_2$

The variable temperature diffraction data collected from the hydrogenated and deuterated versions of lithium amide are clearly very different. Firstly, upon heating to ~ 325 °C, $LiND_2$ decomposed to form Li_2ND, whilst decomposition of $LiNH_2$ was not observed up to a temperature of 350 °C. Secondly, a first order transition in lattice parameters was observed in $LiNH_2$ at 295 °C, which was not observed in $LiND_2$.

These variations appear to be too marked to arise purely from isotopic effects, and are therefore also attributed to the initial state of the precursor materials.

The $LiNH_2$ used was shown to be a stoichiometric, ordered material (section 3.3.3) whereas the $LiND_2$ used was an intrinsically disordered material (section 3.5.1)

Ordered $LiNH_2$ was seen to undergo a first order transition in *c/a*, apparently triggered by the increased disorder of the phase during heating, whilst no structural transition was observed when disordered $LiND_2$ was heated under similar conditions. These findings lead to the conclusion that the structural change observed during the heating of $LiNH_2$ was an order-disorder transition.

Since the disordered $LiND_2$ studied here was observed to decompose at a lower temperature than ordered $LiNH_2$, it may be that disorder within the lithium amide structure plays an important role in the decomposition properties of the material. Isotopic effects may also be partly responsible, however, previous studies have shown that the decomposition of $LiND_2$ progresses in an identical fashion to $LiNH_2$.[14]

The data collected for the two samples also shared a number of features, including the thermal expansion of the unit cells of the amide phases, the reaction of the amides with oxygen to form Li_2O (which is more thermodynamically stable than $LiNH_2$) and the increased disorder observed in the amides at higher temperatures.

3.5 Synthesis and Neutron Diffraction Studies of $LiND_2$ and Li_2ND

3.5.1 The Synthesis and Characterisation of $LiND_2$

A sample of $LiND_2$ was synthesised in the IGA *via* the reaction of Li_3N with ND_3 as outlined in section 2.6.2.1. The equation for the anticipated reaction is presented in Equation 3.6.

$$Li_3N + 2\,ND_3 \longrightarrow 3\,LiND_2 \qquad \text{Equation 3.6}$$

The thermogravimetric mass-uptake data of the Li_3N sample are presented in Figure 3.10, and shows that the sample mass increased by 82 % during the ND_3 uptake reaction. A stoichiometric reaction of Li_3N with ND_3 according to Equation 3.6 should result in a mass gain of 114 mass%, which suggests that the ND_3-uptake reaction presented here did not reach completion. Indeed, if we look closely at the thermogravimetric data towards the end of the reaction, the gradient of the sample mass is slightly positive, indicating that ND_3 uptake was not complete. The kinetics of ND_3

uptake after this point were, however, very slow, suggesting that the sample had reached saturation. Using the original and final sample masses, the anticipated and actual ND_3 uptake measurements, and assuming that the observed mass increase was due solely to the ND_3 uptake, molar calculations gave a sample stoichiometry of $Li_{1.24}ND_{1.76}$.

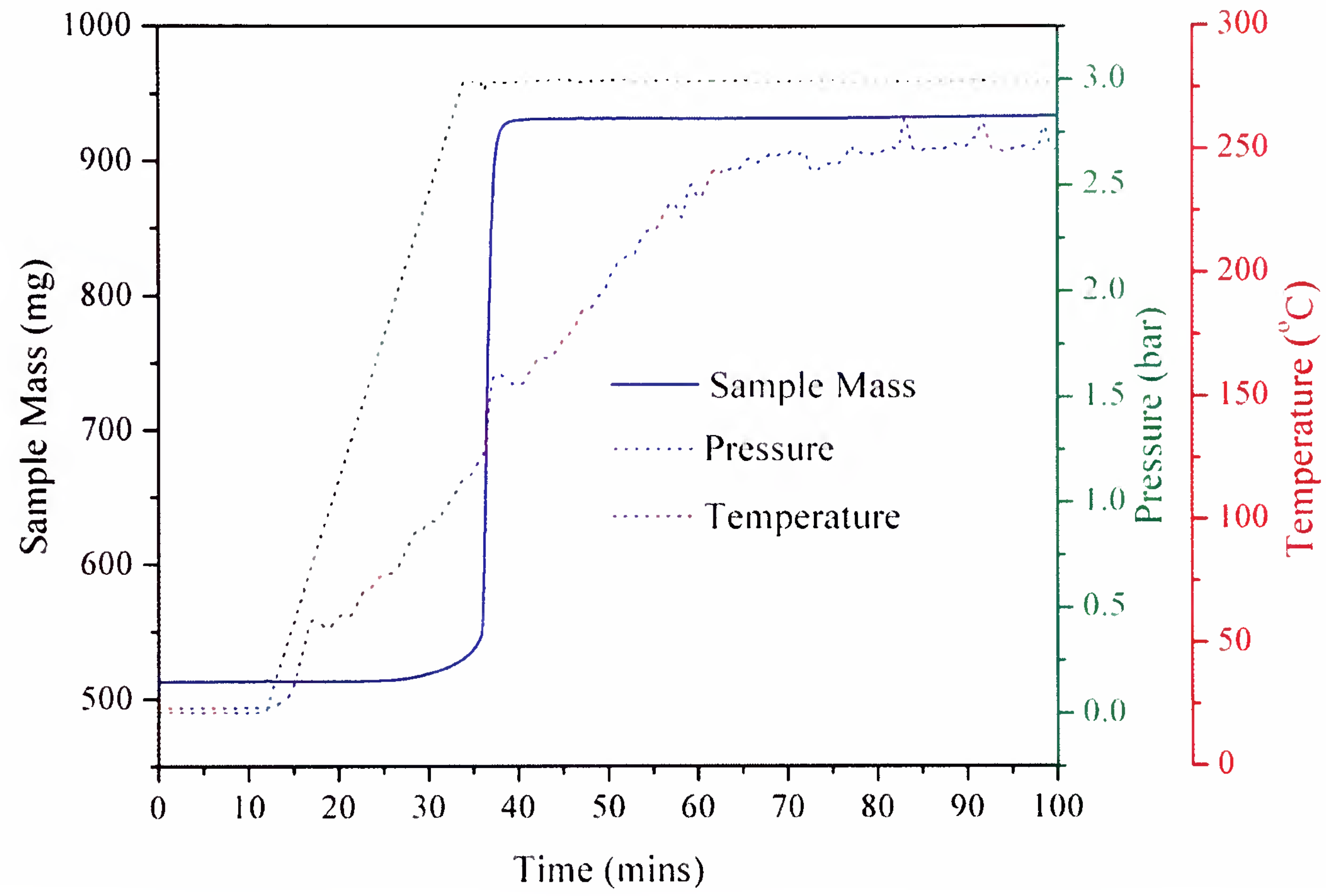

Figure 3.10 : Thermogravimetric data following the reaction of Li_3N (Aldrich, 80% mesh) with ND_3 (BOC special gases) to form $Li_{1.24}ND_{1.76}$, collected using Intelligent Gravimetric Analysis. The temperature of the sample was increased at a rate of 4.5 °C/min and the pressure was increased at 150 mbar/min. The blue line represents the sample mass, the dotted red line the temperature and the dotted green line the pressure.

The $LiND_2$ sample thus formed was thoroughly ground, loaded into a vanadium can under inert atmosphere and then loaded into the GEneral Materials diffractometer (GEM) at the ISIS pulsed neutron facility (section 2.1.3.1). Neutron diffraction data from the $LiND_2$ sample were collected at room temperature over a period of 1 hour.

The diffraction data were analysed *via* the Rietveld method[15] (section 2.4.1) using TOPAS Academic software[16] according to the method outlined in section 2.1.4.1. The data collected on banks 4, 5 and 6 were refined simultaneously to ensure the greatest accuracy of the calculated parameters. The diffraction data and refined profiles are presented in Figure 3.11.

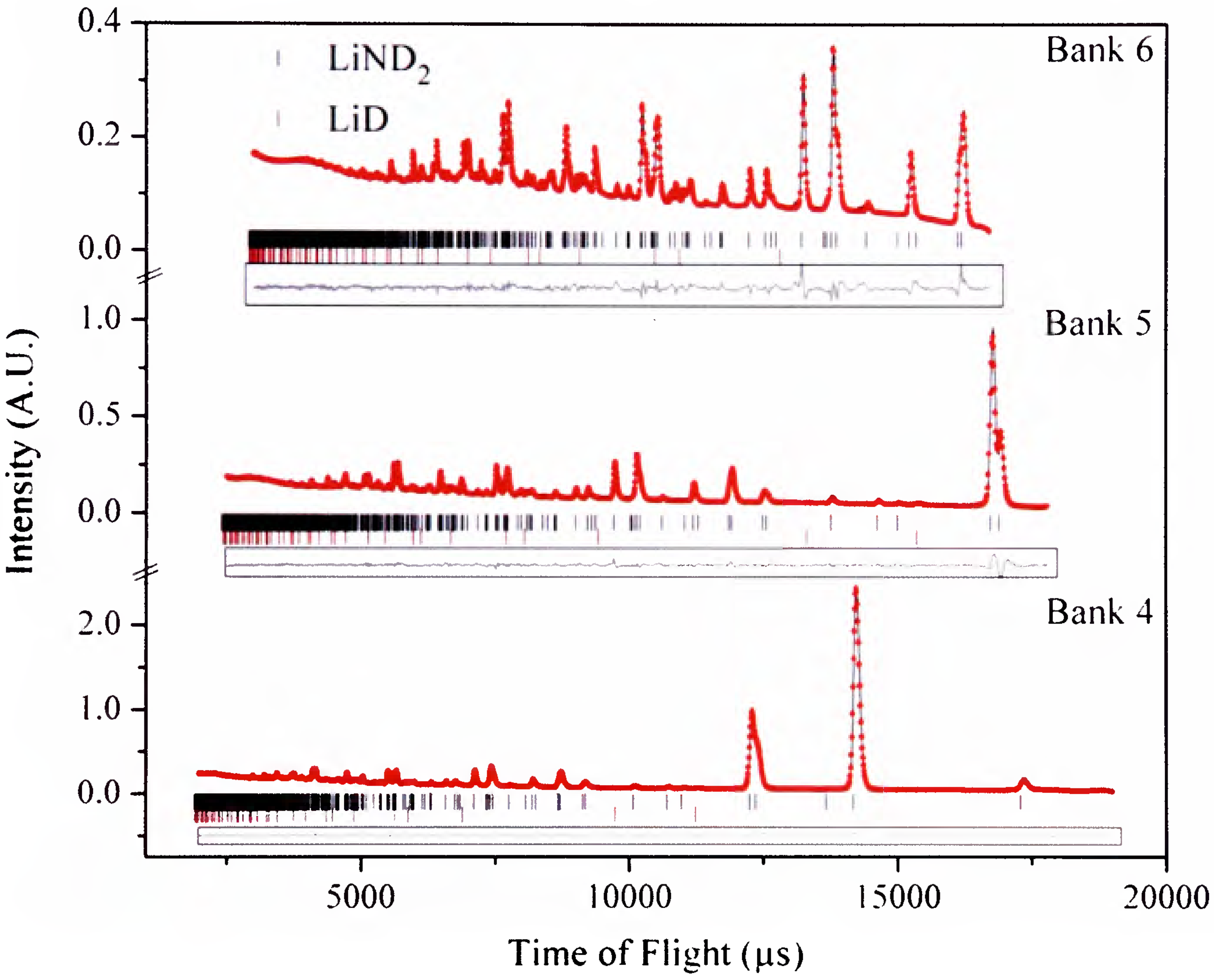

Figure 3.11 : Observed (solid line), calculated (red dots), and difference plots (y_{obsd} - y_{calcd}, solid lines in boxes) for the structure refinement of $Li_{1.24}ND_{1.76}$ (synthesised from Li_3N+ND_3) from neutron diffraction data collected at banks 4, 5 and 6 of the GEM diffractometer at the ISIS pulsed neutron source. The Bragg peak positions for $LiND_2$ and LiD are shown by the vertical tick marks. R_{wp} 3.398, R_{exp} 0.968, goodness of fit 3.509

The $LiND_2$ sample studied here was anticipated, from the thermogravimetric measurements, to have a Li-rich composition. In an attempt to locate all of the lithium ions in the $Li_{1+y}ND_{2-y}$ structure, the refinement model for the phase included Li ions at the 2b (0,0,½), 2d (½ ,0,¼) and 4e (0,0,*z*) lattice sites, as well as the usual 2a (0,0,0), 2c

(0,½,¼) and 4f (0,½,z) sites. The 2b, 2d and 4e sites were included in the refinement model because, as outlined previously (sections 1.4 and 1.7), $LiND_2$ is an ordered super structure of Li_2ND with the 2b, 2d and 4e tetrahedral sites unoccupied. It was therefore postulated that these sites may exhibit partial occupancy in $Li_{1+y}ND_{2-y}$.

The atomic positions, lattice parameters and site occupancies of the $LiND_2$ sample calculated from these refinements are presented in Table 3.2, and a schematic diagram of the $LiND_2$ structure is presented in Figure 3.12, with the various lattice sites labelled for clarity.

$LiND_2$

Atom	Site	*x*	*y*	*z*	Occupancy
Li 1	2a	0	0	0	1
Li 2	4f	0	½	0.005(1)	1
Li 3	2c	0	½	¼	0.67(6)
Li4	2b	0	0	½	0.00(4)
Li5	2d	½	0	¼	0.81(5)
Li6	4e	0	0	0.275(3)	0.24(2)
N	8g	0.2419(7)	0.2460(6)	0.1161(13)	1
D1	8g	0.194(2)	0.176(2)	0.1950(3)	1.00(2)
D2	8g	0.383(13)	0.359(16)	0.1297(6)	0.77(2)

$a = 5.0550(9)$ Å, $c = 10.207(1)$ Å

Table 3.2 : Summary of structural parameters for $LiND_2$, space group $I\bar{4}$ (number 82)

Refinement of the data indicated that the 2a (0,0,0) and 4f (0,½,z) lattice sites were fully occupied by Li, as would be expected in stoichiometric $LiND_2$. It was expected that excess Li ions would occupy the 2d (½,0,¼) sites, given the similarity of the 2c (0,½,¼) and 2d sites which arises from the 4-fold improper rotation axis present in the $LiND_2$ unit cell. In fact, both the 2c and 2d sites were partially occupied in $Li_{1+y}ND_{2-y}$, contrasting with the full occupancy of the 2c sites and full vacancy of the 2d sites usually observed in $LiNH_2$.[17]

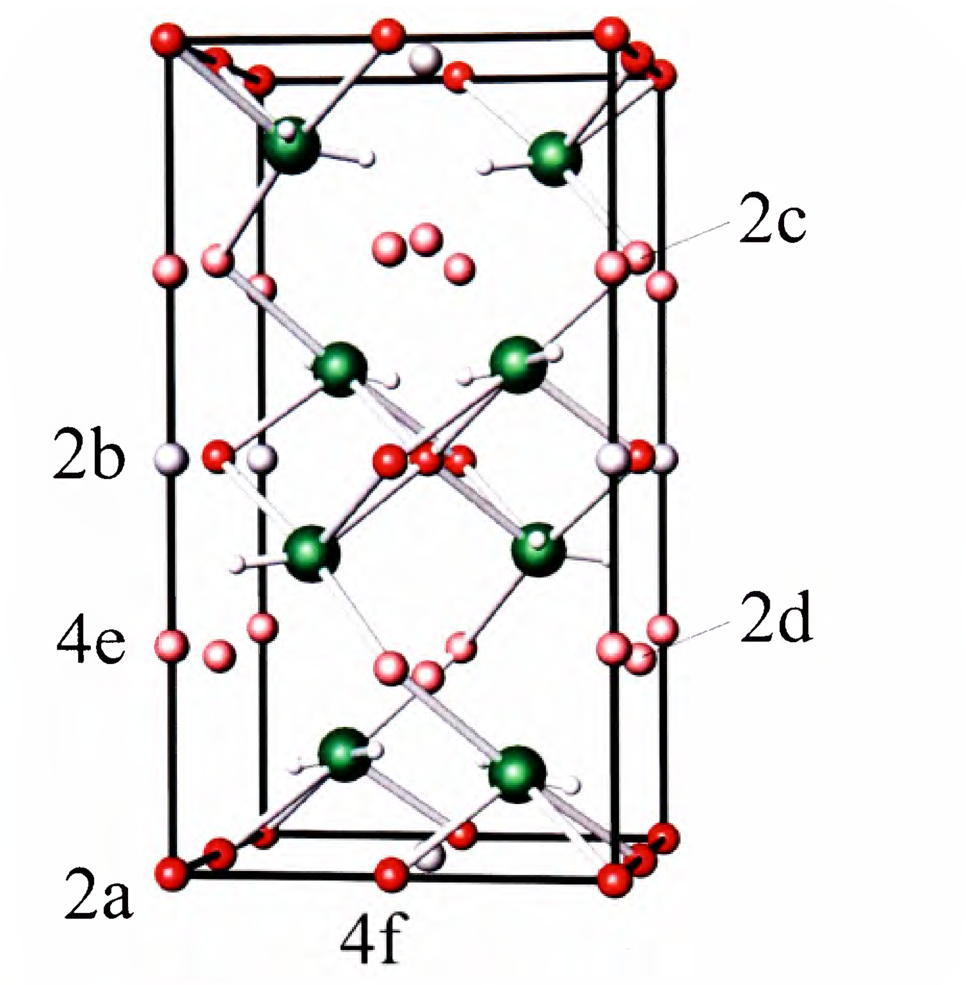

Figure 3.12 : Schematic diagram of the unit cell of the structure of $Li_{1.24(4)}ND_{1.770(9)}$, calculated from Rietveld analysis of neutron diffraction data. Nitrogen is represented by green spheres, deuterium by white spheres and lithium by red spheres. The fully Li-occupied 2a and 4f sites are bright red, the partially occupied 2c, 2d and 4e sites are pale red and the unoccupied 2b sites are grey.

These refinements also showed that the 2b (0,0,½) lattice sites were completely unoccupied in $Li_{1+y}ND_{2-y}$. The 2b site is located at the face centre, surrounded by 6 co-planar Li ions. Li-occupancy of the 2b site would therefore be highly unfavourable.

It was further found that the 4e (0,0,z) lattice site was also partially occupied. Located in the same layer as the 2c (0,½,¼) and 2d (½,0,¼) sites, the 4e site is displaced slightly along the *c*-axis, away from the fully occupied 2a (0,0,0) site and towards the vacant 2b (0,0,½) site. This site is likely to remain partially populated due to the relative emptiness of the 2c / 2d / 4e layer compared to the 2a / 2b / 4f layer. Furthermore, the displacement away from the occupied 2a site towards the vacant 2b site will reduce inter-ionic repulsion, making occupation more likely.

Calculation of the stoichiometry of the $LiND_2$ sample from the refined site occupancies leads to a composition of $Li_{1.24(4)}ND_{1.770(9)}$ which is in excellent agreement with that calculated from the thermogravimetric data ($Li_{1.24}ND_{1.76}$).

This study implies that the formation of $LiND_2$ from the reaction of ND_3 with Li_3N may have proceeded *via* a continuum of $Li_{1+y}ND_{2-y}$ phases. The kinetics of the ND_3 uptake reaction slowed significantly as the material reached a composition of y = 0.24(7), however, it is believed that, had the sample remained under ND_3, the reaction would have continued to completion and ultimately formed fully stoichiometric $LiND_2$.

3.5.2 The Synthesis and Characterisation of Li_2ND

A sample of Li_2ND was prepared *via* the 1:1 reaction of $LiND_2$ with Li_3N (Aldrich, 99 % purity) under flowing Ar gas at 300 °C for 24 hours (section 2.6.2.2).

The sample formed was thoroughly ground, packed into a vanadium can under inert atmosphere and loaded into the GEM diffractometer at the ISIS pulsed neutron facility (section 2.1.3.1). Neutron diffraction data from the sample were collected for 8 hours at a temperature of 25 °C. Rietveld analysis[15] of the diffraction data collected at banks 4 and 5 was performed simultaneously using the TOPAS Academic suite.[16]

It has been suggested[8] that Li_2ND could adopt either an orthorhombic or a cubic structure at room temperature. In light of this suggestion, the diffraction data were modelled using both a cubic $Fd\bar{3}m$ model and an orthorhombic $Ima2$ model. The x coordinates of the 48f (x,⅛,⅛) and 32e (x,x,x) Li sites and the 32e (x,x,x) N sites were refined, in addition to the parameters listed in section 2.1.4.1 for the $Fd\bar{3}m$ model, (with D set at a fixed distance from the N). The y and z coordinates of the 4b (¼,y,z) Li, N and D sites and the x, y and z coordinates of the 8c (x,y,z,) Li, N and D positions were refined in addition to the parameters listed in section 2.1.4.1 in the $Ima2$ model.

The diffraction data and refined $Fd\bar{3}m$ (R_{wp} 3.423, goodness of fit 5.088) and $Ima2$ (R_{wp} 4.260, goodness of fit 6.320) models are presented in Figures 3.13a and b, respectively. Comparison of the R parameters and the goodness of fit values for each model suggests that best match to the data was obtained using the cubic model.

Even though the best fit to the data was provided by the $Fd\bar{3}m$ model, it is nevertheless possible that the structure of Li_2ND may have deviated slightly from ideal cubic symmetry.

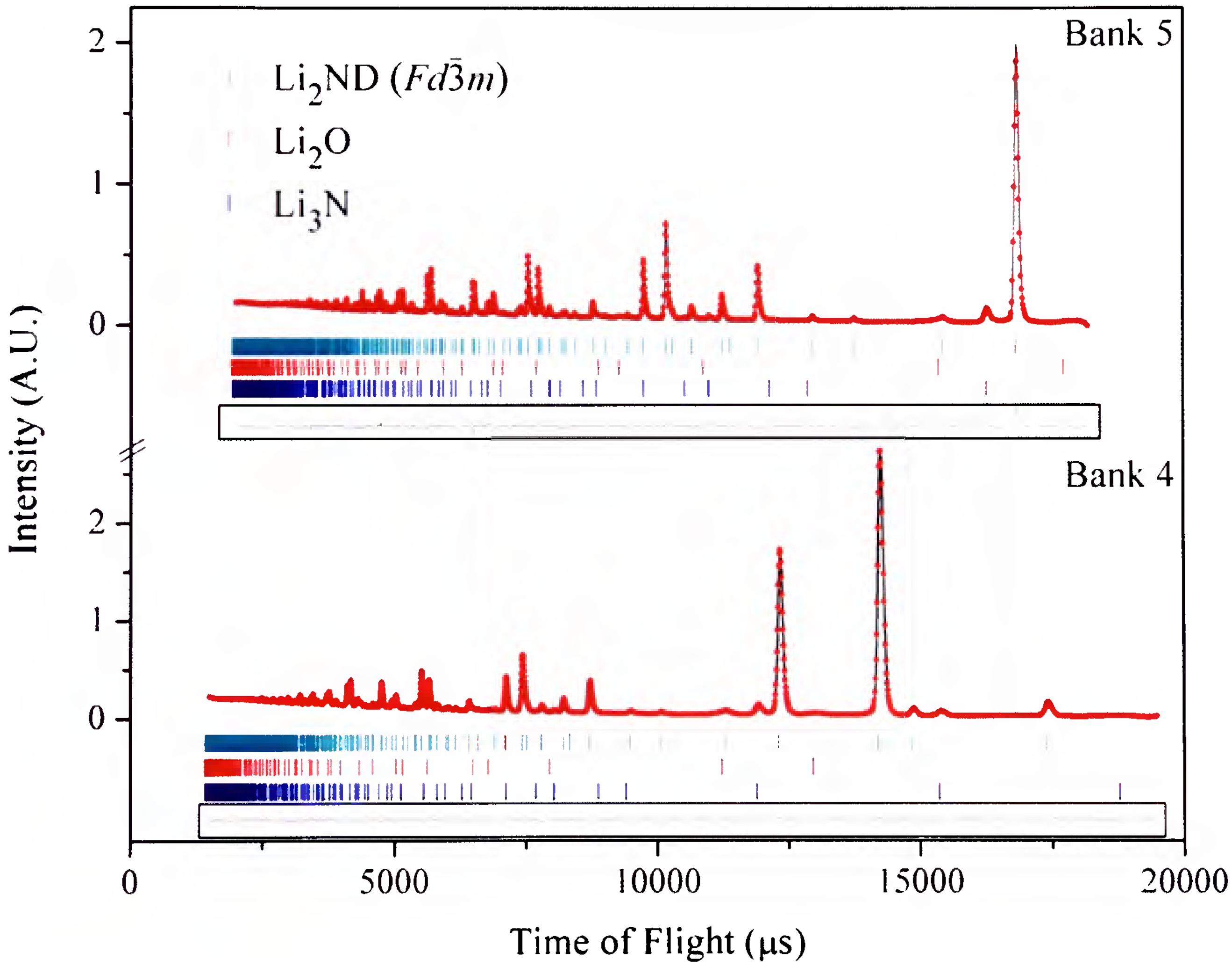

Figure 3.13a : Observed (solid line), calculated (red dots), and difference (y_{obsd} - y_{calcd}, solid line in box) plots for the structure refinement of Li_2ND at room temperature, using the cubic $Fd\bar{3}m$ Li_2ND structure. Neutron diffraction data collected at banks 4 and 5 of the GEM diffractometer were refined simultaneously. The Bragg peak positions for Li_2ND ($Fd\bar{3}m$), Li_3N and Li_2O are shown by the vertical tick marks. R_{wp} 3.423, R_{exp} 0.673, goodness of fit 5.088.

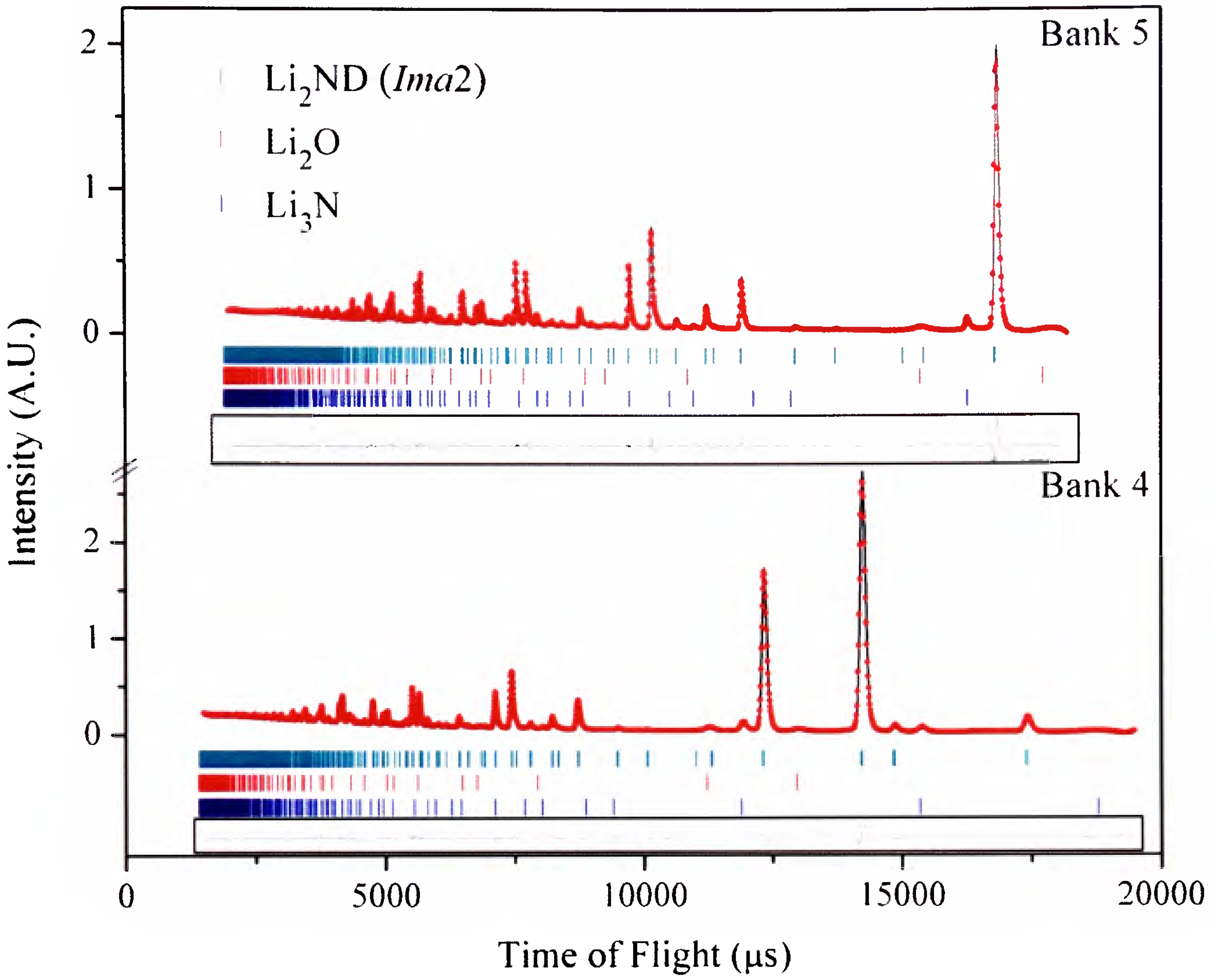

Figure 3.13b : Observed (solid line), calculated (red dots), and difference ($y_{obsd} - y_{calcd}$, solid line in box) plots for the structure refinement of Li_2ND at room temperature, using the cubic *Ima*2 Li_2ND structure. Neutron diffraction data collected at banks 4 and 5 of the GEM diffractometer were refined simultaneously. The Bragg peak positions for Li_2ND (*Ima*2), Li_3N and Li_2O are shown by the vertical tick marks. R_{wp} 4.260, R_{exp} 0.674, goodness of fit 6.320.

Small deviations from ideal cubic symmetry become manifest in anisotropic line broadening. Such effects can be modelled by using a Gaussian function, according to the method outlined by Stephens.[18] These methods involve the calculation of two parameters, S_{220} and S_{400}, and the degree of anisotropic line-broadening is determined by the deviation of (2 S_{400} / S_{220}) - 1 from 0 (where a value of 0 indicates an ideal cubic system).

In this study, S_{220} and S_{400} were calculated from refinement to be 0.00241 ± 0.00024 and 0.00154 ± 0.00012, respectively. Within experimental error, these values suggest that the Li_2ND studied adopted the cubic structure although a small amount of *Ima2* symmetry may have been present on a local scale.

A schematic diagram of the $Fd\bar{3}m$ structure of Li_2ND calculated during this study is presented in Figure 3.14. The unit cell parameters and atomic positions of the phase are summarised in Table 3.3.

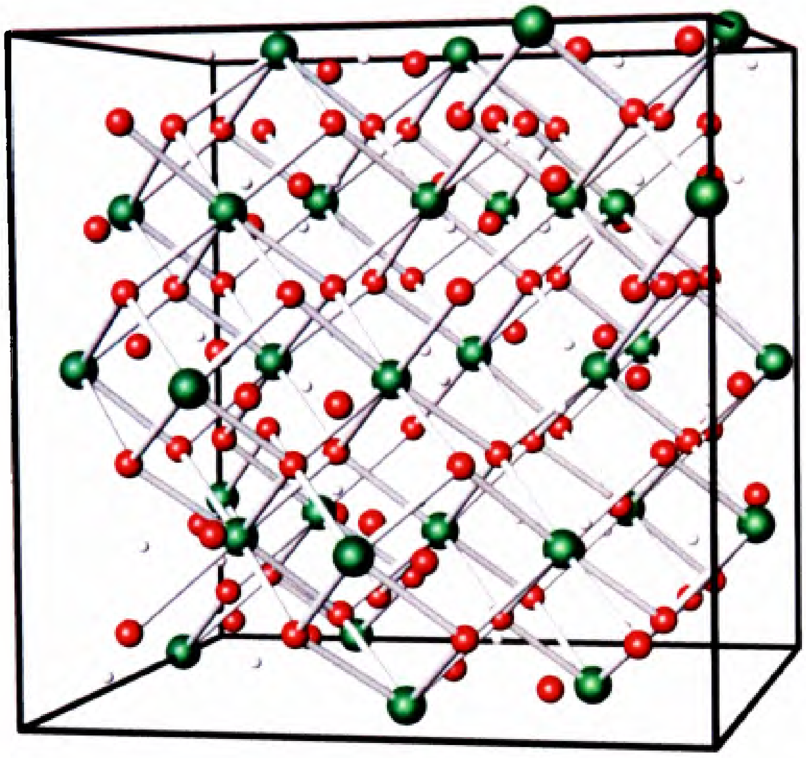

Figure 3.14 : Schematic diagram of the unit cell of $Fd\bar{3}m$ Li_2ND, calculated from Rietveld refinement of neutron diffraction data collected at room temperature. Li is represented by red spheres, N by green spheres and D by grey spheres.

Li_2ND

Atom	Site	*x*	*y*	*z*	Occupancy
Li 1	48f	0.3703(2)	⅛	⅛	0.935(4)
Li 2	8a	⅛	⅛	⅛	1.000(19)
Li 3	32e	0.0277(6)	0.0277(6)	0.0277(6)	0.180(6)
N	32e	0.24627(2)	0.24627(2)	0.24627(2)	1
D 1	32e	0.29834(1)	0.29834(1)	0.29834(1)	1

a = 10.138(10) Å

S_{400} = 0.00154(12), S_{220} = 0.00241(24)

Table 3.3 : Summary of structural parameters for room temperature Li_2ND (space group $Fd\bar{3}m$, number 227), calculated from Rietveld analysis of neutron diffraction data.

3.6 In Situ Diffraction 2 : Intelligent Gravimetric Analysis with Neutron Diffraction Studies of the Li –N – D System

Intelligent gravimetric analysis combined with neutron diffraction (IGA^{n}) has been used previously to study the D_2 uptake reaction of Li_3N.[19] The following sections present the data gathered from further IGA^{n} studies of the Li – N – D system, which were performed in order to gain a greater understanding of the crystallographic processes which occur during sorption reactions of Li – N – D materials. The results generated from two different studies are presented.

The starting material used in the first study (sections 3.6.1 – 3.6.6) was a mixture of $LiND_2$ and LiD. This material was subjected to a number of decomposition / D_2 absorption cycles under varying conditions of temperature and pressure, and the thermogravimetric and crystallographic changes of the sample were monitored throughout the experiment.

The second study (section 3.6.7) compared the D_2-sorption processes of two samples of Li_2ND + LiD, with varying concentrations of lattice defects. These materials were studied in order to determine the effect that defect concentration has on the D_2 sorption properties of the Li – N – D system.

3.6.1 Synthesis and Primary Characterisation of the $LiND_2$ + LiD Sample.

A sample of $LiND_2$ was synthesised *via* the reaction of LiD with ND_3 (section 2.6.2.1). The material was ground and loaded into a vanadium can under inert atmosphere, which was transferred into the GEM diffractometer (section 2.1.3.1). Neutron diffraction data for this sample were collected at room temperature over a period of one hour in order to determine the composition of the $LiND_2$ sample to be studied during the *in situ* diffraction experiments.

Rietveld analysis[15] of the data using TOPAS Academic[16] (section 2.1.4) indicated that the sample was majority phase $LiND_2$ (75 mass%) with LiD impurity (25 mass%), meaning that the sample studied was approximately 1:1 $LiND_2$: LiD by mole.

3.6.2 Overview of the Combined Thermogravimetric Analysis and Neutron Diffraction Experiment of $LiND_2$ + LiD

Having collected neutron diffraction data from the $LiND_2$ + LiD sample at room temperature (section 3.6.1), the sample was loaded into a quartz bucket, which was in turn loaded into the IGA^n apparatus, as outlined in section 2.2.2. The stainless steel reaction chamber was outgased to a pressure of 6 mbar and the sample was heated to 260 °C. The temperature was maintained at 260 °C until no further mass loss was observed from the sample. The pressure of the reaction vessel was maintained at 6 mbar throughout the desorption experiment, except for a brief spike to 8.5 mbar at $t = 300$ minutes.

Once desorption from the sample appeared to be complete (as determined by the thermogravimetric data), the reaction vessel was pressurised to 3 bar with D_2 at 260 °C to facilitate D_2-absorption. These conditions were maintained until the mass of the sample became constant, at which point the sample was heated further to 300 °C and subsequently pressurised to 5, 6 and 7 bar with D_2.

The temperature of the sample was then set to 260 °C and the system was cycled between outgas (6 mbar) and 3 bar of D_2 in order to facilitate cycling of the Li – N – D system between $LiND_2$ + LiD and Li_2ND.

Neutron diffraction data were collected at intervals of 2.52 minutes throughout the course of the experiments, and thermogravimetric data were recorded approximately every 5 seconds.

3.6.3 Neutron Diffraction Data of the Start- and End-points of the $LiND_2 - Li_2ND$ cycle.

Refinement from diffraction data of a mixture of Li_2ND and $LiND_2$ can often be a difficult task due to the overlap of many of the $LiND_2$ and Li_2ND Bragg peaks. The best resolution of the $LiND_2$ and Li_2ND Bragg peaks is found in the d-spacing region of 2.5 – 2.6 Å, wherein lie the (020) and (004) $LiND_2$ reflections and the (002) Li_2ND reflection. These Bragg reflections are illustrated in Figures 3.15 a and b, which show the time of flight region of 15000 – 17600 μs (d-spacing ~2.3 – 2.7 Å) for the start- and end-points of $LiND_2$ decomposition.

Transformation of $LiND_2$ into Li_2ND can be identified by the coalescence of the (020) and (004) $LiND_2$ Bragg reflections into the (002) Li_2ND reflection, and similarly, the reverse reaction can be identified by the splitting of the (002) Li_2ND Bragg reflection into the (020) and (004) $LiND_2$ reflections. Nevertheless, even these reflections can become difficult to resolve, particularly when both $LiND_2$ and $LiND_2$ are present.

Further complications can arise in refinement of diffraction data from mixtures of $LiND_2$ and Li_2ND if the scale factor of $LiND_2$ in the sample becomes low and the diffraction peaks become weak.

As outlined in Chapter One, $LiND_2$ is essentially an (*a* x *a* x 2*a*) superstructure of Li_2ND, and often, due to the similarity of the crystal structures of the materials, transformation of $LiND_2$ into Li_2ND is accompanied by an apparent decrease in the length of the refined $LiND_2$ c-parameter. At such points, the c/a ratio of $LiND_2$ approaches 2 (*cf* 2.037 in $LiNH_2$[20]), and $a(LiND_2) \approx a(Li_2ND)$ and $c(LiND_2) \approx 2a(Li_2ND)$. The scale factor of Li_2ND at such points is very much higher than that of $LiND_2$, indicating that the best fit to the data is obtained using a Li_2ND model, rather than a $LiND_2$ model. This suggests that the variation observed in the $LiND_2$ lattice parameters during such times is merely an artefact of the refinement, although it could also be suggestive of the presence of a $Li_{2-x}ND_{1+x}$ phase with an expanded cubic structure.

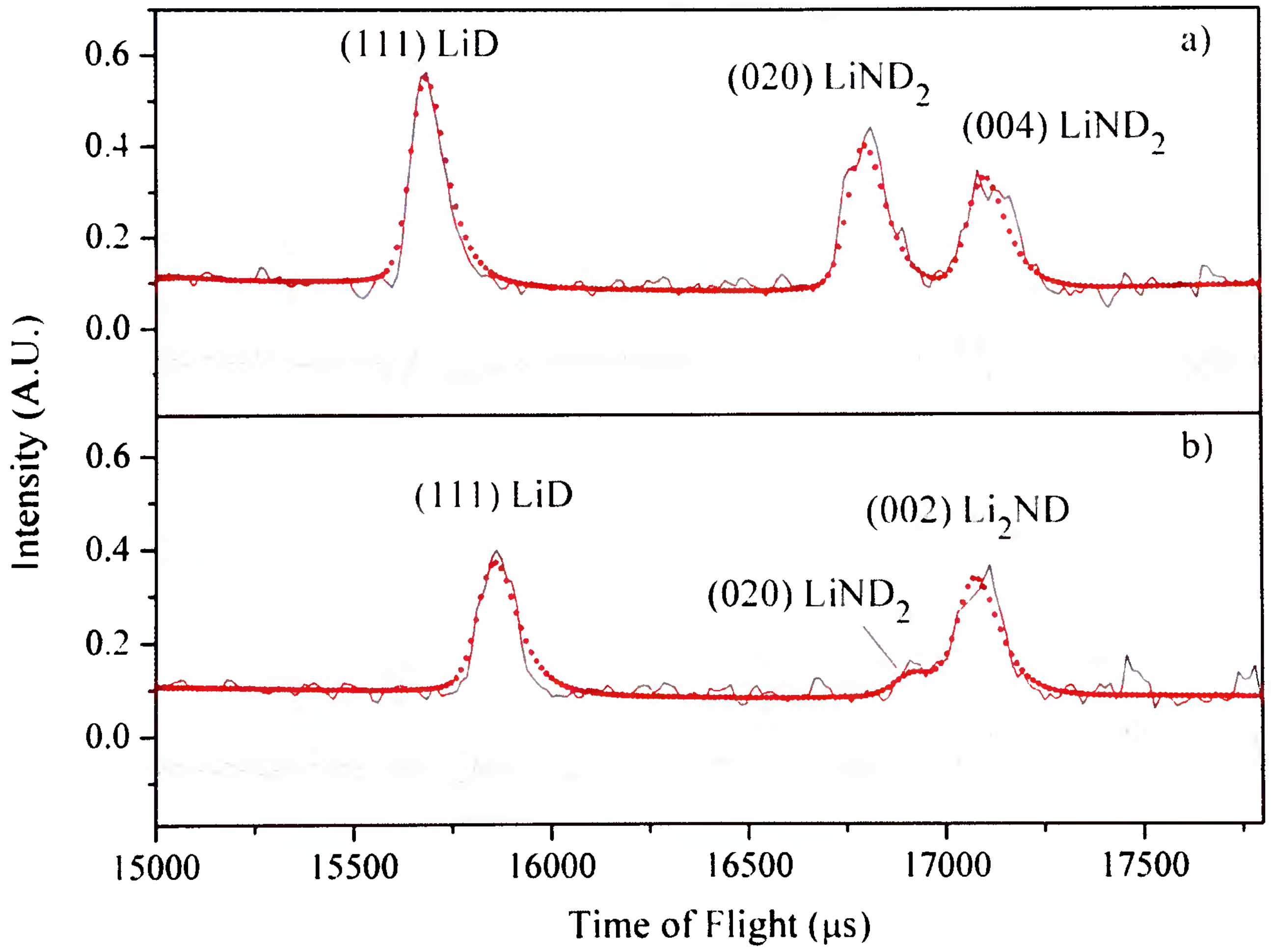

Figure 3.15 : Observed (solid line), calculated (red dots), and difference plots (y_{obsd} - y_{calcd}, grey line) for the structure refinement of a) the start and b) the end-points of the decomposition of $LiND_2$ + LiD from neutron diffraction data collected using the IGAn in conjunction with the GEM diffractometer. Time of flight region of 15000 – 17600 μs (d – spacing of ~ 2.3 – 2.7 Å) is shown, highlighting the resolution of a) the (020) and (004) reflections of $LiND_2$ and b) the (002) reflection of Li_2ND. a) R_{wp} 8.084, R_{exp} 5.502, goodness of fit a) 1.469. b) R_{wp} 8.078, R_{exp} 5.908, goodness of fit 1.367

3.6.4 Decomposition of the $LiND_2$ + LiD Sample.

The $LiND_2$ + LiD sample outlined in section 3.6.1 was studied using the IGA^n apparatus in order to gain more information regarding the crystallographic changes occurring during D_2-sorption in the Li – N – D system.

Under a pressure of 6 mbar Ar, the sample was heated to 225 °C at a rate of 2 °C per minute and then to 260 °C at 0.5 °C per minute. The rate of heating to 225 °C was greater than that to 260 °C as the sample was not anticipated to begin decomposition below 225 °C. The temperature and pressure of the sample were maintained at 260 °C and 6 mbar, respectively, until no variation was observed in the sample mass.

A surface plot (section 3.4) of the diffraction data collected is presented in Figure 3.16, together with the corresponding thermogravimetric data. The intensity of the Bragg reflections is indicated by the colour of the lines, ranging from dark blue (background intensity) through pale blue (low intensity) and red (medium intensity) up to yellow (high intensity).

The Bragg reflections were indexed to $LiND_2$, Li_2ND and LiD. A d-spacing range of 2.1 – 2.7 Å is presented as this range includes the (020) and (004) reflections of $LiND_2$, the (002) reflection of Li_2ND and the (111) reflection of LiD, and excludes reflections arising from diffraction by the steel walls of the reaction vessel.

The positions of the Bragg reflections for each phase present appeared to vary linearly with temperature, which is consistent with thermal expansion. The intensity of the two Bragg reflections between d-spacing 2.5 and 2.6 Å, (indexed to (020) and (004) reflections of $LiND_2$) began to decrease as the temperature of the sample reached 220 °C (run number 42).

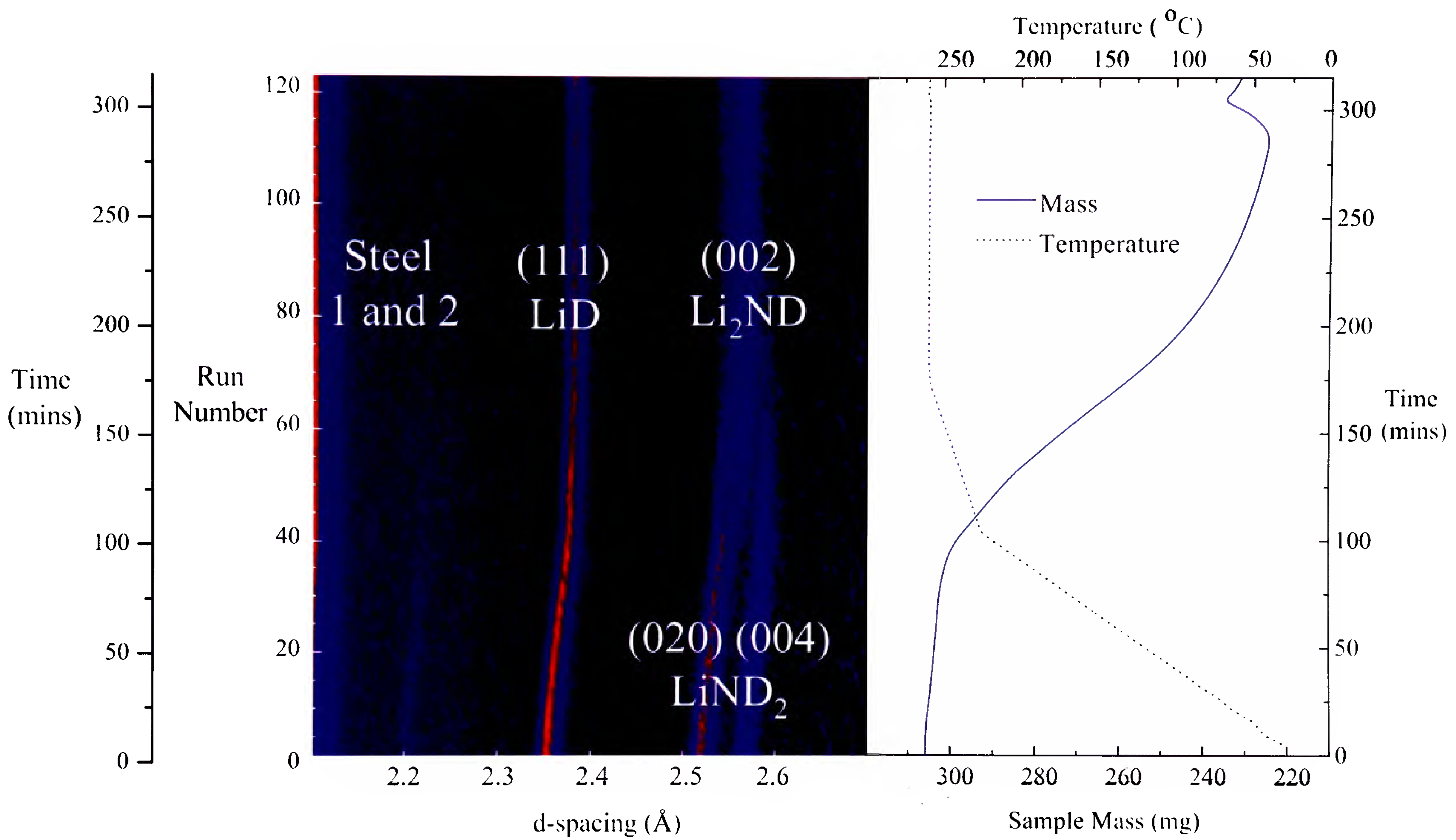

Figure 3.16 : Comparison of the surface plot of neutron diffraction data (collected at bank 5) and thermogravimetric data collected during the decomposition of $LiND_2$ + LiD in the IGA^n apparatus at constant pressure (6 mbar). d-spacing region of 2.1 – 2.7 Å chosen to highlight coalescence of (020) and (004) $LiND_2$ Bragg reflections into (002) Li_2ND Bragg reflection, and the change in intensity of the (111) LiD Bragg reflection. The peak observed in the sample mass at 320 mins arose due to a spike in the pressure of gas to 8 mbar.

As the temperature of the sample increased to 235 °C (run number 50), a new reflection became visible at d-spacing 2.55 Å, which was indexed to the (002) reflection of Li_2ND.

These changes suggest that a transition occurred at 235 °C between a tetragonal and cubic phase, which is consistent with the transformation of $LiND_2$ into Li_2ND. The tetragonal and cubic phases then appeared to co-exist until the sample reached a temperature of 260 ° C.

Study of the corresponding thermogravimetric data indicates that the mass of the sample began to decrease immediately upon heating, which presumably arose due to the desorption of physisorbed gas from powder grains. This slow mass loss was followed by a rapid mass loss of 25 mass% from the sample, beginning as the temperature reached 210 °C. Comparison of the thermogravimetric data and the surface plot implies that the mass loss occurred during the transformation of the tetragonal phase into the cubic phase.

The mass loss expected during decomposition of the $LiND_2$ + LiD sample, according to Equation 3.7, would be 13.9 mass %.

$$LiND_2 + LiD \longleftrightarrow Li_2ND + D_2 \qquad \text{Equation 3.7}$$

The mass loss anticipated from direct decomposition of $LiND_2$ (without interaction with the 25 mass% LiD) according to Equation 3.8, would be 30 mass %.

$$2\,LiND_2 \longleftrightarrow Li_2ND + ND_3 \qquad \text{Equation 3.8}$$

Clearly both of these values differ from the mass change observed experimentally, and Rietveld analysis[15] of the diffraction data is necessary in order to gain greater understanding of the processes that occurred during the experiment.

3.6.4.1 Rietveld Analysis of Neutron Diffraction Data Collected During the Decomposition of the $LiND_2$ + LiD Sample.

Study of the surface plot of the experiment allowed us to view a great deal of data at a glance. However, information regarding the crystallographic changes occurring during such reactions can only be obtained through full Rietveld analysis[15] of each diffraction pattern. Such analysis was performed using the batch facility of the TOPAS Academic software suite,[16] according to the general procedure outlined in section 2.1.4.2.

The refined scale factors and lattice parameters of the phases present are presented in Figures 3.17a and b, respectively. To place the scale factor values in context, the start point composition of the $LiND_2$ + LiD sample prior to decomposition was 75 mass% $LiND_2$ with 25 mass% LiD and the end-point composition was 9 mass % $LiND_2$, 33 mass % LiD, and 58 mass % Li_2ND.

Study of Figure 3.17a indicates that the scale factor of LiD decreased from 0.1 to just over 0.05 during the course of the decomposition reaction. The temperature required for the direct decomposition of LiD (500 °C) is far above the temperature of the sample during this experiment, which suggests that the decrease in the scale factor of LiD was not due to direct LiD decomposition. It is therefore surmised that LiD was consumed by ND_3 capture and that the sample decomposed, at least in part, according to Equation 3.7.

Given that the sample prior to decomposition was ~1:1 $LiND_2$ + LiD by mole (75 mass% $LiND_2$ + 25 mass% LiD), had ND_3 capture by LiD been 100 % effective, we would expect the scale factor of LiD to have decreased to ~zero by the end of the experiment. This was clearly not the case, and therefore ND_3 capture was not 100 % in this experiment.

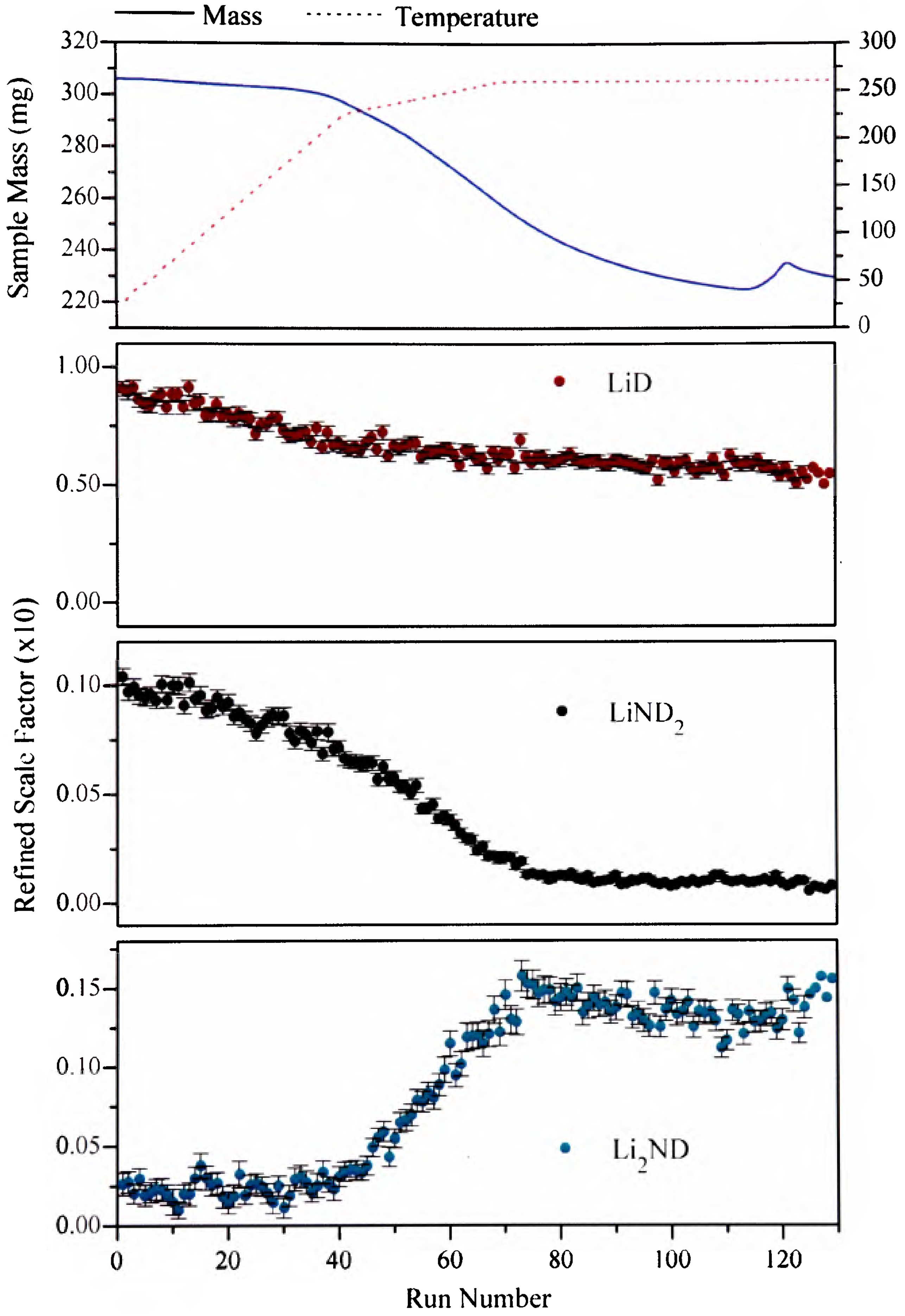

Figure 3.17a : Summary of refined scale factors, obtained from Rietveld analysis (*via* batch refinement) of the neutron diffraction data collected during $LiND_2$ + LiD decomposition in the IGA^n. The thermogravimetric data are also presented for ease of comparison (pressure was constant at 6 mbar). Mean errors LiD ± 0.002, $LiND_2$ ± 0.0002, Li_2ND ± 0.0007

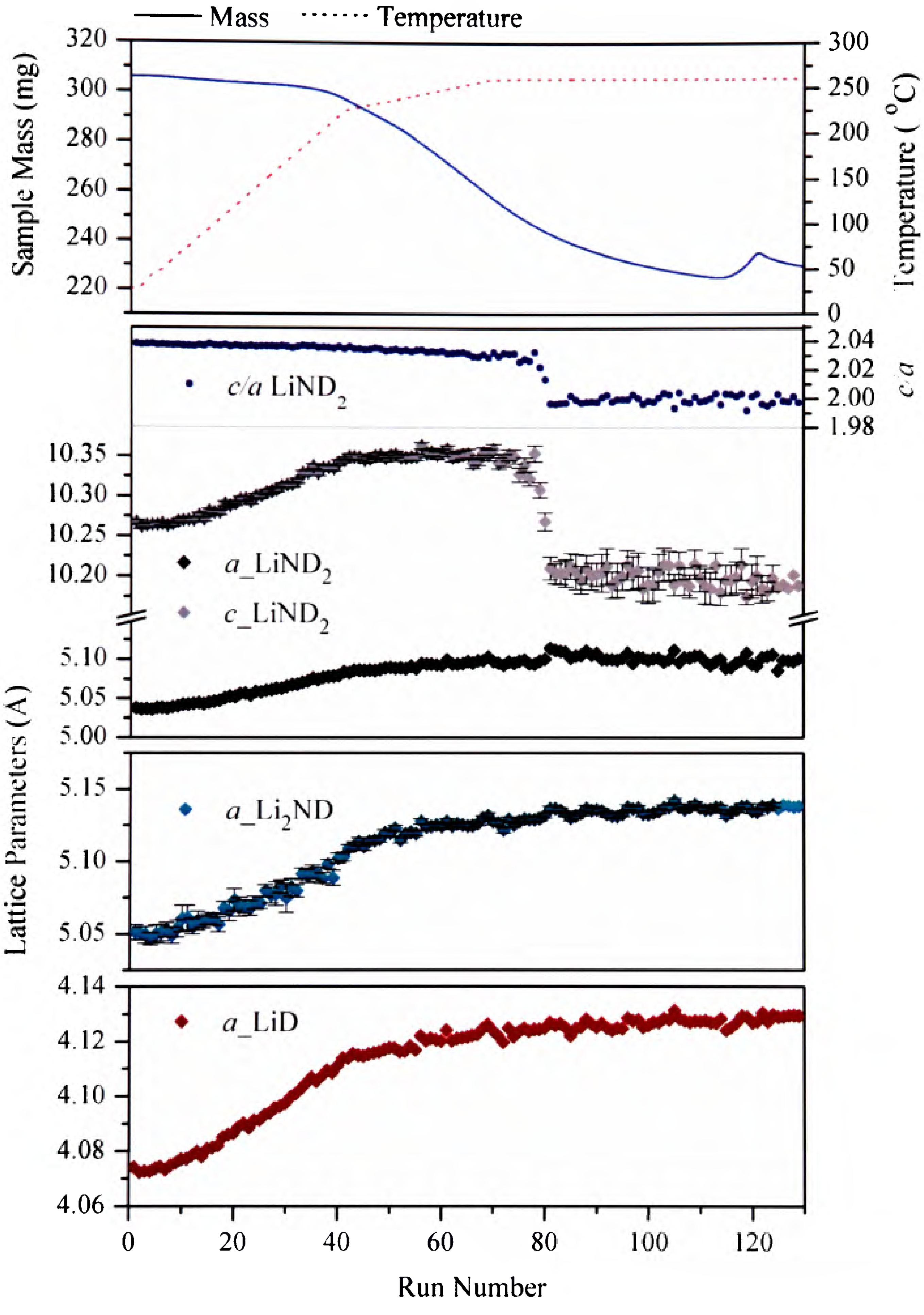

Figure 3.17b : Summary of refined lattice parameters, obtained from Rietveld analysis (*via* batch refinement) of the neutron diffraction data collected during $LiND_2$ + LiD decomposition in the IGA^n. The thermogravimetric data are also presented for ease of comparison. Mean errors *a*_LiD ± 0.0011, *a*_$LiND_2$ ± 0.003, *c*_$LiND_2$ ± 0.009, *a*_Li_2ND ± 0.003. Error bars only shown if larger than data points

The scale factor of $LiND_2$ was seen to decrease with increasing temperature. The rate at which this decrease occurred was greatest between temperatures of 220 °C and 260 °C (run numbers 40 – 80), corresponding to the period during which the increase of the Li_2ND scale factor was at its fastest. The sample mass decreased sharply during this period, but continued to decrease after the scale factor of Li_2ND became constant, implying that the gas released during the decomposition took time to diffuse through and away from the sample.

These data imply that mass loss from the $LiND_2$ + LiD sample arose both from D_2 loss according to Equation 3.7, and to ND_3 loss according to Equation 3.8. ND_3 capture was likely to be less than 100 % due to insufficient sample mixing and large grain size.

The variation of the unit cell parameters of the phases during the experiment is presented in Figure 3.17 b. The lattice parameters of $LiND_2$ were both observed to vary linearly with the temperature of the sample up to 260 °C, indicating thermal expansion. Above 260 °C, the *c*-lattice parameter of $LiND_2$ was observed to decrease rapidly. Comparison of this data to the scale factors in Figure 3.17a indicates that the sharp drop in the $LiND_2$ *c*-parameter began as the proportion of $LiND_2$ tended towards zero. As the *c/a* ratio of $LiND_2$ was approximately 2 at this point, the sudden decrease observed in the $LiND_2$ *c*-parameter may be interpreted as an artefact of the refinement, brought about by the similarity of the Li_2ND and $LiND_2$ crystal structures as outlined in section 3.6.3.

The lattice parameters of Li_2ND and LiD were observed to vary linearly with temperature, indicating thermal expansion of the phases.

A full summary of the refined structural parameters is presented in Appendix A1.2.

3.6.5 Deuteration of the Decomposed $LiND_2$ + LiD Sample

In order to gain more information on the behaviour of Li_2ND during re-deuteration, the desorbed $LiND_2$ + LiD sample was pressurised with D_2 to facilitate D_2-absorption.

The reaction chamber was maintained at a temperature of 260 °C and pressurised to 3 bar with D_2. These conditions were maintained until the sample mass became constant, at which point the temperature of the sample was raised to 300 °C, and the pressure was increased successively to 5, 6 and 7 bar D_2.

The neutron diffraction data and the thermogravimetric data collected for the sample during D_2 absorption are presented in Figure 3.18. The gaps in the surface plot correspond to loss of the neutron beam during the experiment.

Study of the surface plot shows splitting of the Bragg peak at d-spacing 2.56 Å (indexed to the (002) reflection of Li_2ND), suggesting the transformation of the cubic phase into a tetragonal phase. The splitting of this peak was accompanied by an increase in the intensity of the reflection at 2.38 Å (indexed to the (111) reflection of LiD), which is consistent with the re-deuteration of Li_2ND to form $LiND_2$ + LiD. Just prior to splitting, the (002) reflection of Li_2ND was observed to shift suddenly to lower d-spacing, which is indicative of a unit cell contraction.

The thermogravimetric data indicate a mass increase in the sample prior to the changes observed in the surface plot. The mass increase was rapid and continued until the sample reached 300 °C. From this point the sample mass began to decrease regardless of further increases in pressure to 5, 6 and 7 bar D_2.

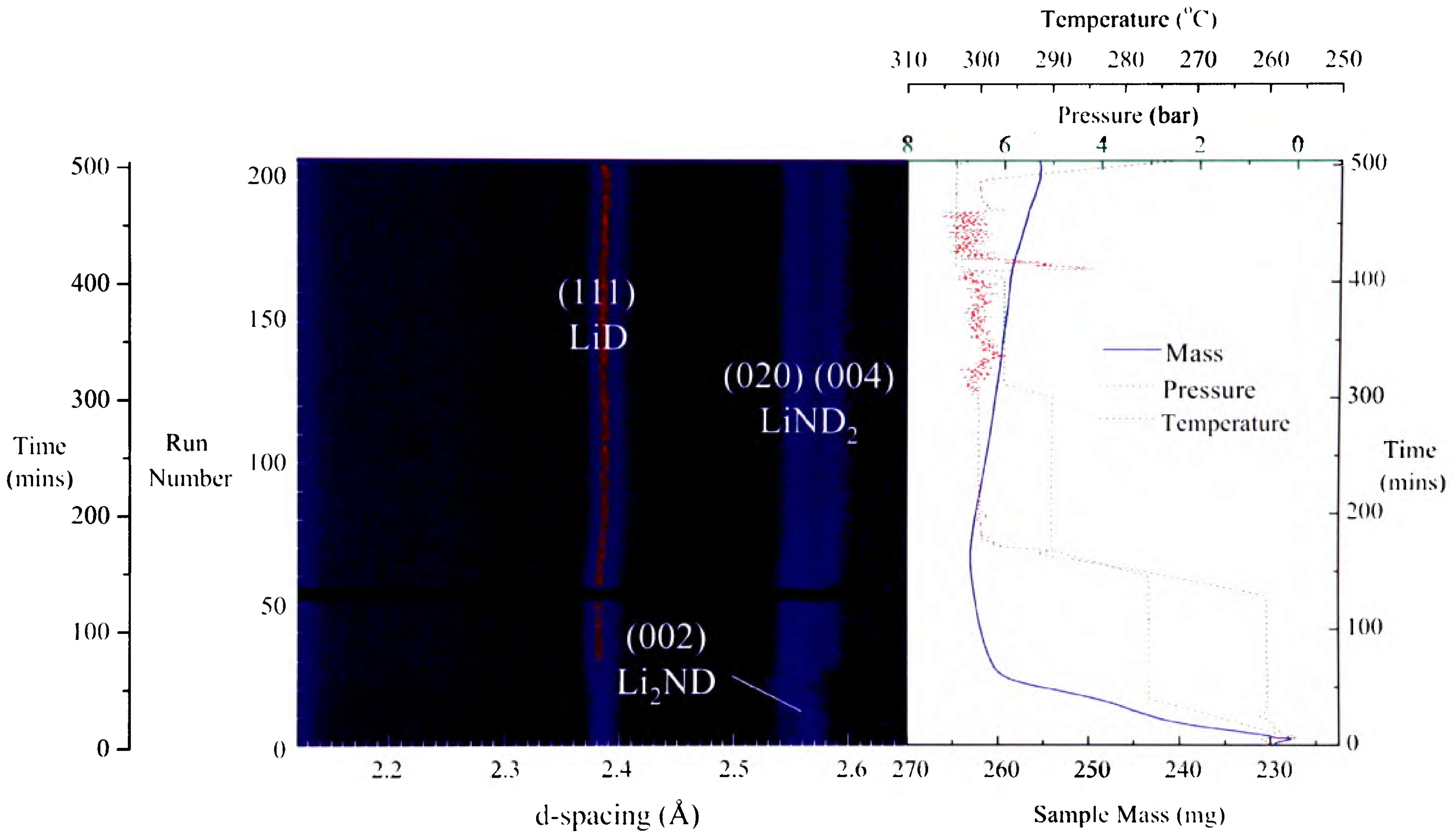

Figure 3.18 : Comparison of the surface plot of neutron diffraction data (collected at bank 5) and thermogravimetric data collected during D_2 absorption on the desorbed $LiND_2$ + LiD mixture, studied using the IGA^n apparatus. d-spacing region of 2.1 – 2.7 Å was chosen to highlight the splitting of the (002) Li_2ND Bragg reflection into the (020) and (004) $LiND_2$ reflections, and the change in intensity of the (111) LiD Bragg reflection.

3.6.5.1 Rietveld Analysis of Neutron Diffraction Data Collected, During Deuteration of Desorbed Li_2ND + LiD Sample.

The neutron diffraction data collected during the D_2-absorption reaction were analysed by Rietveld refinement,[15] using the batch processing facility of the TOPAS Academic software suite[16] as outlined in section 2.1.4.2.

The refined scale factors and lattice parameters of the phases are presented in Figures 3.19a and b, respectively.

To put the relative scale factors of the materials in context, the start point composition of the sample for the D_2 absorption step was 9 mass % $LiND_2$, 33 mass % LiD, and 58 mass % Li_2ND and the end point composition was 47 mass% $LiND_2$, 41 mass% LiD, and 12 mass% Li_2ND.

Figure 3.19a shows that as the pressure above the sample reached 1.5 bar, the scale factor of Li_2ND began to decrease. A simultaneous increase was observed in the scale factors of $LiND_2$ and LiD, indicating that the D_2-absorption reaction proceeded according to Equation 3.10.

$$\mathrm{Li_2ND + D_2 \longleftrightarrow LiND_2 + LiD} \qquad \text{Equation 3.10}$$

Once the pressure of the system had reached 3 bar, the scale factors of $LiND_2$ and LiD showed little variation during the subsequent variations in pressure and temperature. Even so, the thermogravimetric data indicated that there was a slow, steady mass loss during these steps. The normalised scale factor of Li_2ND continued to decrease slowly, but did not reach zero, implying that re-deuteration of the sample to form $LiND_2$ + LiD was not complete.

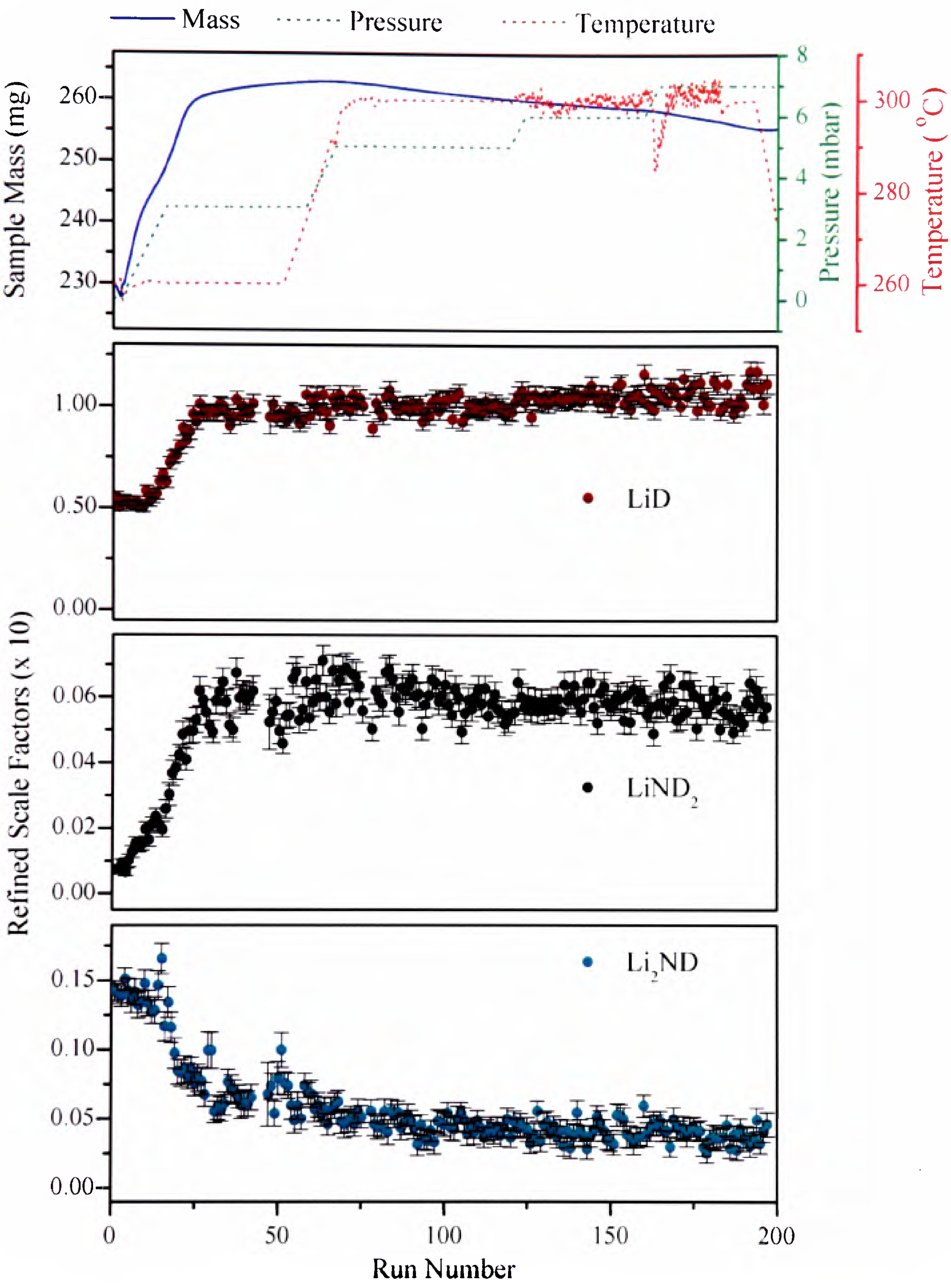

Figure 3.19a : Summary of scale factors obtained from Rietveld analysis (*via* batch refinement) of the neutron diffraction data collected during D_2 absorption on the decomposed $LiND_2$ + LiD mixture, studied using the IGA^n apparatus. The thermogravimetric data are also presented for ease of comparison. Mean errors LiD ± 0.004, $LiND_2$ ± 0.0003, Li_2ND ± 0.0008

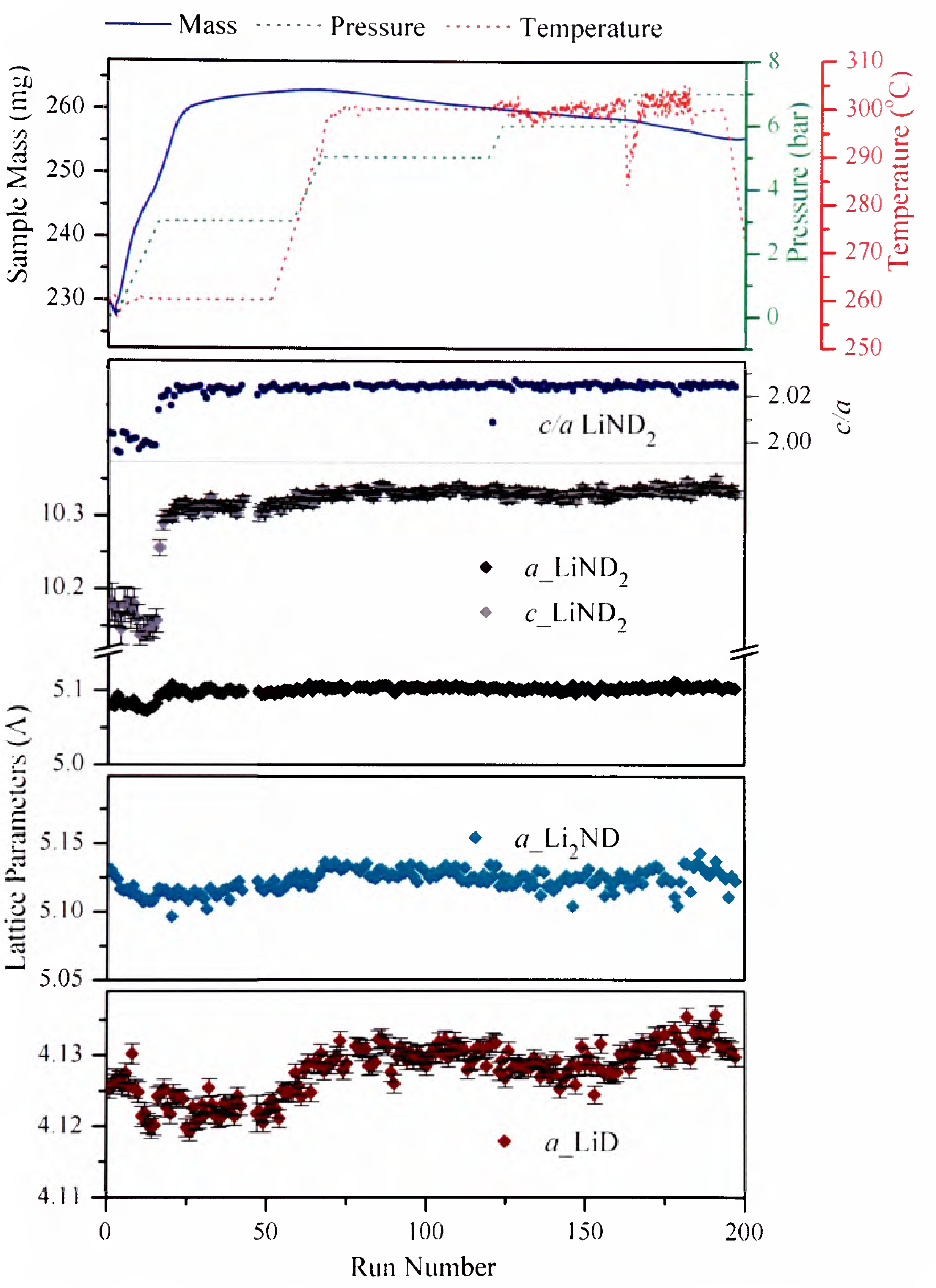

Figure 3.19b : Summary of refined lattice parameters obtained from Rietveld analysis (*via* batch refinement) of the neutron diffraction data collected during D_2 absorption on the decomposed $LiND_2$ + LiD mixture, studied using the IGA^n apparatus. The thermogravimetric data are also presented for ease of comparison. Mean errors *a*_LiD ± 0.0012, *a*_$LiND_2$ ± 0.002, *c*_$LiND_2$ ± 0.005, *a*_Li_2ND ± 0.002.

Figure 3.19b shows the variation of the refined lattice parameters of the phases during the experiment. The *c/a* ratio of $LiND_2$ at the beginning of the D_2-absorption step was 1.99. This is assumed to be an artefact of the refinement, arising due to the similarity of the crystal structures of $LiND_2$ and Li_2ND (as outlined in section 3.6.3) and the weakness of the $LiND_2$ Bragg reflections at this point.

A sudden and sharp increase from 1.99 – 2.02 was observed in the *c/a* ratio of the $LiND_2$ lattice parameters as the scale factor of $LiND_2$ increased and the diffraction peaks became stronger. Heating of the sample to 300 °C resulted only in a slight increase in the length of the $LiND_2$ lattice parameters, which is consistent with thermal expansion of the phase.

The refined lattice parameter of Li_2ND was observed to decrease just prior to the transformation of Li_2ND into $LiND_2$ (as evidenced by decreasing Li_2ND phase fraction and increasing $LiND_2$ phase fraction, run numbers 1-10). This sudden change in lattice parameter is indicative of a structural transition, and was observed just before the scale factor of $LiND_2$ began to increase and yet after the sample-mass began to increase.

The increase in sample mass prior to crystallographic transformation could be the result of two processes. Firstly, D_2 could have physisorbed onto the surface of the powder grains, but not reacted with Li_2ND until the gas concentration had reached a certain threshold value. Alternatively, the Li_2ND may have taken deuterium into its crystal structure, reducing the Li – stoichiometry of the imide phase and forming an expanded cubic $Li_{2-x}ND_{1+x}$ phase. The observed structural transition may therefore have been triggered by the compositional change of the sample prior to rearrangement of the material into tetrahedral $LiND_2$.

The presence of a structural transition when the sample was under isothermal conditions is evidence for the second scenario, supporting the theory that conversion between Li_2NH and $LiNH_2$ may occur *via* a continuum of non-stoichiometric Li – N – H intermediates.[10]

The lattice parameter of LiD varied linearly with the temperature of the system, indicating thermal expansion of the phase.

A full summary of the refined structural parameters for this step is presented in Appendix A1.2

3.6.6 Deuterium Cycling of the Desorbed and Re-deuterated $LiND_2$ + LiD Sample.

The D_2-sorption processes of Li – N – D compounds in the presence of LiD were further studied by cycling the re-deuterated sample described in section 3.6.5 between pressures of 6 mbar and 3 bar with D_2 at 260 °C. This temperature was chosen as both absorption and desorption had been observed 260 °C under varying conditions of pressure (sections 3.6.4 and 3.6.5). Data were collected for two full decomposition / D_2-absorption cycles.

The neutron diffraction data and thermogravimetric data collected during the cycling reactions are presented in Figure 3.20. The gaps in the surface plot correspond to loss of the neutron beam during the experiment.

Focusing again on the d-spacing region of 2.5 – 2.6 Å in the surface plot, the splitting and convalescence of the peaks suggests that cycling occurred between a tetragonal and a cubic phase. The cubic to tetragonal transformation was accompanied by an increase in the intensity of the peak at a d-spacing of 2.38 Å (indexed to the (111) reflection of LiD).

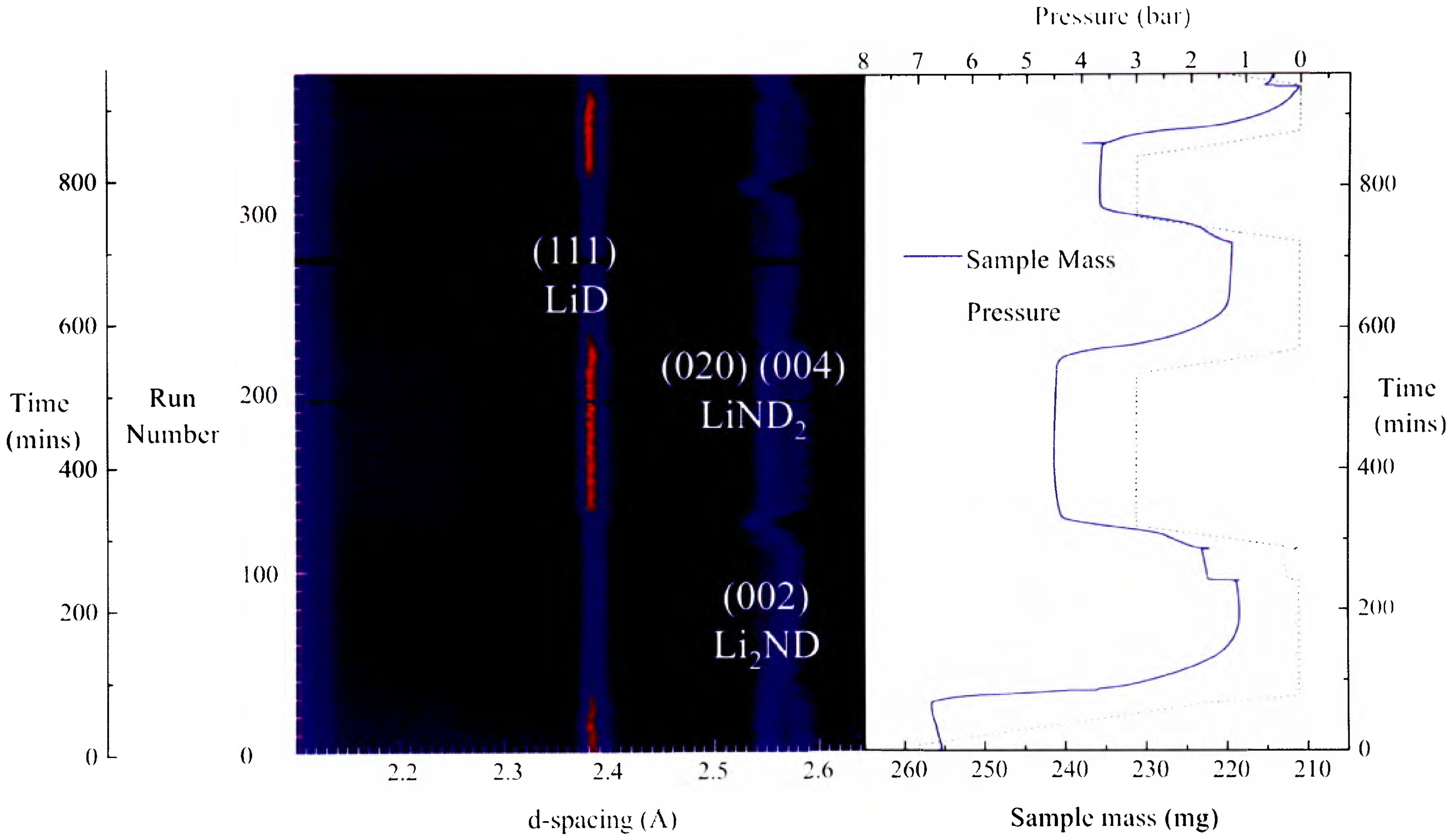

Figure 3.20 : Comparison of the surface plot of neutron diffraction data (collected at bank 5) and thermogravimetric data collected during isothermal D_2 cycling of the decomposed and re-deuterated $LiND_2$ + LiD mixture at 260 °C, studied using the IGA^n apparatus. d-spacing region of 2.1 – 2.7 Å chosen to highlight the splitting and coalescence of $LiND_2$ and Li_2ND Bragg reflections, and the change in intensity of the (111) LiD Bragg reflection.

This is consistent with the cycling of the reaction mixture between $LiND_2$ + LiD and $Li_2ND + D_2$.

The position of the Bragg peak indexed to the (002) reflection of Li_2ND was observed to fluctuate greatly just prior to splitting into the (020) and (004) $LiND_2$ reflections during each cycle. This suggests that a significant contraction occurred in the lattice parameter of Li_2ND prior to its transformation into $LiND_2$.

Unsurprisingly, the plot of the sample mass largely followed the pressure variations of the system, excepting the presence of a slight shoulder that was observed in the sample mass at the beginning of the absorption steps. This shoulder probably arose due to temperature fluctuations upon the introduction of cold gas into the system, which would retard the rate of D_2 absorption.

The mass of the sample increased by 10 mass% during the first absorption step and only 8.25 mass% during the second absorption step, implying that the storage capacity, or D_2 absorption kinetics, degraded during cycling. The mass of the sample appeared to take longer to plateau after the first absorption of D_2 compared to the second absorption, which is consistent with a degradation of absorption kinetics.

3.6.6.1 Rietveld Analysis of Neutron Diffraction Data Collected During the Cycling Reaction of $LiND_2$ + LiD.

The neutron diffraction data collected during this experiment were analysed by Rietveld refinement[15] using the TOPAS Academic software suit.[16] Due to the complex nature of the reaction, particularly the number of phase changes observed during the D_2 cycling, it was necessary to refine the data using a combination of batch (section 2.1.4.2) and individual refinements (section 2.1.4.1). The data collected during phase transformations were largely refined individually whilst batch refinements were used for the remaining data.

The refined scale factors and lattice parameters for $LiND_2$, Li_2ND and LiD are presented in Figures 3.21a and b, respectively. To put the relative scale factors of the phases present in context, the start point composition of the sample for the D_2 cycling reaction was 47 mass% $LiND_2$, 41 mass% LiD and 12 mass% Li_2ND and the end point sample composition for this step was 13 mass% $LiND_2$, 45 mass% LiD and 42 mass% Li_2ND.

Figure 3.21a shows that the plots for the $LiND_2$ and LiD scale factors follow the same trends as those observed for the sample mass and pressure (albeit shifted slightly). This implies that the proportions of $LiND_2$ and LiD present in the sample increased during the pressurisation steps and decreased during the outgas steps. The refined scale factor of Li_2ND approximately followed the reverse of the pressure and mass trends. The additional peaks in the Li_2ND scale factor coincided with structural transitions of the phase prior to transformation into $LiND_2$ (Figure 3.21.b).

These results are consistent with a cycling reaction between $LiND_2$ + LiD and Li_2ND + D_2 in the presence of excess LiD.

The lattice parameter of Li_2ND (Figure 3.21b) appeared generally to respond to the pressure changes of the system, excepting sharp unit cell contractions just prior to the transformation of Li_2ND into $LiND_2$ (Figure 3.21a). Such a contraction was also observed prior to the transformation of Li_2ND into $LiND_2$ in section 3.6.5, and was attributed to a structural transition.

As observed in section 3.6.5, the sample mass increased prior to the structural transitions, which may have been due to physisorption of D_2 gas on the surface of the powder grains, or due to the formation of non-stoichiometric $Li_{2-x}ND_{1+x}$ phases.

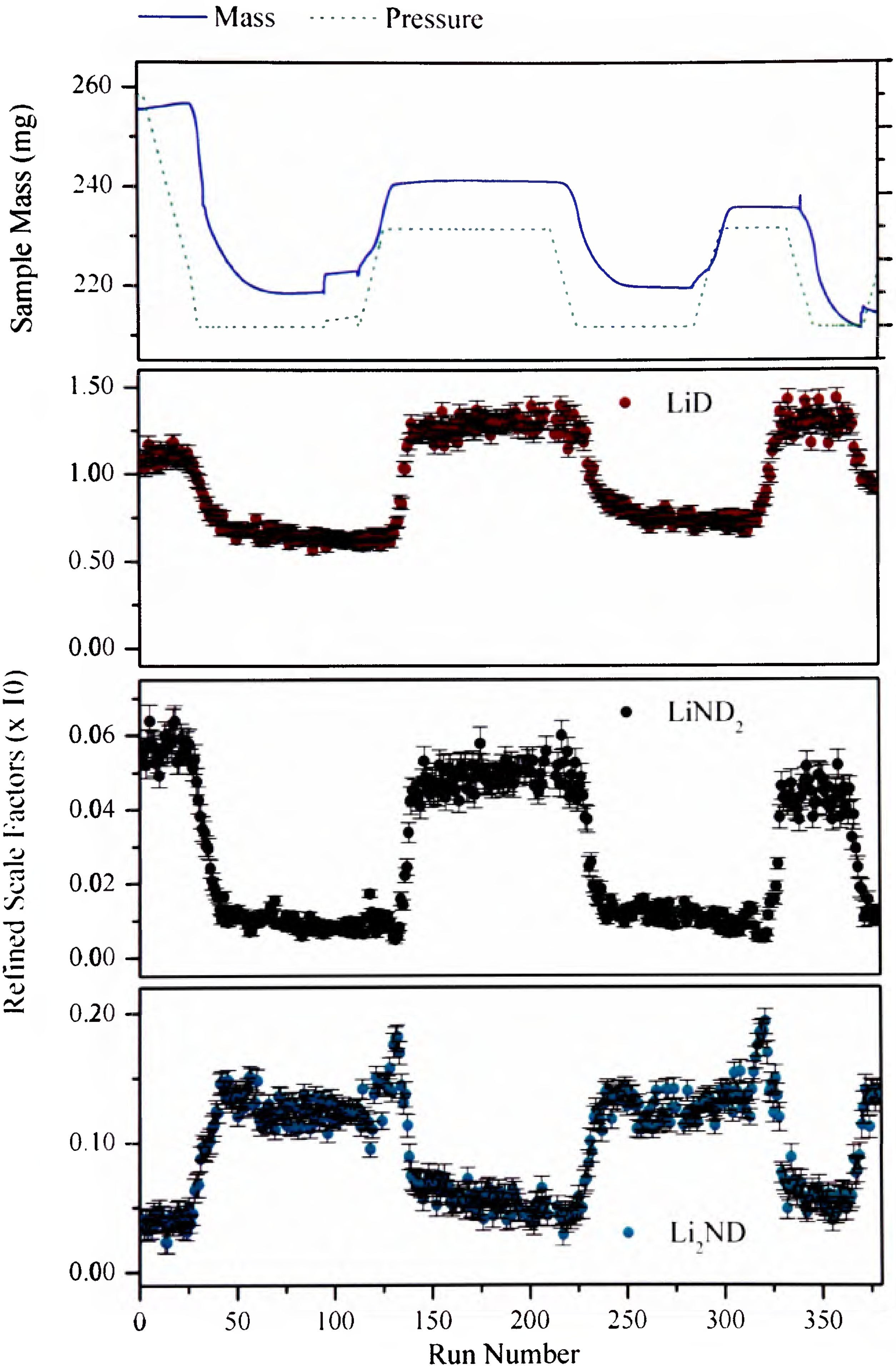

Figure 3.21a : Summary of refined scale factors, obtained from Rietveld analysis (*via* batch refinement) of the neutron diffraction data collected during isothermal D_2 cycling on the decomposed and re-deuterated $LiND_2$ + LiD mixture at 260 °C. The thermogravimetric data are also presented for ease of comparison. Mean errors LiD ± 0.003, $LiND_2$ ± 0.0002, Li_2ND 0.0008

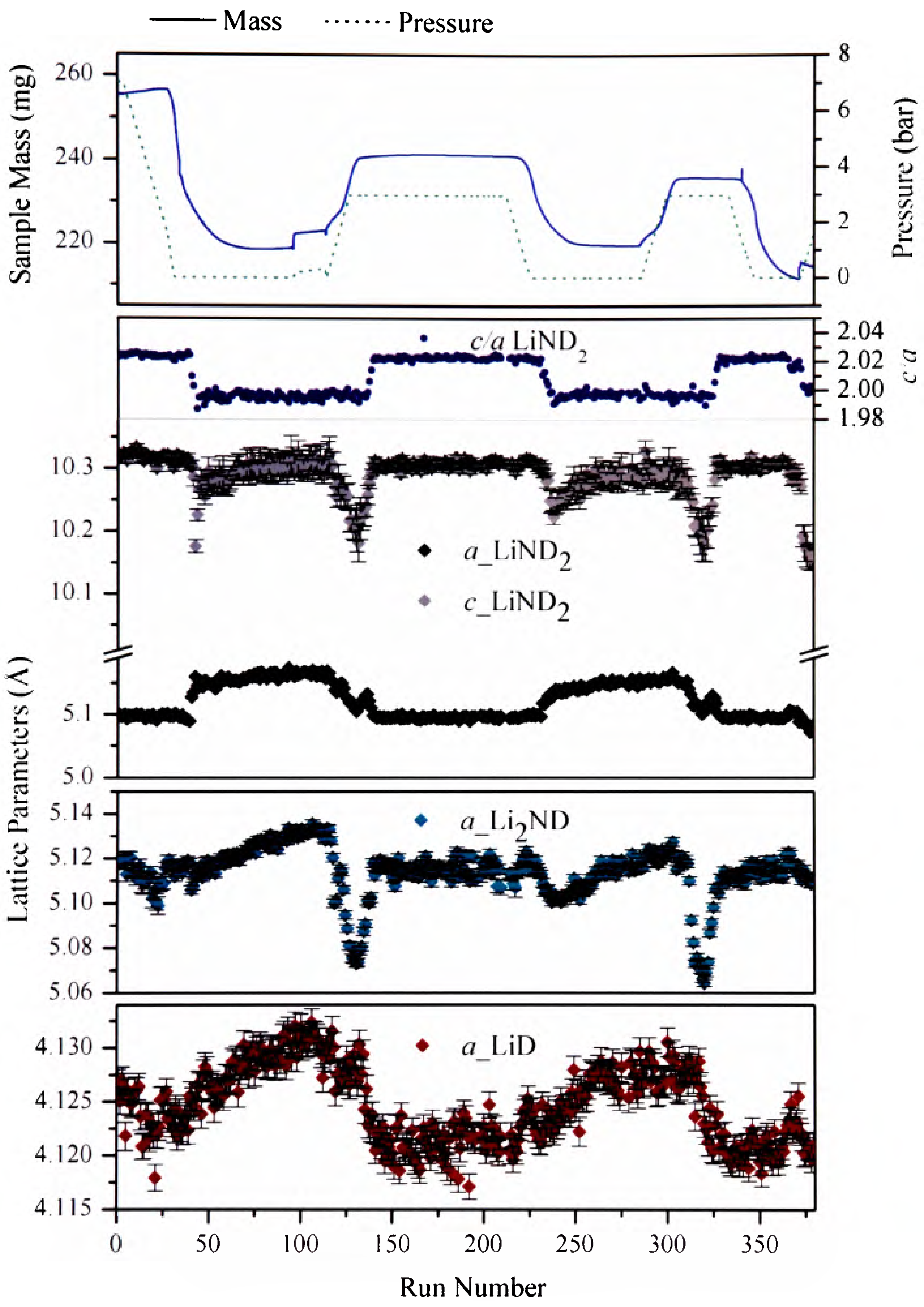

Figure 3.21b : Summary of refined lattice parameters, obtained from Rietveld analysis (*via* batch refinement) of the neutron diffraction data collected during isothermal D_2 cycling on the decomposed and re-deuterated $LiND_2$ + LiD mixture at 260 °C. The thermogravimetric data are also presented for ease of comparison. Mean errors *a*_LiD ± 0.0012, *a*_$LiND_2$ ± 0.003, *c*_$LiND_2$ ± 0.012, *a*_Li_2ND ± 0.002

The *c/a* ratio of $LiND_2$ was consistently >2 (with *a* and *c* parameters ~ 5.10 Å and 10.32 Å, respectively) provided that the $LiND_2$ scale factor was greater than zero and the $LiND_2$ Bragg reflections were suitably strong. As the $LiND_2$ phase fraction tended towards zero and the Bragg reflections became weak, the $LiND_2$ lattice parameters altered greatly, first behaving erratically and then displaying a *c/a* ratio of 2. During these times, the $LiND_2$ parameters followed the trends observed in the Li_2ND lattice parameter, and as such, this can be regarded as an artefact of the refinement as outlined in section 3.6.3.

The unit cell parameter of LiD (Figure 3.21b) increased and decreased only in response to pressure increases and decreases in the system.

A full summary of the refined structural parameters for this step is presented in Appendix A1.2.

3.6.7 The Potential Role of Defects in the Cycling Properties of Li_2ND + LiD

It was anticipated that the presence of defects would improve the cycling properties of the Li_2ND + LiD system due to the increased potential for ionic migration and gas diffusion through the sample. In light of this hypothesis, two experiments were performed using the IGA^n apparatus at the ISIS pulsed neutron facility.

The samples were composed of LiD (Aldrich, 99.99 atom% D) and Li_2ND (synthesised according to the procedure outlined in section 2.6.2.1).

Sample A was a 1:1 mixture of Li_2ND + LiD which was ball milled at 350 rpm for 3 hours, as outlined in section 2.6.2.3. After the initial milling process, an aliquot of Sample A was taken and ground by hand with additional LiD to form Sample B, which was of composition 1:1:1 Li_2ND_{milled} + LiD_{milled} + LiD_{ground}.

Neutron diffraction data were collected from both samples in vanadium cans using the GEM diffractometer. Refined scale factors, calculated from Rietveld analysis[15] of the data, indicated that Samples A and B contained approximately 2 mass% and 1.5 mass% tungsten carbide, respectively, which had arisen from the milling process.

Both samples were then studied individually using intelligent gravimetric analysis combined with neutron diffraction. The samples were each subjected to the same sequence of pressure and temperature variations, which is outlined below.

The samples were first pressurised to 1 bar with D_2 and heated to 260 °C at a rate of 2 °C/min in order to facilitate D_2 absorption. The samples were then outgased to facilitate decomposition, and then cooled to 70 °C. This procedure was repeated two further times, using pressures of 2 bar and 3 bar of D_2, respectively.

It was anticipated that, of the two samples, Sample B would have a lower concentration of structural defects due to the presence of both milled LiD (with many structural defects) and ground LiD (with fewer defects). The presence of different numbers of defects was anticipated to influence not only the rate of D_2 sorption, but also the rate of variation of the LiD lattice parameters.

Additionally, due to the decreased proportion of Li_2ND in the sample, the mass changes observed during the cycling of Sample B were expected to be smaller than those of Sample A.

3.6.7.1 Study of the Surface Plots for Samples A and B

The neutron diffraction data and the thermogravimtric data collected for Samples A and B during these studies are presented in Figures 3.22 and 3.23 respectively.

Given that the starting masses of Samples A and B were different, the thermogravimetric mass data were normalised for ease of comparison between the data sets. The gaps in the surface plots correspond to loss of the neutron beam during the experiment.

For both samples, an increase in the temperature and D_2 pressure of the sample led to the splitting of the Bragg peak at d-spacing 2.5 Å (indexed to the (002) reflection of Li_2ND) into two reflections (which were indexed to the (020) and (004) reflections of $LiND_2$). This is consistent with the transformation of cubic Li_2ND into tetragonal $LiND_2$, which would be expected during the deuteration of Li_2ND.

The splitting of the Bragg reflection at d-spacing 2.5 Å was accompanied by an increase in the intensity of the Bragg reflection at d-spacing 2.35 Å (indexed to (111) reflection of LiD).

These findings are consistent with D_2 absorption in Li_2ND according to Equation 3.11 (where x is 1 for Sample A and 2 for Sample B)

$$\mathrm{Li_2ND} + x\mathrm{LiD} + \mathrm{D_2} \longleftrightarrow \mathrm{LiND_2} + (x+1)\,\mathrm{LiD} \qquad \text{Equation 3.11}$$

Decrease in pressure of the samples was accompanied by the coalescence of the Bragg reflections at d-spacing 2.5 – 2.6 Å and a decrease in the intensity of the Bragg reflection at ~2.35 Å.

These observations are consistent with the transformation of $LiND_2$ + LiD into Li_2ND +D_2, according to the reverse of Equation 3.11.

The positions of all Bragg reflections appeared to vary linearly with temperature, which is suggestive of thermal expansion and contraction of the phases present.

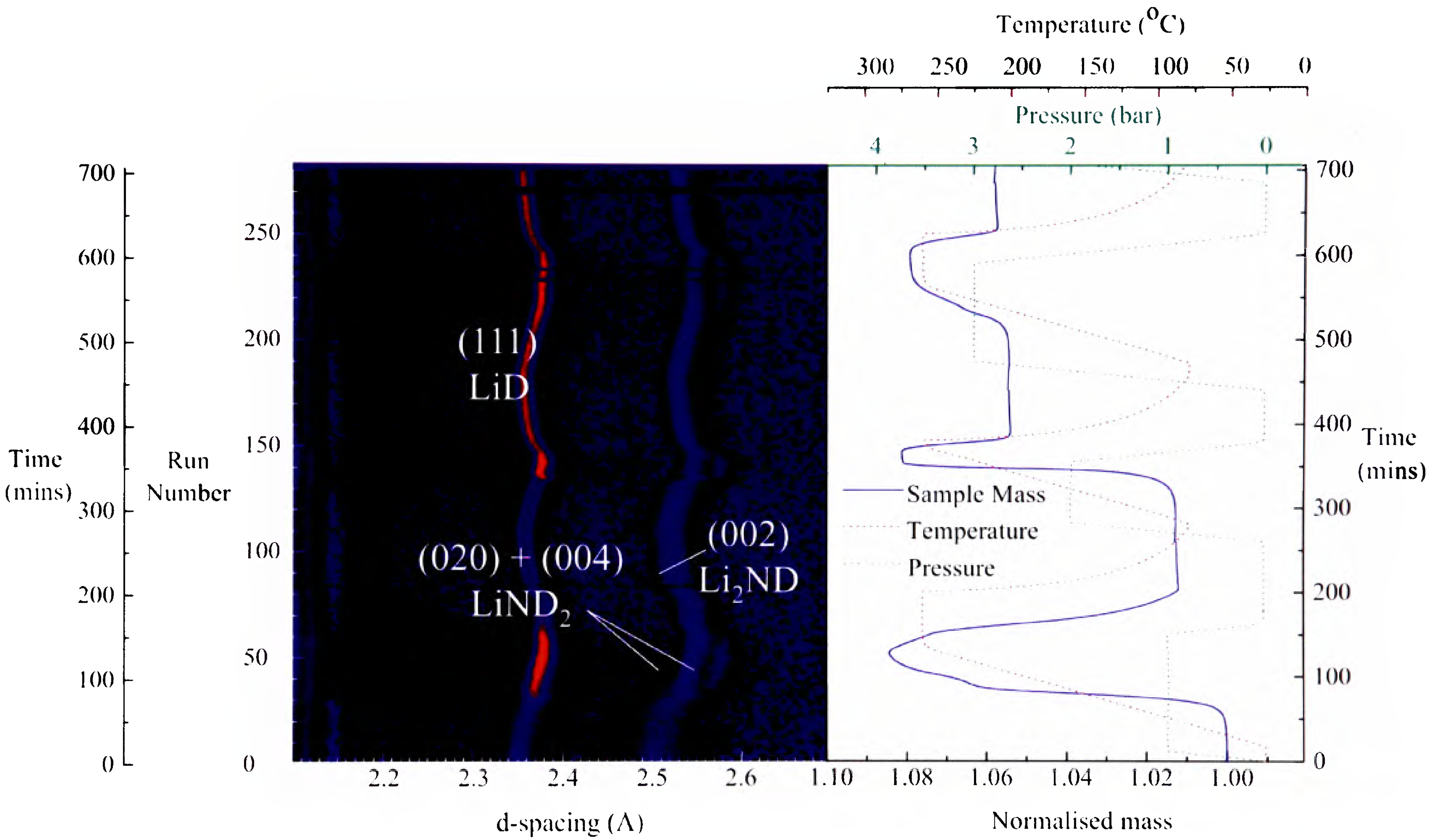

Figure 3.22 : Comparison of the surface plot of neutron diffraction data (collected at bank 5) and thermogravimetric data collected during the D_2 cycling of the ball milled Li_2ND + LiD sample, studied using the IGA^n apparatus. d-spacing region of 2.1 – 2.7 Å chosen to highlight the splitting and coalescence of the $LiND_2$ and Li_2ND Bragg reflections, and the change in intensity of the (111) LiD Bragg reflection.

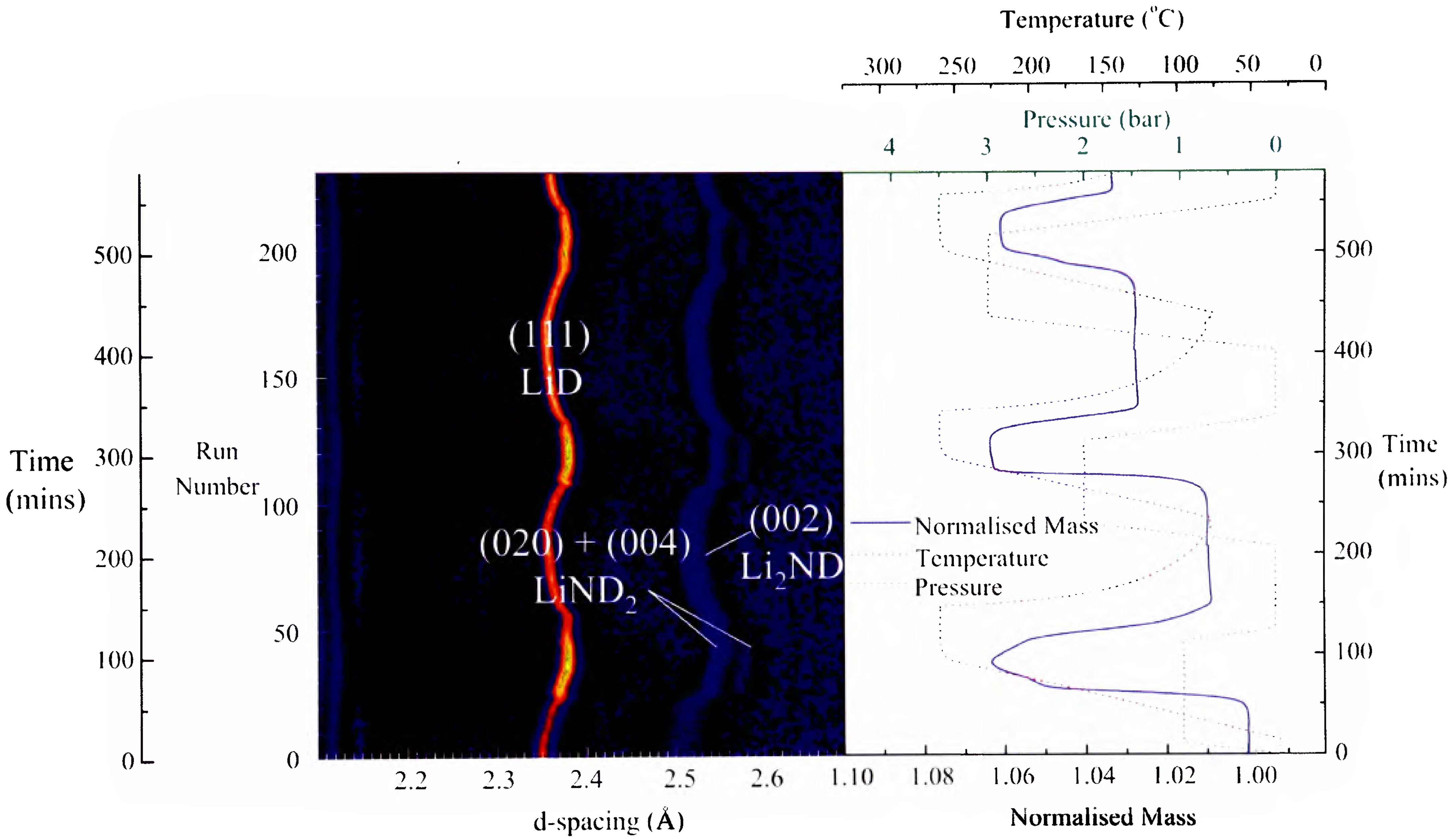

Figure 3.23 : Comparison of the surface plot of neutron diffraction data collected at bank 5 and thermogravimetric data collected during the D_2 cycling of the sample of Li_2ND_{milled} + LiD_{milled} + LiD_{ground}, studied using the IGA^n apparatus. d-spacing region of 2.1 – 2.7 Å chosen to highlight the splitting and coalescence of the $LiND_2$ and Li_2ND Bragg reflections, and the change in intensity of the (111) LiD Bragg reflection.

3.6.7.2 Comparison of Thermogravimetric Data for Samples A and B

Comparison of the thermogravimetric data collected during the D_2 cycling of Samples A and B showed that the percentage mass increase observed for Sample A was greater than that of Sample B. This was to be expected, given the lower Li_2ND content of Sample B.

Assuming that the deuteration of Sample A proceeded according to Equation 3.12, the theoretical mass increase for this sample was calculated at 10.4 mass%.

$$Li_2ND + LiD + D_2 \longleftrightarrow LiND_2 + 2\,LiD \qquad \text{Equation 3.12}$$

The mass increase observed experimentally was lower than that anticipated from Equation 3.12, at around 8.4 wt%.

D_2 absorption on Sample B was anticipated to result in a mass increase of 8.4 mass%, assuming that the reaction occurred according to Equation 3.13.

$$Li_2ND + 2LiD + D_2 \longleftrightarrow LiND_2 + 3\,LiD \qquad \text{Equation 3.13}$$

The experimental mass increase for this sample was shown to be 6.3 wt %, which was again was around 2 % lower than that calculated from theory.

It is likely that the mass increase of the samples upon deuteration was lower than anticipated due to the formation of sub-stoichiometric $Li_{1+y}ND_{2-y}$.

A small proportion of this discrepancy may also be accounted for by the 1 - 2 % tungsten carbide contamination of the samples from the ball milling process.

Comparison of the thermogravimetric data for successive D_2 absorptions indicated that the peak masses observed for both samples decreased by approximately 0.2% every cycle. This suggests that the storage capacity of both samples degraded during cycling, presumably due to loss of nitrogen in the form of ND_3.

The first desorption step of both samples resulted in an almost complete return to the starting mass, meaning virtually all of the D_2 adsorbed in the previous step was released during decomposition. The second and third decomposition reactions resulted in only partial decomposition of the samples, with mass losses of only ~2-3 mass%. This was observed because the temperatures of both materials were dropped too quickly after outgasing, and so the decomposition reactions were not allowed to reach equilibrium.

3.6.7.3 Rietveld Analysis of Neutron Diffraction Data Collected during D_2 Cycling of Samples A and B.

Rietveld analysis[15] (section 2.1.4) of the neutron diffraction data collected during D_2-cycling of Samples A and B was performed using the TOPAS Academic software suite (section 2.1.4.1).[16] Refinements were performed on an individual basis (section 2.1.4.1) for the data collected at the beginning and end of phase transformations, and batch techniques (section 2.1.4.2) were used for the remainder of the data.

The intensities of the Bragg reflections arising from tungsten carbide (WC) impurity were such that the WC peaks could not be resolved from the background data. As such, WC was not included in the refinement models of the diffraction data.

The refined scale factors and lattice parameters of the phases present during D_2 cycling of Sample A are presented in Figure 3.24a and b, respectively. The refined scale factors and lattice parameters of the phases present during D_2 cycling of Sample B are presented Figures 3.25a and b, respectively.

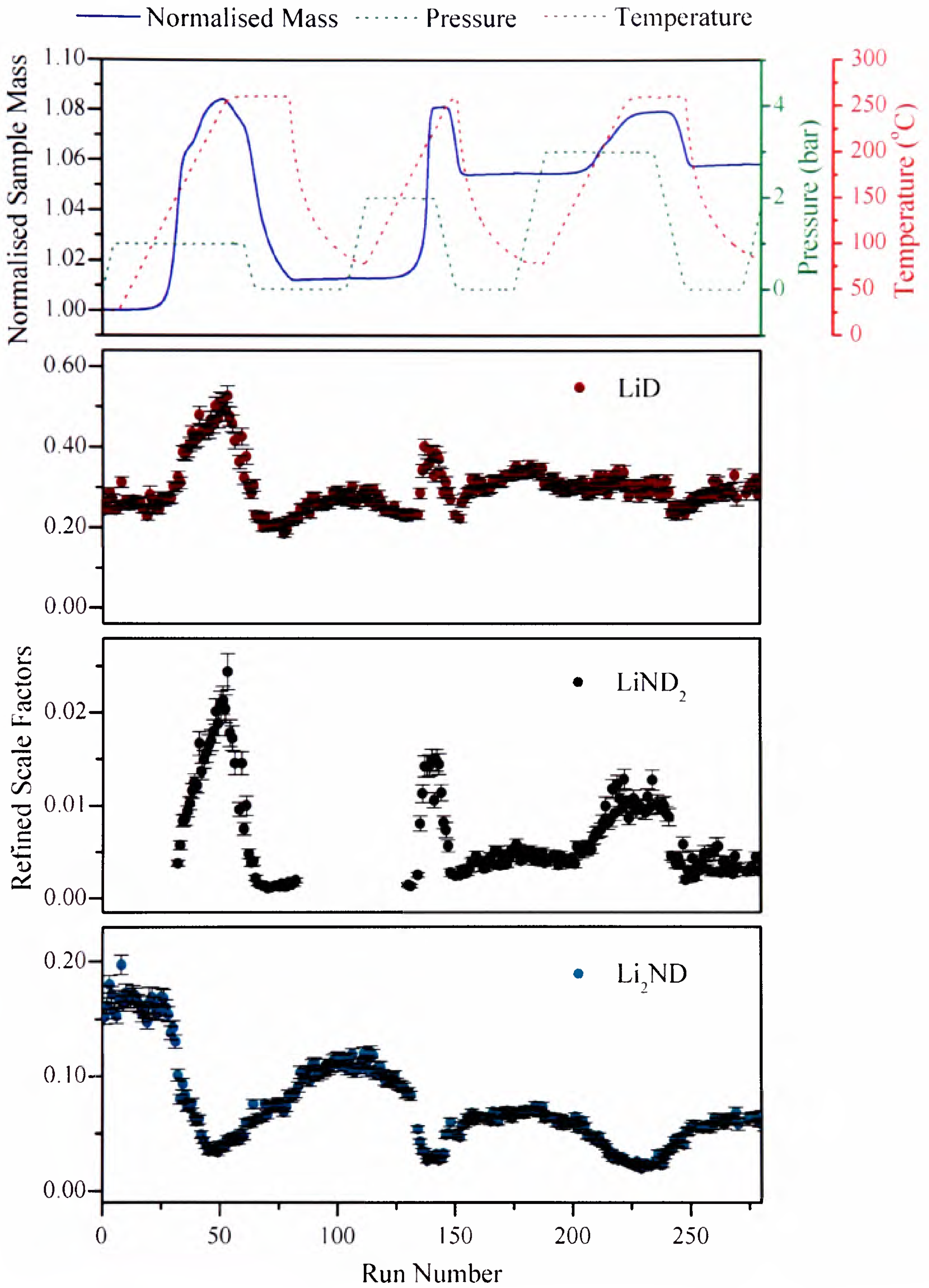

Figure 3.24a : Summary of refined scale factors, obtained from Rietveld analysis (*via* batch refinement) of the neutron diffraction data collected during D_2 cycling of the ball milled mixture of Li_2ND + LiD, studied using the IGA^n apparatus. The thermogravimetric data are also presented for ease of comparison. Mean errors LiD ± 0.012, $LiND_2$ ± 0.0005, Li_2ND 0.003

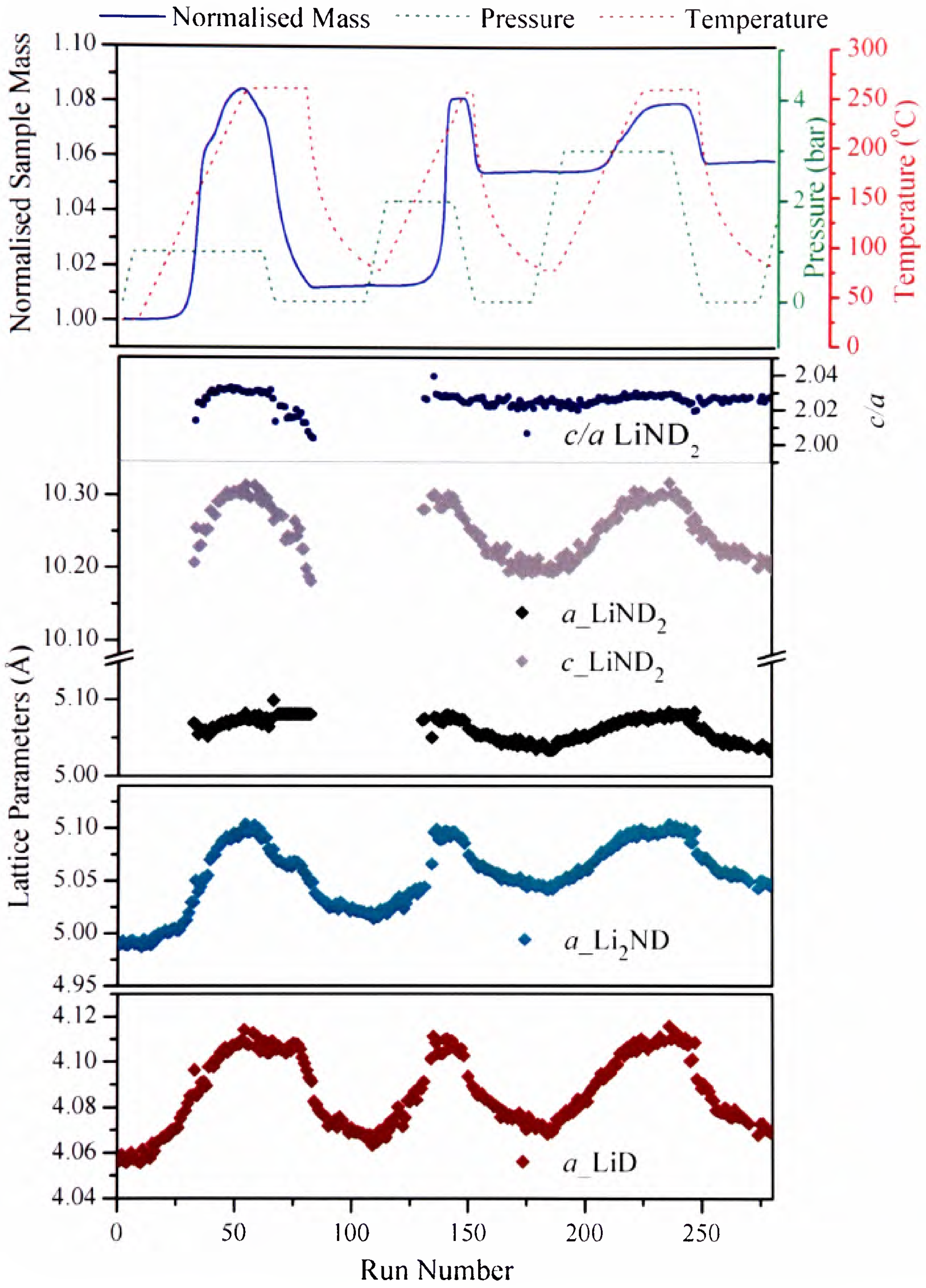

Figure 3.24b : Summary of refined lattice parameters, obtained from Rietveld analysis (*via* batch refinement) of the neutron diffraction data collected during D_2 cycling of the ball milled mixture of Li_2ND + LiD, studied using the IGA^n apparatus. The thermogravimetric data are also presented for ease of comparison. Mean errors *a*_LiD ± 0.0017, *a*_$LiND_2$ ± 0.004, *c*_$LiND_2$ ± 0.012, *a*_Li_2ND ± 0.002. Error bars smaller than data markers.

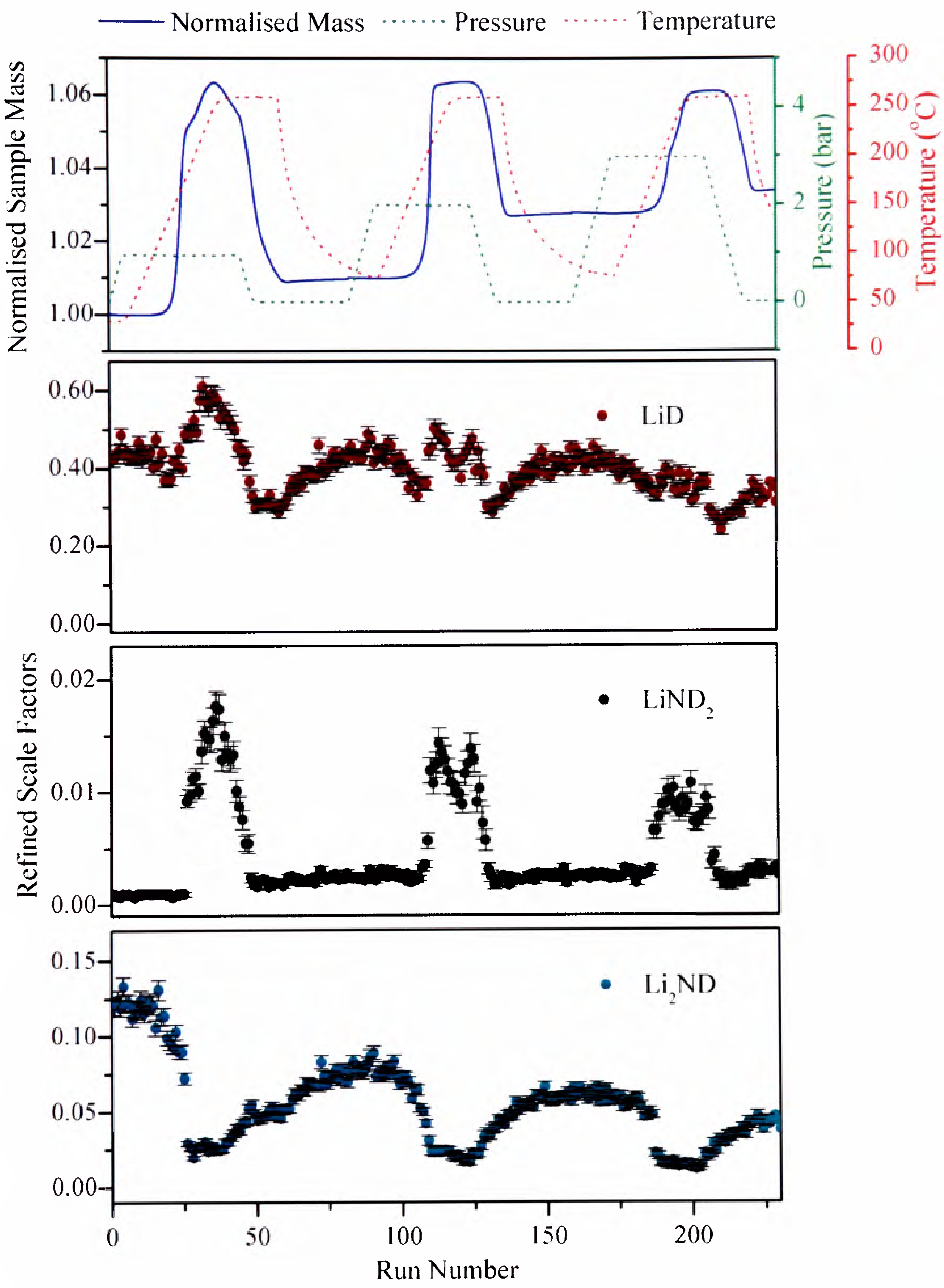

Figure 3.25a : Summary of refined scale factors, obtained from Rietveld analysis (*via* batch refinement) of the neutron diffraction data collected during D_2 cycling of the Li_2ND_{milled} + LiD_{milled} + LiD_{ground} sample, studied using the IGA^n apparatus. The thermogravimetric data are also presented for ease of comparison. Mean errors LiD ± 0.017, $LiND_2$ ± 0.0004, Li_2ND ± 0.003

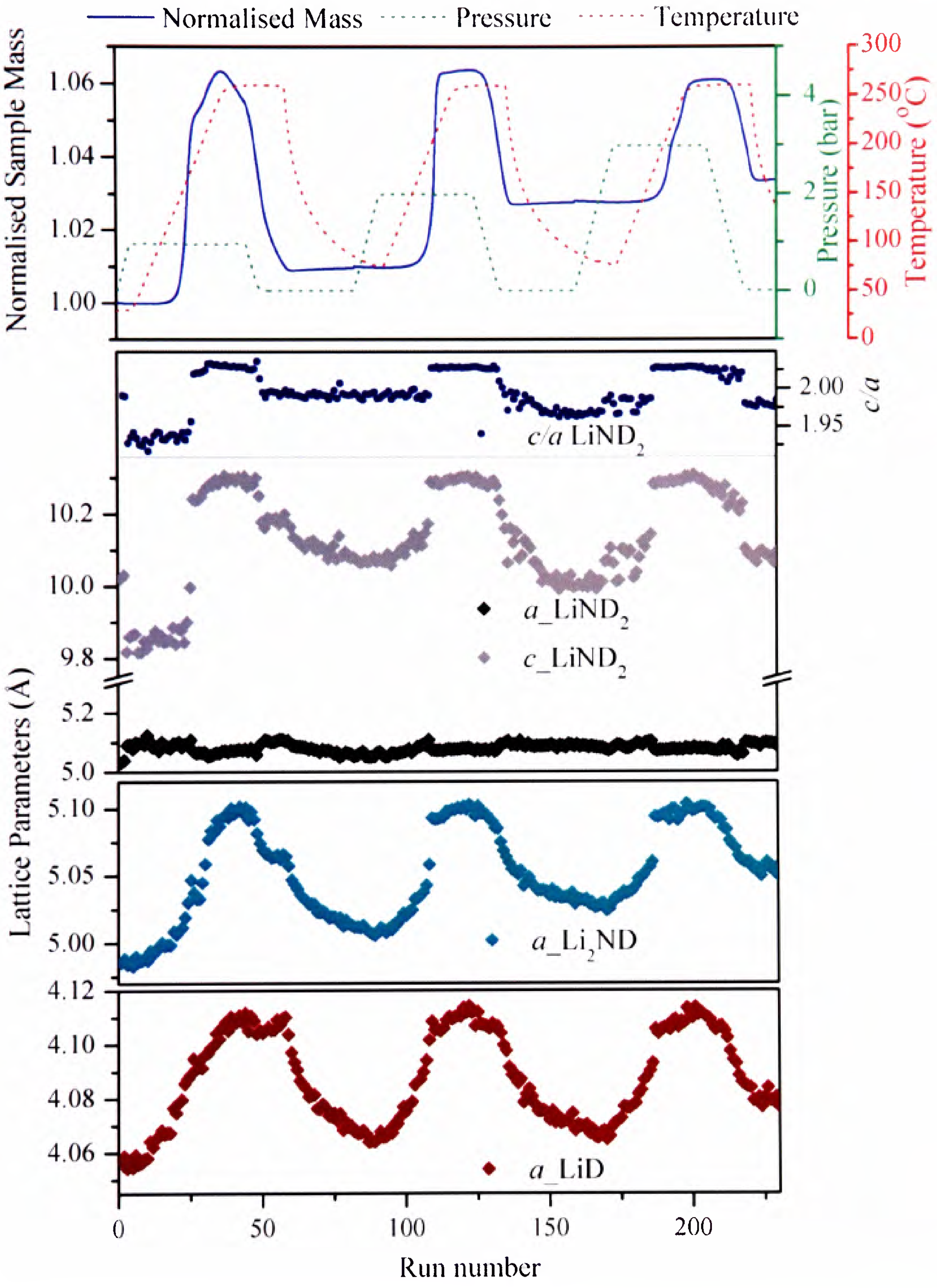

Figure 3.25b : Summary of refined lattice parameters, obtained from Rietveld analysis (*via* batch refinement) of the neutron diffraction data collected during D_2 cycling of the Li_2ND_{milled} + LiD_{milled} + LiD_{ground} sample, studied using the IGA^n apparatus. The thermogravimetric data are also presented for ease of comparison. Mean errors *a*_LiD ± 0.0016, *a*_$LiND_2$ ± 0.004, *c*_$LiND_2$ ± 0.012, *a*_Li_2ND ± 0.002. Error bars smaller than data markers

Figures 3.24a and 3.25a indicate that the trends in the scale factors for $LiND_2$ and LiD followed the trends observed in the thermogravimetric data of the samples. Thus, the proportions of $LiND_2$ and LiD present in Samples A and B increased during absorption steps and decreased during desorption steps. The scale factor of Li_2ND in the samples followed approximately the reverse of this trend, increasing during desorption and decreasing during absorption. These observations are consistent with the reaction schemes described in Equations 3.12 (Sample A) and 3.13 (Sample B).

Given that Sample A contained a higher defect concentration than Sample B, gas diffusion was expected to be more facile through Sample A. Faster gas diffusion was expected to improve the kinetics of D_2-sorption and thus cause faster phase transformations between $Li_2ND + D_2$ and $LiND_2 + LiD$. The gradients of the scale factor plots of Sample A were therefore expected to be steeper than those of Sample B during phase transformations.

Comparison of Figures 3.24a and 3.25a shows that the gradients of the scale factor plots for Sample B were, in fact, slightly steeper than those of Sample A. This indicates that the conversion between phases during D_2 sorption was slower in Sample A than Sample B. This may be a packing effect due to the combination of small and large grain-sizes in Sample B, or may simply be due to the additional LiD present in the sample. The rate of mass increase and decrease appeared to be unaffected by the variations in the defect concentration of the samples.

The scale factor of $LiND_2$ did not return to zero during either the second or third outgasing steps of both samples, indicating that the decomposition reactions during these cycles did not reach completion. This conclusion is supported by the thermogravimetric data of the second and third cycles for both samples (section 3.6.7.2) and is the result of the rapid decrease in temperature of the systems before the materials reached equilibrium. This accounts for the slight increase observed in the scale factor of LiD present in both samples during the 2nd and 3rd outgasing steps.

The refined lattice parameters of the phases present in Samples A and B are presented in Figures 3.24b and 3.25b, respectively.

The plots of the refined LiD, Li_2ND and $LiND_2$ lattice parameters for Samples A and B all exhibited small shoulders during the first desorption reaction, which probably arose due to the sudden changes in the pressure of the systems at these points. Other than these minor deviations, the lattice parameters of Li_2ND and LiD appeared to be linearly related to temperature, which is consistent with thermal expansion and contraction of the phases with increasing and decreasing temperature, respectively.

Due to the presence of both milled and ground LiD in Sample B, it was anticipated that the diffraction peaks corresponding to LiD in Sample B would be split. Refinement of the data was therefore attempted using two distinct LiD phases with varying size and strain effects. Unfortunately, the resolution of the neutron data was such that no splitting was observed, and the diffraction data had to be modelled using a single, LiD structure.

The lower concentration of defects in Sample B was expected to affect the length of the LiD lattice parameter and the rate at which this length varied with temperature. Comparison of refined LiD a-parameters for Samples A and B (Figures 3.24b and 3.25b) suggests that length-range and the rate of variation of this parameter was identical for both samples. This suggests that the defect concentration did not have any visible effect on the length or rate of variation of the LiD a-parameter, within the resolution of the experiment.

Figures 3.24b and 3.25b suggest that the lattice parameters of the $LiND_2$ in Samples A and B varied linearly with temperature. The only deviation from this trend was observed during the first D_2-absorption step, where the *c*-parameter of the $LiND_2$ present in Sample B was calculated to be much shorter than would be expected. This can be viewed as an artefact of the refinement, as outlined in (section 3.6.3), arising from the weakness of the $LiND_2$ diffraction peaks at this point.

A point of particular interest is raised upon comparison of the refined Li_2ND lattice parameters of Samples A and B with those observed for Li_2ND in sections 3.6.5 and 3.6.6.

The transformation of Li_2ND into $LiND_2$ in section 3.6.5 was preceded by a sharp and sudden decrease in the lattice parameter of Li_2ND, which was attributed to a structural transition. In the milled samples, no such unit cell contraction was observed, which suggests that a structural transition is not necessary if the Li_2ND is milled (disordered). This indicates that the structural transition observed in the un-milled sample described in sections 3.6.5 and 3.6.6 was an order-disorder transition.

A full summary of the refined structural parameters is presented Appendix A1.2.

3.7 Conclusions.

Thermogravimetric data were collected for samples of $LiNH_2$ and 1:1 $LiNH_2$ + LiH using Intelligent Gravimetric Analysis with Mass Spectrometry. These studies confirmed the decomposition properties of the Li – N – H system reported previously in the literature.[1, 11]

Synchrotron X-ray diffraction data were collected for samples of $LiNH_2$ (Aldrich), Li_2NH (synthesised from Li_3N + $LiNH_2$) and Li_3N (Aldrich). Rietveld analysis[15] of the diffraction data indicated that the $LiNH_2$ studied was a stoichiometric material of purity 95 mass%, with Li_2O impurity. The Li_3N studied was majority α-phase, with a small proportion of β-Li_3N and Li_2O and LiOH impurities. Refinement of the diffraction data for Li_2NH indicated that the sample was majority $Fm\bar{3}m$-Li_2NH, together with a small proportion of $Fd\bar{3}m$-Li_2NH and $LiNH_2$, Li_3N and Li_2O impurities.

A sample of $LiND_2$ was synthesised *via* the reaction of Li_3N with ND_3 in the IGA. The thermogravimetric data for the ND_3-uptake reaction indicated that the $LiND_2$ formed in this way was Li-rich, with a stoichiometry of $Li_{1.24}ND_{1.77}$, which was confirmed by Rietveld analysis[15] of neutron diffraction data collected from the sample. Refinement of the diffraction data also indicated that the Li-sublattice of the material was highly disordered, with all of the tetrahedral sites except the 2b (0,0,½) site at least partially occupied by Li ions.

Variable temperature synchrotron X-ray diffraction studies of $LiNH_2$ and $LiND_2$ produced very different results. The $LiNH_2$ studied (95%, Aldrich) was known from Rietveld analysis of room temperature synchrotron data, to be an ordered stoichiometric material (section 3.3.3). Decomposition of the sample was not observed up to a temperature of 350 °C (significantly higher than the usual decomposition point of $LiNH_2$), and a first order transition in lattice parameters was observed at 295 °C. The $LiND_2$ studied was formed from the reaction of Li_3N with ND_3, and was known to be a Li-rich disordered material (section 3.5.1). This sample did not undergo a first order transition in lattice parameters, but decomposed to form Li_2ND at 325 °C.

The differences observed in the behaviour of $LiNH_2$ and $LiND_2$ were attributed to the degree of disorder in the starting materials, and as such, the first order structural transition observed in $LiNH_2$ was concluded to be an order-disorder transition. This conclusion was supported by the increased disorder observed in the Li^+ sub-lattice of the hydrogenated sample after the transition.

Combined intelligent gravimetric analysis with neutron diffraction (IGA^n) studies also indicated that the disorder of Li – N – D materials influenced their D_2-sorption properties.

D_2-absorption on an ordered sample of Li_2ND + LiD was accompanied by a sharp decrease of the Li_2ND unit cell parameter prior to the formation of $LiND_2$, however, such a contraction was not observed in samples containing ball milled (disordered) Li_2ND.

The presence of a unit cell contraction during D_2-absorption on un-milled Li_2ND, and the absence of such a contraction during similar reactions using milled Li_2ND, suggested that the observed contraction was the result of an order-disorder transition in Li_2ND. After this transition, transformation of the cubic imide structure into the tetragonal amide structure did not appear to vary between the milled and un-milled samples.

The effect of defect concentration on the sorption properties of the Li – N – D system was also studied using the IGA^n apparatus. Sample A (ball milled LiD and Li_2ND), was synthesised to have a higher concentration of lattice defects than Sample B (ground LiD with milled LiD and Li_2ND) and was therefore expected to demonstrate a faster variation in the scale factors of the constituent phases, due to improved gas diffusion through the sample. Rietveld analysis[15] of the neutron diffraction data collected during D_2 cycling of the sample indicated that this was not the case, and that the scale factors of the phases present in Sample B varied at a slightly faster rate than those of Sample A.

The length-range of the LiD *a*-parameter, and the rate at which it varied during D_2-sorption were also expected to differ between Samples A and B, however, no variation was observed experimentally. This may have been due to the resolution of the diffraction data collected, as milled LiD could not be distinguished from ground LiD within the resolution of the data.

In conclusion, the order-disorder transitions observed in this work may play a significant role in the hydrogen sorption reactions of $LiNH_2$ and Li_2NH. Negating these transitions through increasing the disorder of the materials may lead to lower decomposition temperatures, more facile kinetics and improved reversibility of the Li – N – H hydrogen storage system.

3.8 Suggestions for Further Work

The results presented in this chapter imply that disorder in Li-N-H(D) materials has an important effect on the crystallographic processes occurring during their hydrogen sorption reactions. Ball milling of $LiNH_2$ with LiH has been shown to reduce the decomposition temperature of the system, improve the kinetics and greatly reduce the release of ammonia.[4, 21] These occurrences were attributed to the more intimate mixing of the amide and hydride materials and the enhanced diffusion of gas through the sample. The current work however, implies that ball milling $LiNH_2$ (which increases the disorder of the material) may also negate a structural transition, and thus reduce the decomposition temperature of the material.

Further study of $LiNH_2$ and $LiND_2$ are necessary in order to confirm this hypothesis, particularly regarding how the sample history controls the material's disorder, and how the disorder affects the decomposition process.

Suggested paths for further research include variable temperature synchrotron diffraction studies of two samples of $LiNH_2$, one purchased from Aldrich and ball milled, and the second synthesised from $Li_3N + H_2$. The comparison of the data from such studies with that presented in section 3.4.1 would indicate whether a structural transition is observed in both ordered and disordered $LiNH_2$ prior to decomposition, and any difference between the temperatures at which the materials transform into Li_2NH could be determined. If the results of these studies prove favourable, and disorder in $LiNH_2$ does result in lower-temperature $LiNH_2$ decomposition, without an observed structural transition, combined thermogravimetric analysis and neutron diffraction studies of ordered and disordered samples of $LiND_2$ + LiD could then be performed using the IGA^n apparatus.

This work has also reported an order-disorder transition in ordered Li_2ND prior to deuteration, which is absent in ball milled samples. Few investigations have been carried out previously to study the effect that ball milling has upon the hydrogen sorption properties of lithium imide. In light of the data presented in this work, it is suggested that research into this area may yield useful results. If the re-hydrogenation reaction of ordered lithium imide could be quenched prior to, during and after the structural change, valuable crystallographic data of the transformation process would be obtained.

In addition, valuable kinetic and thermodynamic information for the Li – N – H system could be gained through the isothermal study of H_2 and NH_3 sorption in $LiNH_2$, Li_2NH and Li_3N. If such reactions were performed at a number of temperatures using the IGA apparatus, the rates of the absorption and desorption reactions could be monitored as a function of temperature, and the activation energies of the sorption processes at each temperature could be calculated using the Avrami relation.[22] Isothermal intelligent gravimetric analysis could also be used in conjunction with neutron diffraction to study the isothermal D_2 and ND_3 sorption processes of the Li – N – D system. Such studies would allow determination of the rates and activation energies of crystallographic phase changes, through the consideration of the rate of variation of the refined scale factors and the construction of Avrami plots.[22]

3.9 References

1. P. Chen, Z. T. Xiong, J. Z. Luo, J. Y. Lin and K. L. Tan, *Nature*, 2002, **420**, 302-304.
2. P. Chen, Z. T. Xiong, J. Z. Luo, J. Y. Lin and K. L. Tan, *Journal of Physical Chemistry B*, 2003, **107**, 10967-10970.
3. T. Ichikawa, N. Hanada, S. Isobe, H. Leng and H. Fujji, *Journal of Physical Chemistry B*, 2004, **108**, 7887 - 7892.
4. T. Ichikawa, S. Isobe, N. Hanada and H. Fujii, *Journal of Alloys and Compounds*, 2004, **365**, 271-276.
5. S. Isobe, T. Ichikawa and H. Fujii, *Journal of the Japan Institute of Metals*, 2006, **70**, 865-869.
6. K. Miwa, N. Ohba, S. Towata, Y. Nakamori and S. Orimo, *Physical Review B*, 2005, **71**, 1-6.
7. T. Noritake, H. Nozaki, M. Aoki, S. Towata, G. Kitahara, Y. Nakamori and S. Orimo, *Journal of Alloys and Compounds*, 2005, **393**, 264-268.
8. M. P. Balogh, C. Y. Jones, J. F. Herbst, J. L. G. Hector and M. Kundrat, *Journal of Alloys and Compounds*, 2006, **420**, 326-336.
9. J. B. Yang, X. D. Zhou, Q. Cai, W. J. James and W. B. Yelon, *Applied Physics Letters*, 2006, **88**.
10. W. I. F. David, M. O. Jones, D. H. Gregory, C. M. Jewell, S. R. Johnson, A. Walton and P. P. Edwards, *Journal of the American Chemical Society*, 2007, **129**, 1594 – 1601
11. F. E. Pinkerton, *Journal of Alloys and Compounds*, 2005, **400**, 76 - 82.
12. R. Juza and K. Opp, *Zeitschrift fur Anorganische und Allgemeine Chemie*, 1951, **226**, 313 - 324.
13. Y. H. Hu and E. Ruckenstein, *Journal of Physical Chemistry A*, 2003, **107**, 9737-9739.
14. S. Isobe, T. Ichikawa, S. Hino and H. Fujii, *Journal of Physical Chemistry B*, 2005, **109**, 14855-14858.
15. H. M. Rietveld, *Journal of Applied Crystallography*, 1969, 65-71.
16. A. Coelho, *TOPAS, General Profile and Structure Analysis Software for Powder Diffraction Data, version 4.0, Bruker AXS, Karlsruhe, Germany, 2004; http://members.optusnet.com.au/_alancoelho*, 1992-2004.
17. H. Jacobs and R. Juza, *Zeitschrift fur Anorganische und Allgemeine Chemie*, 1972, **391**, 271-&.
18. P. W. Stephens, *Journal of Applied Crystallography*, 1999, **32**, 281-289.
19. M. O. Jones, W. I. F. David, S. R. Johnson, M. Sommariva, R. M. Ibberson and P. P. Edwards, *In preparation*, 2009.
20. J. B. Yang, X. D. Zhou, Q. Cai, W. J. James and W. B. Yelon, *Applied Physics Letters*, 2006, **88**, 3.
21. T. Markmaitree, R. M. Ren and L. L. Shaw, *Journal of Physical Chemistry B*, 2006, **110**, 20710-20718.
22. S. Tanaka, J. D. Clewley and T. B. Flanagan, *The Journal of Physical Chemistry*, 1977, **81**, 1684-1688.

~ Chapter Four ~

The Synthesis and Structural Characterisation of the Mixed Li/Na Amides

4.1 Introduction and Scope of Chapter

The previous chapter was concerned with the crystallographic changes occurring within the Li – N – H system during decomposition and re-hydrogenation.

A number of studies[1-11] have been focused on the improvement of the hydrogen sorption properties of this system through the reaction of $LiNH_2$ with other metal amides and hydrides. These studies have resulted in the formation of a number of mixed Li – M – N – H systems,[1-11] with particular focus given to the Li – Mg – N – H system (section 1.8.5).[1-9]

The mixed Li / Na amides, $Li_5Na(NH_2)_6$, $Li_3Na(NH_2)_3$ and $LiNa_2(NH_2)_3$,[10] have potential hydrogen storage capacities of 7.9, 7.5 and 6.0 wt% respectively, however, little is known about their behaviour during decomposition.

The following chapter presents a synthetic, crystallographic and thermogravimetric study of the mixed Li / Na amides. Firstly, the $LiNH_2$ / $NaNH_2$ and Li_2NH / $NaNH_2$ phase spaces are explored using synchrotron X-ray powder diffraction. This is followed by an in-depth study of high-purity samples of the mixed Li / Na amide phases, with particular regard to the crystal structures and decomposition behaviour of the materials. Finally, the hydrogen storage potential of these materials is discussed.

4.2 The Synthesis of the Li / Na Amides.

The mixed Li / Na amides were first synthesised by Jacobs and Harbrecht *via* the condensation of supercritical ammonia over a mixture of Li and Na metals (section 1.9).[10]

Rather than using ammonia directly, this work explores the potential of forming the mixed Li / Na amides *via* a solid state route. Two systems were investigated, involving the reaction of sodium amide ($NaNH_2$) with both the start and end-points of the $LiNH_2$ / Li_2NH system.

In order to investigate the phase space between $LiNH_2$ and $NaNH_2$, solid state reactions were performed using mixtures of $(LiNH_2)_x(NaNH_2)_{(1-x)}$ where $x = m/12$, $m = 0,1,2\ldots12$. Intervals of 1/12 were chosen between compositional steps in order to include stoichiometric ratios of 5:1, 3:1, and 1:2 $LiNH_2$: $NaNH_2$, thus potentially allowing the formation of pure samples of $Li_5Na(NH_2)_6$, $Li_3Na(NH_2)_4$ and $LiNa_2(NH_2)_3$.

The reactants were intimately ground under an Ar atmosphere and placed into quartz tubes, which were evacuated and sealed (according to the method outlined in section 2.5.3.1). The tubes were heated in a muffle furnace at a rate of 1 °C/min to the reaction temperature, which was maintained for 12 hours.

A reaction temperature of 200 °C was chosen, as it was deemed low enough to ensure minimal $LiNH_2$ decomposition, and yet high enough to encourage cation migration within the material. This temperature also approaches the melting point of $NaNH_2$ (210 °C), therefore also promoting high mobility of the Na cations.

The phase space between Li_2NH and $NaNH_2$ was investigated through the solid state reaction of $(Li_2NH)_x(NaNH_2)_{(1-x)}$ mixtures ($x = m/12$, $m = 0,1,2\ldots12$). These reactions were performed in sealed evacuated tubes in an identical fashion to those of the $(LiNH_2)_x(NaNH_2)_{(1-x)}$ system. The Li_2NH used was prepared *via* the reaction of $LiNH_2$ with LiH under flowing Ar at 400 °C, as outlined in Section 2.6.4.3.

The starting materials and products from both sets of reactions were thoroughly ground and examined by Synchroton X-ray diffraction at the European Synchrotron Radiation Facility (ESRF, section 2.1.2.3). For synchrotron studies, the powders were packed under inert atmosphere into silica glass capillary tubes, which were then sealed and mounted onto the sample changing robot (section 2.1.2.3). Diffraction data were collected using the ID31 beamline with wavelength, $\lambda = 0.8015$ and step size 0.003°. Rietveld analysis of the data[11] was performed using the TOPAS Academic software suite (section 2.1.4.).[12]

4.3 Crystallographic Study of the Starting Materials

4.3.1 $LiNH_2$

The $LiNH_2$ used in these reactions was the same batch as that outlined in section 3.3.3. Rietveld analysis[11] of the diffraction data (section 2.1.4) indicated that the majority phase present in the material was $LiNH_2$ (95 mass%) with impurity Li_2O (5 mass%). The lattice parameters, atomic positions and thermal parameters for the phase have been summarised in Table 3.1.

4.3.2 Li_2NH

The Li_2NH used during these reactions was shown by Rietveld analysis of synchrotron diffraction data to be majority phase Li_2NH (95.4 wt%) with impurity phase Li_2O (4.6 mass%). The unit cell parameters, atomic positions and thermal parameters for the Li_2NH sample were shown to be in good agreement with those reported in literature and summarised in section 1.4.2.

4.3.3 $NaNH_2$

Rietveld analysis[11] (section 2.1.4) of the data collected during the synchrotron diffraction study of $NaNH_2$ (Aldrich, 90%) was performed using TOPAS Academic[12] according to the method outlined in section 2.1.4.1.

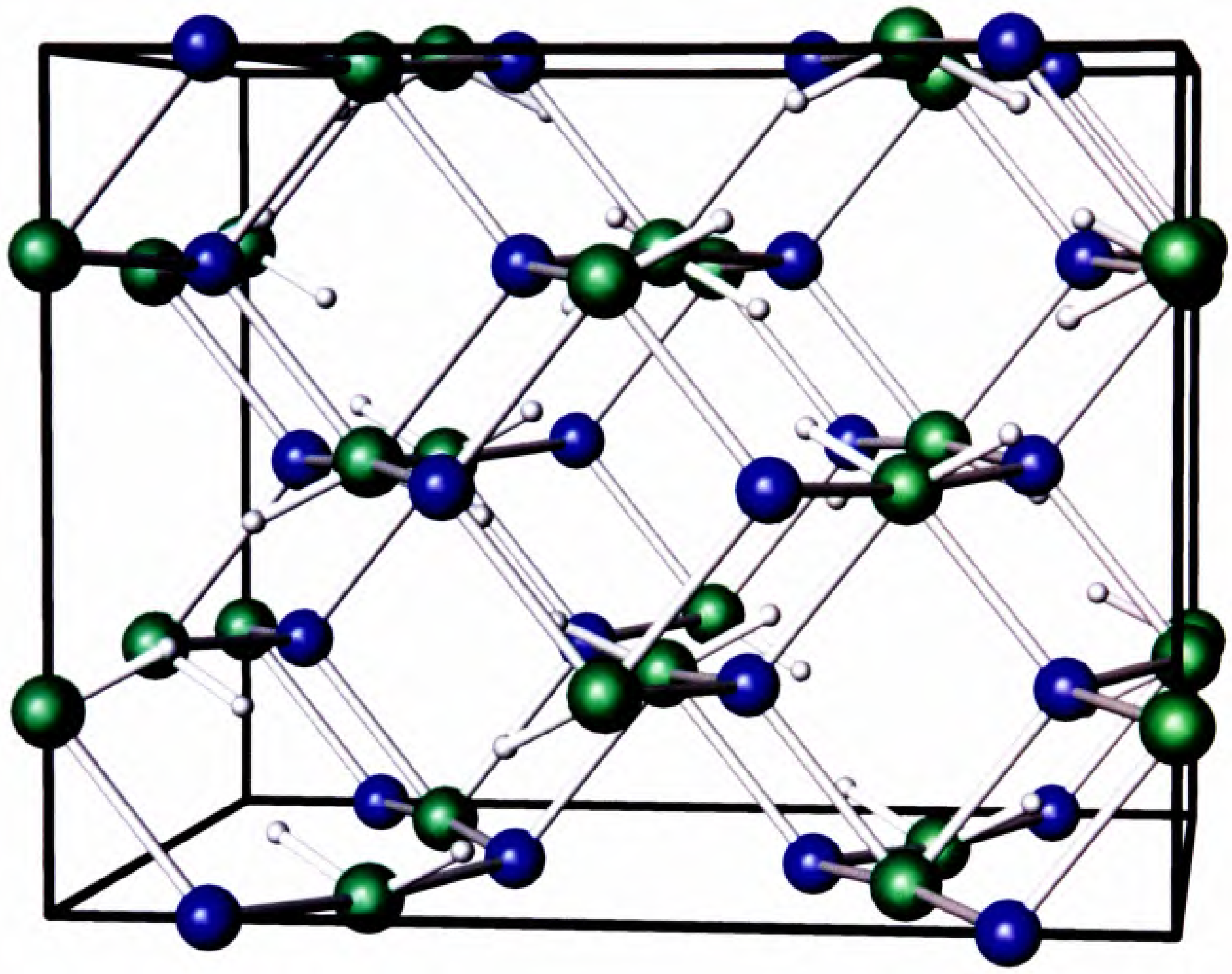

Figure 4.1 : Schematic diagram of the crystal structure of $NaNH_2$. Sodium is represented by blue spheres, nitrogen by green spheres and hydrogen by white spheres.

A schematic representation of the crystal structure of this phase is presented in Figure 4.1 and a summary of the lattice parameters, atomic positions and thermal parameters is presented in Table 4.1.

$NaNH_2$

Atom	Site	x	y	z	Occupancy
Na	16f	0	0.14447(7)	0	0.905(3)
N	16g	0.0	0.0	0.23528(1)	1
H	32h	0.063	0.903	0.305	1

a =8.96056(2) Å, b = 10.455680(2) Å, c = 8.07383(2) Å

Table 4.1: Summary of refined structural parameters for $NaNH_2$ (space group *Fddd*, number 70)

This refinement indicated that the sample was majority phase $NaNH_2$ (99.45 mass%) with NaOH impurity. The material was shown to adopt the *Fddd* space group with lattice parameters a = 8.96056(2) Å, b = 10.45568(2) Å and c = 8.07383(2) Å, with Na located at the 16f (0,y,0) sites, N at 16g (0,0,z) sites and H at the 32h (x,y,z) sites.

The diffraction data and the structural model calculated *via* Rietveld refinement[11] are presented in Appendix A2.

4.4 Study of the Lithium Amide / Sodium Amide System

A typical synchrotron pattern (x = 0.667) for the products of the $(LiNH_2)_x(NaNH_2)_{(1-x)}$ phase space is presented in Figure 4.2. The diffraction data and refined models for the other values of x are presented in Appendix A2.

Rietveld analysis[11] (section 2.1.4) of the diffraction data for each value of x was performed using TOPAS Academic fitting software[12] according to the general method outlined in section 2.1.4.1.

This analysis indicated that the predominant phases present across the $(LiNH_2)_x(NaNH_2)_{(1-x)}$ phase space were un-reacted $LiNH_2$ and $NaNH_2$ together with Li_2O and two new phases, phase A and phase B.

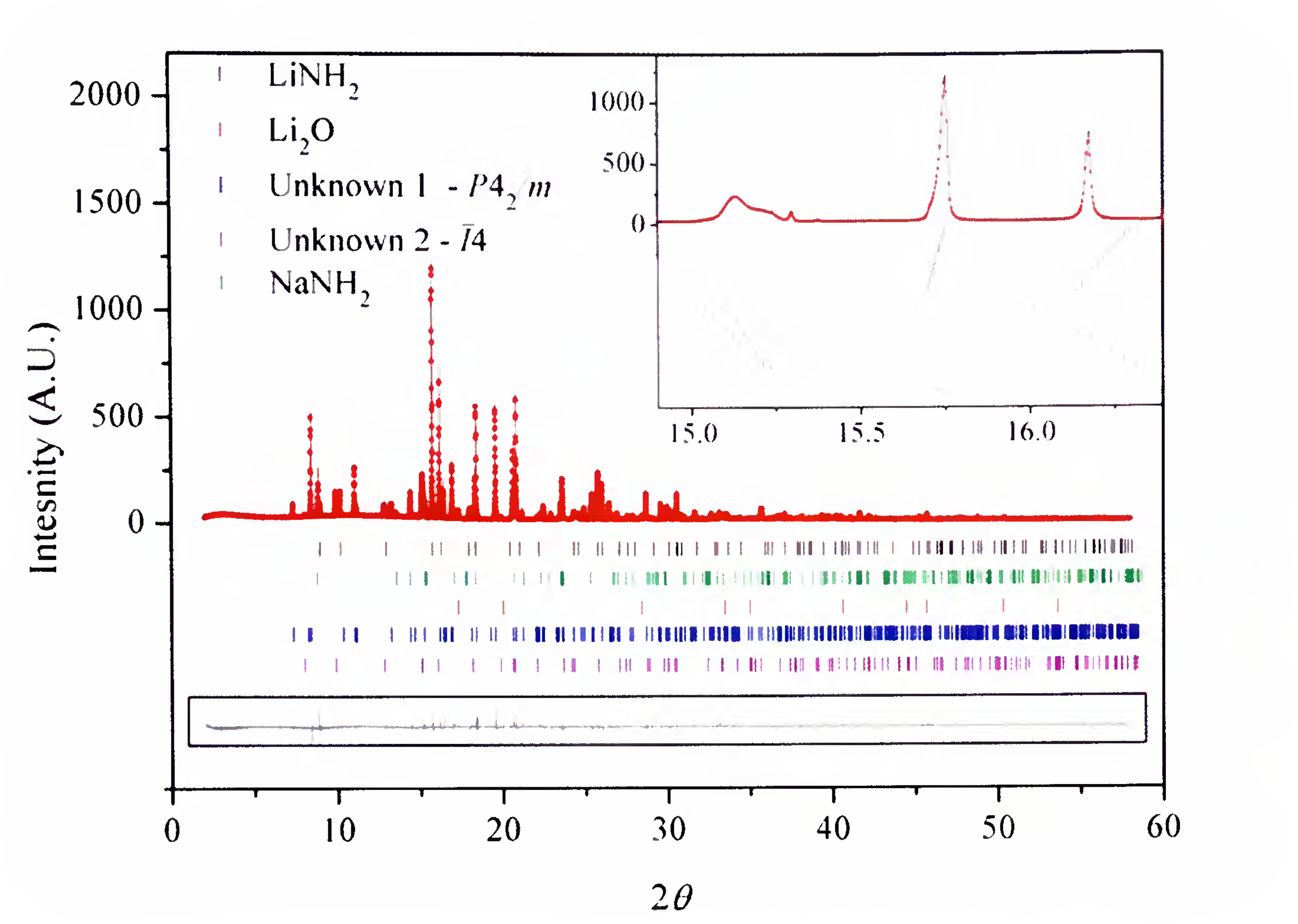

Figure 4.2 : Observed (solid line), calculated (red dots), and difference plots (y_{obsd} - y_{calc}, solid line in box) for the structure refinement of a sample of $(LiNH_2)_x$ $(NaNH_2)_{1-x}$ for x = 0.667 from synchrotron diffraction data, collected at λ = 0.8015 Å with step size of 0.003 Å. The Bragg peak positions for $LiNH_2$, Li_2O, $NaNH_2$ and two unknown phases (space groups $P4_2/m$ and I-4) are shown by the vertical tick marks. R_{wp} 9.860, R_{exp} 5.803, goodness of fit 1.699. Insert: Expansion of 2θ region of 14.9-16.4, highlighting asymmetry in the diffraction peaks of $LiNH_2$ and $Li_3Na(NH_2)_4$

4.4.1 Characterisation and Crystal Structure Solution of the Product Phases.

Phase A was indexed to the $P4_2/m$ space group (number 84) with unit cell parameters $a = b$ = 6.2838 (1) Å and c = 11.1485 (2) Å. Phase B was indexed to the $I\bar{4}$ space group (number 82) with parameters $a = b$ = 5.081 (1) Å and c = 11.511 (5) Å.[13]

The lattice parameters calculated for phase A are very similar to those reported by Jacobs and Harbrecht for $LiNa_2(NH_2)_3$ (a = 6.278(2)Å and c = 11.142(4)Å).[10] Although Jacobs and Harbrecht were able to index their diffraction data (and hence calculate the lattice parameters of this material and assign its space group), the quality of their data did not allow for a complete crystal structural solution.

Rietveld analysis[11] of the diffraction data collected from the samples studied here was undertaken utilizing the $P4_2/m$ space group and the lattice parameters identified by cell indexing. The atomic positions from the structure of $K_2Li(NH_2)_3$ were taken as a starting model,[14] whereby Na ions were located at the 4i (½,0,*z*), 2a (0,0,0) and 2f (½,½,¼) lattice sites, Li at the 4j (*x*,*y*,0) site, and N at the 8k (*x*,*y*,*z*) and 4j (*x*,*y*,0) sites, and the hydrogen atoms were confined to the surface of a sphere of fixed radius from the nitrogen atoms. Having refined the zero-point error, background profile, lattice parameters and scale factor of Phase A, the atomic positions for the Na, Li and N atoms were refined, followed by the atomic thermal parameters and preferred orientation of the phase.

A schematic diagram of the calculated $LiNa_2(NH_2)_3$ crystal structure is presented in Figure 4.3 and the corresponding refined structural parameters for the phase are listed in Table 4.2.[13]

The lattice parameters calculated for phase B, a = 5.081(1)Å, c = 11.511(5)Å, are very similar to those reported previously for $Li_3Na(NH_2)_4$ (a = 5.072(4)Å, c = 11.478(5)Å).[10] Rietveld refinement[11] of this phase was undertaken using the crystal structure suggested by Jacobs as a starting model,[10] with Li ions located at the 2a (0,0,0) and 4f (0,½,*z*) lattice sites, Na ions at the 2c (0,½,¼) site and N and H ions in three distinct 8g (*x*,*y*,*z*) sites.

A schematic diagram of the structure of $Li_3Na(NH_2)_4$ obtained from this refinement is shown in Figure 4.4, together with a representation of $LiNH_2$ for comparison. The corresponding lattice parameters, atomic positions and thermal factors calculated from these refinements are listed in Table 4.3.[13]

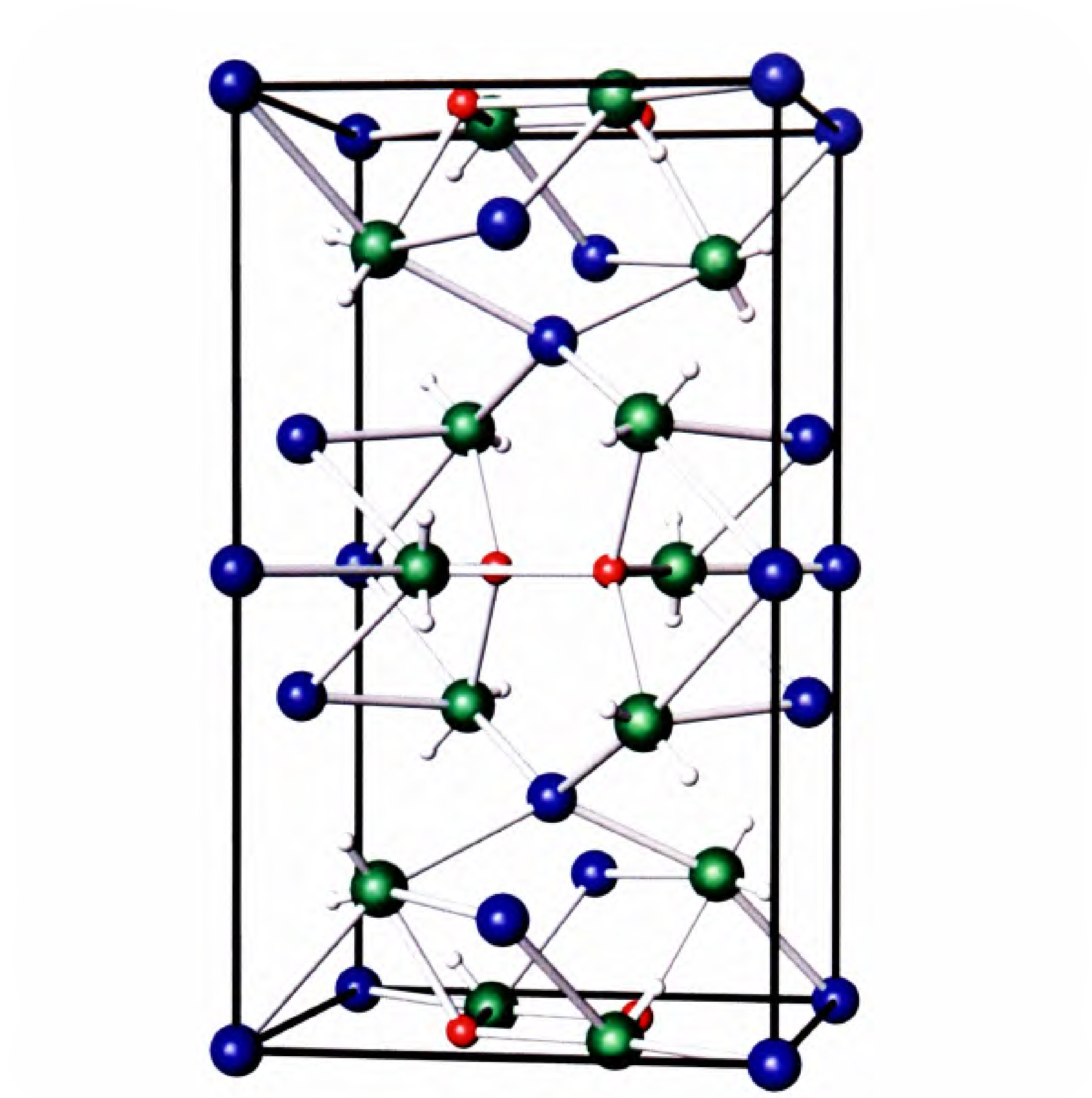

Figure 4.3 : Schematic diagram of the crystal structure of $LiNa_2(NH_2)_3$, calculated from Rietveld analysis of synchrotron X-ray diffraction data. Lithium is represented by red spheres, sodium by blue spheres, nitrogen by green spheres and hydrogen by white spheres.

$LiNa_2(NH_2)_3$

Atom	Site	x	y	z	Occupancy	B_{iso} (Å^2)
Na1	4i	0.50	0.0	0.1421(2)	1	2.0
Na2	2a	0.0	0.0	0.0	1	2.0
Na3	2f	0.50	0.50	0.25	1	2.0
Li1	4j	0.3535(2)	0.3609(3)	0.0	1	2.0
N1	4j	0.6631(9)	0.2759(8)	0.0	1	2.0
N2	8k	0.2073(6)	0.2733(6)	0.1576(5)	1	2.0
H1	8k	0.7369(9)	0.2982(8)	0.056	1	2.0
H2	8k	0.1636(9)	0.1811(8)	0.2118(5)	1	2.0
H3	8k	0.1036(9)	0.3231(8)	0.1412(5)	1	2.0

a = 6.28327(3) Å, c = 11.14844(9) Å

Table 4.2 : Summary of refined structural parameters for $LiNa_2(NH_2)_3$ (space group $P4_2/m$, number 84) formed from the solid state reaction of $LiNH_2$ with $NaNH_2$ in sealed evacuated tubes.

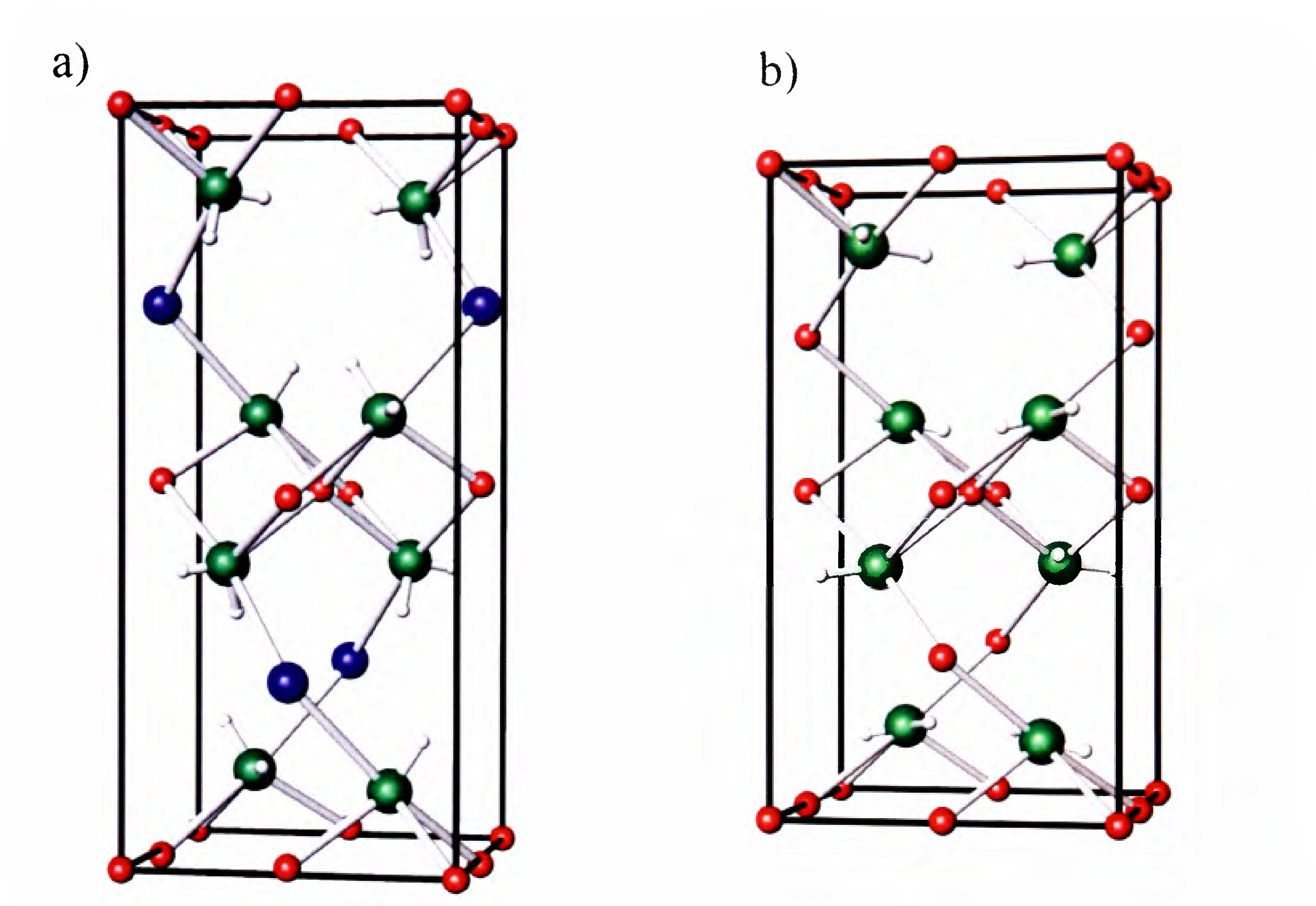

Figure 4.4 : Schematic diagram of the crystal structure of a) $Li_3Na(NH_2)_4$, calculated from Rietveld analysis of synchrotron X-ray diffraction data and b) $LiNH_2$. Li is represented by red spheres, sodium by blue spheres, nitrogen by green spheres and hydrogen by white spheres

$Li_3Na(NH_2)_4$

Atom	Site	x	y	z	Occupancy	B_{iso} (Å^2)
Na1	2c	0.0	0.50	0.25	oNa_n	2.0
Li1	2c	0.0	0.50	0.25	1-oNa_n	2.0
Li2	2a	0.0	0.0	0.0	1	2.0
Li3	4f	0.0	0.5	0.0087	1	2.0
N1	8g	0.2390(7)	0.2390(9)	z_N	1	2.0
H1	8g	0.365	0.29	0.11	1	2.0
H2	8g	0.233	0.139	0.168	1	2.0

a = 5.081(1) Å, c = 11.511(5) Å

Table 4.3 : Summary of refined structural parameters for $Li_3Na(NH_2)_4$ (space group $I\bar{4}$, number 82) formed from the solid state reaction of $LiNH_2$ with $NaNH_2$ in sealed evacuated tubes

Comparison of the unit cells of $LiNH_2$ and $Li_3Na(NH_2)_4$ shows that the structures of the materials are very much alike. In addition to sharing the $I\bar{4}$ space group, the lattice parameters and unit cell volumes of $LiNH_2$ and $Li_3Na(NH_2)_4$ are also similar, as outlined in Table 4.4.

	Space Group	Number formula units per unit cell	a (Å)	c (Å)	V (Å^3)
$LiNH_2$	$I\bar{4}$	8	5.0344 (2)	10.2555(5)	259.931
$Li_3Na(NH_2)_4$	$I\bar{4}$	2	5.081(1)	11.511(5)	297.1(7)

Table 4.4 : Comparison of $LiNH_2$ and $Li_3Na(NH_2)_4$ unit cells.

This similarity arises because $Li_3Na(NH_2)_4$ is an ordered variant of $LiNH_2$ with ¼ of the Li^+ sites occupied by Na^+ ions in an ordered fashion.

Three tetrahedral coordination environments exist for the Li^+ ions in $LiNH_2$, with Li – N bond distances of 2.0779(2) Å, 2.0933(2) Å and 2.1919(3) Å at the 2a (0,0,0), 4f (1,½,z) and 2c (0,½,¼) sites, respectively. The substitution of a large Na^+ ion for a smaller Li^+ ion will be most favourable at the largest lattice site, and Na is therefore observed at the 2c site of $Li_3Na(NH_2)_4$.

Substitution of Na for Li at the 2c sites of $LiNH_2$ results in a unit cell expansion of 1.2555(5) Å along the *c*-axis. This expansion is accompanied by an increase in the length of the 2c metal – nitrogen bond from 2.1919(3) Å in $LiNH_2$ up to 2.4945(3) Å in $Li_3Na(NH_2)_4$ (*cf* Na – N bond length of 2.44 Å in $NaNH_2$).[15]

A small expansion of 0.047 (2) Å is also observed in the *a* and *b*-axes upon transformation of $LiNH_2$ into $Li_3Na(NH_2)_4$. The *a*-axis expansion is much smaller than the *c*-axis expansion due to the fully occupied nature of the 2a / 4f layer, which requires the coordination spheres for the Li^+ ions at the 2a and 4f sites to remain virtually the same upon transformation from $LiNH_2$ into $Li_3Na(NH_2)_4$.

Interestingly, no $Li_5Na(NH_2)_6$ was observed across the entire compositional range of the $(LiNH_2)_x(NaNH_2)_{(1-x)}$ system, implying that this material cannot be formed under these reaction conditions. Given that $Li_5Na(NH_2)_6$ was also indexed to the $I\bar{4}$ space group,[10] it is plausible that the crystal structure of this material would be similar to that of $Li_3Na(NH_2)_4$, with alternating layers of Li and Na at the 2c sites.

4.4.2 Peak Symmetry and Material Stoichiometry

Closer inspection of the diffraction profiles of the $(LiNH_2)_x(NaNH_2)_{(1-x)}$ samples reveals that the Bragg reflections of $Li_3Na(NH_2)_4$ and $LiNH_2$ exhibit significant 2θ dependent asymmetry. This is not the case for the Bragg reflections from $LiNa_2(NH_2)_3$ and $NaNH_2$, which appear to be highly symmetrical (insert of Figure 4.2).

Peak asymmetry of this type is characteristic of compositional non-stoichiometry, which in $LiNH_2$ and $Li_3Na(NH_2)_4$, originates from variations in the Li and Na occupancies of the 2c (0,½,¼) lattice sites. As such, the $Li_3Na(NH_2)_4$ and $LiNH_2$ observed after the reaction of $LiNH_2$ with $NaNH_2$ can be better described as $Li_{3+y}Na_{1-y}(NH_2)_4$ and $Li_{1-z}Na_zNH_2$, respectively.

$Li_{3+y}Na_{1-y}(NH_2)_4$ with $y < 0$ were not observed as such materials would require Na substitution at the 2a or 4f lattice sites, which would be highly unfavourable due to the small size of these sites and the lack of a clear migration pathway. As such the limiting values of $y = 0$ and $z = 0$ can be regarded as the two end-compositions of a solid solution of $NaNH_2$ in $LiNH_2$.[13]

The peak asymmetry of $Li_{3+y}Na_{1-y}(NH_2)_4$, was modelled using eleven uniformly varying phases of varying y (y_n, $0 \leq n \leq 10$). The value of y_n was calculated using the fractional Na occupancy of the 2c (0,½,¼) site and the site multiplicity (which is 2 for the 2c site). The sodium occupancy of this site, s, was calculated using $s_n = 0.1[(10-n)\ s_0 + n\ s_{10}]$, with the values of s_0 and s_{10} obtained by refinement to be 0.938(7) and 0.79(2), respectively. The total occupancy of the 2c site was set at 1 and so the Li occupancy of the site, t_n, was set equal to $1-s_n$. The Li-occupancy of the 2a (0,0,0) and 4f (0,½,z) sites were fixed at 1.

A linear variation of lattice parameter with n was assumed, according to Vegard's law, such that $a_n = 0.1[(10-n)\ a_0 + n\ a_{10}]$ and $c_n = 0.1[(10-n)\ c_0 + n\ c_{10}]$, with the limits of a and c determined by refinement to be $a_0 = 5.08280(4)$ Å, $a_{10} = 5.0700(2)$ Å, $c_0 = 11.5415(2)$ Å and $c_{10} = 11.2562(9)$ Å. A variation in the z-coordinate of the nitrogen (z_N) with composition was also observed, which was modelled as $z\_N_n = 0.1[(10-n)\ z\_N_0 + n\ z\_N_{10}]$ with values of $z\_N_0 = 0.0997(2)$ and $z\_N_{10} = 0.1014(7)$ obtained by refinement. These data, together with the refined 2c site occupancy and phase stoichiometry for $Li_{3+y}Na_{1-y}(NH_2)_4$ phases are summarised in Table 4.5.

n	Stoichiometric formula	Na occupancy of 2c site (s_n)	z_N_n	2c M-N bond length	a (Å)	c (Å)
0	$Li_{3.062(7)}Na_{0.938(7)}(NH_2)_4$	0.938(7)	0.0997(2)	2.4992(3)	5.08280(4)	11.5415(2)
1	$Li_{3.077(8)}Na_{0.923(8)}(NH_2)_4$	0.923(8)	0.0998(3)	2.4945(3)	5.08152(6)	11.5130(3)
2	$Li_{3.09(1)}Na_{0.91(1)}(NH_2)_4$	0.91(10)	0.1000(3)	2.4899(3)	5.08024(7)	11.4844(3)
3	$Li_{3.11(1)}Na_{0.89(1)}(NH_2)_4$	0.89(11)	0.1002(4)	2.4853(3)	5.07896(9)	11.4559(4)
4	$Li_{3.12(1)}Na_{0.88(1)}(NH_2)_4$	0.88(12)	0.1003(4)	2.4808(4)	5.0777(1)	11.4274(5)
5	$Li_{3.13(1)}Na_{0.87(1)}(NH_2)_4$	0.87(13)	0.1005(5)	2.4762(4)	5.0764(1)	11.3988(6)
6	$Li_{3.15(1)}Na_{0.85(1)}(NH_2)_4$	0.85(14)	0.1007(5)	2.4716(4)	5.0751(1)	11.3703(6)
7	$Li_{3.17(2)}Na_{0.83(2)}(NH_2)_4$	0.83(16)	0.1008(6)	2.4671(5)	5.0738(2)	11.3418(7)
8	$Li_{3.18(2)}Na_{0.82(2)}(NH_2)_4$	0.82(17)	0.1010(6)	2.4625(5)	5.0726(2)	11.3132(8)
9	$Li_{3.19(2)}Na_{0.81(2)}(NH_2)_4$	0.81(19)	0.1012(7)	2.4580(6)	5.0713(2)	11.2847(8)
10	$Li_{3.21(2)}Na_{0.79(2)}(NH_2)_4$	0.79(2)	0.1014(7)	2.4535(4)	5.0700(2)	11.2562(9)

Table 4.5 : Summary of the refined formulae, Na 2c (0,½,¼) site occupancies, nitrogen z-coordinates, 2c metal-nitrogen bond lengths and lattice parameters of the eleven modelled phases of $Li_{3+y}Na_{1-y}(NH_2)_4$

The average metal – N bond distance for the 2c sites was observed to decrease with the sodium site occupancy, which is a clear consequence of the larger ionic radius of Na (1.02 Å) compared to Li (0.76 Å). The average metal-nitrogen bond distance at the 2c lattice site varied in length from 2.4992(3) – 2.4535 (4) Å, but always remained considerably larger than the 2a Li – N and 4f Li – N bond distances (mean bond distance 2.062 (4)Å).

The asymmetry observed in the Bragg reflections of $Li_{1-z}Na_zNH_2$ was modelled in a similar fashion to that described for $Li_3Na(NH_2)_4$. Values of z_n ($0 \leq n \leq 10$) were calculated from the site occupancies and multiplicities of the Li lattice sites, where the Li occupancy of the 2a (0,0,0) and 4f (0,½,¼) sites was set to 1 and the Li-occupancy of the 2c (0,½,¼) site, p_n, was modelled using $p_n = 0.1[(10\text{-}n)\, p_0 + n\, p_{10}]$. p_0 and p_{10} were determined by refinement to be 0.99(10) and 0.92(4), respectively. The total occupancy of the site was set to 1, and hence the sodium occupancy of the site, q_n was calculated as $1\text{-}p_n$.

The lattice parameters of the various $Li_{1-z}Na_zNH_2$ phases were calculated as outlined for $Li_{3+y}Na_{1-y}(NH_2)_4$, using $a_n = 0.1[(10\text{-}n)\, a_0 + n\, a_{10}]$ and $c_n = 0.1[(10\text{-}n)\, c_0 + n\, c_{10}]$, with values $a_0 = 5.03701(3)$ Å, $a_{10} = 5.04195(6)$ Å, $c_0 = 10.25577(3)$ Å and $c_{10} = 10.3311(2)$ Å determined by refinement. The observed variation of the nitrogen z-coordinate was sufficiently small that the inclusion of a refineable nitrogen-z parameter was not necessary in the model.

The refined crystallographic parameters, site occupancies and stoichiometries for the eleven modelled $Li_{1-z}Na_zNH_2$ phases are summarised in Table 4.6.

n	Stoichiometric formula	Li occupancy of 2c site (p_n)	a (Å)	c (Å)
0	$Li_{0.9967(3)}Na_{0.0027(3)}NH_2$	0.987(3)	5.03701(3)	10.25577(3)
1	$Li_{0.996(1)}Na_{0.004(1)}NH_2$	0.983(4)	5.03750(2)	10.26342(5)
2	$Li_{0.995(1)}Na_{0.005(1)}NH_2$	0.979(5)	5.03800(2)	10.27106(6)
3	$Li_{0.994(1)}Na_{0.006(1)}NH_2$	0.975(6)	5.03849(3)	10.27871(8)
4	$Li_{0.993(1)}Na_{0.007(1)}NH_2$	0.972(7)	5.03899(3)	10.28635(9)
5	$Li_{0.992(1)}Na_{0.008(1)}NH_2$	0.968(8)	5.03948(4)	10.2940(1)
6	$Li_{0.991(2)}Na_{0.009(2)}NH_2$	0.964(9)	5.03997(4)	10.3016(1)
7	$Li_{0.990(2)}Na_{0.010(2)}NH_2$	0.96(1)	5.04047(5)	10.3093(1)
8	$Li_{0.989(2)}Na_{0.011(2)}NH_2$	0.96(1)	5.04096(5)	10.3169(2)
9	$Li_{0.988(2)}Na_{0.012(2)}NH_2$	0.95(1)	5.04146(6)	10.3246(2)
10	$Li_{0.987(3)}Na_{0.013(3)}NH_2$	0.95(1)	5.04195(6)	10.3311(2)

Table 4.6: Summary of the refined formulae, Li 2c (0,½,¼) site occupancies, and lattice parameters of the eleven modelled phases of $Li_{1-z}Na_zNH_2$

No asymmetry was observed in the Bragg reflections of $LiNa_2(NH_2)_3$ or $NaNH_2$, which suggests that both materials were present as line-phases (insert of Figure 4.2).

The presence of non-stoichiometry in $Li_{3+y}Na_{1-y}(NH_2)_4$ and $Li_{1-z}Na_zNH_2$, and its absence in $LiNa_2(NH_2)_3$ and $NaNH_2$ was attributed to the crystal structures of the materials.

As outlined in section 4.4.1 the crystal structures of $LiNH_2$ and $Li_3Na(NH_2)_4$ are extremely similar, with $LiNH_2$ transforming into $Li_3Na(NH_2)_4$ upon substitution of Na for Li at the 2c (0,½,¼) lattice sites. The 2c sites are the largest Li-sites in $LiNH_2$ and increase further in size as the unit cell expands along the *c*-axis.

The unit cells of both $Li_3Na(NH_2)_4$ and $LiNH_2$ contain a slightly distorted cubic close-packed nitrogen sub-lattice, reminiscent of that in anti-fluorite Li_2NH. As such, at elevated temperatures, both $LiNH_2$ and $Li_3Na(NH_2)_4$ are expected to exhibit cation mobility between the close-packed anion layers. At high temperatures, this cation mobility should result in facile Li^+ / Na^+ ion interchange at the large 2c (0,½,¼) lattice sites. A decrease in temperature would cause a significant reduction of ionic exchange, causing the compositions of the $Li_{3+y}Na_{1-y}(NH_2)_4$ and $Li_{1-z}Na_zNH_2$ phases to become fixed, and forming the observed continuum of non-stoichiometric $Li_3Na(NH_2)_4$ and $LiNH_2$ phases.

The space group adopted by $LiNa_2(NH_2)_3$ is the primitive tetragonal $P4_2/m$ group (number 84). The presence of a screw axis indicates that the anionic sub-lattice of $LiNa_2(NH_2)_3$ is vastly distorted from ideal cubic close packing, resulting in very low ionic mobility, and hence fixed stoichiometry.

Non-stoichiometry in $LiNa_2(NH_2)_3$ is further discouraged by the very dissimilar sizes of the Li and Na lattice sites. The Na^+ cations occupy the tetrahedral 2f (½,½,¼) and the octahedral 2a (0, 0, 0) and 4i (½, 0, z) sites, with Na-N bond-lengths measured at 2.5435(1) Å and 2.5222(1) Å - 2.9503(1) Å, respectively. These bond distances are comparable to the Na – N distances observed in $NaNH_2$ (2.44 Å - 2.49 Å).[16] The Li^+ cations occupy the tetrahedral 4j (x,y,0) sites, displaying much smaller Li – N distances of 2.0172(1) Å – 2.28379(1) Å, which are more comparable with the Li – N bond lengths observed in $LiNH_2$ (2.0779 Å, 2.0933 Å and 2.1919 Å).[17]

As such, the Na^+ lattice sites in $LiNa_2(NH_2)_3$ are too large to accommodate the small Li^+ cations, and equally, the Li^+ lattice sites in $LiNa_2(NH_2)_3$ are too small to accommodate a larger Na^+ cation. Expansion of the layered $I\bar{4}$ $LiNH_2$ and $Li_3Na(NH_2)_4$ structures along the *c*-axis increased the size of the 2c lattice site without altering the sizes of the other lattice sites. A large Na or a small Li could, therefore, both be accommodated at the 2c site with relative ease. Expansion or contraction of the $LiNa_2(NH_2)_3$ unit cell would be highly unfavourable, as such changes would disrupt the sizes of other lattice sites in the crystal structure. Cross occupation of the metal sites in $LiNa_2(NH_2)_3$ was therefore not possible, and this phase was therefore formed purely as a stoichiometric, line phase material.

The ions in $NaNH_2$ are expected to be highly mobile at the reaction temperature, as it is only 10 °C below the material's melting point. Nevertheless, non-stoichiometric $NaNH_2$ was not observed post-reaction due to the incompatibility of the small Li ions with the large Na lattice sites. Post-reaction $NaNH_2$ was, therefore, a single-composition material.

4.4.3 Variation of Product Phase Fractions with x

For the $(LiNH_2)_x(NaNH_2)_{(1-x)}$ phase space (as detailed in section 4.4), the relative molar phase fractions of $LiNH_2$, $NaNH_2$, Li_2O, $Li_3Na(NH_2)_4$ and $LiNa_2(NH_2)_3$ were calculated from refined scale factors for all values of x.[13] It was found that the relative proportions of these phases depended greatly on the value of x (Figure 4.5).

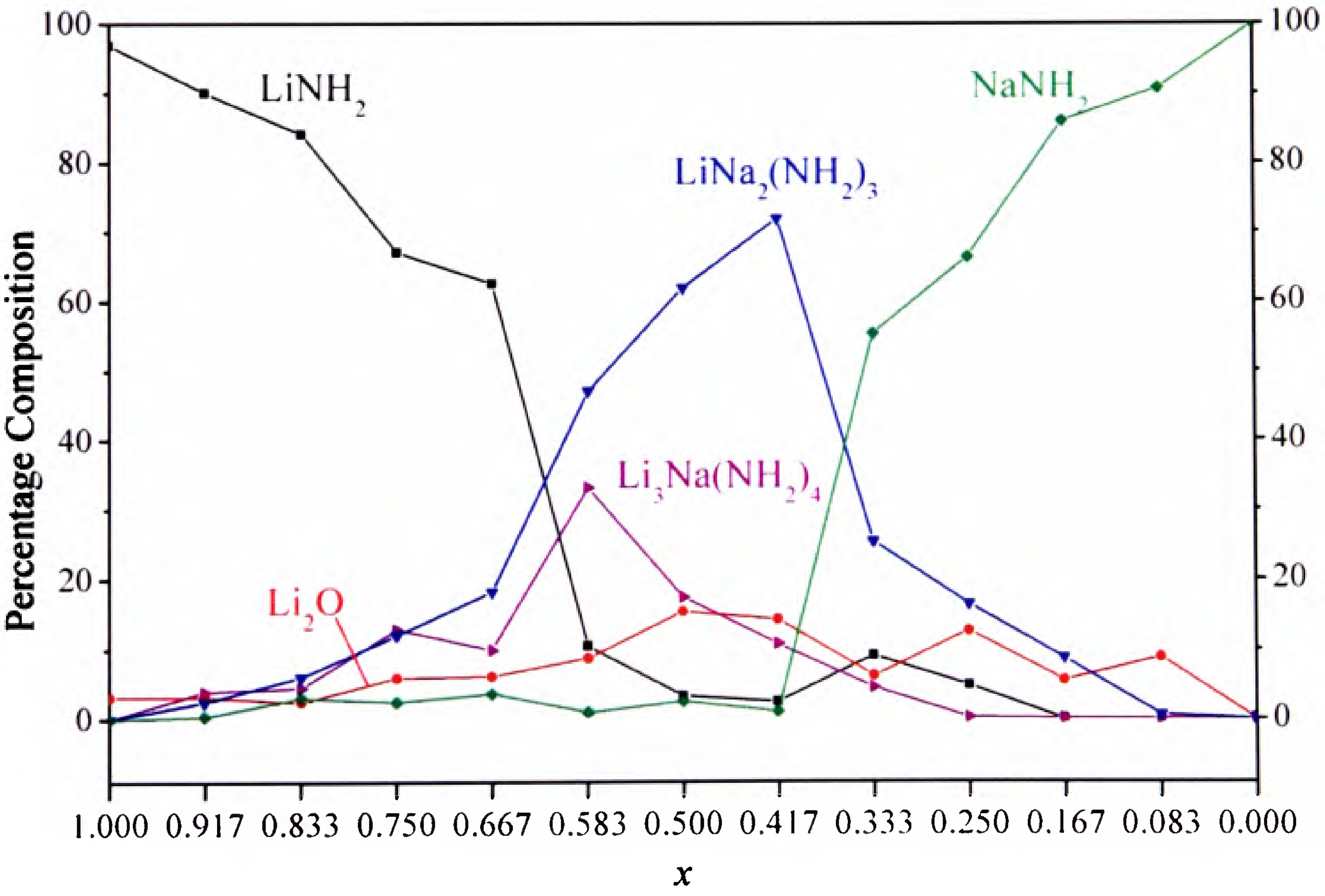

Figure 4.5 : Product phase fractions of the $(LiNH_2)_x(NaNH_2)_{(1-x)}$ system ($0<x<1$), calculated from refined scale factors

Logic would suggest that the major mixed amide phase at high lithium concentrations would be $Li_3Na(NH_2)_4$, and that the major mixed amide phase at high sodium concentrations would be $LiNa_2(NH_2)_3$.

Interestingly, Figure 4.5 highlights that $LiNa_2(NH_2)_3$ was the more favoured of the mixed amide products across the entire compositional range of the $LiNH_2$ / $NaNH_2$ phase space.

This seems odd, given the similarity of the crystal structures of $LiNH_2$ and $Li_3Na(NH_2)_4$, however, the cation disorder evidenced within the $Li_3Na(NH_2)_4$ structure suggests that $Li_3Na(NH_2)_4$ may exist in a reversible equilibrium with $3LiNH_2 + NaNH_2$ at the reaction temperature.

The vacant 2d and 4e lattice sites in $LiNH_2$ and $Li_3Na(NH_2)_4$ provide clear pathways for ionic migration within the structures, meaning that Na and Li ions can easily diffuse both into and out of the 2c lattice sites of $LiNH_2$ and $Li_3Na(NH_2)_4$. Conversely, the $LiNa_2(NH_2)_3$ structure has no such paths for ionic migration, and hence the formation of this phase is believed to be an irreversible process, resulting in the effective trapping of the Na^+ ions. The overall result is an increase in the phase fraction of $LiNa_2(NH_2)_3$, at the expense of $Li_3Na(NH_2)_4$.

Over time, the concentration of free sodium in the reaction mixture decreases due to trapping in $LiNa_2(NH_2)_3$. As such, the chances of finding two sodium ions in close enough contact to form $LiNa_2(NH_2)_3$ becomes very low, and the remaining sodium ions diffuse into (and out of $LiNH_2$), ultimately resulting in the formation of $Li_{3+y}Na_{1-y}(NH_2)_4$ and $Li_{1-z}Na_zNH_2$.

4.4.4 The Effect of Annealing on Product Phase Fractions and Non-Stoichiometry.

A second series of compounds of composition $(LiNH_2)_x(NaNH_2)_{(1-x)}$ $(0 \leq x \leq 1)$ were synthesised as described previously (section 2.6.4.1) and, after re-grinding, underwent an annealing step at 100°C for 12 hours. These reactions were performed with the aim of forming pure samples of $Li_3Na(NH_2)_4$ and $LiNa_2(NH_2)_3$ using compositions x = 0.75 and 0.333, respectively, and reducing the non-stoichiometry exhibited by $Li_3Na(NH_2)_4$ and $LiNH_2$.

Synchrotron X-ray powder diffraction data for these samples were collected using the ID31 diffractometer at the ESRF (section 2.1.2.3) with λ = 0.8015 and step size 0.003°. The data underwent Rietveld analysis[11] using TOPAS Academic[12] according to the methods described in sections 2.1.4.1 and 4.4.2. The calculated molar phase fractions of the products are summarised in Figure 4.6.[13]

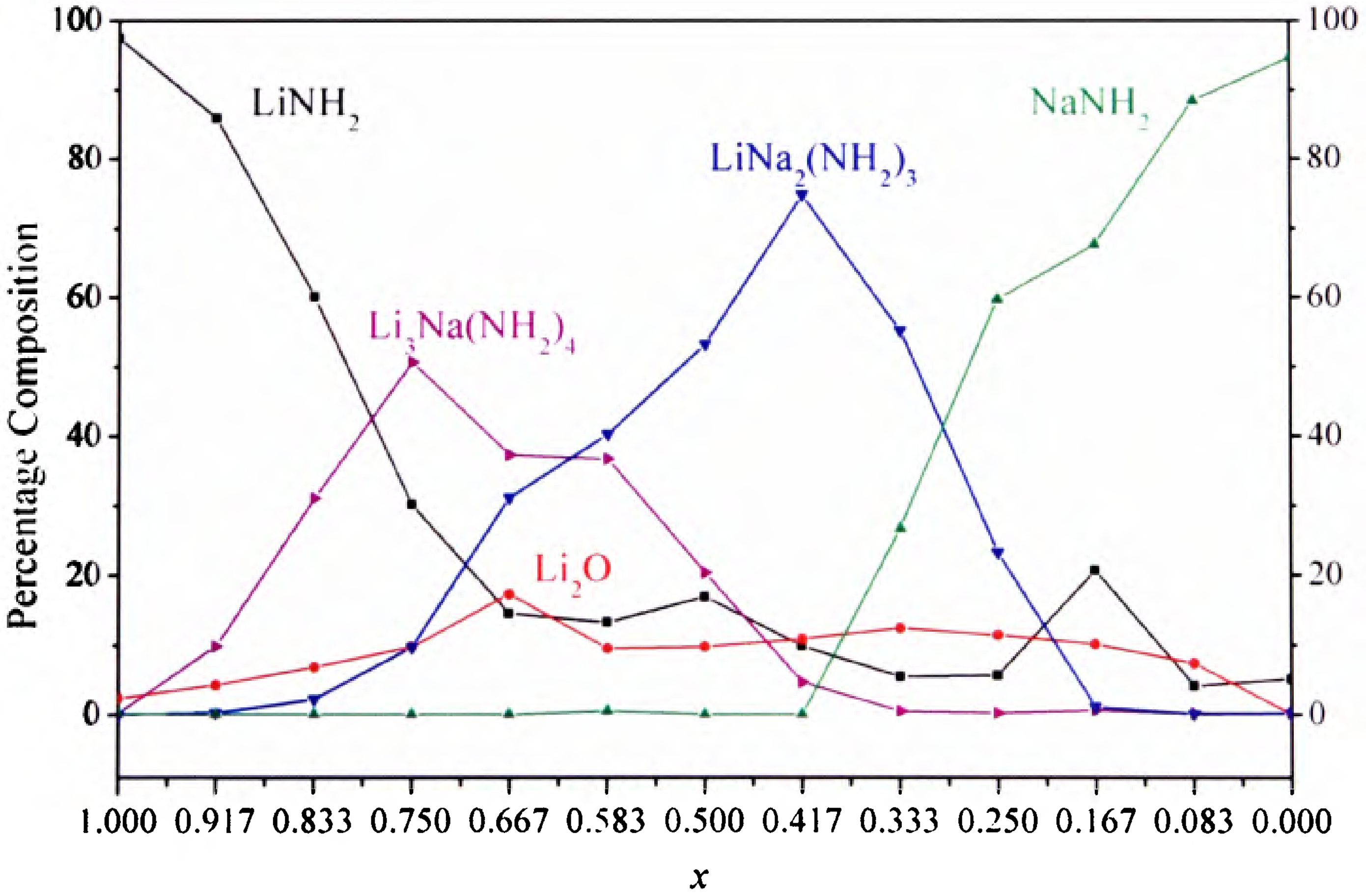

Figure 4.6 : Product phase fractions in the annealed $(LiNH_2)_x(NaNH_2)_{(1-x)}$ system $(0 \leq x \leq 1)$ calculated from refined scale factors

Comparison of the phase fraction data for the original and annealed $LiNH_2$ – $NaNH_2$ systems (Figures 4.5 and 4.6, respectively) suggests that re-grinding and annealing the reaction mixtures reduced the proportion of un-reacted starting materials observed in the products. Indeed, the reaction appeared to have continued until one of the starting materials was entirely used up, and consequentially, the product proportions of both mixed amide phases increased upon annealing. The formation of $Li_3Na(NH_2)_4$ over $LiNa_2(NH_2)_3$ at compositions of high Li-content was also encouraged by the secondary annealing step.[13]

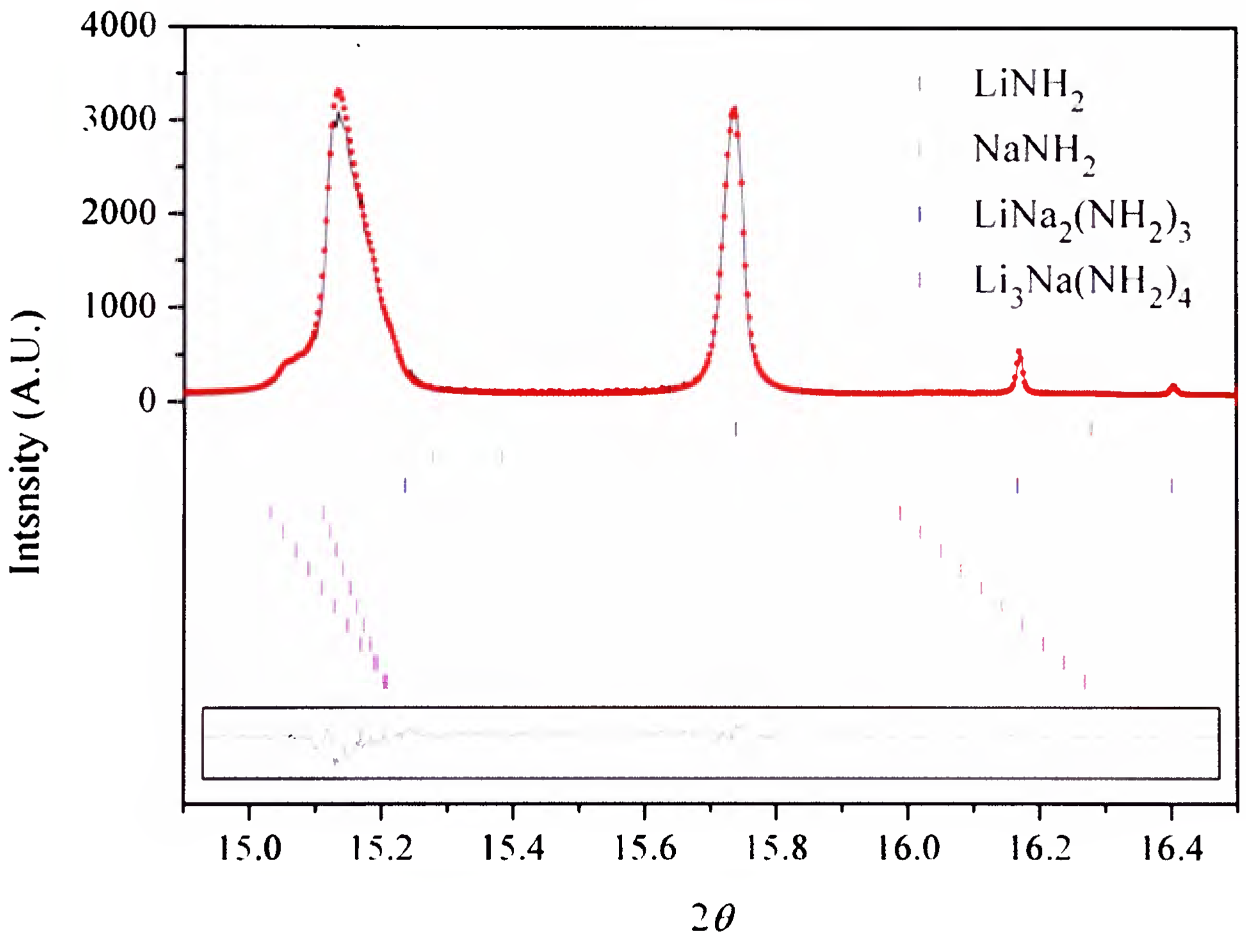

Figure 4.7 : Observed (solid line), calculated (red dots), and difference plots (y_{obsd} - y_{calcd}, solid line in box) for the structure refinement of a sample of annealed $(LiNH_2)_x(NaNH_2)_{(1-x)}$ for $x = 0.833$ from synchrotron X-ray diffraction data, collected at $\lambda = 0.8015$ Å with step size of 0.003 Å. 2θ region of 14.9 – 16.5 ° highlighting the symmetry of the $LiNH_2$ peaks and the asymmetry of the $Li_3Na(NH_2)_4$ peaks, indicative of the presence of stoichiometric and nonstoichiometric materials, respectively. The Bragg peak positions for $LiNH_2$, Li_2O, $LiNa_2(NH_2)_3$ and $Li_{3+y}Na_{1-y}(NH_2)_4$ are shown by the vertical tick marks. R_{wp} 14.061, R_{exp} 9.243, goodness of fit 1.521.

The peak proportions of $Li_3Na(NH_2)_4$ (50 mole%) and $LiNa_2(NH_2)_3$ (78 mole%) were observed at compositions of $x =$ 0.75 and 0.417, respectively, suggesting that different synthetic conditions are required to form high-purity samples of the mixed amide phases.

The 2θ region of 14.9 – 16.5° of the diffraction pattern from the annealed $x =$ 0.833 $(LiNH_2)_x(NaNH_2)_{(1-x)}$ mixture is presented in Figure 4.7 (profiles for other values of x can be found in Appendix A2).

The $LiNH_2$ Bragg reflections observed in this data do not exhibit the peak asymmetry that was observed for the $LiNH_2$ reflections in the un-annealed samples (Figure 4.2). This indicates that annealing $LiNH_2$ / $NaNH_2$ mixtures results in the formation of stoichiometric $LiNH_2$, rather than sodium-doped $LiNH_2$. The $Li_3Na(NH_2)_4$ Bragg reflections observed in the diffraction data of the annealed samples were slightly more asymmetric than those observed for the original samples, suggesting that annealing the reaction mixtures increased non-stoichiometry within $Li_3Na(NH_2)_4$.

4.4.5 An Equilibrium Model for the Formation of $Li_3Na(NH_2)_4$ and $LiNa_2(NH_2)_3$

It can be seen from Figures 4.5 and 4.6 that $Li_3Na(NH_2)_4$ formed most successfully in a lithium-excess environment and that the phase fraction decayed rapidly as a function of lithium concentration. In the annealed system, $Li_3Na(NH_2)_4$ was formed at a higher $LiNH_2$ concentration, and its phase fraction decayed more slowly as a function of x (compared to the un-annealed system). Both of these observations are consistent with an equilibrium and ionic mobility model for the formation of $Li_3Na(NH_2)_4$.

One may therefore describe three regimes within the reactions of $LiNH_2$ and $NaNH_2$; namely, lithium-rich, sodium-rich and intermediate.[13] For lithium-rich compositions one can write:

$$LiNH_2 + xNaNH_2 \longleftrightarrow (1-3x)LiNH_2 + xLi_3Na(NH_2)_4 \qquad \text{Equation 4.1}$$

intermediate compositions;

$$x\,LiNH_2 + y\,NaNH_2 \longleftrightarrow \frac{y}{2}LiNa_2(NH_2)_3 + \frac{x}{3}Li_3Na(NH_2)_4 \qquad \text{Equation 4.2}$$

and sodium-rich compositions;

$$x\,LiNH_2 + NaNH_2 \longleftrightarrow (1-2x)NaNH_2 + xLiNa_2(NH_2)_3 \qquad \text{Equation 4.3}$$

At high $LiNH_2$ concentrations, while the Na^+ (and Li^+) cations would migrate out of the $Li_3Na(NH_2)_4$ structure, the low Na^+ concentrations make the formation of $LiNa_2(NH_2)_3$ unlikely. As the concentration of Na^+ in the reaction mixture increased, so too did the phase fraction of $LiNa_2(NH_2)_3$. The lack of ionic mobility in $LiNa_2(NH_2)_3$ effectively trapped Li^+ and Na^+ cations within its structure, and thus $LiNa_2(NH_2)_3$ dominated the phase fraction in the intermediate region. At high $NaNH_2$ concentrations the formation of $Li_3Na(NH_2)_4$ became unlikely due to the lack of $LiNH_2$; $NaNH_2$ impurities were detected and the phase fraction of $LiNa_2(NH_2)_3$ was observed to decrease with decreasing $LiNH_2$ concentration.

4.5 Study of the Lithium Imide / Sodium Amide System

A series of compounds of composition $(Li_2NH)_{(1-x)}(NaNH_2)_{(x)}$ $(0 \leq x \leq 1)$ were formed in sealed evacuated tubes to investigate the phase space between Li_2NH and $NaNH_2$. The materials formed were studied using synchrotron X-ray powder diffraction using the ID31 beamline at the ESRF (section 2.1.2.3). The diffraction data collected underwent Rietveld analysis[11] using TOPAS Academic,[12] according to the general method outlined in section 2.1.4.1. The diffraction data and refined models for all values of *x* are presented in Appendix A2.

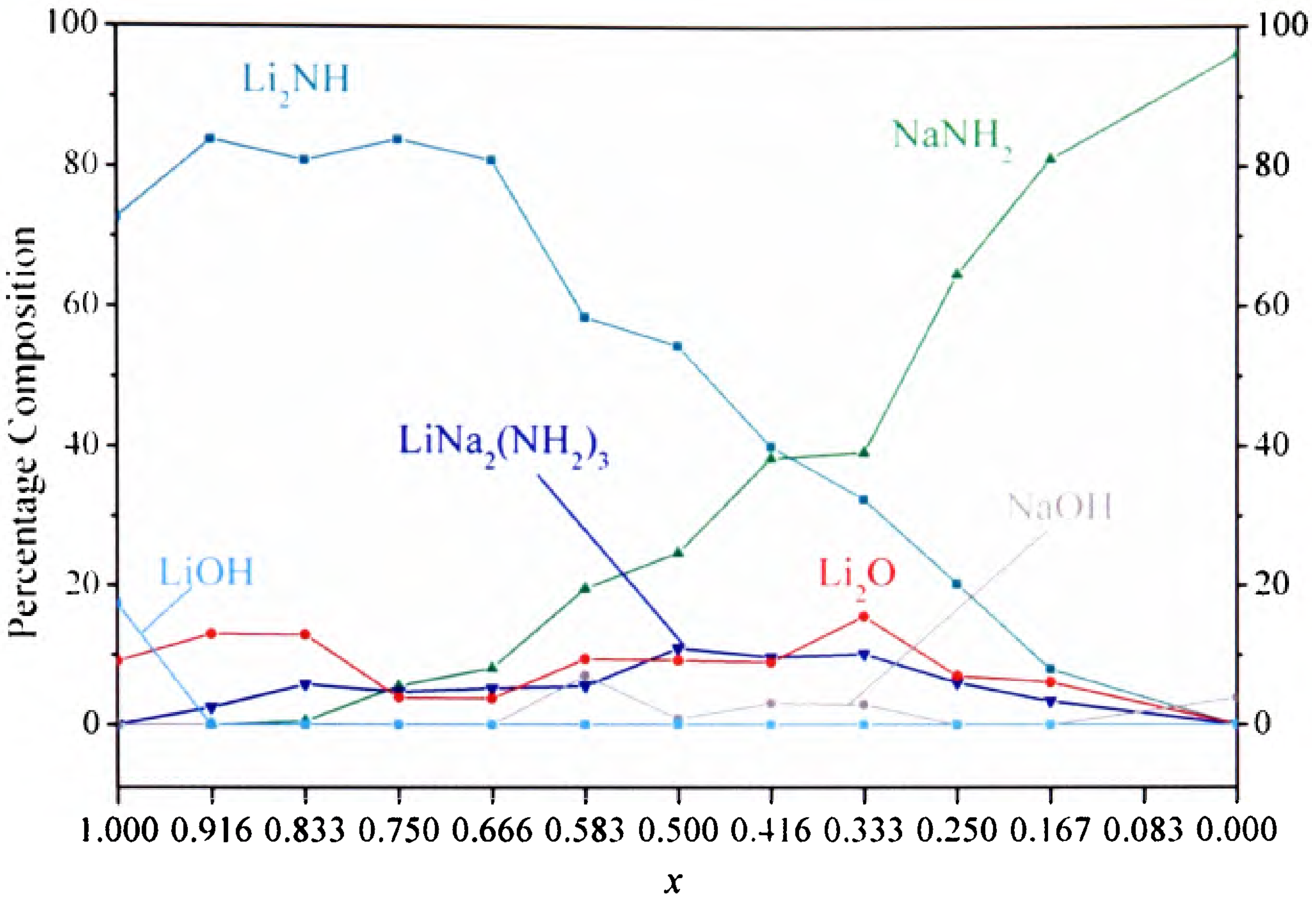

Figure 4.8 : Product phase fractions of the $(Li_2NH)_x$ $(NaNH_2)_{(1-x)}$ system, $(0 \leq x \leq 1)$ calculated from refined scale factors.

Reactions between Li_2NH and $NaNH_2$ in sealed evacuated tubes were shown to result in the formation of mixture of products, with the relative proportions of the product phases varying with *x* (Figure 4.8). In addition to the Bragg reflections corresponding to the un-reacted starting materials, and small amounts of oxide and hydroxide impurities, there were also a number of additional Bragg peaks which were indexed to the sodium-rich mixed amide, $LiNa_2(NH_2)_3$. Interestingly, the lithium-rich phase $Li_3Na(NH_2)_4$ was not observed even though the reaction system was lithium-rich in nature. The lack of $Li_3Na(NH_2)_4$ in the products can be attributed to the different crystal structures of $LiNH_2$ and Li_2NH.

Focusing firstly on the structure of $LiNH_2$, this material is constructed from layers of $[2NH_2^-]$ ions, alternately separated by layers of $[3Li^+]$ (the 2a and 4f sites) and

[1Li$^+$] (the 2c sites), as shown in Figure 4.9a. Substitution of a Li$^+$ by a Na$^+$ occurs at the 2c lattice site not only because this is the largest of the three Li sites in $LiNH_2$ (section 4.4.1), but also because it is the only cation site with a clear pathway for ionic migration (*via* the vacant 2d and 4e sites). Expansion of the $LiNH_2$ unit cell in the *c*-direction is also possible without disrupting the other Li – N bond lengths, and so, the larger Na cation can be easily accommodated within the structure.

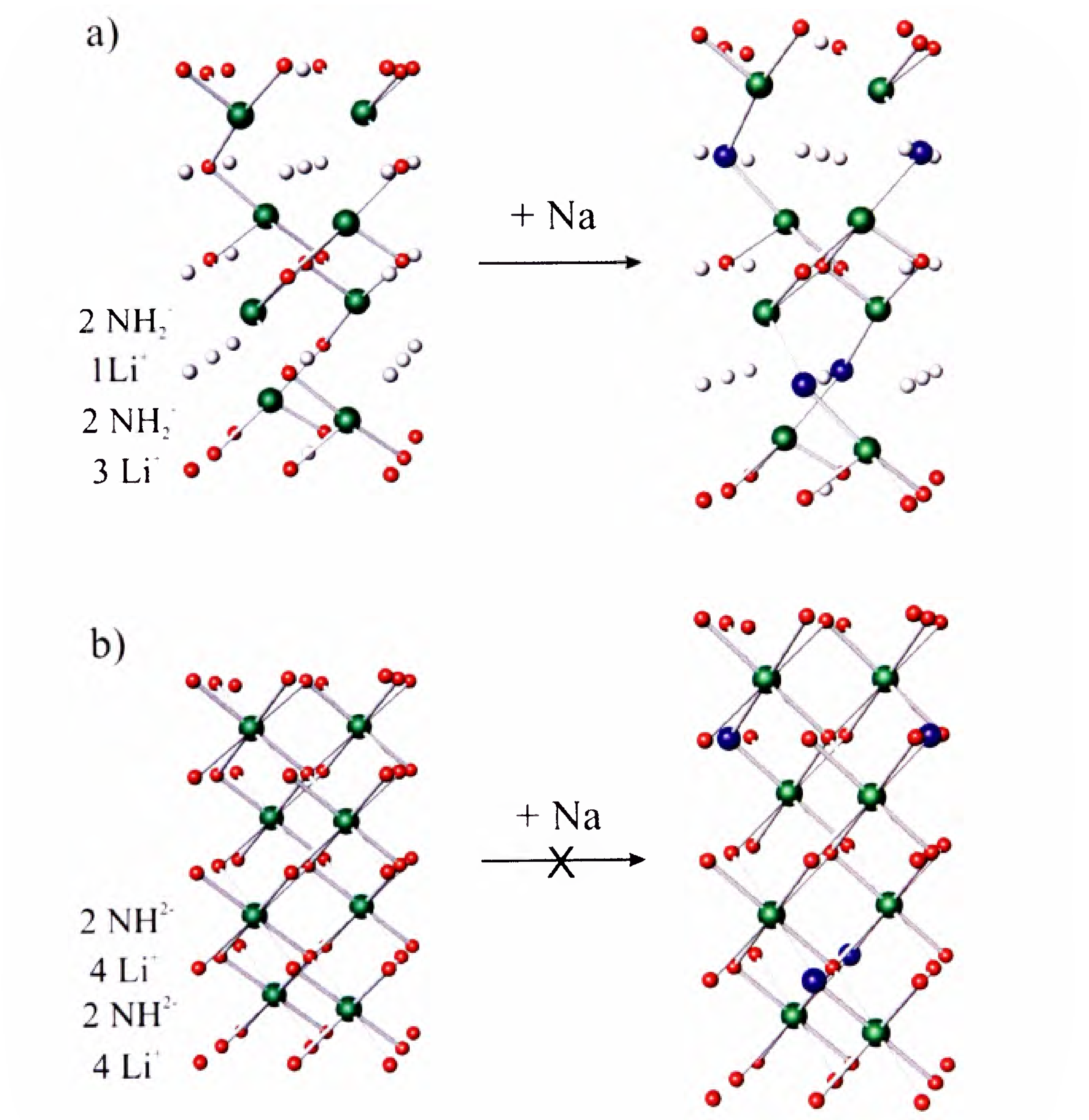

Figure 4.9 : Schematic diagrams of the crystal structures of a) $LiNH_2$ and b) Li_2NH, highlighting the layered nature of the materials and how this influences their behaviour during reaction with Na. Na can migrate into $LiNH_2$ *via* the unoccupied 4e and 2d lattice sites. The unit cell can expand to accommodate the larger Na ion, forming $Li_3Na(NH_2)_4$. This is not possible in Li_2NH. Li is represented by red spheres, Na by blue spheres, N by green spheres, and the vacant 4e and 2d sites by grey spheres.

Li_2NH adopts a structure in which layers of $[2NH^{2-}]$ are separated by layers of $[4Li^+]$ (Figure 4.9b) and in which all cation sites are equivalent and occupied. Expansion of the unit cell upon cation substitution is therefore not possible without disruption of all Li – N bond-lengths in the substituted layer, (Figure 4.9b) which would be a most energetically unfavourable process. Furthermore, due to the Li-occupancy of all of the tetrahedral sites in Li_2NH, no clear paths for migration of Na into the structure exist, and $Li_3Na(NH_2)_4$ is not formed from the reaction of lithium imide with sodium amide.

4.6 Thermogravimetric Study of the Decomposition of $LiNH_2$ and $NaNH_2$.

In order to evaluate the decomposition properties of the mixed Li / Na amides, it was first necessary to study the desorption behaviour of $NaNH_2$ and $LiNH_2$.

Section 3.2.1 presented a study of the decomposition of $LiNH_2$ (95%, Aldrich) using intelligent gravimetric analysis combined with mass spectrometry (IGA-MS). The $LiNH_2$ sample was observed to decompose upon reaching 269 °C, releasing predominantly NH_3 with a small amount of H_2.

The decomposition reaction of $NaNH_2$ (Aldrich, 95%) was also studied using intelligent gravimetric analysis combined with mass spectrometry (section 2.2.1). The sample was heated under a flow of 1 bar He to 280 °C at a rate of 2 $°Cmin^{-1}$ and maintained at this temperature for 35 hours. The dynamic sampling mass spectrometer (section 2.2.1) was set to scan for 17, 2, 28, 23 and 39 atomic mass units (AMU), corresponding to NH_3, H_2, N_2, Na and $NaNH_2$, respectively. Measurements of the sample temperature, pressure, mass and the partial pressures of the evolved gases were taken every 0.2 minutes. The data collected during this experiment are presented in Figures 4.10.

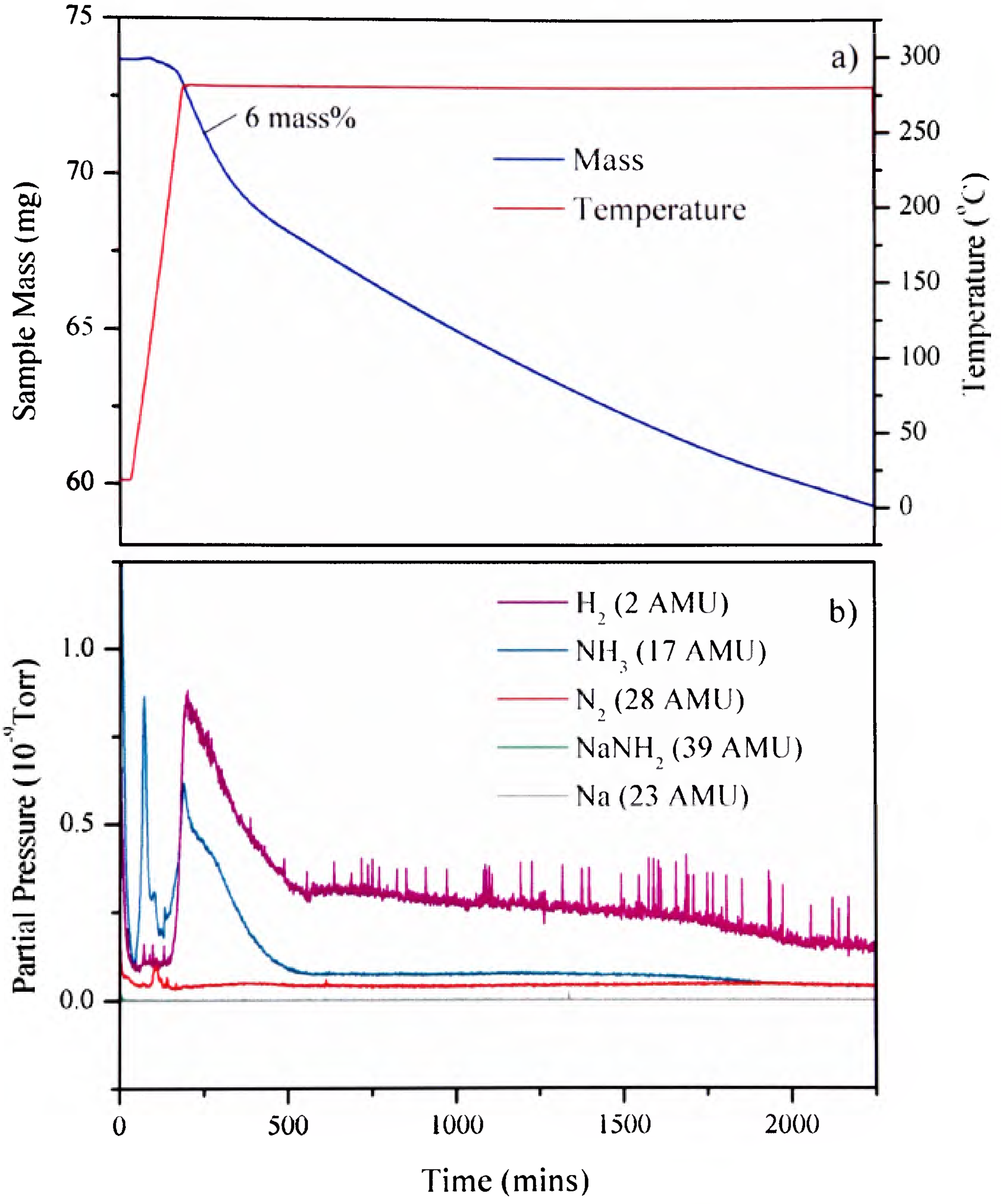

Figure 4.10a and b : a) Thermogravimetric data of $NaNH_2$, collected using intelligent gravimetric analysis with heating rate 2 °C/min and target temperature 280 °C. The red line represents the temperature of the sample and the blue line the sample mass. b) Partial pressures of H_2 (purple line), NH_3 (turquoise line) N_2 (red line), $NaNH_2$ (green line) and Na (grey line), recorded during thermogravimetric study of $NaNH_2$ using *in-situ* mass spectrometry.

The change in gradient of the gravimetric data at ~ 400 mins indicates that $NaNH_2$ decomposition occurred *via* a two-step process. The first step had an onset temperature of 162 °C, accounting for a mass loss of 6 mass% from the sample in 245 mins. The second mass loss began during the isothermal heating at 280 °C and had a much slower rate of 2.4 mass% in 245 mins. This mass loss continued throughout the rest of the study.

Analysis of the partial pressures of the released gases recorded by mass spectrometry (Figure 4.10b) indicated that the first decomposition step occurred primarily with the loss of NH_3 (17 AMU), H_2 (2 AMU) and a minor amount of N_2 (28 AMU). The ratio of gases released during this step (t = 125 - 550 mins) was 3:1 H_2 : NH_3.

Continued heating at 280 °C resulted in release of H_2 at a constant rate, whilst the proportion of NH_3 released tended towards zero and a very broad, shallow peak was observed in the recorded partial pressure of N_2. This indicates that the second decomposition step of the $NaNH_2$ resulted in the release of H_2 and small amounts of N_2 and NH_3.

The thermocouple and pressure inlet in the IGA reaction vessel were discoloured after these measurements, indicating that Na metal may have volatised from the sample during the experiment and condensed within the apparatus. Na is known to have a low vapour pressure (9.3×10^{-3} mbar at 280 °C)[18] and hence evaporation of Na from the sample and condensation within the equipment is not surprising.

The data collected during this study contrasted with the decomposition of $NaNH_2$ reported in the literature, where sodium amide is reported to decompose *via* one of two different pressure-dependent mechanisms at temperatures between 335 and 400

°C.[19, 20] At pressures greater than the dissociation pressure of sodium hydride (NaH), $NaNH_2$ decomposition is reported to occur *via* Equation 4.4:

$$NaNH_2 \rightarrow NaH + \tfrac{1}{2}N_2 + \tfrac{1}{2}H_2 \quad ^{19,20} \qquad \text{Equation 4.4}$$

At pressures lower than the dissociation pressure of NaH, decomposition is reported to occur *via* Equation 4.5:

$$NaNH_2 \rightarrow Na + \tfrac{1}{2}N_2 + H_2 \quad ^{19,20} \qquad \text{Equation 4.5}$$

The negative gradient of the gravimetric data at the end of the experiment indicated that the $NaNH_2$ sample was not fully decomposed. In order to allow decomposition of this sample to reach completion, the sample was reheated to 280 °C in the IGA-MS apparatus under flowing He. The mass of the sample continued to decrease slowly during the second heating step, but decomposition remained incomplete after heating for a further 24 hours at 280 °C. The experiment was not continued beyond this point due to concerns regarding the evaporation of Na into the apparatus

4.7 Study of High – Purity $Li_3Na(NH_2)_4$

High purity $Li_3Na(NH_2)_4$ was formed from the reaction of $LiNH_2$ with $NaNH_2$ in an approximate ratio of 3:1 under flowing Ar gas at 200 °C (section 2.6.4.4).

A number of compositions of $(LiNH_2)_x(NaNH_2)_{(1-x)}$ with $x \sim 0.75$ were studied, with highest purity $Li_3Na(NH_2)_4$ obtained using $x = 0.74$. The deviation from an ideal 3:1 ratio is presumed to occur due to impurities in the starting materials ($LiNH_2$ 95%, $NaNH_2$ 90%).

The sample thus formed was analysed using a variety of techniques, including diffraction, spectroscopy, calorimetry and gravimetric analysis.

4.7.1 Synchrotron Diffraction Study of $Li_3Na(NH_2)_4$

The $Li_3Na(NH_2)_4$ formed from the reaction outlined above was thoroughly ground and packed into a silica glass capillary tube under a N_2 atmosphere. The tube was sealed and mounted on to the ID31 diffractometer at the ESRF (section 2.1.2.3) and diffraction data were collected using a wavelength of 0.7995 Å and step-size 0.003°.

Rietveld analysis[11] (section 2.1.4) of the data was performed using TOPAS Academic,[12] according to the general method outlined in section 2.1.4.1. In addition to the parameters listed in section 2.1.4.1, the nitrogen *z*-coordinate, 2c (0,½,¼) Na / Li site occupancy and preferred orientation were also refined in the $Li_3Na(NH_2)_4$ model. The diffraction data and refined model are presented in Figure 4.11.

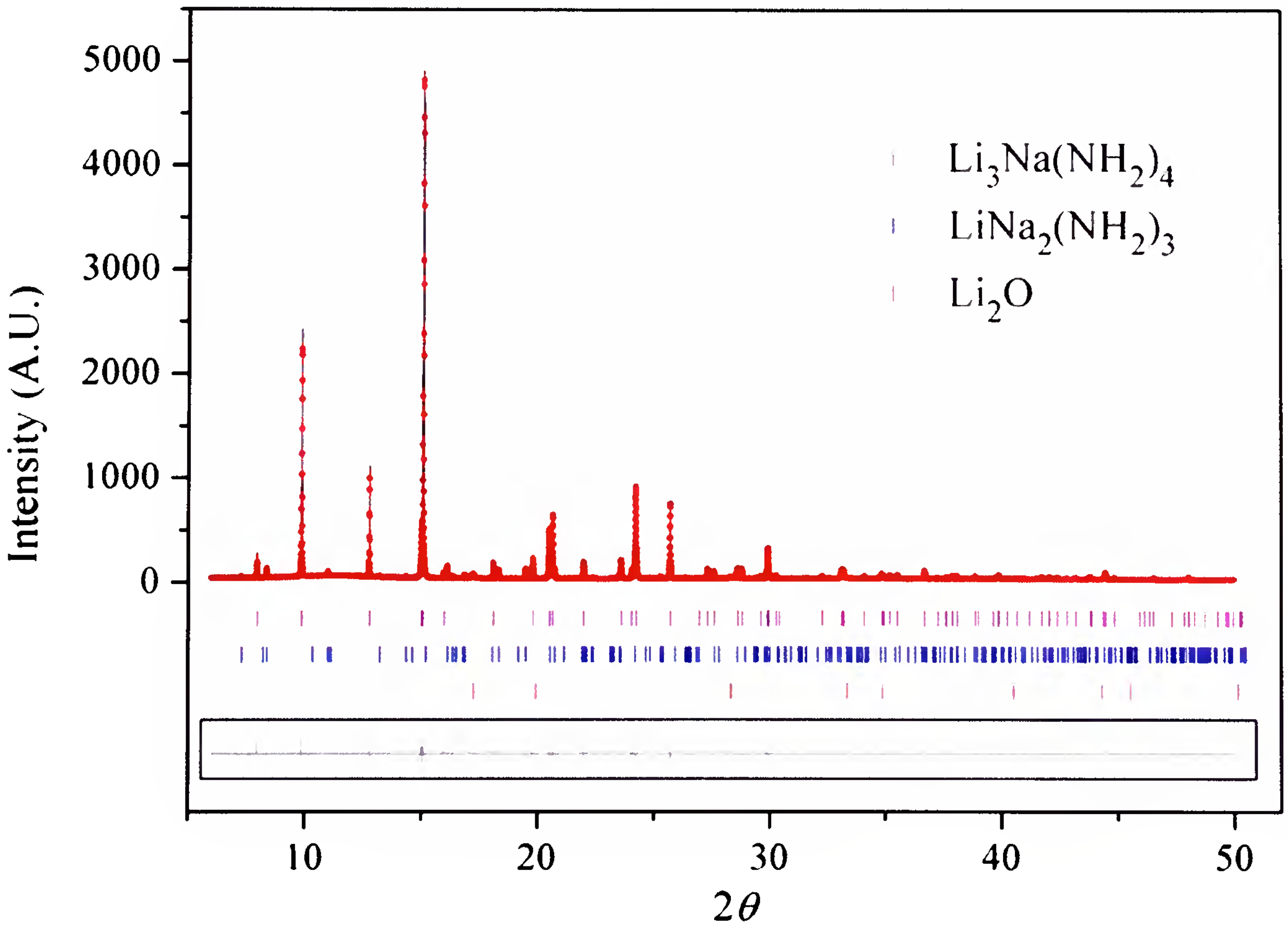

Figure 4.11 : Observed (solid line), calculated (red dots), and difference plots (y_{obsd} - y_{calc}, solid line in box) for the structure refinement of a sample of high-purity $Li_3Na(NH_2)_4$, from synchrotron X-ray diffraction data collected at λ = 0.7995 Å with a step size of 0.003 Å. The Bragg peak positions for $Li_3Na(NH_2)_4$, $LiNa_2(NH_2)_3$ and Li_2O are shown by the vertical tick marks. R_{wp} 7.610, R_{exp} 4.774, goodness of fit 1.594

The sample was shown to be majority phase $Li_3Na(NH_2)_4$ (90 mass%), with impurity phases Li_2O (4 mass%) and $LiNa_2(NH_2)_3$ (6 mass%); no Bragg reflections corresponding to $LiNH_2$ or $NaNH_2$ were observed. Attempts to remove the $LiNa_2(NH_2)_3$ and Li_2O impurities *via* washing the sample using t-butyl amine (section 2.6.4.4) were not successful, and variation of the reaction time from 3 – 60 hours resulted in no significant change in the product phase fractions.

The Bragg reflections of $Li_3Na(NH_2)_4$ from this sample did not exhibit 2θ dependent asymmetry (*cf* section 4.4.2), which suggests that the $Li_3Na(NH_2)_4$ formed under these conditions was of a single composition. Refined site occupancies gave an overall stoichiometry of $Li_{3.120(3)}Na_{0.879(3)}(NH_2)_4$, showing that the material was sodium deficient.

The $Li_3Na(NH_2)_4$ lattice parameters calculated from refinement of the diffraction data were a = 5.08137(2) Å and c = 11.50680(7), which are in very good agreement with those reported by Jacobs and Harbrecht[10] and those identified previously in this report (section 4.4.1).

4.7.2 Neutron Diffraction Study of $Li_3Na(ND_2)_4$

Because hydrogen has a large incoherent neutron scattering cross section (section 2.1.3), neutron diffraction studies required the synthesis of a deuterium enriched sample, $Li_3Na(ND_2)_4$.

$Li_3Na(ND_2)_4$ was synthesised from the reaction of a 3 : 1 mixture of $LiND_2$ (from Li_3N + ND_3, section 2.6.2.1) with $NaND_2$ (from NaH + ND_3, section 2.6.3.1) under flowing Ar at 200°C for 12 hours.' The sample formed was thoroughly ground and loaded into an 8mm diameter vanadium can, and neutron diffraction data from the sample were collected over the course of one hour using the GEneral Materials diffractometer (GEM) at the ISIS pulsed neutron facility (section 2.1.3.1).

The data collected from banks 4 and 5 underwent simultaneous Rietveld analysis[11] (section 2.1.4) using the TOPAS Academic software suite[12] according to the general method outlined in section 2.1.4.1.

The crystal structure of $Li_3Na(NH_2)_4$ generated from the synchrotron studies (section 4.7.1) was used as the starting model for analysis of the neutron diffraction data. In addition to the parameters listed in section 2.1.4.1, the *z*-coordinate of the Li 4f (0,½,*z*) site, the *x*, *y* and *z* coordinates of the 8g (*x*,*y*,z) nitrogen sites and the fractional Na / Li occupancy of the 2c lattice site were also refined in the $Li_3Na(ND_2)_4$ model.

The data collected were of sufficient quality to model the atomic positions of the deuterium atoms within the crystal structure. Calculation of these positions was performed using a rigid rotor model for the ND_2^- ion, which permitted refinement of the deuterium positions, whilst ensuring that the N1 – D1 and N1 – D2 bond lengths remained equal. Using this model, with the N1 as the fixed point of the rotor, the N – D bond length was calculated at 0.949(3) Å and the D1 – N – D2 bond angle was calculated at 96.8(4) ° (*cf* N – D bond length 0.967 Å and 0.978 Å, D – N – D angle 104.0° in $LiND_2$).[21]

The total occupancy of each deuterium site was then set to 1, and the fractional D / H occupancies of these sites were refined in order to estimate the D / H ratio. (A more accurate value of the D / H ratio could be obtained using spectroscopic techniques, however, such studies were not deemed necessary for the level of accuracy required.) The presence of H within the sample is attributed to the use of a hydrogenated starting material (NaH) for the synthesis of the $NaND_2$ precursor material (section 2.6.5.1).

The refined values for the lattice parameters, atomic positions, site occupancies and thermal parameters are presented in Table 4.7 and the neutron diffraction data and refined model are presented in Figure 4.12.

$Li_3Na(ND_2)_4$

Atom	Site	*x*	*y*	*z*	Occupancy	B_{iso} (Å^2)
Na1	2c	0.0	0.50	0.25	0.71(3)	0.1
Li1	2c	0.0	0.50	0.25	0.29(3)	0.518
Li2	2a	0.0	0.0	0.0	1	0.1000
Li3	4f	0.0	0.5	0.008(1)	1	0.1000
N1	8g	0.2360(4)	0.222(3)	0.0988(1)	1	1.9618
D1	8g	0.28562	0.09056	0.15318	0.722(5)	1.9618
H1	8g	0.28562	0.09056	0.15318	0.277	1.9618
D2	8g	0.11826	0.31403	0.14826	0.722(5)	1.9618
H2	8g	0.11826	0.31403	0.14826	0.277	1.9618

a = 5.0829(3) Å, c = 11.514(1) Å

Table 4.7: Refined structural parameters and atomic positions for $Li_3Na(ND_2)_4$ (space group $I\bar{4}$, number 82), calculated from Rietveld analysis of neutron diffraction data. A rigid rotor model was used for the ND_2^- unit, and the N – D bond length and D1 – N1 – D2 bond angle was calculated at 0.949(3) Å and 96.8(4)°, respectively.

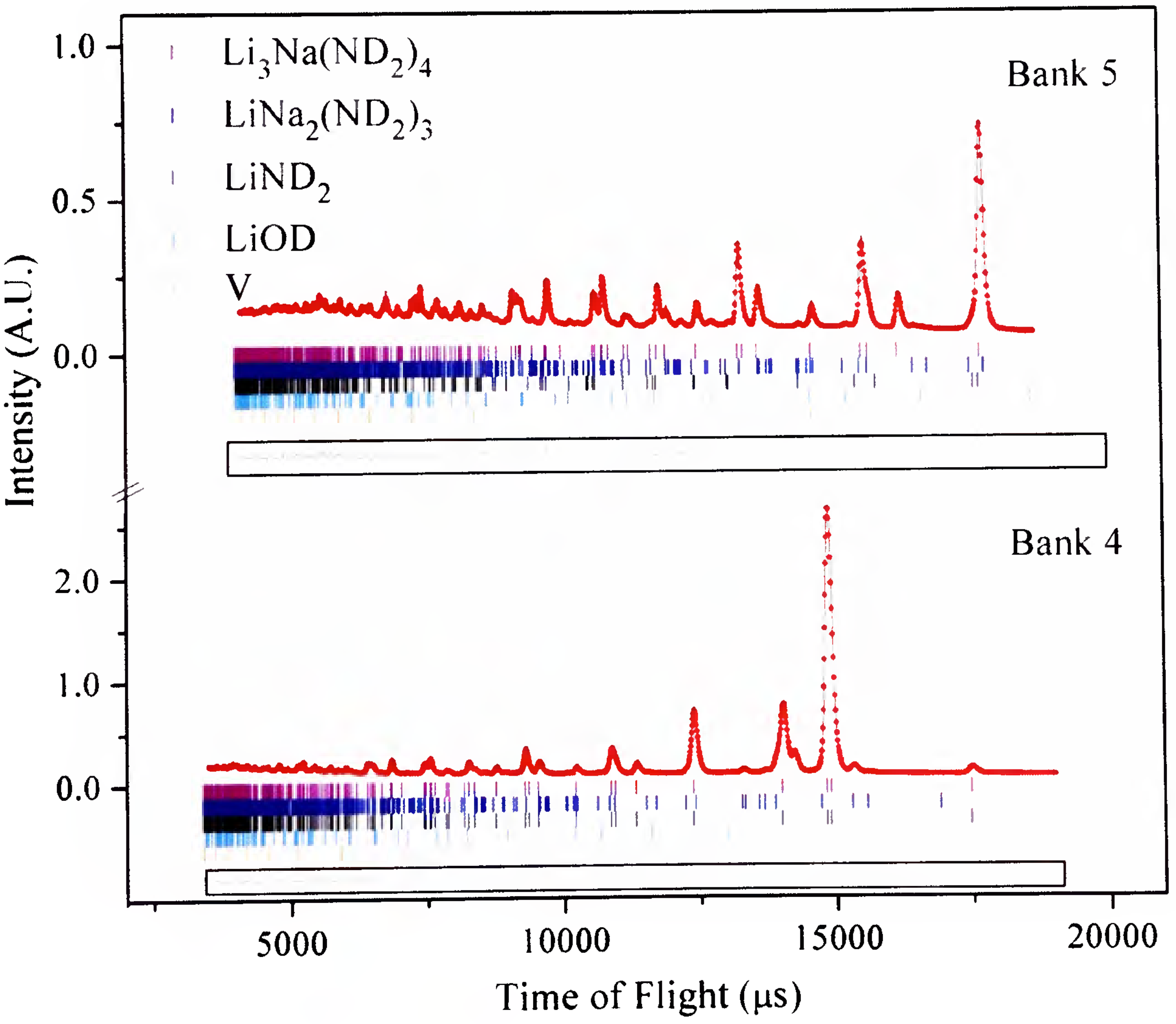

Figure 4.12 : Observed (solid line), calculated (red dots), and difference plots (y_{obsd} - y_{calcd}, solid lines in boxes) for the structure refinement of $Li_3Na(ND_2)_4$, from neutron diffraction data collected at banks 4 and 5 of the GEM diffractometer. The peak positions of the Bragg reflections for $Li_3Na(ND_2)_4$, $LiNa_2(ND_2)_3$, $LiND_2$, LiOD and V are shown by the vertical tick marks. R_{wp} 4.068, R_{exp} 0.766, goodness of fit 5.313.

The $Li_3Na(ND_2)_4$ sample was found to be majority phase $Li_3Na(ND_2)_4$ (87.7 mass%) with $LiND_2$ (2.5 mass%), $LiNa_2(ND_2)_3$ (5.5 mass %) and LiOD (4.3 mass %) impurities also present. $Li_3Na(ND_2)_4$ was found to be highly sodium deficient, with an empirical formula calculated at $Li_{3.29(3)}Na_{0.71(3)}(ND_2)_4$.

4.7.3 Study of $Li_3Na(ND_2)_4$ Using Intelligent Gravimetric Analysis Combined with Neutron Diffraction.

The decomposition reaction of $Li_3Na(ND_2)_4$ was studied using the combined intelligent gravimetric analysis with neutron diffraction apparatus (the IGA^n, section 2.2.2) at the ISIS pulsed neutron facility.

In order to identify the temperatures of interest prior to the online neutron diffraction study, a preliminary offline intelligent gravimetric analysis measurement was performed on a sample of $Li_3Na(NH_2)_4$, the data from which are presented in Appendix A3. The $Li_3Na(NH_2)_4$ sample was heated to 400 °C at a rate of 2 °C per minute under dynamic vacuum, and two decomposition steps were observed, with midpoints at 230 °C and 350 °C. These findings were used to plan the online IGA^n experiment.

The $Li_3Na(ND_2)_4$ sample outlined in section 4.7.2 was placed into a quartz bucket, which was loaded into the IGA^n apparatus under inert conditions (section 2.2.2). The sample was heated under dynamic vacuum to 200 °C at a rate of 2 °C/min, and then to 225 °C at 0.5 °C/min. This temperature was maintained until the mass loss from the sample became very slow (as indicated by the thermogravimetric data), at which point the sample was heated further at a rate of 2 °C/min. A second decomposition step began as the sample reached 320 °C, and the sample was maintained at this temperature until no further mass loss was observed from the thermogravimetric data. Further heating to 350 °C was not necessary for complete decomposition of the sample.

Thermogravimetric readings of the sample mass, temperature and pressure were taken every 5 seconds, and neutron diffraction data were collected at intervals of 2.52 minutes throughout the course of the experiment.

A surface plot (section 3.4) of the diffraction data collected at bank 4 is presented in Figure 4.13, where the colour of the lines reflects the relative intensities of the Bragg reflections. The colours range from dark blue / black (indicating background intensity) through light blue (weak intensity) and red (medium intensity) up to yellow (high intensity). The gaps in the data correspond to loss of the neutron beam during the experiment. The corresponding thermogravimetric data are also presented in Figure 4.13.

Analysis of the thermogravimetric data implies that the decomposition reaction occurred *via* two distinct gas-releasing steps. The first mass loss (14 mass%) occurred at a temperature of 225 °C and the second (43 mass%) occurred at 320 °C.

The diffraction data presented in the surface plot indicates that the Bragg peaks at d-spacing 2.55 Å, 2.88 Å and 3.05 Å (which were indexed to the (020), (004), (112) and (013) reflections of $Li_3Na(ND_2)_4$) decreased dramatically in intensity before any mass loss was observed in the thermogravimetric data. This is consistent with the transformation of $Li_3Na(ND_2)_4$ into an amorphous phase, prior to the evolution of gas. The appearance of Bragg peaks at d-spacing 2.55 and 2.95 Å (indexed to the (002) and (111) reflections of Li_2ND) is consistent with Li_2ND formation.

Comparison of thermogravimetric and diffraction data between times of 300 and 800 minutes suggests that the second mass loss (observed at 320 °C) was not accompanied by any crystallographic change in the sample.

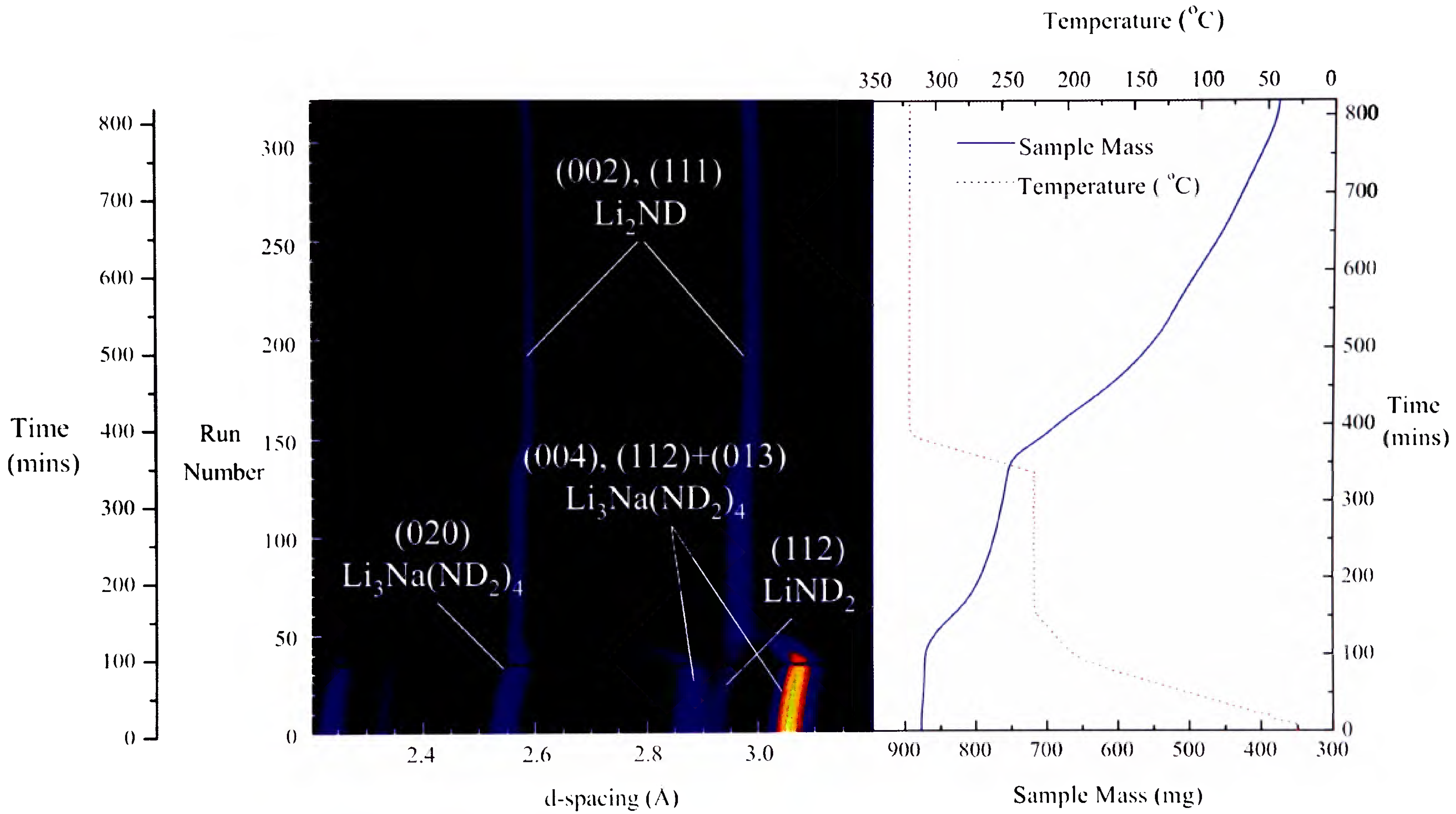

Figure 4.13 : Comparison of the surface plot of neutron diffraction data (collected at bank 4) and thermogravimetric data, collected during the decomposition of $Li_3Na(ND_2)_4$, studied using the IGA^n apparatus under dynamic vacuum. Bragg reflections for the various phases present are indexed.

4.7.3.1 Rietveld Analysis of Diffraction Data Collected During the Decomposition of $Li_3Na(ND_2)_4$

Rietveld analysis[11] (section 2.1.4) of the neutron data collected during this study was performed using a mixture of batch refinements (section 2.1.4.2) and refinement of individual data sets (section 2.1.4.1). Generally, the diffraction data collected during phase transformations were refined individually, and those collected throughout the rest of the experiment were refined using batch techniques. All refinements were performed using TOPAS Academic[12] according to the general methods outlined in sections 2.1.4.1 and 2.1.4.2, with the Na-occupancy of the 2c (0,½,z) $Li_3Na(ND_2)_4$ lattice site refined in addition to the parameters listed in these sections.

Rietveld analysis[11] of the diffraction data collected prior to decomposition (section 4.7.2) indicated that the sample was composed of $Li_3Na(ND_2)_4$ (87.7 mass%) with $LiND_2$ (2.5 mass%), $LiNa_2(ND_2)_3$ (5.5 mass %) and LiOD (4.3 mass %) impurities. The resolution of the diffraction data collected during this experiment was such that the Bragg reflections of LiOD could not be resolved from the background and as such, LiOD was not included in the refinement model for these data.

Rietveld analysis of the final data set collected during the decomposition of $Li_3Na(ND_2)_4$ indicated that the solid decomposed product was comprised of majority phase Li_2ND (98 mass%) with minority LiD (2 mass%) (Figure 4.14).

The refined scale factors calculated for each of the crystalline phases present during the decomposition of the $Li_3Na(ND_2)_4$ sample are presented in Figure 4.15a. The lattice parameters calculated for $Li_3Na(ND_2)_4$, $LiND_2$ and $LiNa_2(ND_2)_3$ are presented in Figure 4.15b and those of Li_2ND and $LiND_2$ are presented in Figure 4.15c. The refined Na-occupancy of the 2c lattice site of $Li_3Na(ND_2)_4$ is presented in Figure 4.15d. A full summary of the refined parameters is presented in Appendix A1.3.

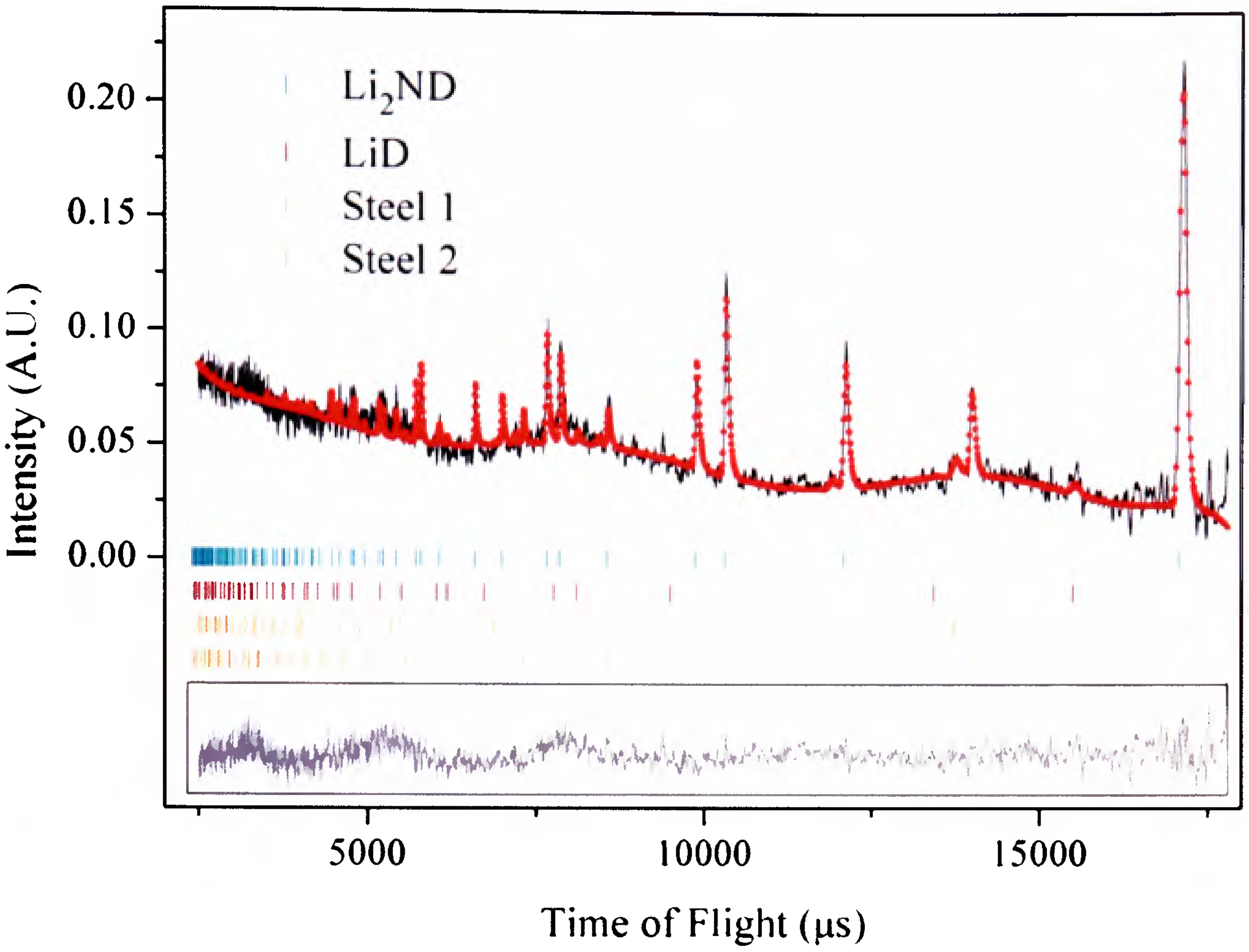

Figure 4.14 : Observed (solid line), calculated (red dots), and difference plots (y_{obsd} - y_{calc}, solid lines in boxes) for the structure refinement of the decomposed $Li_3Na(ND_2)_4$ sample. Presented are the neutron diffraction data collected at bank 5 of the GEM diffractometer. The Bragg peak positions for Li_2ND, LiD and steel are shown by the vertical tick marks. R_{wp} 8.647, R_{exp} 6.988, goodness of fit 1.237

The scale factor of $Li_3Na(ND_2)_4$ (Figure 4.15a) was observed to decrease slowly with increasing temperature, up to 165 °C. Above 165 °C a sharp drop was observed in the $Li_3Na(ND_2)_4$ scale factor, which reached zero as the sample reached 203 °C. No increase was observed in the scale factors of any of the other phases present in the sample during this temperature range, which suggests that a crystalline – amorphous phase transition occurred in $Li_3Na(ND_2)_4$. The corresponding thermogravimetric data suggest that this phase transition was not accompanied by any change in mass.

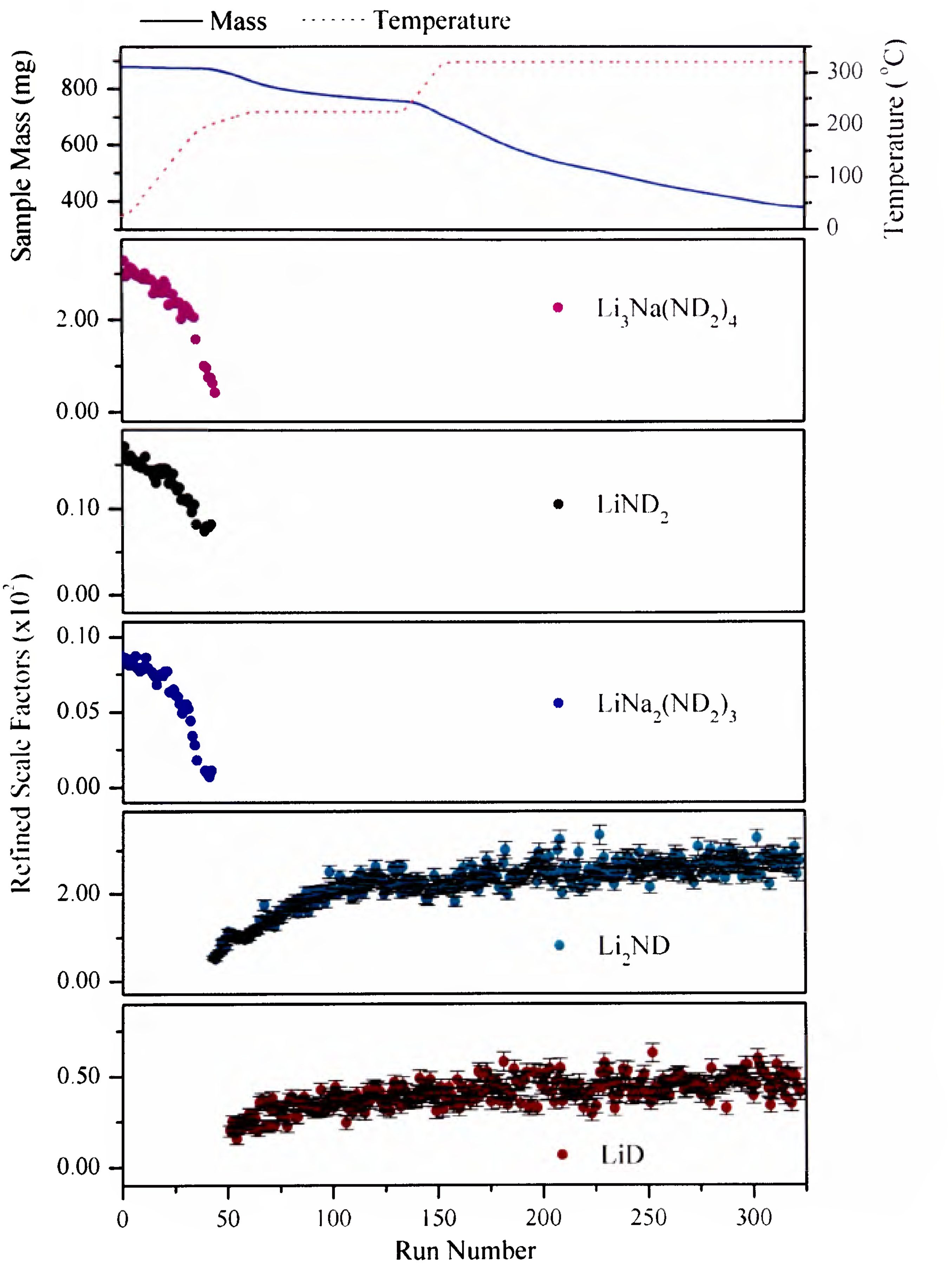

Figure 4.15 a : Summary of refined scale factors obtained, from Rietveld analysis (*via* batch refinement) of the neutron diffraction data collected during $Li_3Na(ND_2)_4$ decomposition in the IGA^n. The thermogravimetric data are presented for ease of comparison. Mean errors $Li_3Na(ND_2)_4$ ± 0.0010, $LiND_2$ ± 0.00006, $LiNa_2(ND_2)_3$ ± 0.00005, Li_2ND ± 0.0014, LiD ± 0.0004. Error bars are presented only if larger than the data markers.

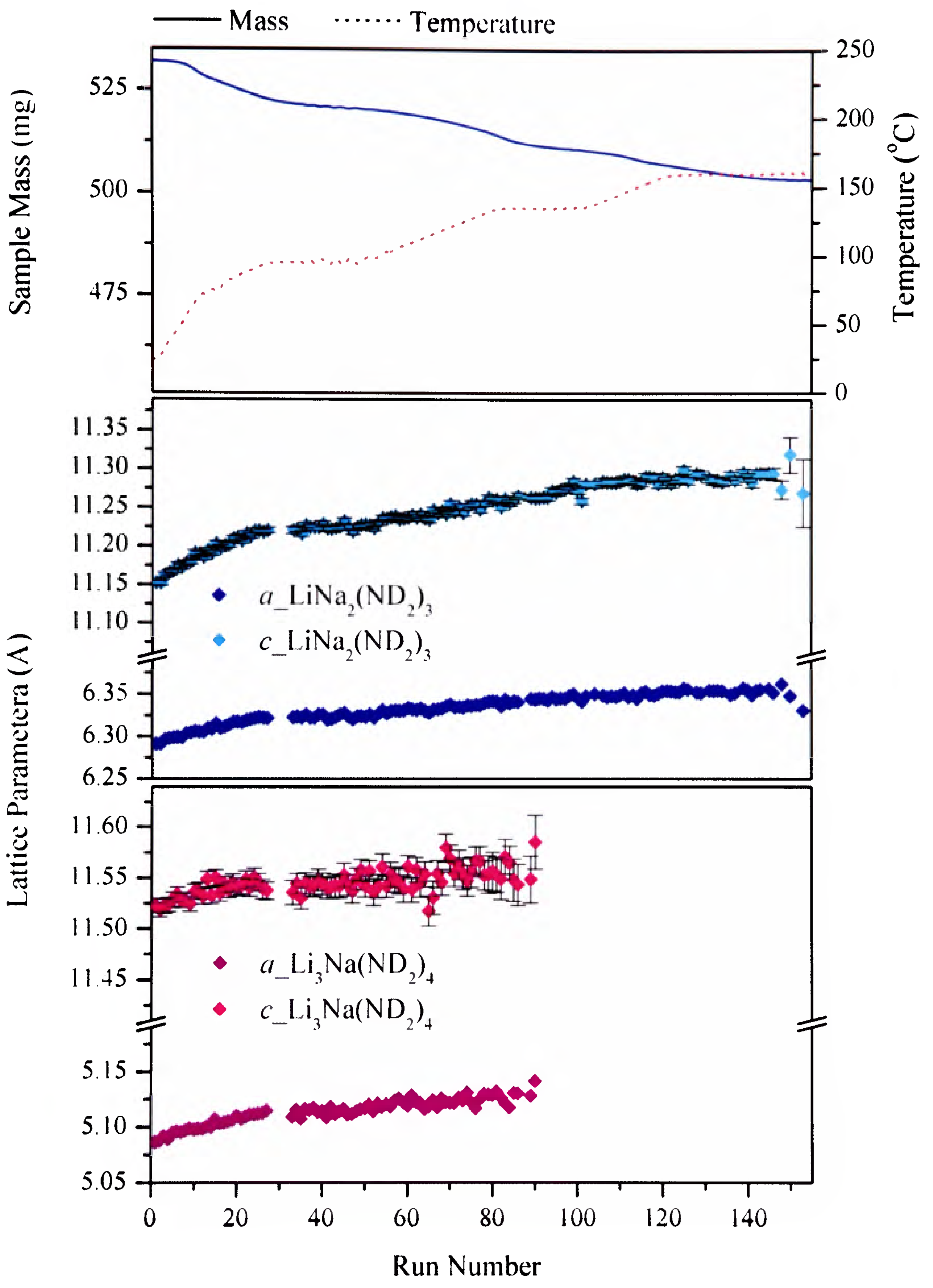

Figure 4.15 b : Summary of the $Li_3Na(ND_2)_4$, $LiNa_2(ND_2)_3$ and $LiND_2$ lattice parameters, calculated from Rietveld analysis (*via* batch refinement) of the neutron diffraction data collected during $Li_3Na(ND_2)_4$ decomposition in the IGA^n. The thermogravimetric data are included for ease of comparison. Mean errors a_ $Li_3Na(ND_2)_4$ ± 0.0017, c_ $Li_3Na(ND_2)_4$± 0.004, a_ $LiND_2$ ± 0.002, c_ $LiND_2$ ± 0.008, a_ $LiNa_2(ND_2)_3$ ± 0.004 and c_ $LiNa_2(ND_2)_3$ ± 0.001. Error bars are smaller than the data markers.

The proportions of $LiND_2$ and $LiNa_2(ND_2)_3$ in the sample prior to decomposition were 2.5 mass% and 5.5 mass%, respectively (section 4.7.2). Due to the small phase fraction of these materials, the scale factors of both phases were observed to decrease during the experiment with no significant mass loss observed in the thermogravimetric data.

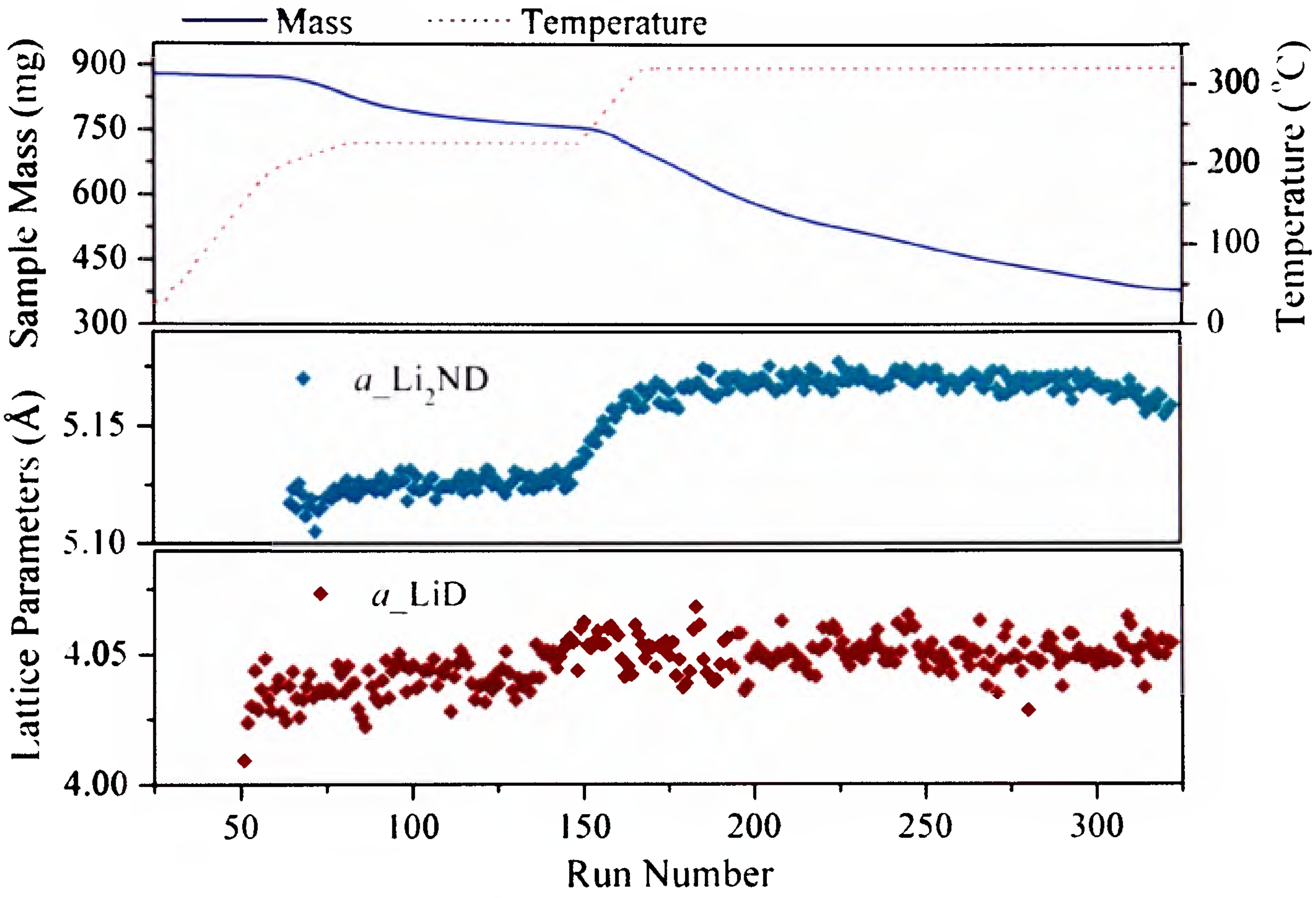

Figure 4.15 c : Summary of the refined Li_2ND and LiD lattice parameters, calculated from Rietveld analysis (*via* batch refinement) of the neutron diffraction data collected during $Li_3Na(ND_2)_4$ decomposition in the IGA^n. The mass and temperature traces are included for ease of comparison. Mean errors a_Li_2ND ± 0.002, and a_LiD ± 0.002. Error bars are smaller than the data markers.

The solid product formed from decomposition of the $Li_3Na(ND_2)_4$ sample was majority phase Li_2ND (98 mass%) with minority phase LiD (2 mass%) (Figure 4.14).

The Li_2ND scale factor increased from zero only after the Bragg reflections from $Li_3Na(ND_2)_4$ were no longer visible in the diffraction data, suggesting that Li_2ND was formed from decomposition of the amorphous phase. The increase observed in the Li_2ND scale factor coincided with the first mass loss in the thermogravimetric data (14 mass%), which continued throughout the isotherm at 225 °C (run numbers 50 – 140). The increase in the LiD scale factor occurred simultaneously with that of Li_2ND.

The *a*-lattice parameter of $Li_3Na(ND_2)_4$ (Figure 4.15b) was observed to increase with temperature up to 194 °C, which is consistent with the thermal expansion of the unit cell. The $Li_3Na(ND_2)_4$ *c*-parameter, however, remained virtually constant up to this temperature, which suggests that the changes observed in the $Li_3Na(ND_2)_4$ lattice parameters were not simply the result of thermal expansion.

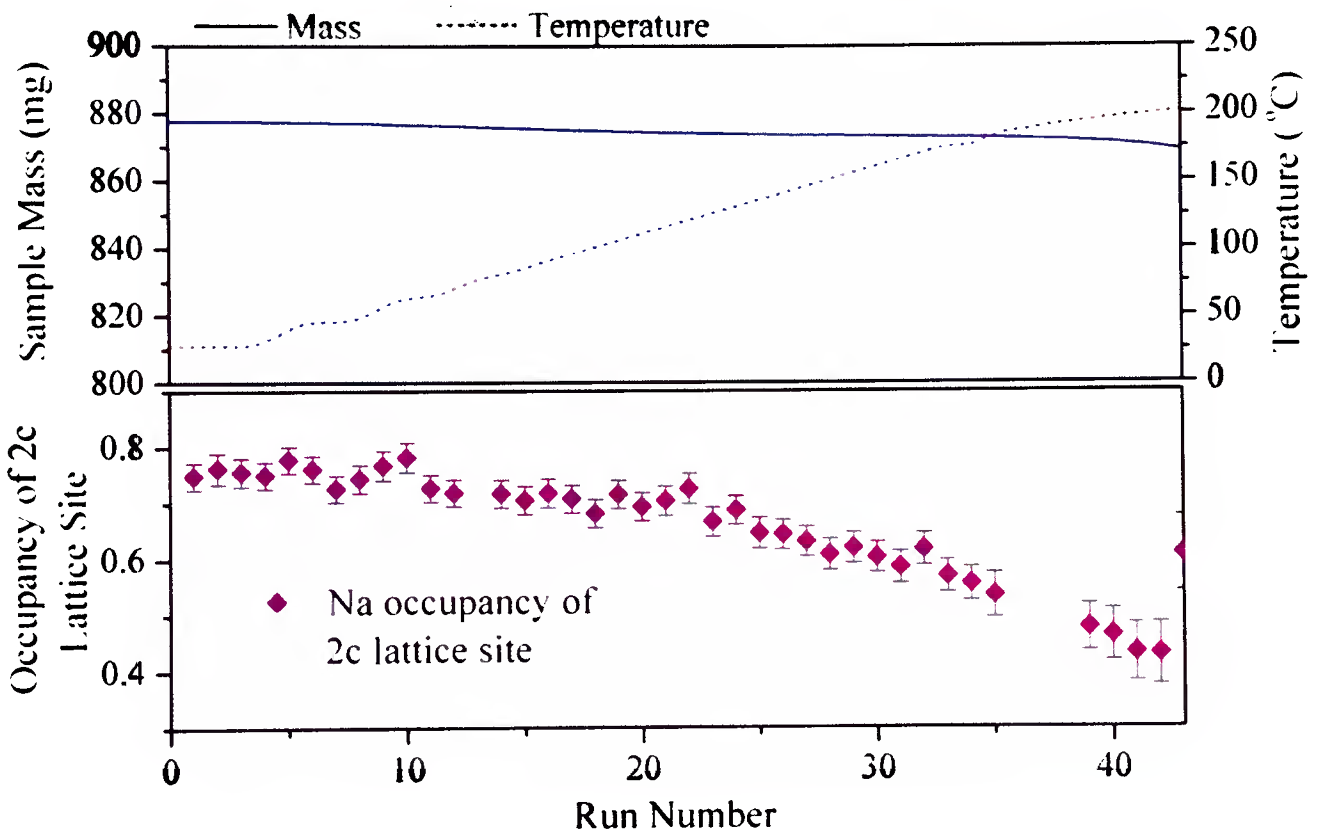

Figure 4.15d : Refined Na occupancy of the 2c (0,½,¼) lattice site in $Li_3Na(ND_2)_4$, obtained from Rietveld analysis (*via* batch refinement) of the neutron diffraction data collected during $Li_3Na(ND_2)_4$ decomposition in the IGA^n. The thermogravimetric data are included for ease of comparison. Mean error ± 0.03

Figure 4.15d shows that the sodium occupancy of the 2c (0,½,¼) lattice site decreased with increasing temperature, which ordinarily would cause a unit cell contraction along the *c*-axis (section 4.4.2). During this study, such a unit cell contraction appears to have been counter-balanced by thermal expansion of the phase, leading overall to a $Li_3Na(ND_2)_4$ *c*-parameter that remained virtually constant with increasing temperature up to 194 °C.

Above 194 °C, the $Li_3Na(ND_2)_4$ *c*-parameter decreased sharply, which coincided with a rapid decrease in the Na-occupancy of the 2c site towards a limiting value of 0.42 at 203 °C. Beyond this temperature, no Bragg peaks were observed for $Li_3Na(ND_2)_4$, indicating that the material had fully transformed into an amorphous phase.

The decreasing Na-occupancy of the 2c lattice site in $Li_3Na(ND_2)_4$ suggests that the rapid decrease observed in the $Li_3Na(ND_2)_4$ scale factor (Figure 4.15a) (with no observable mass loss) may have been caused by the transformation of $Li_3Na(ND_2)_4$ towards a material of composition 3 $LiND_2$ + $NaND_2$. The decrease observed in the Na occupancy of the 2c site was steady, which is consistent with the separation of $Li_3Na(ND_2)_4$ *via* a series of non-stoichiometric reaction intermediates of general formula $Li_3Na_{1-x}(ND_2)_{4-x}$ + *x* $NaNH_2$, according to Equation 4.6.

$$Li_3Na(ND_2)_4 \longrightarrow Li_3Na_{1-x}(ND_2)_{4-x} + x\,NaND_2 \qquad \text{Equation 4.6}$$

The $NaND_2$ formed during such a separation would be a liquid at the temperature of interest, and so, no Bragg peaks would be expected for this material in the diffraction data.[22] The $LiND_2$ formed should be a solid at these temperatures, and therefore, an increase in the $LiND_2$ scale factor of would be expected. Such an increase was not observed experimentally, which suggests that the $LiND_2$ formed may have been amorphous, or that $Li_3Na(ND_2)_4$ separation was not complete, and $Li_3Na_{1-x}(ND_2)_{4-x}$ phases were formed, which had lower melting points than $LiND_2$.

The lattice parameters of $LiNa_2(ND_2)_3$, $LiND_2$ (Figure 4.15b), Li_2ND and LiD (Figure 4.15c) varied linearly with temperature, suggesting thermal expansion.

Comparison of the crystallographic and thermogravimetric data indicates that the first mass loss step (14 mass%) was accompanied by in increase in the Li_2ND scale factor. It therefore appears that the $NaND_2$ and $Li_3Na_{1-x}(ND_2)_{4-x}$ (or amorphous $LiND_2$)

produced from the separation of $Li_3Na(ND_2)_4$ decomposed to form Li_2ND and an amorphous Na phase, releasing gas.

The initial stoichiometry of the $Li_3Na(ND_2)_4$ sample was $Li_{3.29}Na_{0.71}(ND_2)_4$, (section 4.7.2). The calculated mass loss from the release of one mole of ND_3 from such a sample would be 18 mass%, which is 4 mass% higher than that observed experimentally. This may be due to overlap between the first and second mass loss processes in the thermogravimetric data, which is evidenced by the continued increase of the Li_2ND scale factor during the second mass loss step Figure 4.15a).

43 mass% was lost from the sample during the second gas releasing step, which is consistent with the loss of $NaNH_2$ from the sample. Under these reaction conditions, this was likely to have occurred *via* the decomposition of the material into Na + ½ N_2 + D_2 (according to the low pressure pathway outlined in Equation 4.5)[20] and the subsequent volatisation of Na. Such a conclusion is supported by the lack of a Na-containing product in the diffraction data of the end-point material.

Had $Li_{3.29}Na_{0.71}(ND_2)_4$ decomposed to form only 3.29/2 Li_2ND as the solid product, the mass loss would be calculated at 56 mass%. The experimentally observed mass loss was 57 mass%, which is in excellent agreement with the theoretical value.

4.7.4 Thermogravimetric Study of $Li_3Na(NH_2)_4$ Using Intelligent Gravimetric Analysis with Mass Spectrometry

To further study the decomposition reaction of $Li_3Na(NH_2)_4$, thermogravimetric data were collected using intelligent gravimetric analysis combined with mass spectrometry (IGA-MS, section 2.2.1). The $Li_3Na(NH_2)_4$ sample was ground under inert atmosphere, loaded into a stainless steel mesh bucket and then transferred under inert atmosphere to the IGA-MS apparatus (section 2.2.1). The sample was heated under a flow of 1 bar He to 400 °C at a rate of 2 °C per minute, and this temperature was maintained for 12 hours. The outgoing gases were sampled by a dynamic sampling mass spectrometer, which was set in flow mode to detect 17, 2, 28, 23 and 39 atomic mass units (AMU), corresponding to NH_3, H_2, N_2, Na and $NaNH_2$, respectively (section 2.2.1).

The thermogravimetric and mass spectrometry data collected from this study are presented in Figure 4.16 a and b, respectively.

The gradient of the thermogravimetric plot altered a number of times during the experiment (differential of the sample mass is presented in Appendix A3), indicating that the decomposition of $Li_3Na(NH_2)_4$ was a multi-step process. Heating from room temperature to 216 °C caused the sample to lose 2.9 mass% over two small steps. Heating the sample further, from 216 °C to 400 °C, resulted in a loss of 18 mass% from the sample. Three further mass losses were then observed during the isothermal step at 400 °C corresponding to 17.4 mass%, 14.8 mass% and 6.0 mass%, respectively.

The data collected by the mass spectrometer show the partial pressures of NH_3, H_2, N_2, Na and $NaNH_2$ (17, 2, 27, 23 and 39 AMU, respectively) evolved from the sample as a function of time. Comparison of the thermogravimetric and partial pressure data makes it possible to identify the gaseous products released from the sample during each decomposition step.

The first two small mass losses (resulting in a combined mass change of 2.9 mass%, between temperatures of 25 °C and 216 °C) were accompanied by small peaks in the partial pressures of both NH_3 (17 AMU) and N_2 (28). These mass loss steps were attributed to desorption of physisorbed gas from the surface of the powder grains.

The mass loss observed between temperatures of 216 and 400 °C (18 mass%) coincided with a peak in the partial pressure of H_2 (2 AMU), implying that hydrogen release from $Li_3Na(NH_2)_4$ proceeded ammonia release (if the desorption of physisorbed gases is ignored).

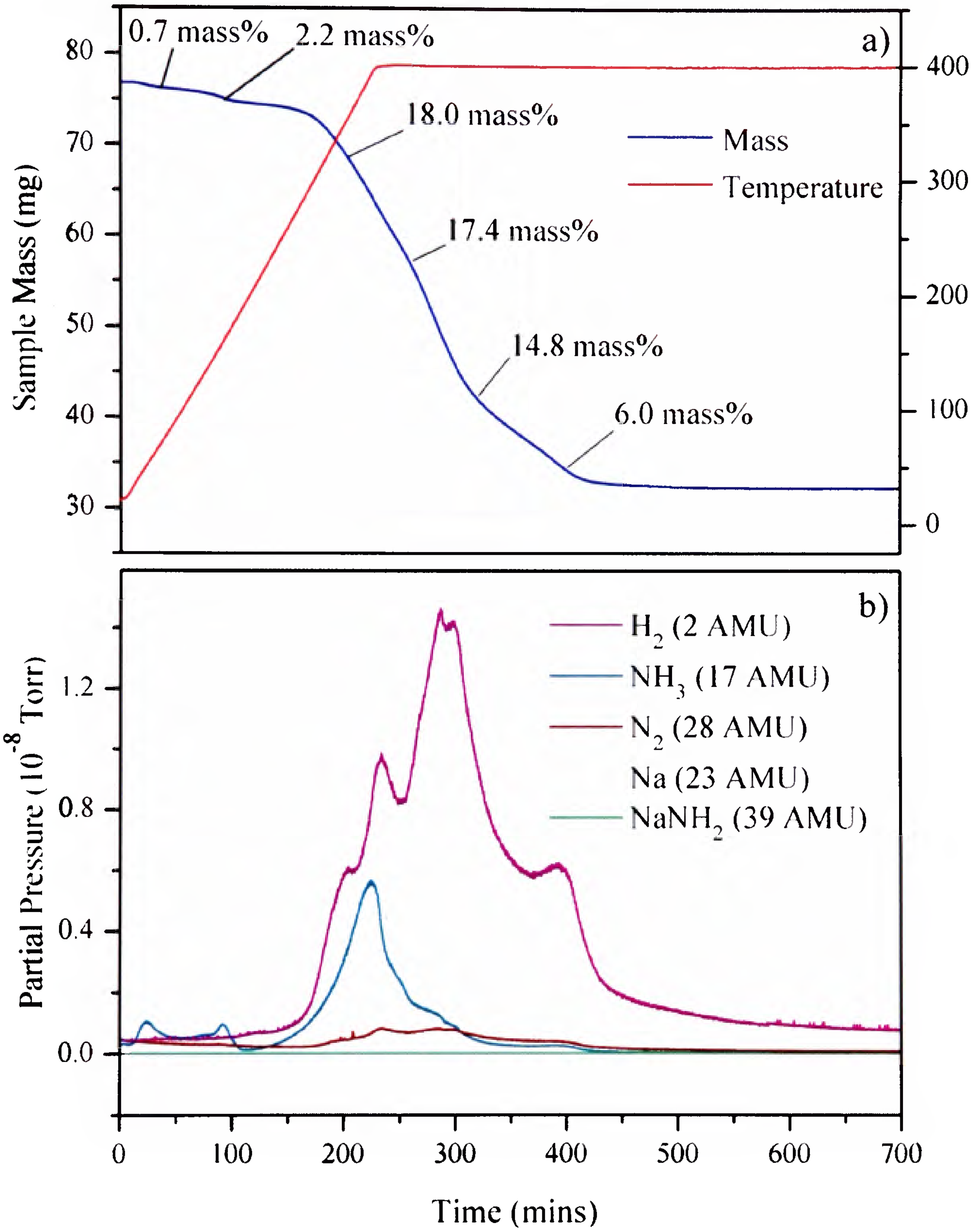

Figure 4.16a and b : a) Thermogravimetric data of high purity $Li_3Na(NH_2)_4$, collected using intelligent gravimetric analysis, with heating rate 2 °C/min and target temperature 400 °C. The red line represents the temperature of the sample and the blue line the sample mass. b) Partial pressures of H_2 (purple), NH_3 (turquoise), N_2 (dark red), Na (grey) and $NaNH_2$ (green), recorded during thermogravimetric study of $Li_3Na(NH_2)_4$ using *in-situ* mass spectrometry

Three mass losses were observed once the temperature of the sample reached 400 °C. The first of these mass losses (17.4 mass%) was accompanied by a peaks in the partial pressures of both H_2 and NH_3. The second and third of these mass losses (14.8 mass% and 6 mass%, respectively) coincided with peaks in the partial pressure of H_2.

The presence of three distinct isothermal H_2-releasing processes supports the premise that $Li_3Na(NH_2)_4$ decomposition occurred *via* the formation of a multi-component material, as suggested in section 4.7.3. The change in the rate of mass loss between the final three mass loss steps (17.4 mass%, 14.8 mass% and 6 mass%, respectively) suggests that the decomposition of the various phase components present occurred in three distinct steps.

Close inspection of Figure 4.16b shows that peaks in the partial pressure of H_2 were always accompanied by peaks in the partial pressure of N_2, suggesting that the formation of H_2 from $Li_3Na(NH_2)_4$ decomposition was always accompanied by N_2 formation (albeit a much smaller amount).

Integration of the partial pressures of, NH_3, H_2 and N_2 with respect to time indicated that the molar ratio of the gases released during the decomposition of $Li_3Na(NH_2)_4$ was 20:4:1 for $H_2 : NH_3 : N_2$.

Synchrotron X-ray diffraction data for the decomposed sample were collected using the ID31 diffractometer at the ESRF (section 2.1.2.3). Rietveld analysis[11] of the data collected showed that the non-gaseous product of $Li_3Na(NH_2)_4$ decomposition in the IGA-MS apparatus was majority phase Li_2NH (76.6 wt%), with LiH (2.1 wt%) and Li_2O (21.3 wt%). No Bragg peaks were observed for any sodium-containing material, suggesting that either the Na-phase formed during the decomposition of $Li_3Na(NH_2)_4$ was amorphous, or that Na was volatised during the experiment. Na is known to have a low vapour pressure (3.3 x 10^{-1} mbar at 400 °C),[18] and hence volatisation at such temperatures would be highly likely.

The volatisation of Na was not confirmed by mass spectrometry, as the partial pressure recorded for Na (23 AMU) was zero throughout the experiment. The presence of a dark crust on the thermocouple and gas inlet tube of the reaction vessel, however, suggests that Na may indeed have volatised from the sample during the experiment, but cooled and condensed inside the IGA apparatus prior to reaching the mass spectrometer.

The total mass lost from the $Li_3Na(NH_2)_4$ sample during the decomposition reaction was 59 mass%. Decomposition of $Li_3Na(NH_2)_4$ to form only 3/2 Li_2NH would result in a mass-loss of 60%, which is in excellent agreement with the experimental data. Therefore, it appears that the $Li_3Na(NH_2)_4$ sample decomposed under these conditions with loss of H_2, NH_3, N_2 and Na.

4.7.5 Study of $Li_3Na(NH_2)_4$ Using Differential Scanning Calorimetry

Differential Scanning Calorimetry (DSC) measurements were performed on a sample of $Li_3Na(NH_2)_4$ according to the method outlined in section 2.4. The $Li_3Na(NH_2)_4$ sample was heated at a rate of 5 °C/minute to a temperature of 400 °C and then cooled at the same rate. The heat exchange between the sample and its surroundings was recorded throughout the experiment, where positive heat-flow indicated an exothermic event, and negative heat-flow indicated an endothermic event.

The data collected during this experiment are presented in Figure 4.17, with each heat exchange event numbered.

The $Li_3Na(NH_2)_4$ sample was shown to undergo a total of 5 heat exchange processes, four upon heating (labelled 1-4) and one upon cooling (labelled 5). The enthalpy changes associated with each thermal event were calculated *via* integration of the relevant heat-flow peak with respect to time. The results from these calculations are presented in Table 4.8.

Event 1 was endothermic, with an enthalpy change of +5.159 kJmol^{-1}, onset temperature of 184 °C and a peak temperature 198 °C. The small enthalpy indicates that this step was likely to correspond to the desorption of physisorbed gases from the powdered sample.

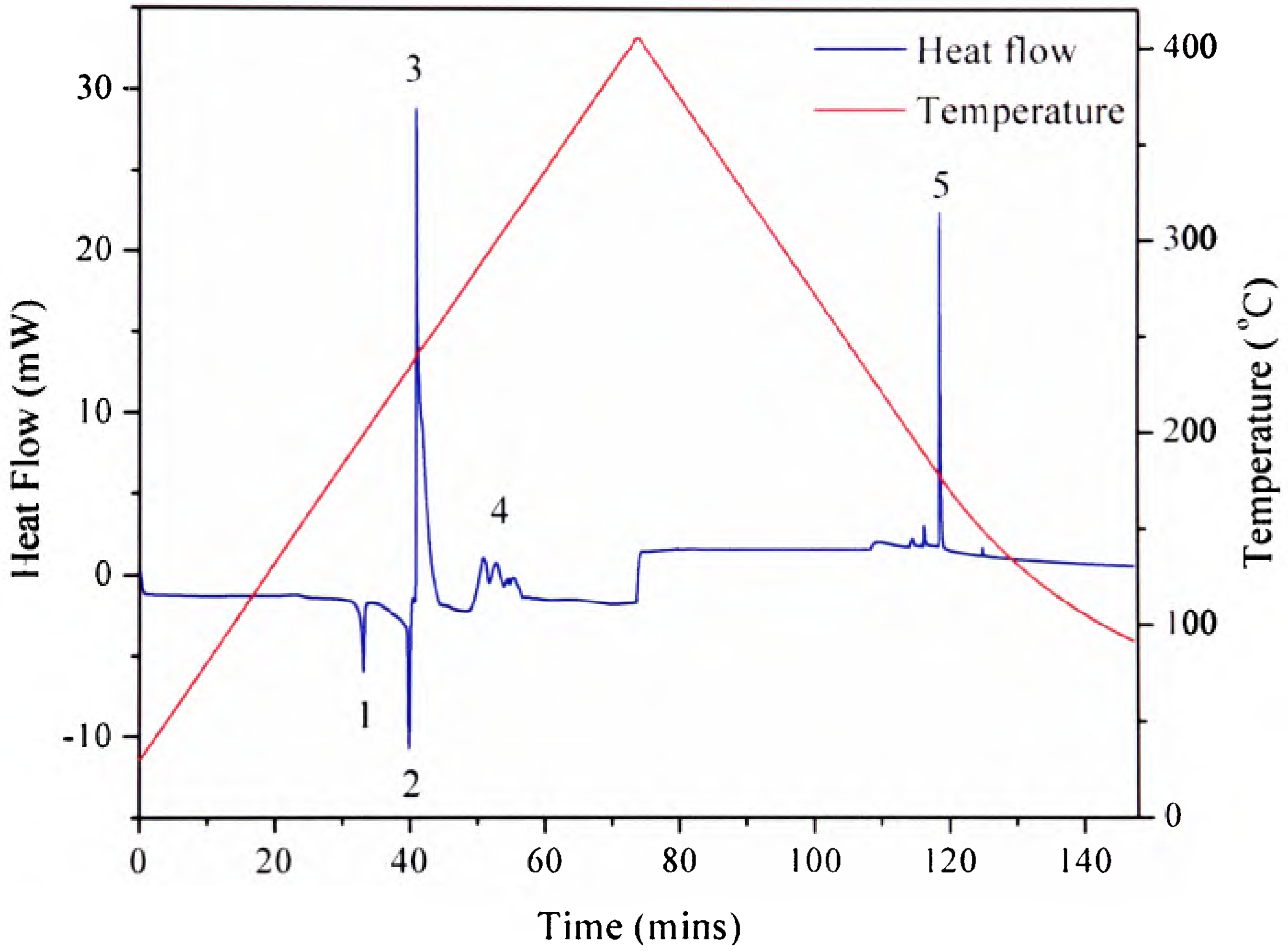

Figure 4.17 : DSC data collected for $Li_3Na(NH_2)_4$, presenting the heat flow (blue line) and temperature (red line) of the sample as a function of time. The sample was heated to 400 °C at a rate of 2 °C per minute.

Event 2 was also endothermic, with an enthalpy change of +15 kJmol^{-1}, onset temperature of 206 °C and a peak temperature of 233 °C. Comparison of this data with the neutron diffraction data in section 4.7.3 indicates that event 2 may have arisen from a crystallographic phase transition. In section 4.7.3, such a transition was observed at temperatures between 165 °C and 203 °C, and involved the migration of Na out of the $Li_3Na(ND_2)_4$ structure and the formation of an amorphous material.

Event number	Endo / exothermic	Onset temperature	Peak temperature	Integrated peak area (ΔH) kJ/mol
1	Endo	184	198	5.159
2	Endo	206	233	15.868
3	Exo	238	239	-52.909
4	Exo	279	289, 299, 308, 312	-24.485
5	Exo	178	178	-11.991

Table 4.8: Summary of DSC data for $Li_3Na(NH_2)_4$. The material was heated to 400 °C at a rate of 5 °C/min and cooled to room temperature at 5 °C/min.

The thermodynamic event labelled 3 was exothermic, with a reaction enthalpy calculated at -52.909 kJ mol^{-1}. The onset and peak temperatures for this event were 238 °C and 239 °C, respectively, which do not match the temperatures for any of the decomposition steps observed during the thermogravimetric studies of either $Li_3Na(NH_2)_4$ or $Li_3Na(ND_2)_4$ (sections 4.7.3 and 4.7.4). If, as anticipated in section 4.7.3, $Li_3Na(NH_2)_4$ separates during heating to form a material approaching $3LiNH_2$ + $NaNH_2$, event 3 may have arisen from the decomposition of either $LiNH_2$ or $NaNH_2$. Previous thermogravimetric studies (sections 3.2.1 and 4.6) have indicated that $NaNH_2$ decomposes at a lower temperature than $LiNH_2$, and hence thermodynamic event 3 is tentatively assigned to the decomposition of $NaNH_2$.

The peaks labelled collectively as event 4 have a combined enthalpy of -4.485 $kJmol^{-1}$. The onset temperature of this event was 279 °C and peaks in the heat exchange were observed at temperatures of 289 °C, 299 °C, 308 °C and 312 °C. The complex nature of this event makes resolution of the peaks difficult and suggests that the decomposition of $Li_3Na(NH_2)_4$ involves a number of thermodynamic processes, many of which occur within a very small temperature range.

Cooling the sample resulted in a sharp exotherm (labelled 5 in Figure 4.17) with enthalpy -11.991 kJmol^{-1} and onset and peak temperature of 178 °C. This indicated the presence of a structural transition in the decomposed product. Diffraction data collected from the products of the thermogravimetric studies (sections 4.7.3 and 4.7.4) showed that $Li_3Na(NH_2)_4$ decomposes to form Li_2NH, which is known to undergo a transition between a high temperature disordered structure and a low temperature ordered structure. This transition is reported at temperatures of 80(3) °C[23] and 87 °C[24], much lower than that observed for the heat exchange event recorded during this experiment.

The onset and peak temperatures of the decomposition events of $Li_3Na(NH_2)_4$ were observed to vary between this calorimetric study and the thermogravimetric studies presented in sections 4.7.3 and 4.7.4. Such variations arise due to differences in the conditions used during the studies, including the heating rates (5 °Cmin^{-1} for DSC, $\leq$2 °C/min^{-1} for IGA-MS and IGA^n)[25] sample sizes (~10 mg for DSC, ~80 mg for IGA-MS and ~900 mg for IGA^n)[26] and reaction pressures (1 bar flowing Ar in the DSC, 1 bar flowing He in the IGA-MS and dynamic vacuum in the IGA^n).

4.7.6 A Suggested Mechanism for the Decomposition of $Li_3Na(NH_2)_4$

Analysis of the diffraction, thermogravimetric and calorimetric data collected during IGA^n, IGA-MS and DSC experiments indicates that decomposition of $Li_3Na(NH_2)_4$ proceeds *via* a complex multi-step process.

The diffraction data collected during the combined thermogravimetric analysis and neutron diffraction experiment (section 4.7.3) indicated that heating $Li_3Na(ND_2)_4$ caused a decrease in the sodium content of the material, as evidenced by the decreasing Na occupancy of the 2c (0,½,¼) lattice site. This suggests that, as the temperature of the $Li_3Na(ND_2)_4$ sample increased, $Li_3Na(ND_2)_4$ may have begun to separate into its constituent amide phases, progressing through varying compositions of the $LiND_2$ /

$Li_3Na(ND_2)_4$ solid solution and tending ultimately towards a composition of $3LiND_2$ + $NaND_2$.

$$\begin{aligned} Li_3Na(ND_2)_4 &\longrightarrow Li_3Na_{1-x}(ND_2)_{4-x} + x\,NaND_2 \\ &\longrightarrow 3\,LiND_2 + NaND_2 \end{aligned} \qquad \text{Equation 4.7}$$

This theory is supported by the corresponding thermogravimetric data, which showed that no mass was lost from the sample (other than that from physisorbed gas) until the $Li_3Na(ND_2)_4$ Bragg reflections were no longer visible in the neutron diffraction data. Furthermore, the crystallographic product from the decomposition of $Li_3Na(ND_2)_4$ was 3/2 Li_2ND, suggesting that the 3 $LiND_2$ formed from $Li_3Na(ND_2)_4$ separation decomposed to form 3/2 Li_2ND. The corresponding thermogravimetric data indicated that the $NaND_2$ present was volatised.

The $Li_3Na_{1-x}(ND_2)_{4-x}$ and $NaND_2$ phases formed as the Na-content of $Li_3Na(ND_2)_4$ decreased were not observed by neutron diffraction, indicating that these materials were amorphous (and possibly molten) at the temperature of interest.

Study of the decomposition of $Li_3Na(NH_2)_4$ using DSC showed that an endothermic process (ΔH +15 kJ/mol) began at a temperature of 206 °C and peaked at 233 °C. It was decided that this endotherm may have arisen from the crystalline to amorphous phase transition observed during the combined intelligent gravimetric analysis and neutron diffraction (IGA^n) study, outlined above. The difference in the temperature at which this event occurred in the two studies can be attributed to the different heating rates (5 $°Cmin^{-1}$ DSC and 2 $°Cmin^{-1}$ IGA^n) and sample sizes (< 10mg DSC, 900 mg IGA^n) used in the experiments.

Analysis of the gases released during $Li_3Na(NH_2)_4$ decomposition was performed using intelligent gravimetric analysis combined with mass spectrometry

(IGA-MS). This study indicated that the major gaseous product released during the decomposition of $Li_3Na(NH_2)_4$ was H_2, with minor amounts of NH_3 and N_2 also formed.

If $Li_3Na(NH_2)_4$ separates upon heating to form a material of composition approaching $3LiNH_2 + NaNH_2$ (as implied above) the gases observed during the IGA-MS study would arise from the decomposition of $NaNH_2$ and $LiNH_2$.

$NaNH_2$ is known to undergo pressure-dependent decomposition processes, releasing N_2, H_2 and forming either Na (at low pressure) or NaH (at high pressure) (section 4.6).[20] We have also found (section 4.6) that $NaNH_2$ can decompose *via* an unknown pathway, releasing mostly H_2 with some NH_3 and N_2. $LiNH_2$ is known to decompose to form Li_2NH with loss of NH_3.[26]

$NaNH_2$ has been observed to decompose at a lower temperature than $LiNH_2$ (section 4.6), and as such, the first peak observed in the H_2 partial pressure during $Li_3Na(NH_2)_4$ decomposition is believed to arise from the breakdown of $NaNH_2$. If the decomposition of sodium amide proceeds as reported in the literature, either Na or NaH will be formed as the solid product.[20] Both of these materials can react with NH_3 to form $NaNH_2$ and release H_2, according to Equations 4.8 and 4.9, respectively.

$$Na + NH_3 \longrightarrow NaNH_2 + \frac{1}{2}H_2 \qquad \text{Equation 4.8}$$

$$NaH + NH_3 \longrightarrow NaNH_2 + H_2 \qquad \text{Equation 4.9}$$

Following the decomposition of $NaNH_2$, the $LiNH_2$ present would decompose, releasing NH_3 and forming Li_2NH. The NH_3 released would then be able to react with the Na or NaH present, according to Equations 4.8 or 4.9, re-forming $NaNH_2$ and releasing hydrogen. The $NaNH_2$ thus formed could then decompose once more, releasing N_2 and H_2, and reforming the NH_3-capturing Na or NaH.

This recycling of the ammonia capturing agent in this way would continue until all of the $LiNH_2$ present in the sample had decomposed to form Li_2NH, at which point the remaining $NaNH_2$ would decompose for the final time.

The thermogravimetric data indicated that Na was volatised from the sample, which was supported by the fact that no Na-containing material was observed in the diffraction data of the decomposed product.

It is clear from the mass spectrometry data that some NH_3 was released during the decomposition reaction of $Li_3Na(NH_2)_4$, which suggests that ammonia capture by Na / NaH was not 100 % effective.

The thermogravimetric data collected during the combined intelligent gravimetric analysis with neutron diffraction study indicated that decomposition of $Li_3Na(ND_2)_4$ occurred with release of ND_3, suggesting that ammonia capture was not possible under conditions of dynamic vacuum.

To summarise, it is hypothesised that $Li_3Na(NH_2)_4$ decomposes at ambient pressures *via* the separation (or partial separation) of the material into its constituent amide components, $3LiNH_2 + NaNH_2$. Of these, $NaNH_2$ decomposes first, releasing H_2 (and possibly some NH_3), and forming Na or NaH. The Na / NaH then acts to capture the ammonia produced during the decomposition of $LiNH_2$, ultimately resulting in the release of H_2 from the system, rather than NH_3, and the reformation of $NaNH_2$. In this way, $NaNH_2$ is potentially decomposed and reformed a number of times before the $LiNH_2$ is completely transformed into Li_2NH. The $NaNH_2$ then decomposes for the final time and the Na / NaH evaporates from the sample.

The overall reaction is therefore tentatively suggested to occur under ambient pressures either by Na formation according to Scheme 1 or by NaH formation according to Scheme 2.

Scheme 1:

$$\begin{aligned}
\mathrm{Li_3Na(NH_2)_4} &\xrightarrow{\qquad} \mathrm{Li_3Na_{1\text{-}x}(NH_2)_{4\text{-}x}} + x\,\mathrm{NaNH_2} \\
&\xrightarrow{x\longrightarrow 1} \mathrm{3LiNH_2} + \mathrm{NaNH_2} \\
&\xrightarrow{\qquad} \mathrm{3LiNH_2} + \mathrm{Na} + \frac{1}{2}\mathrm{N_2}\uparrow + \mathrm{H_2}\uparrow \\
&\xrightarrow{\qquad} \mathrm{LiND_2} + \mathrm{Li_2ND} + \mathrm{NH_3} + \mathrm{Na} \\
&\xrightarrow{\qquad} \mathrm{LiND_2} + \mathrm{Li_2ND} + \mathrm{NaNH_2} + \frac{1}{2}\mathrm{H_2}\uparrow \\
&\xrightarrow{\qquad} \mathrm{LiND_2} + \mathrm{Li_2ND} + \mathrm{Na} + \frac{1}{2}\mathrm{N_2}\uparrow + \mathrm{H_2}\uparrow \\
&\xrightarrow{\qquad} \frac{3}{2}\mathrm{Li_2ND} + \frac{1}{2}\mathrm{NH_3} + \mathrm{Na} \\
&\xrightarrow{\qquad} \frac{3}{2}\mathrm{Li_2ND} + \frac{1}{2}\mathrm{NaNH_2} + \frac{1}{2}\mathrm{Na}\uparrow \\
&\xrightarrow{\qquad} \frac{3}{2}\mathrm{Li_2ND} + \frac{1}{2}\mathrm{Na}\uparrow + \frac{1}{4}\mathrm{N_2}\uparrow + \frac{1}{2}\mathrm{H_2}\uparrow \\
&\xrightarrow{\qquad} \frac{3}{2}\mathrm{Li_2ND}
\end{aligned}$$

Scheme 2:

$$\begin{aligned}
\mathrm{Li_3Na(NH_2)_4} &\xrightarrow{\qquad} \mathrm{Li_3Na_{1\text{-}x}(NH_2)_{4\text{-}x}} + x\,\mathrm{NaNH_2} \\
&\xrightarrow{x\longrightarrow 1} \mathrm{3LiNH_2} + \mathrm{NaNH_2} \\
&\xrightarrow{\qquad} \mathrm{3LiNH_2} + \mathrm{NaH} + \frac{1}{2}\mathrm{N_2}\uparrow + \frac{1}{2}\mathrm{H_2}\uparrow \\
&\xrightarrow{\qquad} \mathrm{LiND_2} + \mathrm{Li_2ND} + \mathrm{NH_3} + \mathrm{NaH} \\
&\xrightarrow{\qquad} \mathrm{LiND_2} + \mathrm{Li_2ND} + \mathrm{NaNH_2} + \mathrm{H_2}\uparrow \\
&\xrightarrow{\qquad} \mathrm{LiND_2} + \mathrm{Li_2ND} + \mathrm{NaH} + \frac{1}{2}\mathrm{N_2}\uparrow + \frac{1}{2}\mathrm{H_2}\uparrow \\
&\xrightarrow{\qquad} \frac{3}{2}\mathrm{Li_2ND} + \frac{1}{2}\mathrm{NH_3} + \mathrm{NaH} \\
&\xrightarrow{\qquad} \frac{3}{2}\mathrm{Li_2ND} + \frac{1}{2}\mathrm{NaNH_2} + \frac{1}{2}\mathrm{NaH} + \frac{1}{2}\mathrm{H_2}\uparrow \\
&\xrightarrow{\qquad} \frac{3}{2}\mathrm{Li_2ND} + \mathrm{NaH} + \frac{1}{4}\mathrm{N_2}\uparrow + \frac{1}{4}\mathrm{H_2}\uparrow \\
&\xrightarrow{\qquad} \frac{3}{2}\mathrm{Li_2ND} + \mathrm{Na}\uparrow + \frac{1}{2}\mathrm{H_2}\uparrow \\
&\xrightarrow{\qquad} \frac{3}{2}\mathrm{Li_2ND}
\end{aligned}$$

Both of these reaction schemes appear to be plausible, however, the decomposition of NaH to form Na + ½ H_2 requires temperatures in excess of 425 °C,[27] which were not attained during these experiments. This suggests that Scheme 1 is the more likely mechanism for the decomposition of $Li_3Na(NH_2)_4$ under ambient pressure, as Na is known to volatise easily under such conditions.

Under dynamic vacuum, after separation of $Li_3Na(NH_2)_4$ into its constituent amide phases, $LiNH_2$ decomposes to release NH_3, and $NaNH_2$ is then volatised from the material. A possible mechanism for this process is presented in Scheme 3:

Scheme 3:

$$\begin{aligned}
\mathrm{Li_3Na(NH_2)_4} &\xrightarrow{\qquad} \mathrm{Li_3Na_{1\text{-}\mathit{x}}(NH_2)_{4\text{-}\mathit{x}}} + x\,\mathrm{NaNH_2} \\
&\xrightarrow{x \longrightarrow 1} \mathrm{3LiNH_2 + NaNH_2} \\
&\xrightarrow{\qquad} \frac{3}{2}\mathrm{Li_2NH} + \frac{3}{2}\mathrm{NH_3}\uparrow + \mathrm{Na}\uparrow + \mathrm{H_2}\uparrow + \frac{1}{2}\mathrm{N_2}\uparrow \\
&\xrightarrow{\qquad} \frac{3}{2}\mathrm{Li_2NH}
\end{aligned}$$

4.7.7 Study of $Li_3Na(NH_2)_4$ Using Raman Spectroscopy

The Raman spectra of $LiNH_2$, (95 % Aldrich), $NaNH_2$ (90 % Aldrich) and $Li_3Na(NH_2)_4$ were collected as outlined in section 2.3.1 and are presented in Figure 4.18. Only the symmetric and anti-symmetric stretching modes of the NH_2^- anions were well resolved for the three materials.

The spectra of $LiNH_2$ and $NaNH_2$ were observed to be extremely similar. As anticipated from previous Raman studies,[22, 28] the $[NH_2^-]$ stretching modes of $LiNH_2$ were located at a higher energy than those of $NaNH_2$, presumably due to inductive effects arising from the different electronegativies of Li^+ and Na^+ (Pauling electronegativities 0.98 and 0.93, respectively). There was also a small shoulder observed on the asymmetric stretch of $LiNH_2$ which is absent from the spectrum of

$NaNH_2$. Such shoulders are observed due to slight variations in the chemical environments of identical atoms.

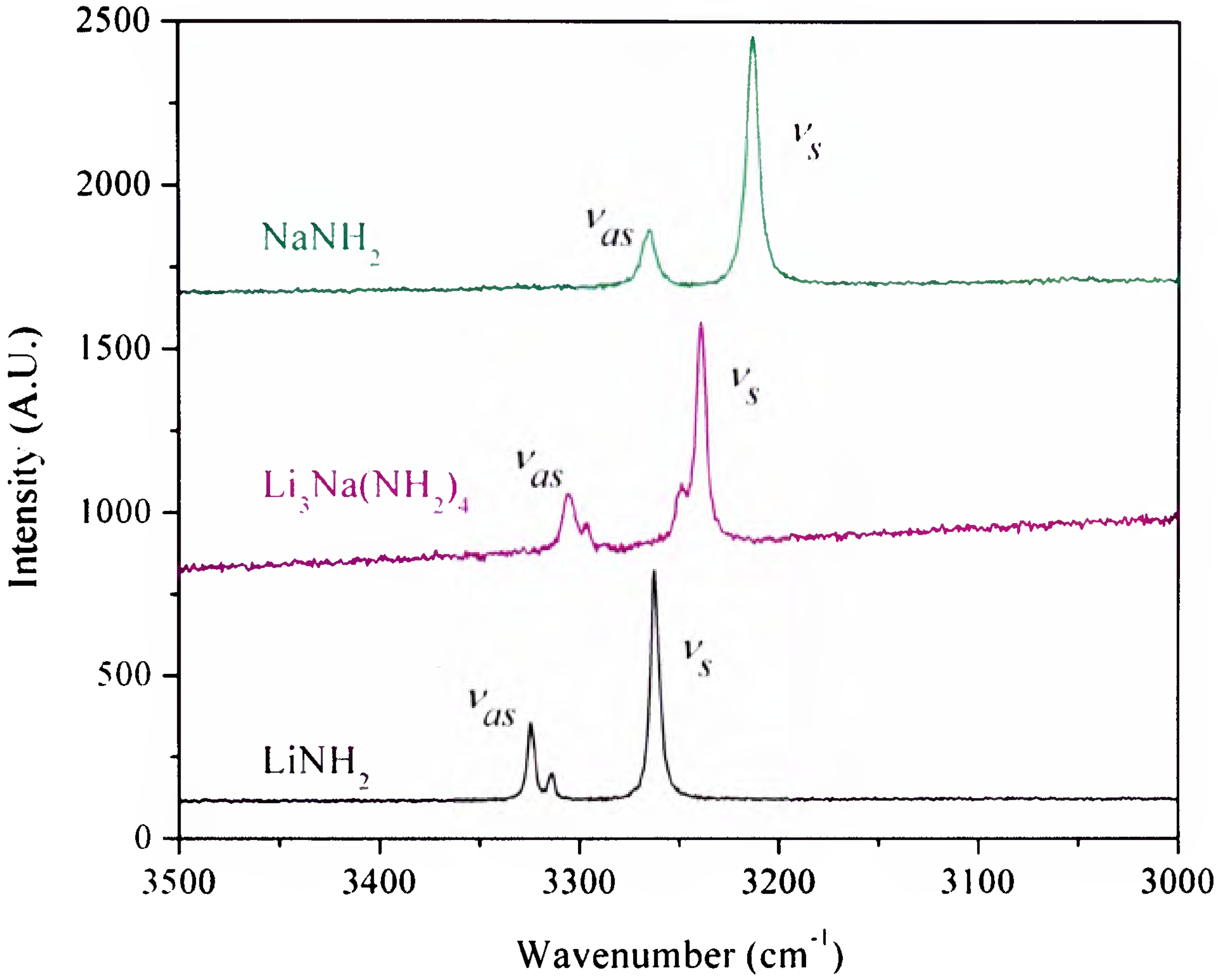

Figure 4.18 : Raman spectra of $LiNH_2$ (black line), $Li_3Na(NH_2)_4$ (purple line) and $NaNH_2$ (green line). The spectral range of 3500 – 3000 cm^{-1} is presented as this contains the well resolved symmetric (ν_s) and antisymmetric (ν_{as}) vibrational modes of the materials

In the case of $LiNH_2$, the environments of the two H atoms of the NH_2^- units are different, due to the orientation of the two N – H bonds with respect to the Li sub-lattice. Given that the amide units in $Li_3Na(NH_2)_4$ coordinate both Li^+ and Na^+ ions, it is not surprising that the energies of the Raman modes for this material lie between those of the two parent compounds. Shoulders were observed on both the symmetric and asymmetric stretching modes of $Li_3Na(NH_2)_4$ which is consistent with slight differences in the H environments due to the orientation of the N – H bonds in the NH_2^- units with respect to the Li and Na ions in the cationic sub-lattice.

4.7.8 Study of $Li_3Na(NH_2)_4$ Using Inelastic Neutron Scattering

Inelastic neutron scattering (INS) spectroscopy was performed on a sample of $Li_3Na(NH_2)_4$ using the TOSCA spectrometer (section 2.3.2) at the ISIS neutron facility. The $Li_3Na(NH_2)_4$ sample was loaded under inert atmosphere into an aluminium can which was lowered into the beamline and cooled to 4K. The INS data were collected over a period of several hours.

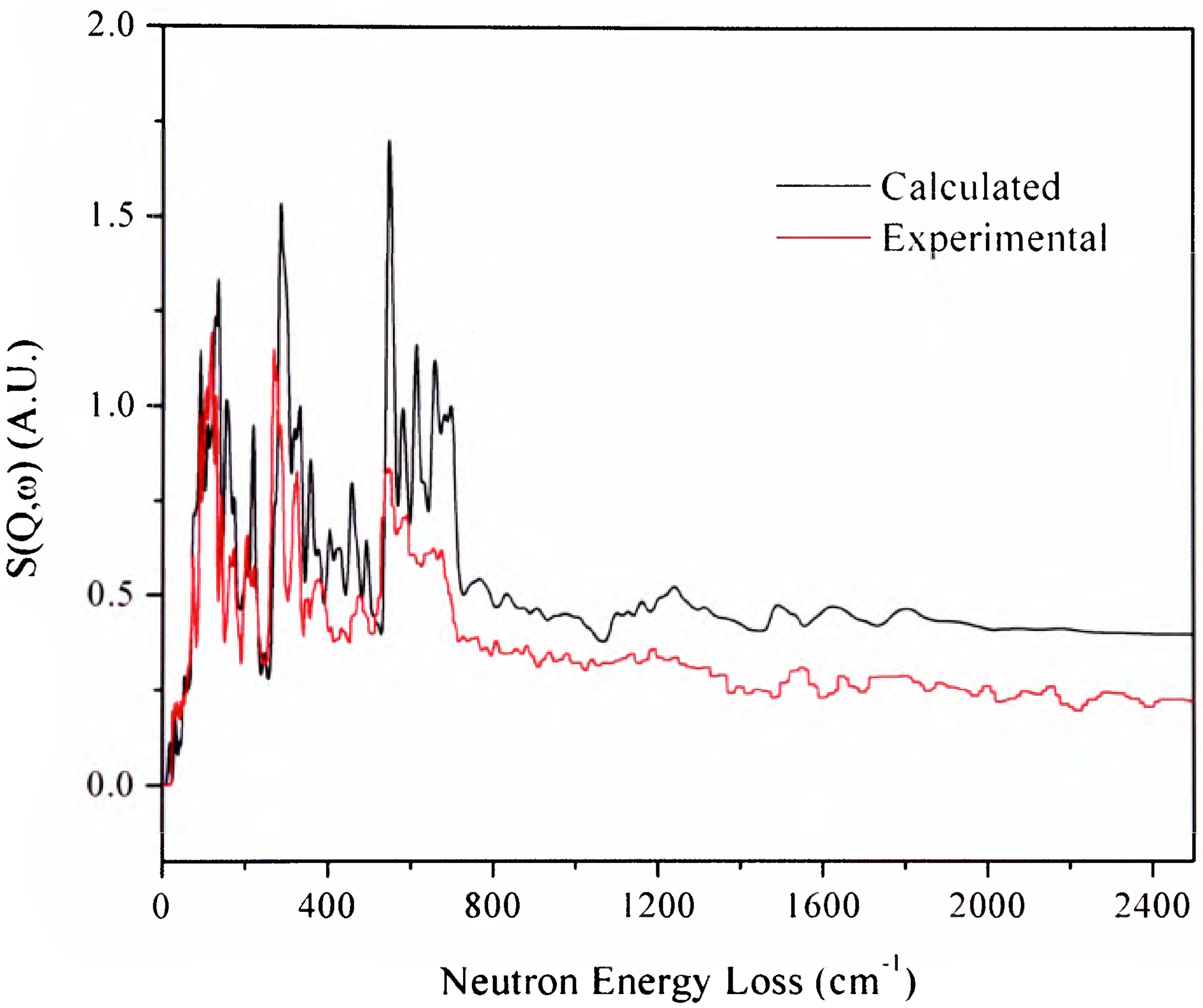

Figure 4.19 : Experimental inelastic neutron scattering data of $Li_3Na(NH_2)_4$ (red line) and structural model (black line) calculated from the geometrically optimised structure using Castep modelling software.

Computer modelling simulations were performed on the $Li_3Na(NH_2)_4$ structure using Castep[29] modelling software (section 2.3.2.1). The crystal structure of $Li_3Na(ND_2)_4$ (as determined by Rietveld[11] analysis of neutron diffraction data in section 4.7.2) was used as the starting model for the $Li_3Na(NH_2)_4$ structure during these calculations. The geometry of this structure was optimised before a phonon density of states calculation was performed using the optimised geometry. A theoretical INS spectrum was calculated for the material using the optimised structure, which is presented with the experimental data in Figure 4.19.

The quality of the fit between the model spectrum and the experimental data can not be statistically calculated (*cf* Rietveld refinement, section 2.1.4) and must therefore be assessed visually.

In this study, the match between the data and model is very good. There appears to be a shift of ~20 cm^{-1} between the vibrations of model and the data, but otherwise, the relative intensities and positions of the vibrational modes appear to be in good agreement. This indicates that the crystal structure calculated by Castep[29] modelling was a good description of the true structure of $Li_3Na(NH_2)_4$.

The geometrically optimised crystal structure is presented in Figure 4.20a, with the crystal structure calculated from refinement of neutron diffraction data shown for comparison in Figure 4.20b.

There appear to be several differences between the two structures. Firstly, the *z* - displacement of the Li^+ ions at the (0,½,z) lattice sites was calculated to be greater in the structure calculated using the Castep software, compared to that obtained from analysis of neutron diffraction data. Secondly, the N-H(D) orientations calculated from the Castep model are different to those calculated from neutron studies. Viewing the unit cells along the *c*-axis, we can see that the structure calculated from neutron diffraction data has ND_2 units located in almost symmetrical positions, creating two perpendicular mirror planes. This symmetry is removed in the Castep calculations due to the imposition of the $P1$ space group, resulting in a more skewed N-D(H) alignment.

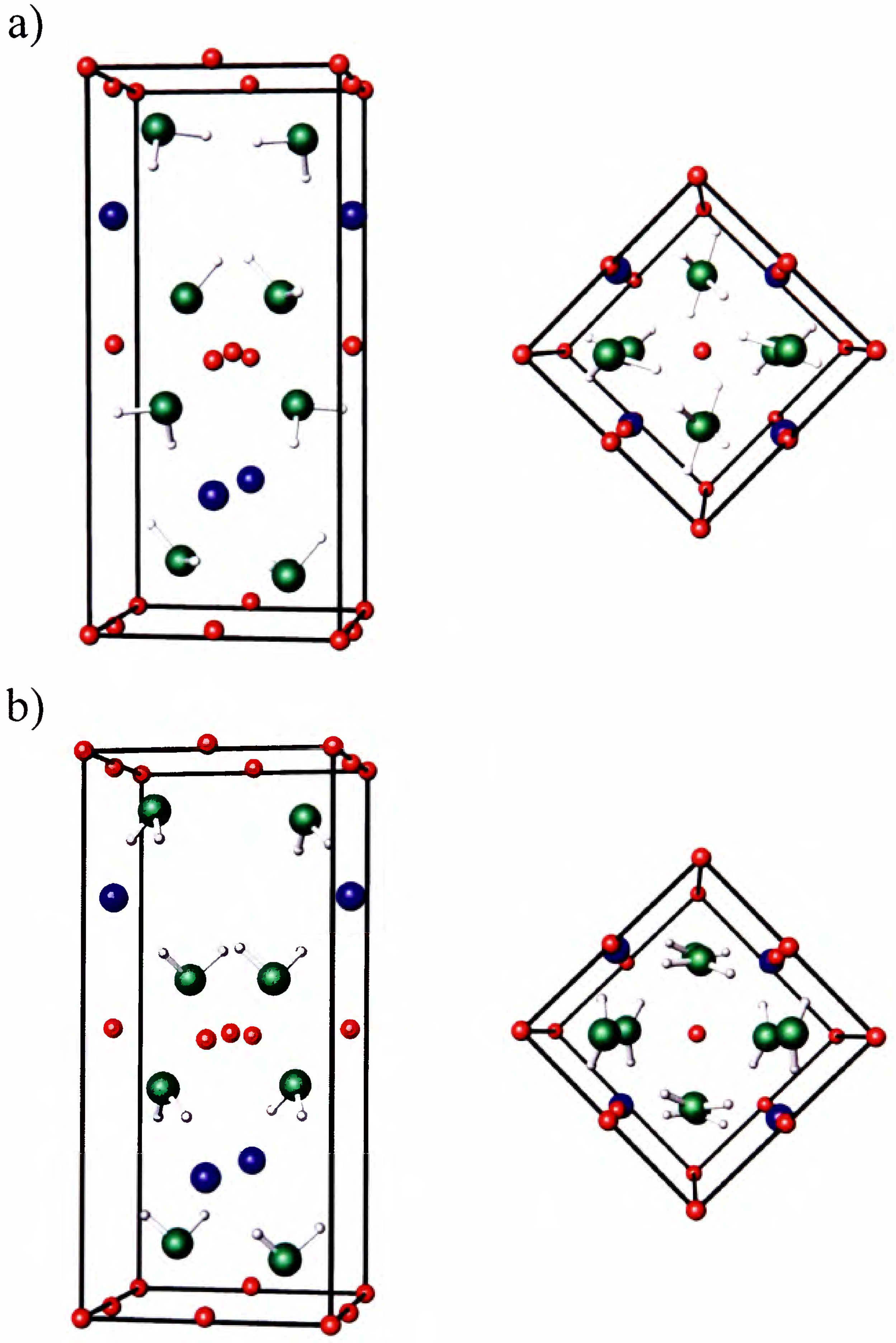

Figure 4.20 : Comparison of crystal structures of a) $Li_3Na(NH_2)_4$ calculated from geometry optimisation using Castep modelling and b) $Li_3Na(ND_2)_4$ calculated from Reitveld analysis of neutron diffraction data. The red spheres are lithium, the blue spheres sodium, the green spheres nitrogen, the white spheres hydrogen and the grey spheres are deuterium.

4.8 Study of High Purity $LiNa_2(NH_2)_3$

High purity $LiNa_2(NH_2)_3$ was formed from the reaction of $LiNH_2$ with $NaNH_2$ in an approximate ratio of 1:2 under flowing Argon gas at 200 °C (section 2.6.4.5).

A number of compositions of $(LiNH_2)_x(NaNH_2)_{(1-x)}$ with $x \sim 0.33$ were studied and the material of highest purity $LiNa_2(NH_2)_3$ was obtained from a composition of $x = 0.38$. The material formed was analysed using a variety of techniques including diffraction, spectroscopy, calorimetry and gravimetric analysis.

4.8.1 Synchrotron X-ray Diffraction Study of $LiNa_2(NH_2)_3$

High resolution synchrotron X-ray diffraction data were collected from a high purity sample of $LiNa_2(NH_2)_4$ using the ID31 beam line at the ESRF (section 2.1.2.3). The $LiNa_2(NH_2)_4$ sample was thoroughly ground under inert atmosphere and packed into a silica glass capillary tube, which was sealed and mounted onto the diffractometer. Diffraction data were collected at wavelength $\lambda = 0.8026$ Å and step size 0.003°, and were then refined using the Rietveld method[11] (section 2.1.4) with TOPAS Academic software,[12] according to the general method outlined in section 2.1.4.1. In addition to the parameters listed in section 2.1.4.1, the z-coordinate of the 4i ($\frac{1}{2}$,0,z) Na position, the x and y-coordinates of the 4j (x,y,0) Li and N1 positions and the x, y and z coordinates of the 8k (x,y,z) N2 position were refined for the $LiNa_2(NH_2)_3$ phase, and preferred orientation of this phase was modelled using a spherical harmonic function. The diffraction data and refined model are presented in Figure 4.21.

The sample was shown from refined scale factors to be majority phase $LiNa_2(NH_2)_3$ (96.4 wt%) with minority Li_2O (1.4 wt%) and $Li_3Na(NH_2)_4$ (2.2 wt%). All further attempts to improve sample purity were unsuccessful.

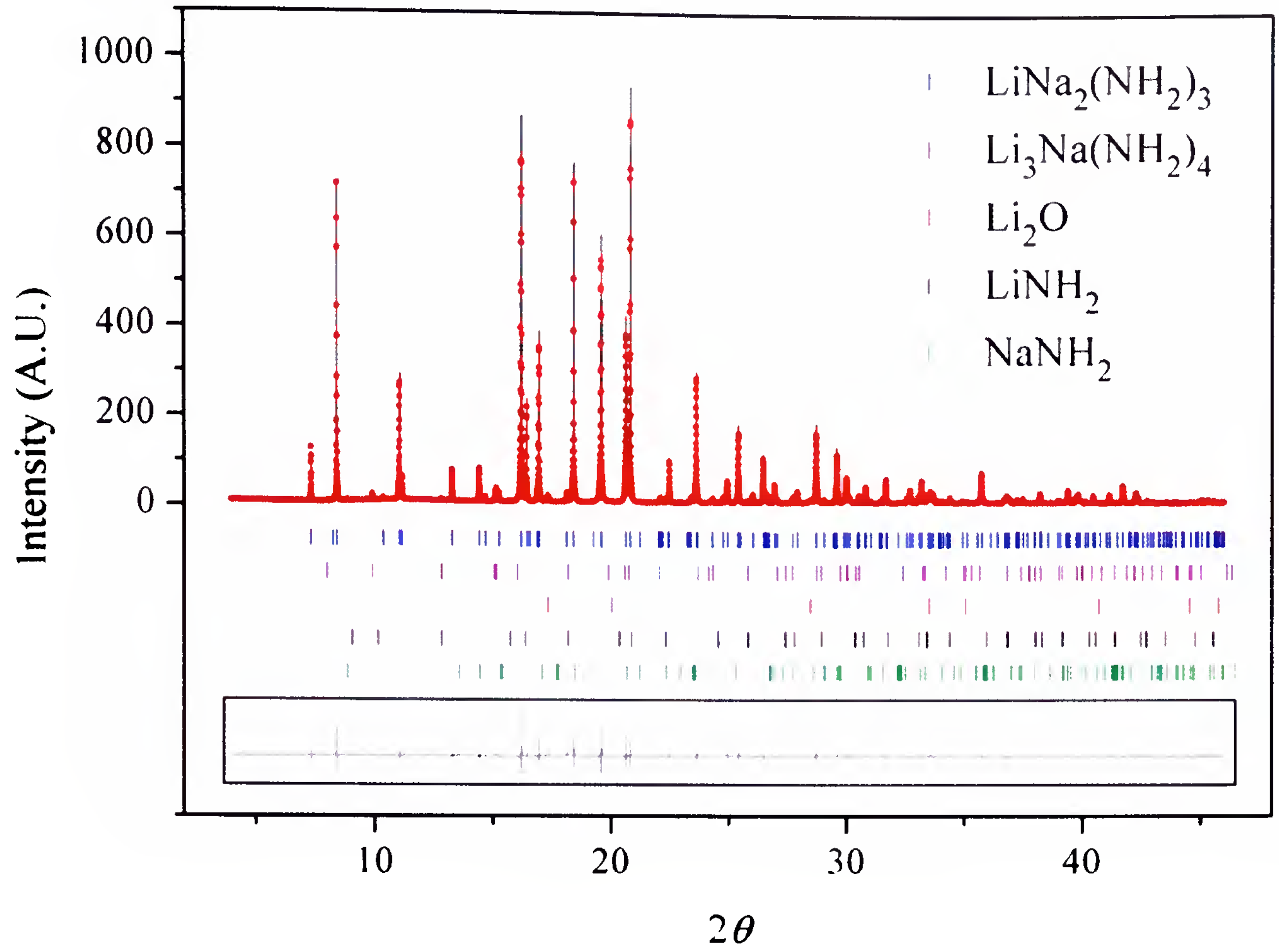

Figure 4.21 : Observed (solid line), calculated (red dots), and difference plots (y_{obsd} - y_{calc}, solid line in box) for the structure refinement of a sample of high-purity $LiNa_2(NH_2)_3$ from synchrotron X-ray diffraction data, collected at λ = 0.8026 Å with a step size of 0.003 Å. The Bragg peak positions for $LiNa_2(NH_2)_3$, $Li_3Na(NH_2)_4$, $LiNH_2$, Li_2O and $NaNH_2$ are shown by the vertical tick marks. R_{wp} 6.362, R_{exp} 2.938, goodness of fit 2.165

The $LiNa_2(NH_2)_3$ Bragg reflections were sharp and symmetrical, indicating the presence of a highly crystalline, stoichiometric phase. The $LiNa_2(NH_2)_3$ lattice parameters were calculated as a = 6.28339 (3) Å and c = 11.14925 (5)Å, which are in very good agreement with the lattice parameters reported for this phase by Jacobs and Harbrecht[10] and those identified previously in this report (section 4.4.1).

4.8.2 Neutron Diffraction Study of $LiNa_2(ND_2)_3$

Neutron diffraction data from a sample of $LiNa_2(ND_2)_3$ were collected in order to determine the positions of deuterium within the crystal structure.

The $LiNa_2(ND_2)_3$ sample was synthesised from a 1:2 reaction of $LiND_2$ (formed from LiD + ND_3, section 2.6.2.1) with $NaND_2$ (from NaH + ND_3, section 2.6.3.1) at 200 °C under flowing argon, according to the method described in section 2.6.5.2. The sample was thoroughly ground and loaded into an 8mm vanadium can, and neutron diffraction data were collected over the period of one hour using the GEM diffractometer at the ISIS pulsed neutron facility (section 2.1.3.1). Rietveld analysis[11] of the data collected at banks 4 and 5 was performed simultaneously using TOPAS Academic software (section 2.1.4.1).[12] The diffraction data and refined profiles are presented in Figure 4.22.

The structural model generated from refinement of the synchrotron data (section 4.8.1) was used as the starting model for Rietveld analysis of the neutron data. In addition to the parameters listed in section 2.1.4.1, the z-coordinate of the 4i (½,0,z) Na site, the x- and y-coordinates of the 4j (x,y,0) Li and N1 sites and the x-, y-and z-coordinates of the 8k (x,y,z) N2 sites of $LiNa_2(ND_2)_3$ were refined. The atomic positions of D were then refined.

Two distinct ND_2^- units exist in the $LiNa_2(ND_2)_4$ structure, the D1 – N1 – D1 unit and the D2 – N2 – D3 unit. Both of the deuterium atoms in the D1 – N1 – D1 unit have the same atomic coordinates, and as such, the N1 – D1 bond lengths remained equal as the site coordinates of D1 and N1 were refined.

This was not the case for the D2 – N2 – D3 unit. Because the atomic coordinates of D2 and D3 are not the same, un-constrained refinement of the D2 and D3 positions resulted in two different N – D bond lengths within the same ND_2 unit. To prevent this, a rigid rotor model was constructed for the $[D2 – N2 – D3]^-$ ion, which ensured that the N2 – D2 and N2 – D3 bonds remained equal as the D positions were refined. Using this model (with the N2 position used as the fixed point of the rotor) the

N2 – D2 and N2 – D3 bond lengths were calculated at 0.978(5) Å and the D2 – N2 – D3 bond angle 99.8(7)° (*cf* N – D bond length 0.967 Å and 0.978 Å, D – N – D angle 104.0° in $LiND_2$).[21] The fractional D / H occupancies of the D sites were then refined (with total site occupancies set to 1) to estimate the D / H ratio of the sample. More accurate values for the D / H ratio could be obtained by using spectroscopic techniques, however, such accuracy was not necessary in this study. The presence of H within the sample is attributed to the use of NaH in the synthesis of the $NaND_2$ precursor material.

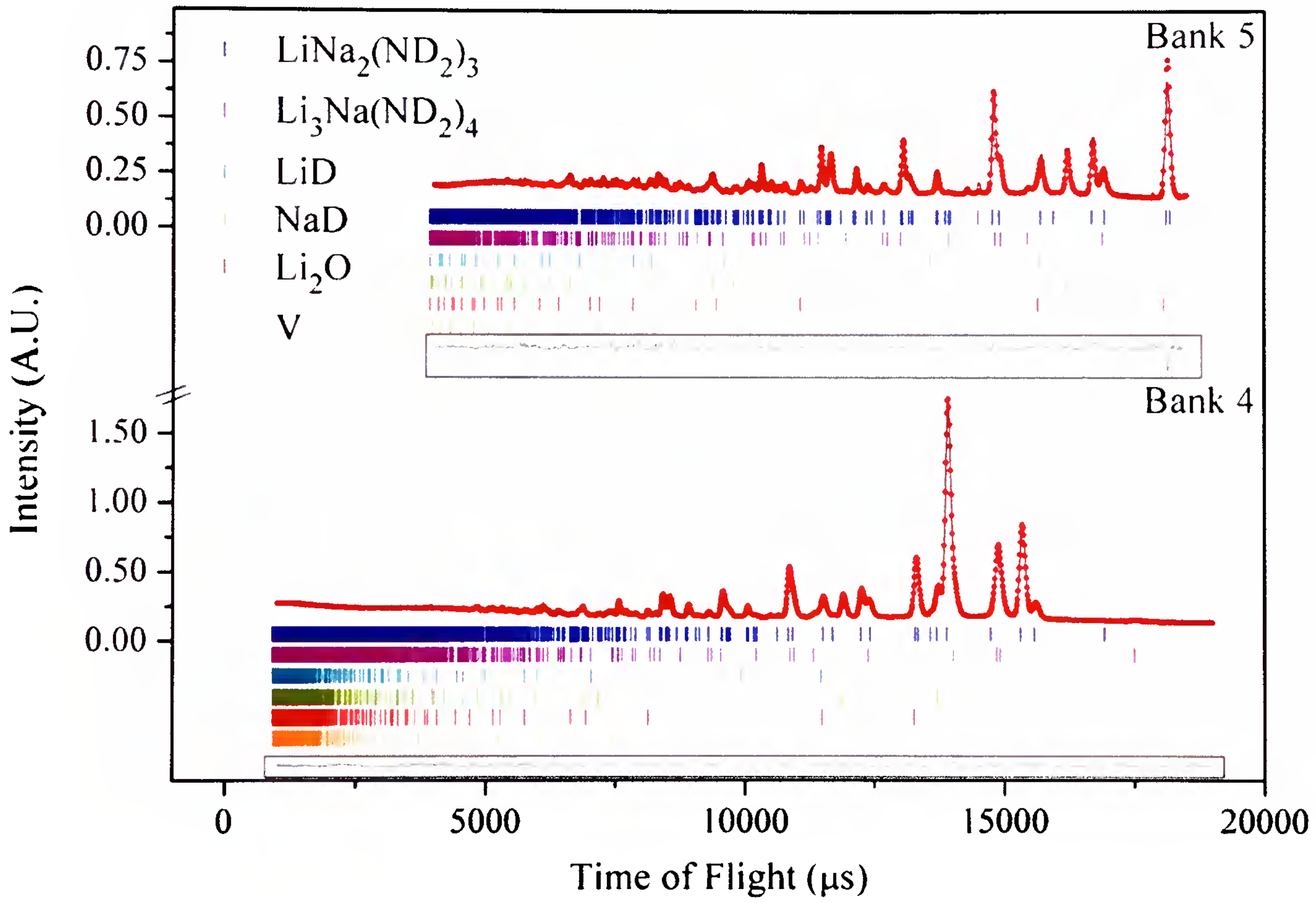

Figure 4.22 : Observed (solid line), calculated (red dots), and difference plots (y_{obsd} - y_{calcd}, solid lines in boxes) for the structure refinement of $LiNa_2(ND_2)_3$, from neutron diffraction data collected at banks 4 and 5 of the GEM diffractometer. The Bragg peak positions for $LiNa_2(ND_2)_3$, $Li_3Na(ND_2)_4$, LiD, NaD, Li_2O and V are shown by the vertical tick marks. R_{wp} 3.491, R_{exp} 0.976, goodness of fit 3.575.

A schematic diagram of the $LiNa_2(ND_2)_3$ crystal structure generated from these refinements is presented in Figure 4.23. The calculated atomic positions, unit cell parameters and thermal parameters are summarised in Table 4.9.

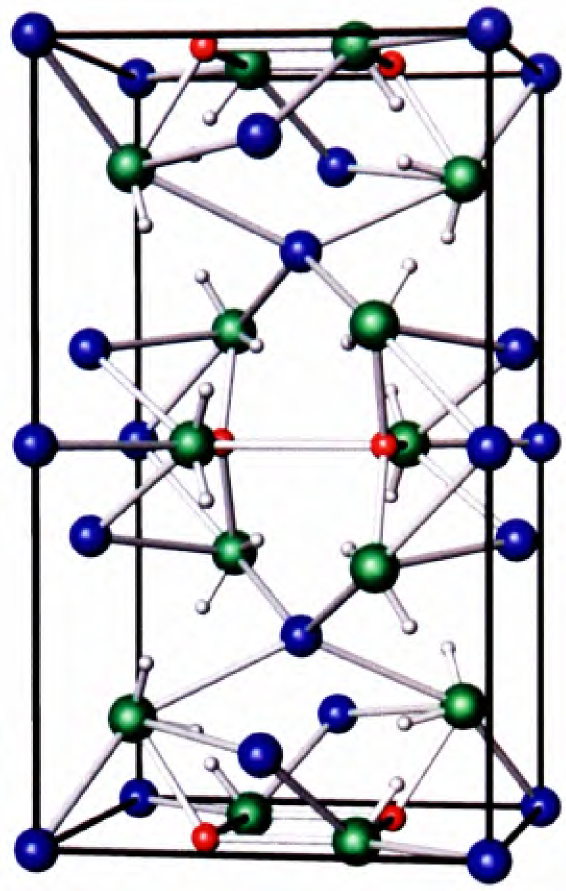

Figure 4.23 : Schematic diagram of the crystal structure of $LiNa_2(ND_2)_3$, calculated from Rietveld analysis of neutron diffraction data. Li is represented by red spheres, sodium by blue spheres, nitrogen by green spheres and deuterium by grey spheres

$LiNa_2(ND_2)_3$

Atom	Site	*x*	*y*	*z*	Occupancy	B_{iso} (Å^2)
Na1	4i	0.50	0.0	0.122(1)	1	4.7172
Na2	2a	0.0	0.0	0.0	1	4.7172
Na3	2f	0.50	0.50	0.25	1	4.7172
Li1	4j	0.321(6)	0.276(4)	0.0	1	4.7172
N1	4j	0.685(3)	0.278(2)	0.0	1	3.6946
D1	8k	0.749(3)	0.328(3)	0.069(1)	0.79(1)	4.1252
H1	8k	0.749(3)	0.328(3)	0.069(1)	0.20(1)	4.1252
N2	8k	0.152(1)	0.272(1)	0.1505(7)	1	4.1252
D2	8k	0.280(1)	0.352(1)	0.1304(7)	0.79(1)	4.1252
H2	8k	0.280(1)	0.352(1)	0.1304(7)	0.20(1)	4.1252
D3	8k	0.199(1)	0.202(1)	0.2243(7)	0.79(1)	4.1252
H3	8k	0.199(1)	0.202(1)	0.2243(7)	0.20(1)	4.1252

$a = b = 6.2908(1)$ Å, $c = 11.1524(4)$ Å

Table 4.9 : Refined structural parameters and atomic positions for $LiNa_2(ND_2)_3$ (space group $P4_2/m$, number 82), from Rietveld analysis of neutron diffraction data. A rigid rotor model was employed for D2 – N2 – D3 unit, giving an N – D bond length of 0.978(5) Å, and a D2 – N2 – D3 bond angle of 99.8(7) °.

The sample studied was shown to be majority phase $LiNa_2(ND_2)_3$ (74.3 mass%) with $Li_3Na(ND_2)_4$ (11 mass%), NaD (11.3 mass%), Li_2O (1.5 mass%) and LiD (1.7 mass%) impurities. These impurity phases were thought to arise from the presence of un-reacted LiD in the precursor $LiND_2$ (section 3.6.1).

The lattice parameters and atomic positions calculated for Na, Li and N were found to be in good agreement with those obtained from Rietveld analysis of the synchrotron diffraction data (section 4.8.1).

4.8.3 Study of $LiNa_2(ND_2)_3$ Using Intelligent Gravimetric Analysis Combined with Neutron Diffraction

A combined thermogravimetric and crystallographic study of the decomposition of $LiNa_2(ND_2)_3$ was performed using the IGA^n apparatus (section 2.2.2).

The $LiNa_2(ND_3)_4$ sample outlined in section 4.8.2 was loaded under inert conditions into a quartz bucket, which was then loaded into the IGA^n apparatus as described in section 2.2.2. The sample was heated under dynamic vacuum to 95 °C, 135 °C, 160 °C, 250 °C, 300 °C and 310 °C, holding at each set-point until the gravimetric data showed no further mass loss from the sample. The mass, temperature and pressure of the sample were recorded at intervals of 5.7 seconds throughout the experiment. Neutron diffraction data were collected at intervals of 2.52 minutes during the experiment until the sample reached 250 °C, at which point the neutron beam was lost.

The diffraction data collected are summarised in a surface plot (section 3.4), which is presented together with the corresponding thermogravimetric data in Figure 4.24. The thermogravimetric data for the full decomposition reaction are presented in Figure 4.24b.

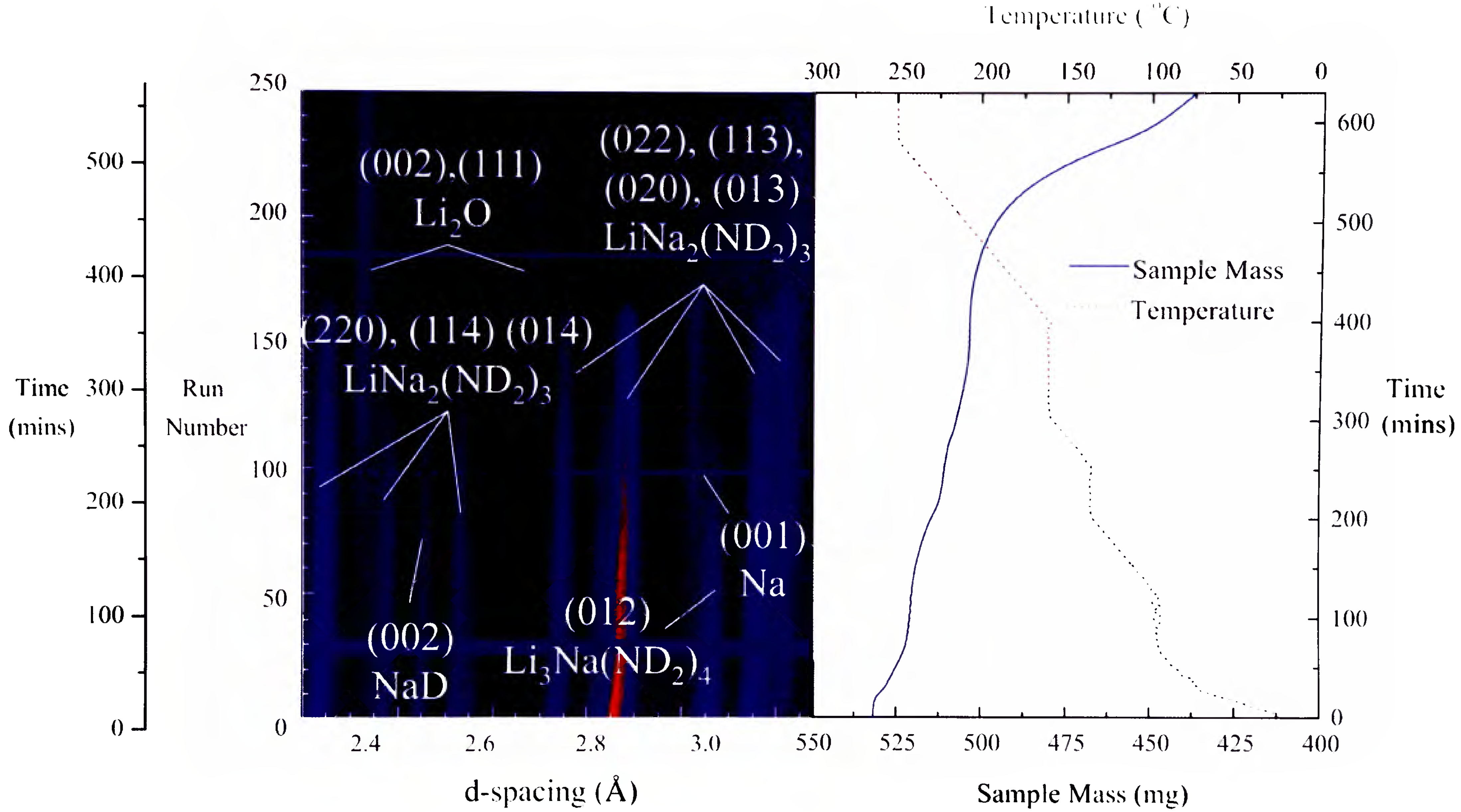

Figure 4.24 : Comparison of the surface plot of neutron diffraction data (collected at bank 4) and thermogravimetric data of the decomposition reaction of $LiNa_2(ND_2)_3$ performed using the IGA^n apparatus under dynamic vacuum. Bragg reflections for the various phases present are indexed.

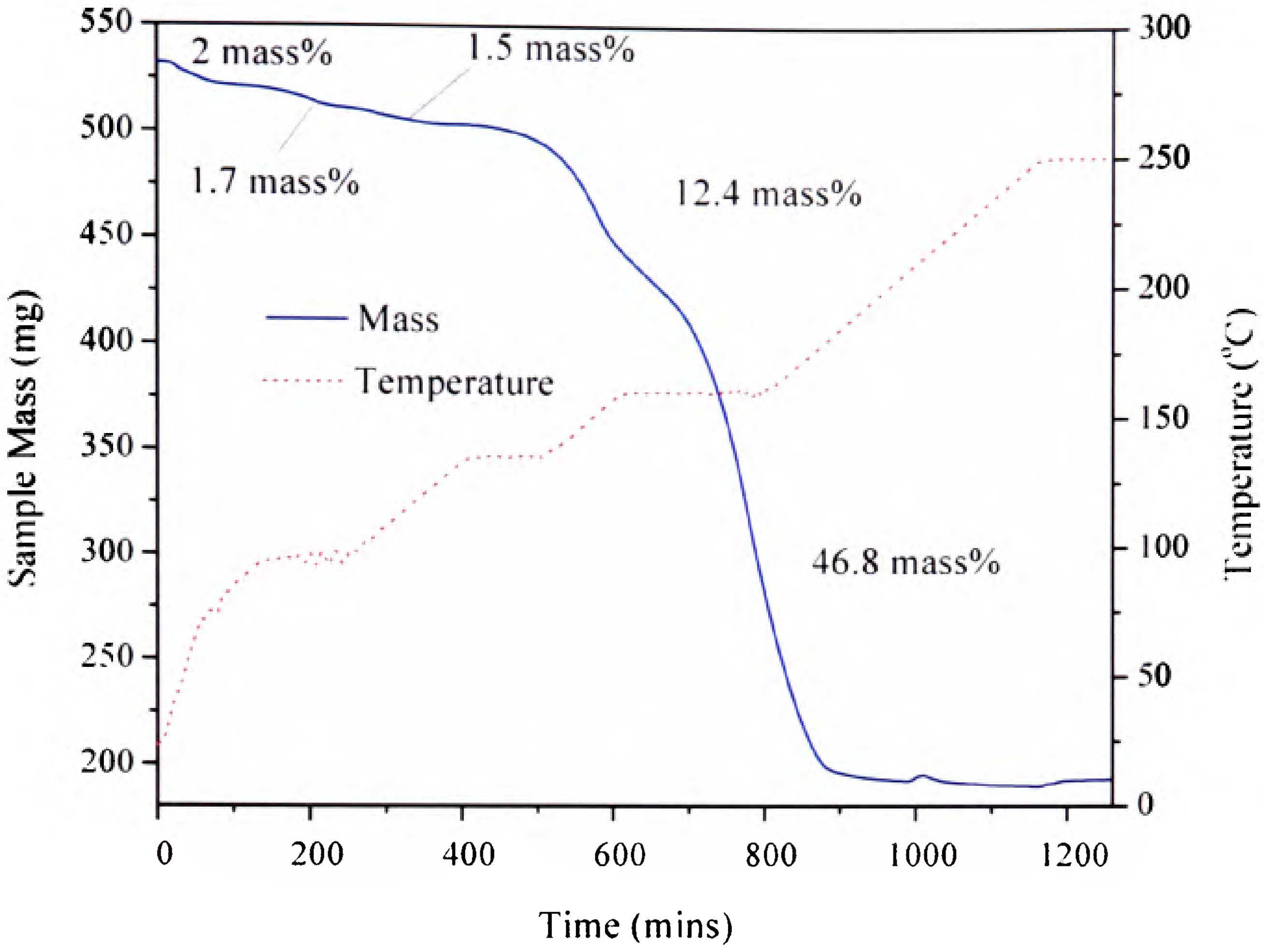

Figure 4.24 b : Thermogravimetric data for the full decomposition of $LiNa_2(ND_2)_3$ in the IGA^n apparatus. The blue line is the sample mass and the red line the sample temperature.

Figure 4.24a suggests that the decomposition of the $LiNa_2(ND_2)_3$ sample was an extremely complex process. The Bragg reflection at d-spacing 3.06 Å (indexed to the (012) reflection of $Li_3Na(ND_2)_4$) was the first to decrease in intensity (as the temperature reached 100 °C) and was no longer visible in the diffraction data above 160 °C. The decrease in intensity of the 3.06 Å reflection was accompanied by the appearance of a new reflection at d-spacing 3.02 Å, which was indexed to the (001) reflection of Na.

The next crystallographic change was observed as the sample temperature reached 140 °C, when the intensities of the reflections at d-spacing 2.23 Å, 2.37 Å, 2.52 Å, 2.74 Å, 2.85 Å, 3.15 Å and 3.21 Å decreased. These peaks were indexed, respectively, to the (220), (114), (014), (022), (113), (020) and (013) reflections of

$LiNa_2(ND_2)_3$. The decreasing intensity of these reflections was accompanied by the appearance of two new reflections at d-spacing 2.3 and 2.7 Å, which were indexed to the (1 1 1) and the (002) reflections of Li_2O, respectively.

The thermogravimetric data collected during the decomposition of $LiNa_2(ND_2)_3$ (Figure 4.24b) shows a total of five mass-loss steps. The first and second mass losses had onset temperatures of 43 °C and 95 °C, and resulted in the loss of 2 mass% and 1.7 mass %, respectively. The third mass loss (1.5 mass%) occurred as the sample temperature was increased from 137 °C to 160 °C, and the fourth (12.4 mass%) occurred between temperatures of 170 °C to 250 °C. The fifth and final mass loss (46.8 mass%) was observed as the sample temperature increased from 250 °C up to 310 °C, and continued as the temperature was maintained at 310 °C.

4.8.3.1 Rietveld Analysis of Neutron Diffraction Data Collected During Decomposition of the $LiNa_2(ND_2)_3$ Sample

Refinement of the neutron diffraction data collected during this experiment was performed by the Rietveld method[11] (section 2.1.4), using the batch facility of TOPAS Academic,[12] according to the general method outlined in section 2.1.4.2.

Rietveld analysis[11] of the neutron diffraction data of the sample prior to decomposition (section 4.8.2) indicated that the composition was $LiNa_2(ND_2)_3$ (74.3 wt%), $Li_3Na(ND_2)_4$ (11 wt%), NaD (11.3 wt%), Li_2O (1.5 wt%) and LiD (1.7 wt%). The resolution of the diffraction data collected during this experiment was such that the Bragg reflections of Li_2O and LiD could not be resolved from the background data, and so these phases were not included in the starting refinement model.

The refined scale factors and lattice parameters calculated for the phases present during the decomposition of the $LiNa_2(ND_2)_3$ sample are presented in Figures 4.25a, b and c. A full summary of the refined parameters is presented in Appendix A1.3.

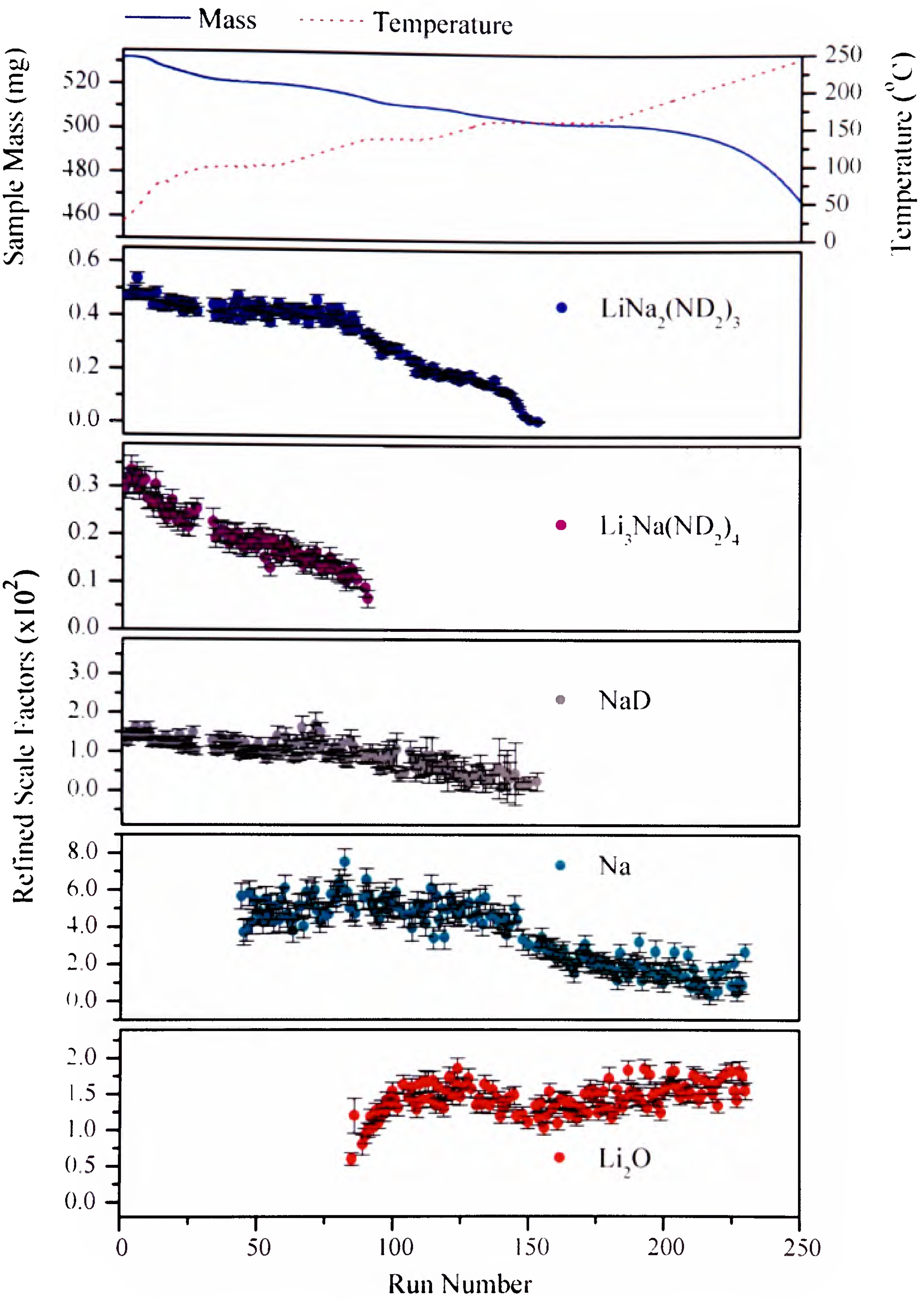

Figure 4.25a : Summary of refined scale factors, calculated from Rietveld analysis (*via* batch refinement) of the neutron diffraction data collected during $LiNa_2(ND_2)_3$ decomposition in the IGA^n. The mass and temperature traces are included for ease of comparison. Mean errors $LiNa_2(ND_2)_3$ ± 0.00015, $Li_3Na(ND_2)_4$ ± 0.0002, NaD ± 0.002, Na ± 0.005, Li_2O ± 0.0011

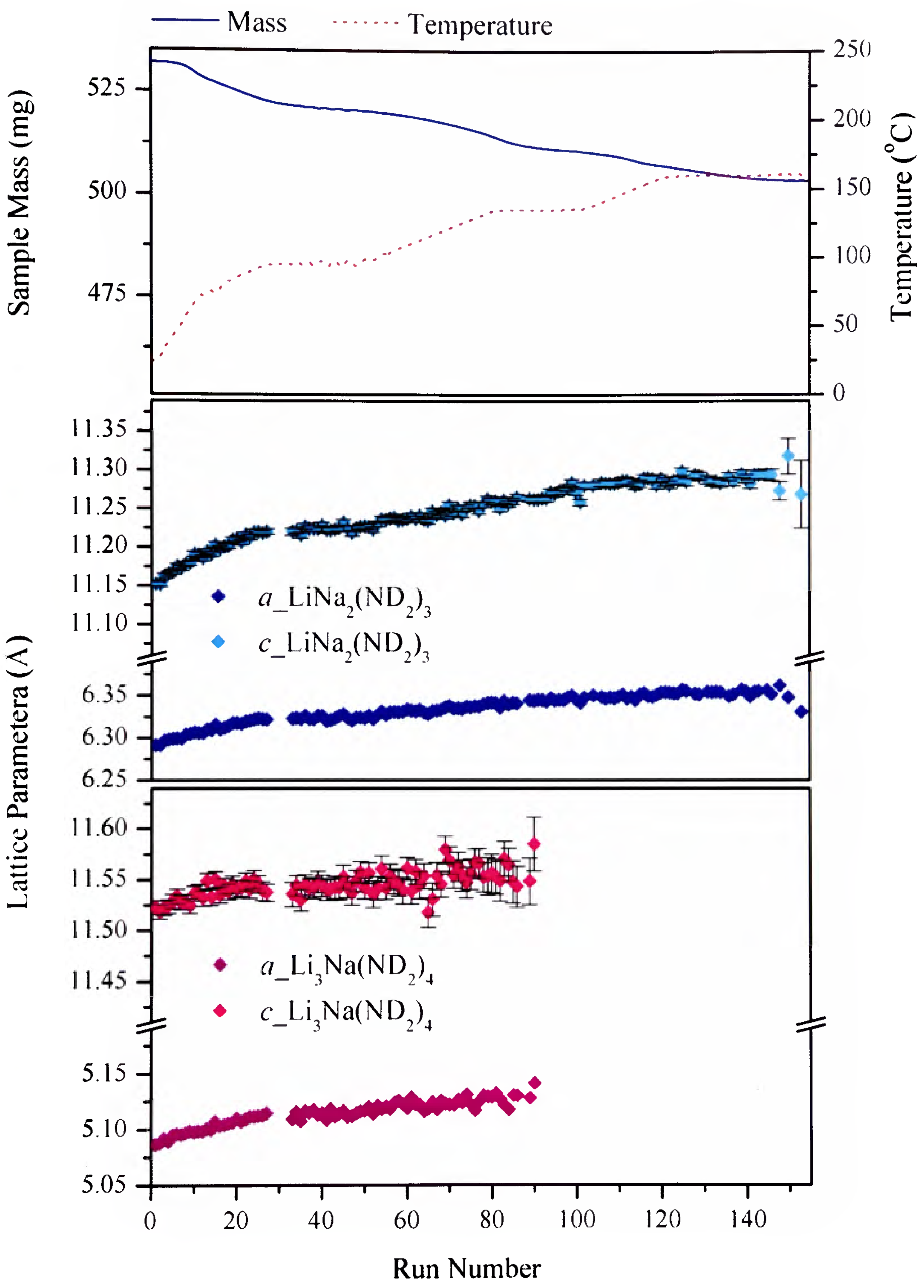

Figure 4.25b : Summary of the refined lattice parameters of $LiNa_2(ND_2)_3$ and $Li_3Na(ND_2)_4$, calculated from Rietveld analysis (*via* batch refinement) of the neutron diffraction data collected during the decomposition of the $LiNa_2(ND_2)_3$ sample in the IGA^n apparatus. The mass and temperature traces are included for ease of comparison. Mean errors a_$LiNa_2(ND_2)_3$ ± 0.002, c_$LiNa_2(ND_2)_3$ ± 0.005, a_$Li_3Na(ND_2)_4$ ± 0.002 and c_$Li_3Na(ND_2)_4$ ± 0.0010. Error bars only presented if larger than the data markers.

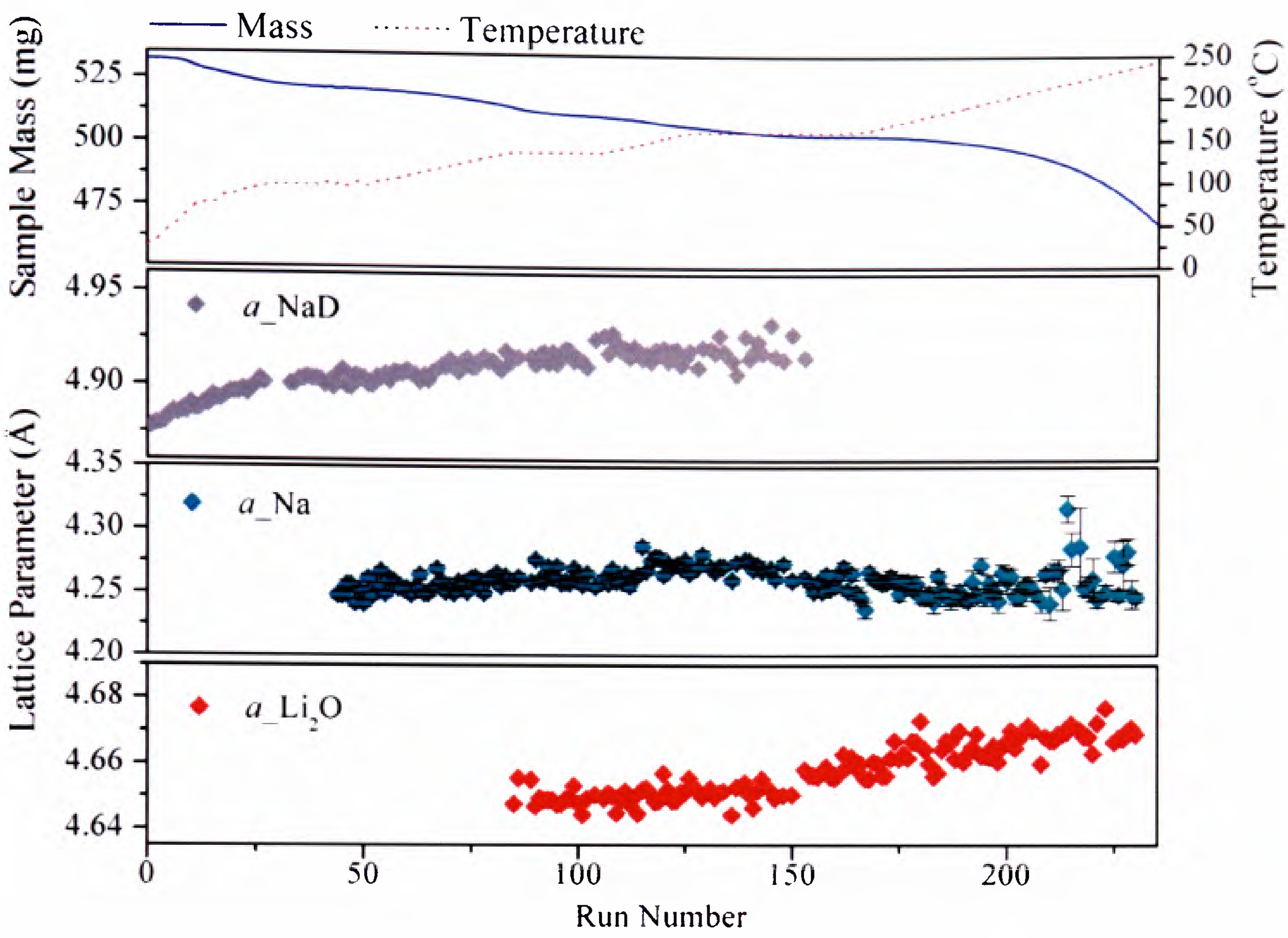

Figure 4.25c : Summary of the refined lattice parameters of Li_2O, Na and NaD, calculated from Rietveld analysis (*via* batch refinement) of the neutron diffraction data collected during the decomposition of the $LiNa_2(ND_2)_3$ sample in the IGAn apparatus. The mass and temperature traces are included for ease of comparison. Mean errors a_Li_2O ± 0.0018, a_Na ± 0.006, a_NaH ± 0.004. Error bars only presented if larger than data markers.

The scale factor of $Li_3Na(ND_2)_4$ (Figure 4.25a) was the first observed to decrease. This decrease began as the temperature of the sample reached 50 °C and continued steadily up to a temperature of 135 °C. A sharp decrease to zero was then observed during the isothermal step at 135 °C, and Bragg reflections for $Li_3Na(ND_2)_4$ were not observed in the diffraction data above this temperature.

The scale factor of $LiNa_2(ND_2)_3$ decreased slowly between temperatures of 45 °C and 90 °C. The decrease in $LiNa_2(ND_2)_3$ scale factor became more rapid as the sample reached 135 °C, but slowed during the isothermal step at 135 °C, and remained slow as the sample temperature was increased to 160 °C. During the isothermal step at

160 °C, the $LiNa_2(ND_2)_3$ scale factor decreased rapidly to zero, and Bragg reflections arising from $LiNa_2(ND_2)_4$ were not observed in the diffraction data above this temperature.

The decrease observed in the $LiNa_2(ND_2)_3$ scale factor at 135 °C was accompanied by an increase in the scale factor of Li_2O. This is consistent with the reaction of some $LiNa_2(ND_2)_3$ with oxygen, (most probably derived from the SiO_2 sample bucket) forming Li_2O. After the initial increase, the Li_2O scale factor remained virtually constant during the remainder of the experiment, indicating that all $LiNa_2(ND_2)_3$ in contact with the bucket had reacted with the quartz, and therefore, all of the accessible oxygen had been utilised.

The scale factor of NaD decreased slowly throughout the course of the experiment. The temperatures used during the study were significantly lower than the decomposition temperature reported for NaD (425 °C),[27] which indicates that the NaD present in the sample was consumed through reaction with ammonia.

The $LiNa_2(ND_2)_3$ and $Li_3Na(ND_2)_4$ lattice parameters, calculated from Rietveld analysis[11] of the diffraction data, are presented in Figure 4.25b. The lattice parameters of $LiNa_2(ND_2)_3$ were observed to increase linearly with temperature, indicating that the material underwent thermal expansion prior to decomposition. The lattice parameters of $Li_3Na(ND_2)_4$ behaved in a similar fashion to that observed in section 4.7.3, suggesting that sodium migrated out of the $Li_3Na(ND_2)_4$ structure, before the phase became amorphous.

The lattice parameters of Li_2O, Na and NaD are presented in Figure 4.25c. The a-parameters of Li_2O and NaD were observed to increase linearly as a function of temperature, which is consistent with thermal expansion of the materials. The lattice parameter of Na did not demonstrate a particular dependence on temperature, but became less accurately determined as the temperature reached 160 °C. This coincided with a significant decrease in the Na scale factor, indicating that the sodium metal present in the sample melted at 160 °C.

No Bragg reflections were observed corresponding to the product of the decomposition reaction, suggesting that the non-gaseous material formed during $LiNa_2(ND_2)_3$ decomposition was amorphous under these conditions.

The cooled, solid decomposition product was unloaded from the IGA^n apparatus, and then re-ground and loaded into an 8mm diameter vanadium can. Neutron diffraction data from this sample were collected using the GEM diffractometer, and the unknown phase was indexed from this data to a body centred unit cell of space group *Immm*, with lattice parameters a = 5.543(18) Å, b = 5.5426(3) Å and c = 3.9192(2) Å.

The thermogravimetric data indicates that five mass losses were observed during the decomposition of $LiNa_2(ND_2)_3$ (Figure 4.24b). The first mass loss (2 mass%) had an onset temperature of 43 °C and the second mass loss (1.7 mass%) was observed as the temperature increased from 95 °C. These two steps are attributed to desorption of physisorbed gas from the surface of the powder grains.

Upon heating from 137 °C to 162 °C a third mass loss of 1.5 mass% was observed, occurring just after the $Li_3Na(ND_2)_4$ scale factor had reached zero. The data outlined in section 4.7.3 suggested that $Li_3Na(ND_2)_4$ released gas only after it had transformed into an amorphous phase, and as such, the third mass loss observed in this study is thought to arise from decomposition of the $Li_3Na(ND_2)_4$ impurity.

The final two mass loss steps (Figure 4.24b) were observed between 162 °C and 250 °C (12.4 mass%) and 250 °C to 310 °C (46.8 mass%), respectively. These mass changes do not correspond to loss of ND_3, D_2, N_2 or Na from the sample. As such, further study is required to identify both the solid and gaseous products formed from the decomposition of $LiNa_2(ND_2)_3$.

4.8.4 Thermogravimetric Study of $LiNa_2(NH_2)_3$ Using Intelligent Gravimetric Analysis With Mass Spectrometry

The decomposition reaction of $LiNa_2(NH_2)_3$ was further studied using intelligent gravimetric analysis combined with mass spectrometry (IGA-MS, section 2.2.1). The ground sample was loaded, under inert conditions, into the IGA-MS apparatus as outlined in section 2.2.1. The sample was heated under a flow of 1 bar He at a rate of 2 °C per minute to 400 °C, and this temperature was maintained for 12 hours. The outgoing gases were sampled by the dynamic sampling mass spectrometer, which was set to scan for materials of 17, 2, 28, 23 and 39 atomic mass unite (AMU), corresponding to NH_3, H_2, N_2, Na and $NaNH_2$, respectively. Measurements of the sample mass, temperature, pressure, and the partial pressures of the released gases were taken every 0.2 minutes.

The thermogravimetric data for the decomposition of $LiNa_2(NH_2)_3$ are presented in Figure 4.26, together with the partial pressures of NH_3, H_2, N_2, Na and $NaNH_2$ (17, 2, 28, 23 and 39 AMU, respectively), recorded by *in-situ* mass spectrometry.

A total of three mass loss steps were observed during the decomposition of the $LiNa_2(NH_2)_3$ sample (determined from the gradient changes in the sample mass data, differential presented in Appendix A3). The first mass loss (6.1 mass%) was observed as the temperature of the sample increased from 50 °C to 182 °C and the second mass loss (1.4 mass%) occurred between temperatures of 182 °C and 204 °C. The final mass loss (62.6 mass%) commenced at 204 °C, and continued throughout the temperature increase to 400 °C, and during the subsequent isotherm.

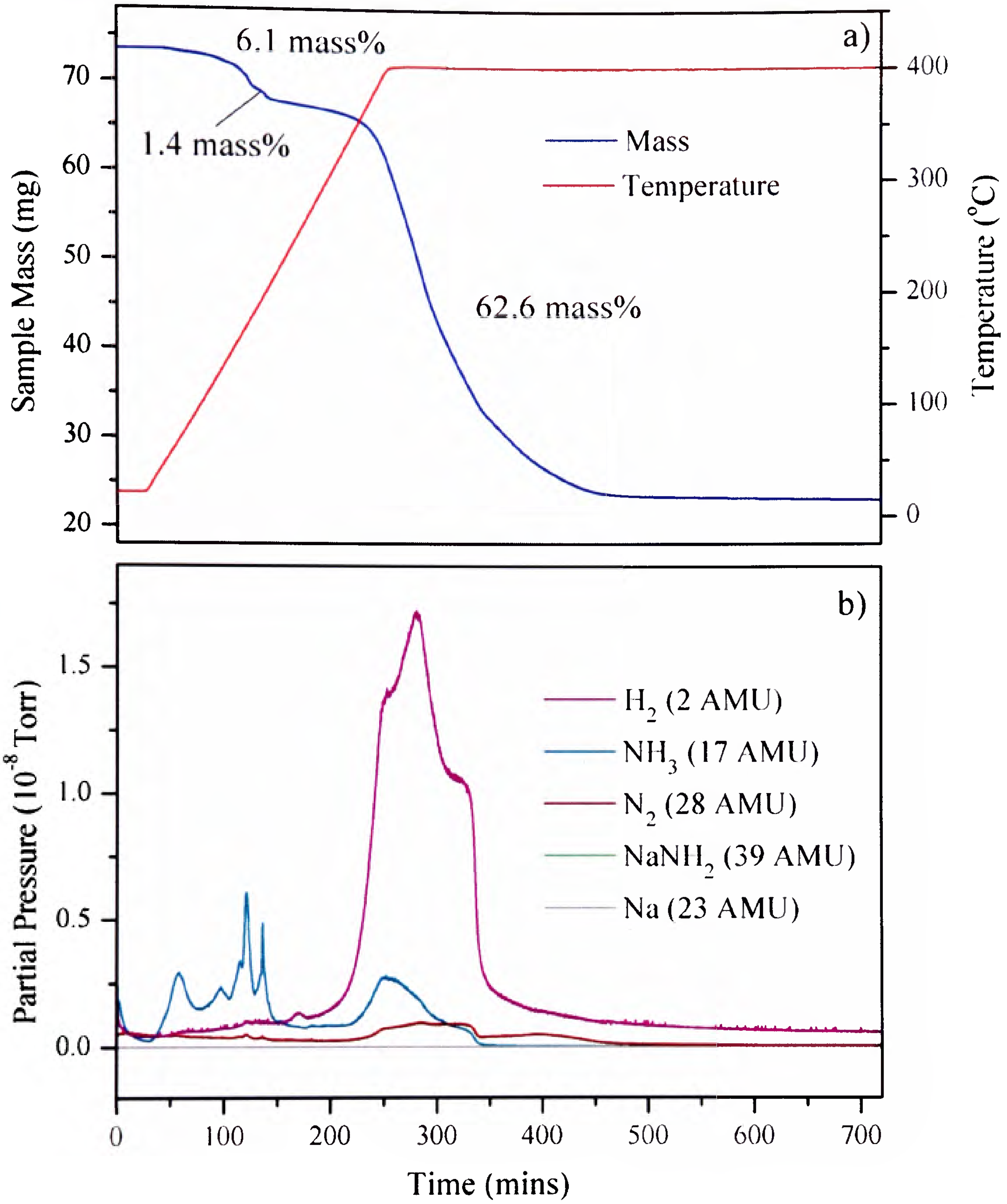

Figure 4.26a and b : a) Thermogravimetric data of high purity $LiNa_2(NH_2)_3$, collected using intelligent gravimetric analysis, with heating rate 2 °C/min and target temperature 400 °C. The red line represents the temperature of the sample and the blue line the sample mass. b) Partial pressures of H_2 (purple), NH_3 (turquoise), N_2 (dark red), Na (grey) and $NaNH_2$ (green), recorded during the thermogravimetric study of $LiNa_2(NH_2)_3$ using *in-situ* mass spectrometry.

The first and second mass loss steps were accompanied by several peaks in the partial pressure of NH_3 (17 AMU). These steps were attributed to the desorption of physisorbed ammonia from the powder grains.

The third desorption step resulted in a mass loss of 62.6 mass% from the sample, beginning as the temperature increased above 204 °C. This decomposition step was accompanied by a large peak in the recorded partial pressure of H_2 (2 AMU) and a small peak in the partial pressure of NH_3.

The 62.6 mass% lost during this desorption was far too great to be accounted for purely by the release of gases from the sample; indeed, if all N and H were released from $LiNa_2(NH_2)_3$, the observed mass loss would not exceed 48 mass%. It therefore appears that the decomposition of $LiNa_2(NH_2)_3$ proceeded with the evaporation of some metal from the sample.

Na has been shown previously to be volatised under such conditions (sections 4.6 and 4.7). No Na was recorded by the mass spectrometer, which indicates that the volatised Na condensed within the apparatus. This was evidenced by the presence of a dark crust on the gas inlet tube and thermocouple in the IGA reaction vessel.

It is possible that $LiNa_2(NH_2)_3$ decomposed during this experiment to release H_2, NH_3, N_2 and Na, leaving behind Li_3N. This would account for a mass loss of 65 mass%, which is in good agreement with the experimental value of 62.6 mass%.

4.8.5 Study of $LiNa_2(NH_2)_3$ Using Differential Scanning Calorimetery

In order to gain a greater understanding of the thermodynamic processes occurring during the decomposition of $LiNa_2(NH_2)_3$, Differential Scanning Calorimetry (DSC) measurements were performed on the material. The measurements were carried out under an Ar flow, with the sample heated at a rate of 5 °C/minute to 400 °C, and then cooled to room temperature at the same rate. The heat flow between the sample and its surroundings was measured as a function of time, with positive heat flow corresponding to exothermic events and negative heat flow corresponding to endothermic events.

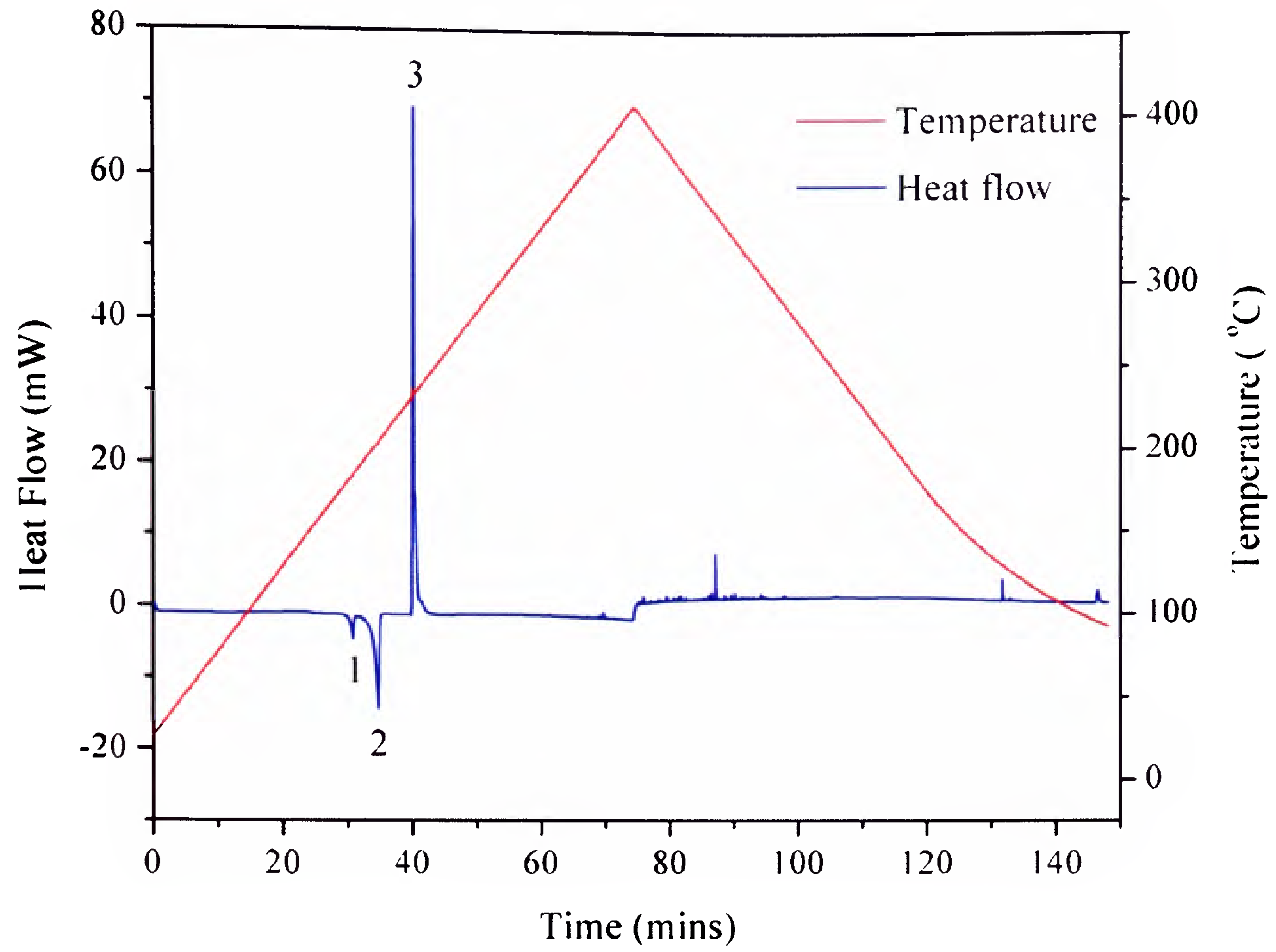

Figure 4.27: DSC study of $LiNa_2(NH_2)_3$, presenting heat flow (blue line) and temperature (red line) as a function of time. The sample was heated to 400 °C at a rate of 2 °C per minute.

The data collected during this experiment are presented in Figure 4.27, where the individual thermal events are numbered. The material was shown to undergo a total of three heat-exchange processes, all of which occurred as the temperature of the sample increased towards 400 °C. The enthalpy change of each event was calculated *via* integration of the relevant heat flow peak with respect to time. The thermodynamic data associated with each event are summarised in Table 4.10.

The first thermal event (numbered 1 in Figure 4.27) was an endothermic process with onset temperature 178 °C, peak temperature 183 °C and enthalpy change +3.669 $kJmol^{-1}$. This event is likely to have arisen from the desorption of physisorbed gases from the $LiNa_2(NH_2)_3$ sample.

Event number	Endo / exothermic	Onset temperature	Peak temperature	Integrated peak area (ΔH) kJ/mol
1	Endo	178	183	+3.669
2	Endo	189	203	+24.533
3	Exo	229	232, 234	-50.969

Table 4.10 : Summary of DSC data for $LiNa_2(NH_2)_3$. The material was heated to 400 °C at a rate of 5 °C/min and cooled to room temperature at 5 °C/min.

Event 2 was an endothermic process, with onset temperature of 189 °C, peak temperature of 203 °C and enthalpy change +24.533 kJmol^{-1}. This endotherm is likely to correspond to the transformation of $LiNa_2(NH_2)_3$ into an amorphous phase, which was observed at 160 °C in the intelligent gravimetric analysis and neutron diffraction study of $LiNa_2(ND_2)_3$ (section 4.8.4). This transformation was believed to arise from the melting of $LiNa_2(ND_2)_3$.

The third event was highly exothermic, with a reaction enthalpy of -50.969 kJ mol^{-1}. This exothermic peak is a doublet, with onset temperature 229 °C and peak temperatures of 232 and 234 °C. Decomposition at such temperatures was not observed in the thermogravimetric data described in sections 4.8.3 or 4.8.4, where the major mass losses commenced at temperatures of 170 °C and 204 °C, respectively.

The onset and peak temperatures of the decomposition events of $LiNa_2(NH_2)_3$ varied between this calorimetric study and the thermogravimetric studies presented in sections 4.8.3 and 4.8.4. Such variations are expected to have occurred due to the different experimental conditions used during data collection, including heating rates (5 °C/min for DSC, ≤ 2 °C/min for IGA-MS and IGA^n)[25] sample sizes (~10 mg for DSC, ~80 mg for IGA-MS and ~500 mg for IGA^n)[26] and pressures (1 bar flowing Ar in the DSC, 1 bar flowing He in the IGA-MS and dynamic vacuum in the IGA^n).

4.8.6 Study of $LiNa_2(NH_2)_3$ Using Raman Spectroscopy

The Raman spectrum (section 2.3.1) of $LiNa_2(NH_2)_3$ is presented in Figure 4.28, together with the spectra of $LiNH_2$, $Li_3Na(NH_2)_4$ and $NaNH_2$ for comparison.

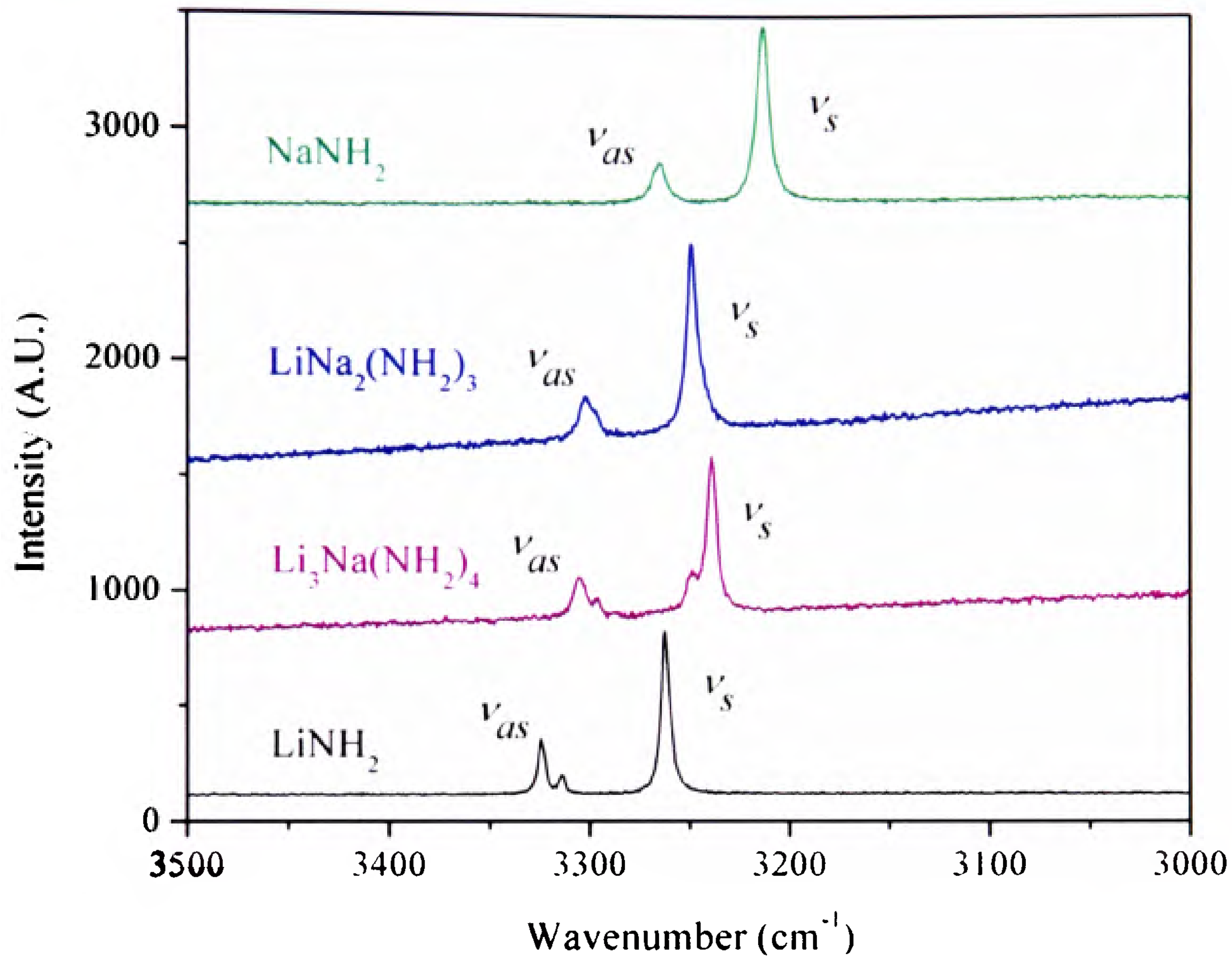

Figure 4.28 : Raman spectra of $LiNH_2$ (black line), $Li_3Na(NH_2)_4$ (purple line), $LiNa_2(NH_2)_3$ (blue line) and $NaNH_2$ (green line). The spectral range of 3500 – 3000 cm^{-1} is presented as this contains the well resolved symmetric (ν_s) and antisymmetric (ν_{as}) vibrational modes of the materials.

The only well resolved vibrational modes in the spectra of all four compounds were the symmetric and anti-symmetric stretching modes of the NH_2^- anion. The NH_2^- vibrational modes of $LiNa_2(NH_2)_3$ can be found at energies between those of the parent $LiNH_2$ and $NaNH_2$ compounds, presumably due inductive effects on the N – H bonds, arising from the presence of both Li and Na in the material (Pauling electronegativities of Li and Na 0.98 and 0.93, respectively). There was a small shoulder observed on the asymmetric stretch of $LiNa_2(NH_2)_3$, although this shoulder is much less pronounced than those observed on the asymmetric stretches of $LiNH_2$ and $Li_3Na(NH_2)_4$. This suggests that the orientation of the N – H bonds in $LiNa_2(NH_2)_3$ was such that the chemical environments of the H atoms in the structure were more similar than those in either $LiNH_2$ or $Li_3Na(NH_2)_4$.

4.8.7 Study of $LiNa_2(NH_2)_3$ Using Inelastic Neutron Scattering

Inelastic neutron scattering (INS) experiments were performed on a sample of $LiNa_2(NH_2)_3$ using the TOSCA spectrometer (section 2.3.2) at the ISIS pulsed neutron facility. The $LiNa_2(NH_2)_3$ sample was loaded under inert atmosphere into an aluminium can, which was lowered into the beamline and cooled to 4K. The INS data were collected over a number of hours.

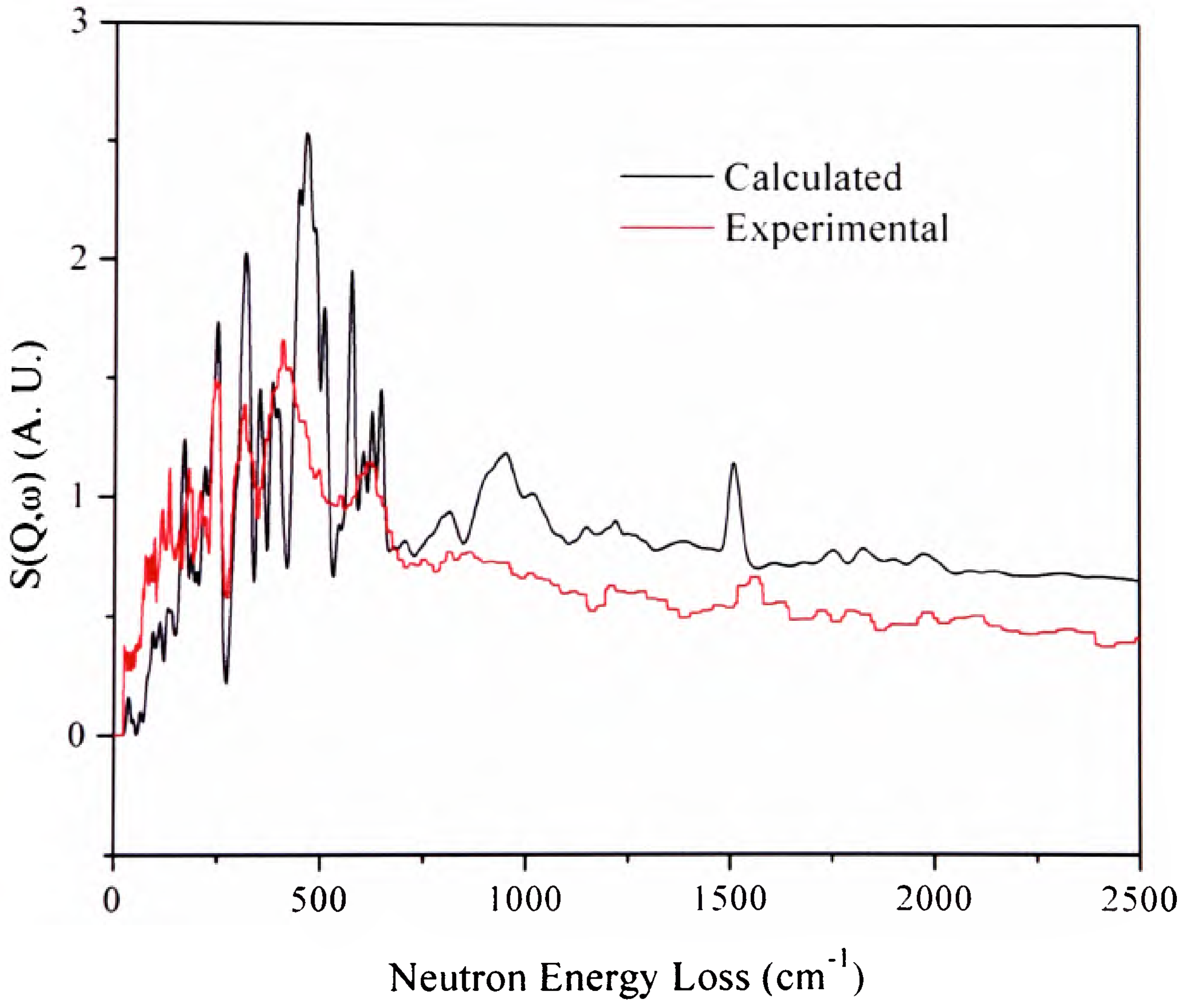

Figure 4.29: Experimental inelastic neutron scattering data of $LiNa_2(NH_2)_4$ (red line) and structural model (black line) calculated from the geometrically optimised structure using Castep modelling software.

Computer modelling simulations were performed on the $\mathrm{LiNa_2(NH_2)_3}$ structure using the Castep[29] modelling code (section 2.3.2.1), with the crystal structure of $\mathrm{LiNa_2(ND_2)_3}$ (as determined by Rietveld[11] refinement from neutron diffraction data in section 4.8.2) used as the starting model. The geometry of this structure was optimised by imposing a $P1$ space group, before a phonon density of states calculation was performed using the optimised geometry. This calculation was used to generate a theoretical INS spectrum for the material, which is presented together with the experimental data in Figure 4.29.

The match between the data and model is acceptable by INS standards. Most of the experimental peaks have counterpart peaks in the model, and though the intensity matches are not good, the peak positions are in good agreement. The sharp peaks observed at 360 cm^{-1} and 575 cm^{-1} and the broad peak between 450 and 500 cm^{-1} in the model are conspicuously absent from the experimental data. These peaks may form part of the three broad humps which are observed between 275 and 650 cm^{-1} in the experimental data. This indicates that the geometrically optimised crystal structure calculated by Castep[29] modelling was a fair representation of the true structure of $\mathrm{LiNa_2(NH_2)_3}$.

The geometrically optimised crystal structure calculated using Castep[29] software is presented in Figure 4.30a, with that calculated from Rietveld analysis of neutron diffraction data shown for comparison in Figure 4.30b.

There is good agreement between the positions of Na and N calculated from Rietveld analysis[11] of the neutron diffraction data and Castep[29] modelling. The Li positions in the structure calculated using Castep are closer towards the intersection of the (110) and $(\bar{1}10)$ plane in the unit cell, compared to the positions calculated from refinement of the neutron diffraction data.

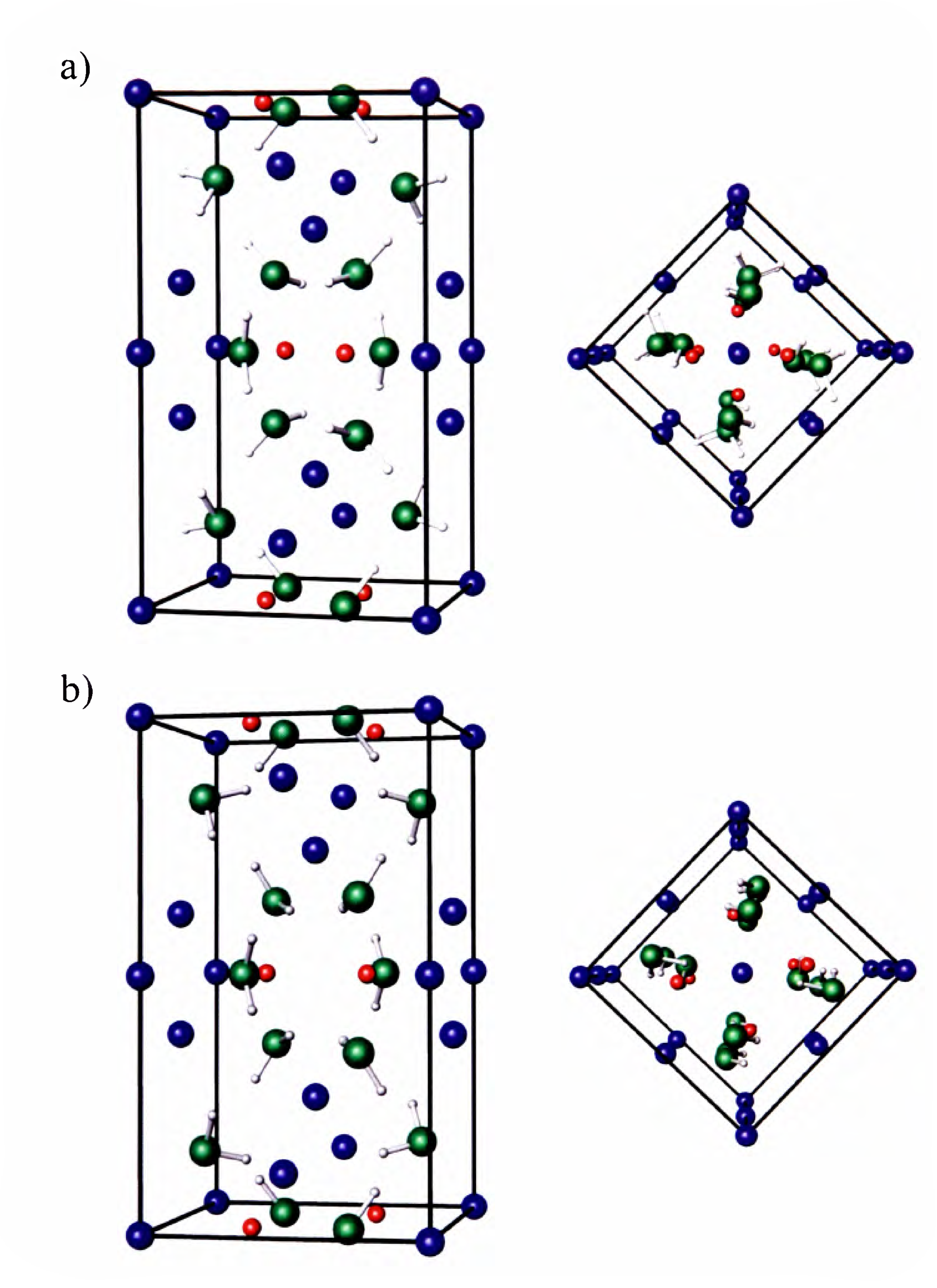

Figure 4.30 : Comparison of the crystal structures of a) $LiNa_2(NH_2)_3$ calculated from geometry optimisation using Castep modelling and b) $LiNa_2(ND_2)_3$, calculated from Rietveld analysis of neutron diffraction data. The red spheres are lithium, the blue spheres sodium, the green spheres nitrogen, the white spheres hydrogen and the grey spheres deuterium.

4.9 Study of High-Purity $Li_{(1-z)}Na_zNH_2$.

The synchrotron diffraction data collected for the $(LiNH_2)_x(NaNH_2)_{(1-x)}$ samples studied in section 4.4 implied that a small amount of sodium was soluble in $LiNH_2$ through cationic Li / Na exchange at the 2c (0,½,¼) lattice sites. This solubility resulted in the formation of a series of non-stoichiometric sodium-doped lithium amides of general formula $Li_{1-z}Na_zNH_2$.

The synthesis of pure samples of $Li_{1-z}Na_zNH_2$ was attempted through reactions of $(LiNH_2)_v(NaNH_2)_{(1-v)}$ mixtures (with v = 1, 0.99...0.9) at 200 °C, both under flowing gas and in sealed evacuated tubes. The reactions performed under flowing gas resulted in mixtures of stoichiometric $Li_3Na(NH_2)_4$ and $LiNH_2$ but reactions performed in sealed evacuated tubes formed mixtures of non-stoichiometric $Li_{3+y}Na_{1-y}(NH_2)_4$ and $Li_{1-z}Na_zNH_2$.

The range of z in $Li_{1-z}Na_zNH_2$ and the proportion of $Li_{3+y}Na_{1-y}(NH_2)_4$ impurity was shown to increase with decreasing v for the samples formed in sealed evacuated tubes. As such, a compromise between the $Li_{1-z}Na_zNH_2$ purity and the range of z was necessary for further studies. Optimal $Li_{1-z}Na_zNH_2$ purity and z-range was obtained for samples synthesised using a mixture of $(LiNH_2)_v(NaNH_2)_{(1-v)}$ with $v = 0.95$.

4.9.1 Synchrotron X-ray Diffraction Study of $Li_{1-z}Na_zNH_2$.

A $Li_{1-z}Na_zNH_2$ sample was synthesised from the v = 0.95 reaction of $(LiNH_2)_v(NaNH_2)_{(1-v)}$ in a sealed evacuated tube, and synchrotron X-ray diffraction data from the sample were collected using the ID31 beamline at the ESRF (section 2.1.2.3). The powdered sample was packed into a silica glass capillary tube, which was sealed and mounted onto the diffractometer. Diffraction data were collected from the sample using a wavelength of 0.8026 Å and step size 0.003°. Rietveld analysis[11] (section 2.1.4) was performed on the data using TOPAS Academic software[12] according to the general procedure outlined in section 2.1.4.1, with the non-stoichiometry of $Li_{1-z}Na_zNH_2$ phases modelled as outlined below. The diffraction data and refined model are presented in Figure 4.31.

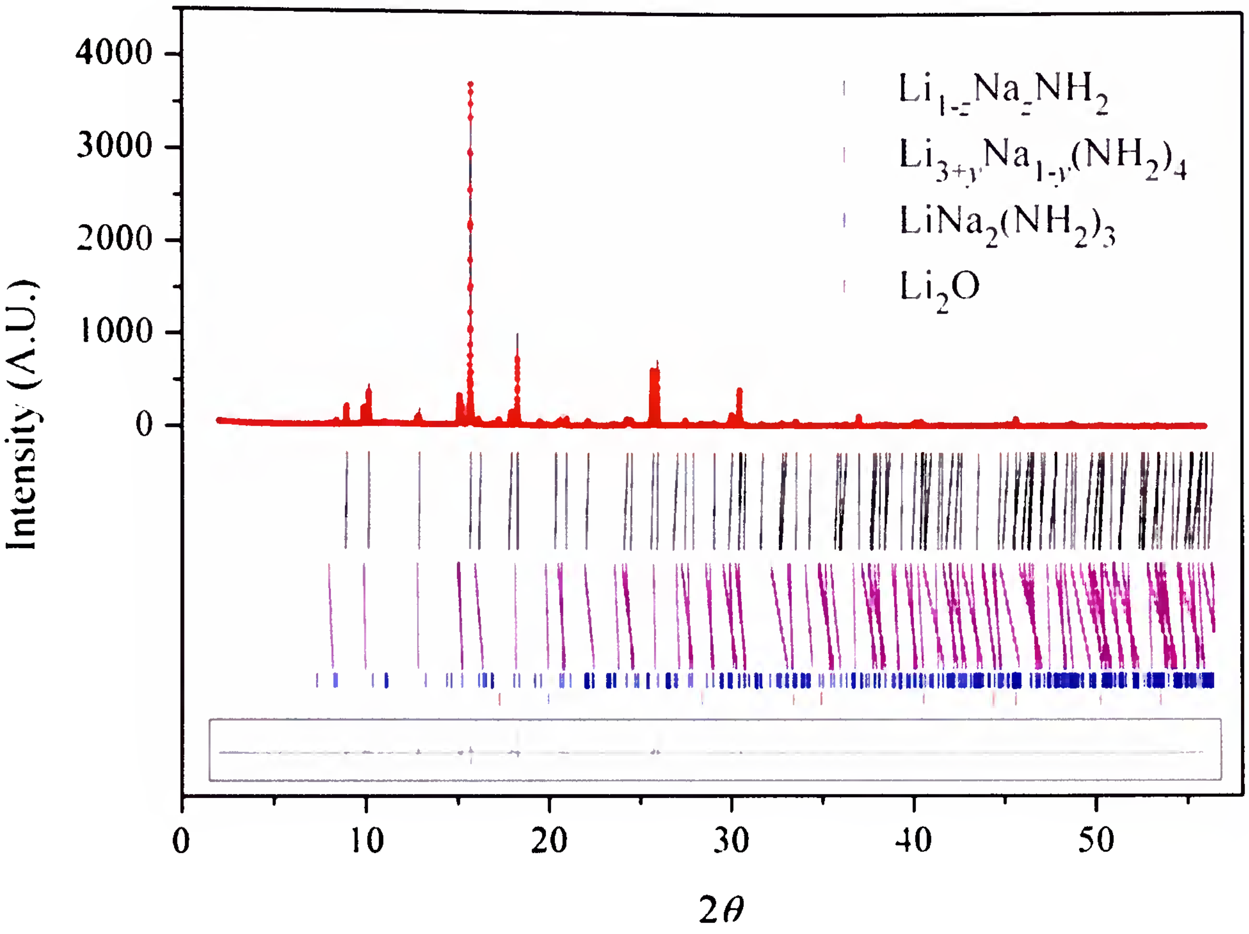

Figure 4.31 : Observed (solid line), calculated (red dots), and difference plots (y_{obsd} - y_{calc}, solid line in box) for the structure refinement of a sample of $Li_{(1-z)}Na_zNH_2$ ($(LiNH_2)_v(NaNH_2)_{(1-v)}$ for $v = 0.95$) from synchrotron X-ray diffraction data collected at λ = 0.8026 Å with step size 0.003 Å. The Bragg peak positions for $Li_{(1-z)}Na_zNH_2$, $Li_{3+y}Na_{1-y}(NH_2)_4$, $LiNa_2(NH_2)_3$ and Li_2O are shown by the vertical tick marks. R_{wp} 11.237, R_{exp} 6.003, goodness of fit 1.872

The non-stoichiometry of $Li_{1-z}Na_zNH_2$ was modelled as outlined in section 4.4.2 for values of z (z_n, $0 \leq n \leq 10$), where z_n was calculated using site occupancies and multiplicities. The Li-occupancy of the 2c (0,½,¼) site, p_n, was modelled using p_n = $0.1[(10\text{-}n)\, p_0 + n\, p_{10}]$ where p_0 and p_{10} were determined from refinement to be 0.99(10) 0.92(4), respectively. The total occupancy of the 2c site was set to 1, and hence the sodium occupancy of the site, q_n was set to equal to 1-p_n. Using the refined values of p_0, p_{10}, q_0 and q_{10}, the values of, z_0 and z_{10} were calculated to be 0.001(3) and 0.02(1), respectively. The level of sodium doping in $Li_{1-z}Na_zNH_2$ therefore ranged from 0.1% up to 2%.

The lattice parameters of the eleven $Li_{1-z}Na_zNH_2$ phases were modelled according to Vegard's law using $a_n = 0.1[(10-n)\ a_0 + n\ a_{10}]$ and $c_n = 0.1[(10-n)\ c_0 + n\ c_{10}]$, with the values of a_0 = 5.0365(10) Å, a_{10} = 5.0423(2) Å, c_0 = 10.255(2) Å and c_{10} = 10.358(9) Å, determined by refinement.

The lattice parameters, stoichiometries, scale factors, and 2c (0,½,¼) Li occupancies for the eleven $Li_{1-z}Na_zNH_2$ phases are summarised in Table 4.11. It is clear from the scale factors that the phases of low sodium content (0.1 – 1%) were most readily formed during the reaction of $LiNH_2$ with 5 mol% $NaNH_2$.

n	Stoichiometric formula	Scale factor (x 10^{-2})	Li occupancy of the 2c (0, ½, ¼) site	a (Å)	c (Å)
0	$Li_{0.999(3)}Na_{0.001(3)}NH_2$	0.001(6)	0.99(10)	5.0365(10)	10.255(2)
1	$Li_{0.997(3)}Na_{0.003(3)}NH_2$	0.726(9)	0.99(13)	5.0370(11)	10.265(2)
2	$Li_{0.996(4)}Na_{0.004(4)}NH_2$	0.668(9)	0.98(16)	5.0376(12)	10.275(3)
3	$Li_{0.995(5)}Na_{0.006(5)}NH_2$	0.425(8)	0.97(19)	5.0382(13)	10.286(4)
4	$Li_{0.992(6)}Na_{0.008(6)}NH_2$	0.243(6)	0.96(2)	5.0388(14)	10.296(4)
5	$Li_{0.990(6)}Na_{0.010(6)}NH_2$	0.120(5)	0.96(2)	5.0394(15)	10.306(6)
6	$Li_{0.988(7)}Na_{0.012(7)}NH_2$	0.072(4)	0.95(2)	5.0399(16)	10.317(6)
7	$Li_{0.986(8)}Na_{0.014(8)}NH_2$	0.052(4)	0.94(3)	5.0405(17)	10.327(7)
8	$Li_{0.984(9)}Na_{0.016(9)}NH_2$	0.035(3)	0.93(3)	5.0411(18)	10.337(8)
9	$Li_{0.982(9)}Na_{0.018(9)}NH_2$	0.025(3)	0.93(4)	5.0417(19)	10.348(8)
10	$Li_{0.98(10)}Na_{0.02(10)}NH_2$	0.042(2)	0.92(4)	5.0423(2)	10.358(9)

Table 4.11: Summary of the refined stoichiometries, Li occupancy of the 2c (0,½,¼) site, scale factors, and lattice parameters of the eleven modelled phases of high-purity $Li_{1-z}Na_zNH_2$.

$Li_{3+y}Na_{1-y}(NH_2)_4$ was modelled in an identical fashion to that outlined in section 4.4.2, using eleven uniformly varying phases of varying y (y_n, $0 \leq n \leq 10$), with y determined from the 2c Na site occupancy and the lattice parameters calculated according to Vegard's law.

4.9.2 Variable Temperature Synchrotron X-ray Powder Diffraction Study of $Li_{1-z}Na_zNH_2$

A second v = 0.95 $(LiNH_2)_v(NaNH_2)_{(1-v)}$ mixture was reacted in a sealed evacuated tube at 200 °C. The $Li_{1-z}Na_zNH_2$ product formed was ground and loaded into a quartz capillary, which was sealed and then mounted onto the ID31 diffractometer at the ESRF (section 2.1.2.3). The diffractometer was fitted with a blower heater, and the sample was heated in the synchrotron beam to a temperature of 325 °C in intervals of 5 °C. The sample was allowed to equilibrate for 60 seconds at each temperature set point, and diffraction data were then collected at that temperature over a 2θ range of 8 – 32° for a period of three minutes. A surface plot (section 3.4) of the diffraction data is presented in Figure 4.32.

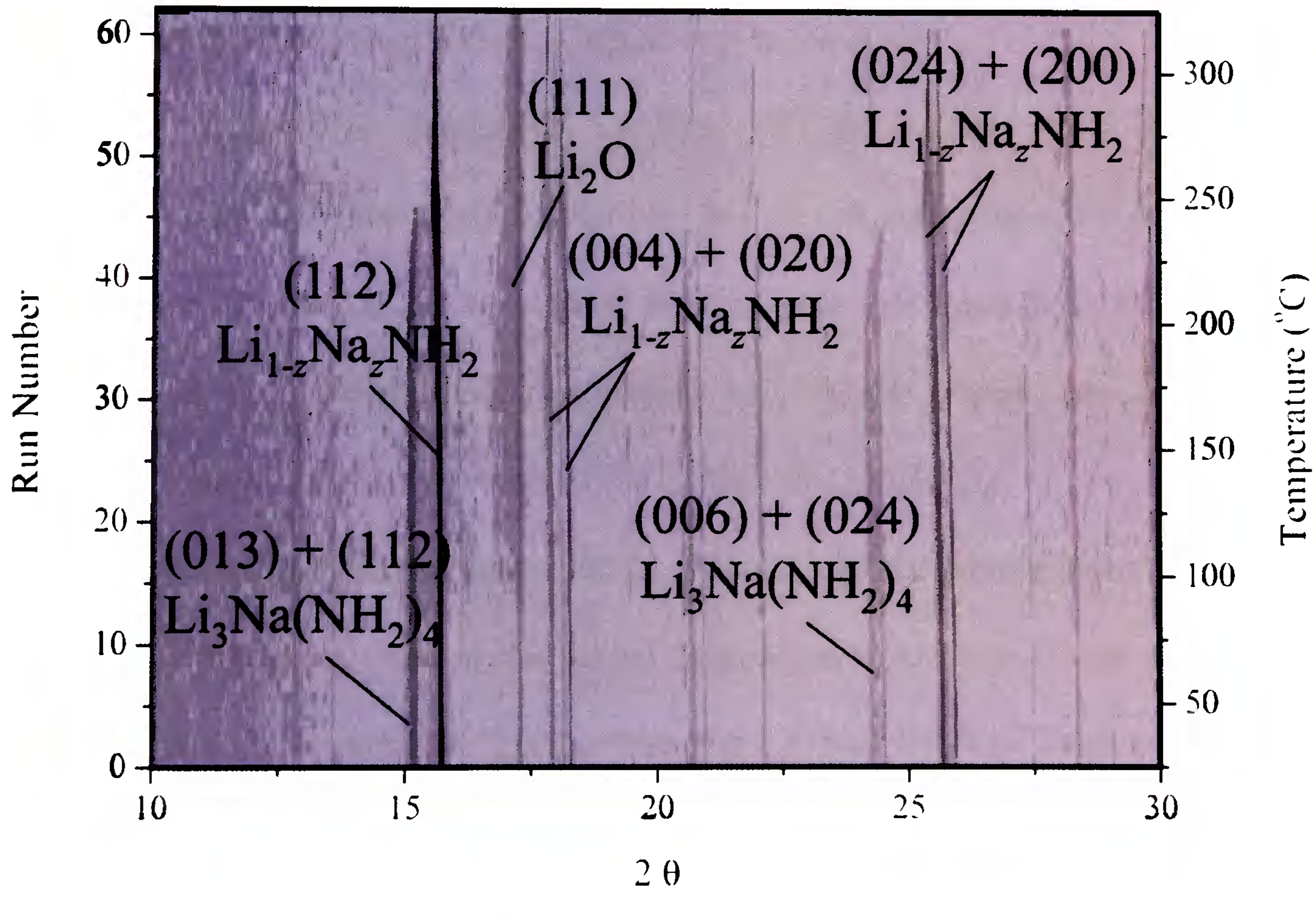

Figure 4.32 : Surface plot of synchrotron X-ray diffraction data collected during the heating of $Li_{(1-z)}Na_zNH_2$ (formed from the reaction of 95:5 $LiNH_2$ + $NaNH_2$) to 325 °C in a sealed glass capillary. Lines corresponding to Bragg reflections for the various phases are indexed.

The synchrotron diffraction data collected were analysed using the Rietveld method[11] (section 2.1.4), utilising the batch facility of the TOPAS Academic software suite,[12] and according to the method outlined in section 2.1.4.2.

Eleven $Li_{1-z}Na_zNH_2$ phases were modelled as outlined in section 4.9.1, with the a_0, a_{10}, c_0 and c_{10} parameters allowed to refine, in order to model thermal expansion of the phases. The maximum and minimum lithium occupancies of the 2c (0,½,¼) lattice site (p_0 and p_{10}) were fixed at their room temperature values (0.97(11) and 0.88(3), respectively) and the minimum and maximum sodium occupancy of the 2c site (q_0 and q_{10}) were therefore fixed at $1-p_0 = 0.03(11)$ and $1-p_{10} = 0.12(3)$, respectively. These values were used to calculate the end-point stoichiometries of $Li_{1-z}Na_zNH_2$, which were $Li_{0.99}Na_{0.01}NH_2$ ($Li_{1-z}Na_zNH_2$_00) and $Li_{0.97}Na_{0.03}NH_2$ ($Li_{1-z}Na_zNH_2$_10). The relative phase fractions of the eleven $Li_{1-z}Na_zNH_2$ phases were refined, which allowed changes in the overall stoichiometry of the $Li_{1-z}Na_zNH_2$ to be modelled.

The temperature dependent variation of the refined phase fractions of $Li_3Na(NH_2)_4$, Li_2O and the total $Li_{1-z}Na_zNH_2$ phase fraction is presented in Figure 4.33a. The error bars for the $Li_{1-z}Na_zNH_2$ phase fraction were calculated from the sum of the error bars of the 11 individually modelled $Li_{1-z}Na_zNH_2$ phases, and as such, are significantly larger than those observed for $Li_3Na(NH_2)_4$ and Li_2O.

Study of Figure 33a suggests that $Li_{1-z}Na_zNH_2$ did not decompose to form Li_2NH during this experiment. Given the sealed pressurised conditions of the sample, it is likely that local NH_3 pressures greater than the $Li_{1-z}Na_zNH_2$-NH_3 equilibrium vapour pressure developed during the experiment, suppressing $Li_{1-z}Na_zNH_2$ decomposition until higher temperatures (with correspondingly higher equilibrium vapour pressures).[26] $Li_{1-z}Na_zNH_2$ was therefore observed to behave in a similar fashion to the $LiNH_2$ studied in section 3.4.

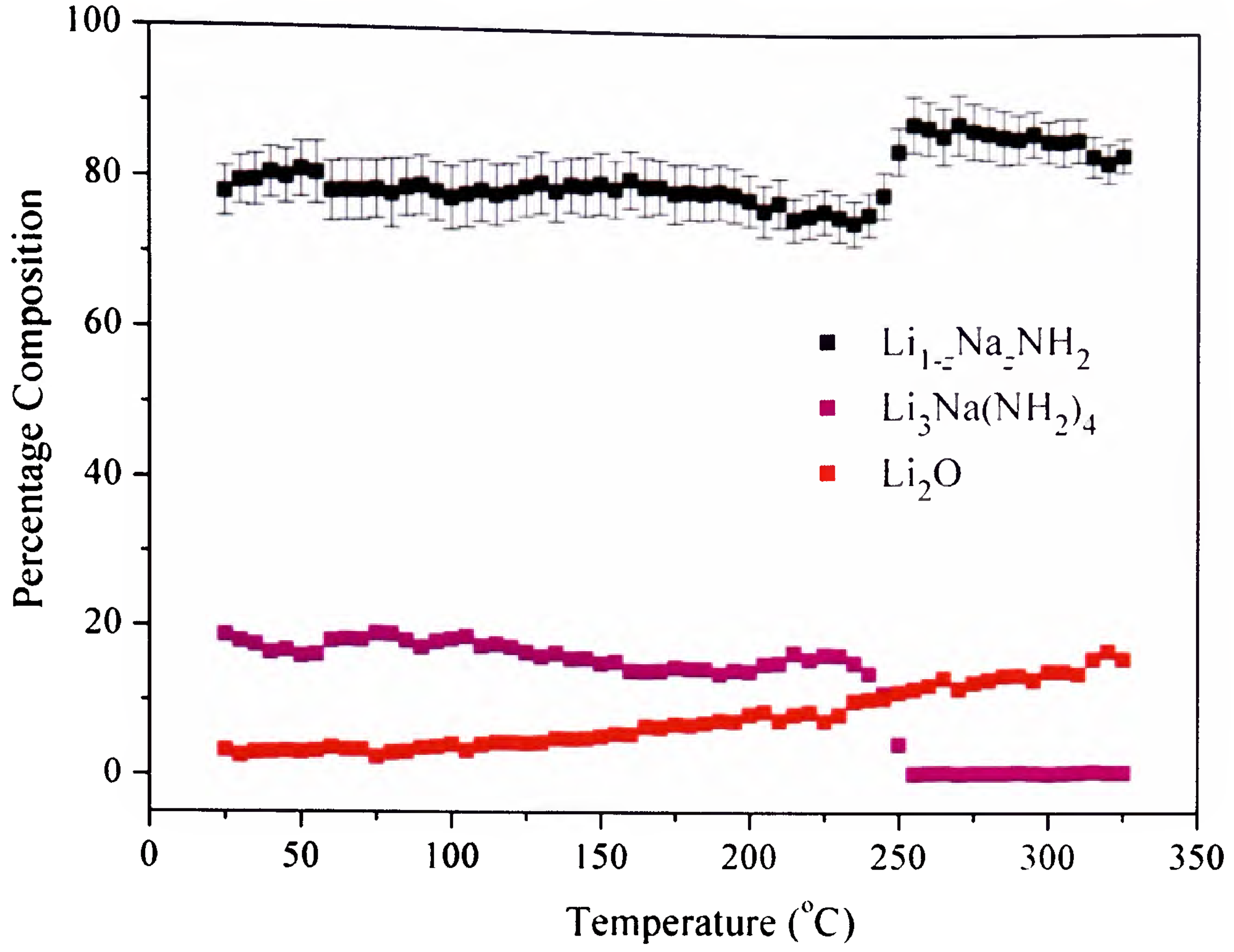

Figure 4.33a : Summary of refined phase fractions of $Li_{1-z}Na_zNH_2$, $Li_3Na(NH_2)_4$ and Li_2O, obtained from Rietveld analysis (*via* batch refinement) of synchrotron X-ray diffraction data collected during the variable temperature study of $Li_{1-z}Na_zNH_2$. Mean errors $Li_{1-z}Na_zNH_2$ ± 3, $Li_3Na(NH_2)_4$ ± 0.4, Li_2O ± 0.5. Error bars only shown if larger than data markers.

The phase fraction of $Li_{1-z}Na_zNH_2$ remained fairly constant until the sample reached a temperature of 240 °C, at which point it increased sharply. This increase coincided with a decrease in the $Li_3Na(NH_2)_4$ phase fraction, indicating that $Li_3Na(NH_2)_4$ decomposed *via* the formation of $Li_{1-z}Na_zNH_2$ and $NaNH_2$ (as suggested in section 4.7). The temperature of the sample at this point was above the melting point of $NaNH_2$, and hence any $NaNH_2$ present was amorphous.

The proportion of Li_2O in the sample increased gradually throughout the experiment, indicating that either the sample reacted with the silica capillary or that there was a small leak in the capillary tube.

Figure 4.33b presents the temperature-dependent variation of the $Li_{1-z}Na_zNH_2$ lattice parameters. The a_0 and a_{10} parameters of $Li_{1-z}Na_zNH_2$ were observed to increase linearly as a function of temperature up to 215 °C, at which point a_{10} began to increase at a faster rate than a_0, until the sample reached 240 °C.

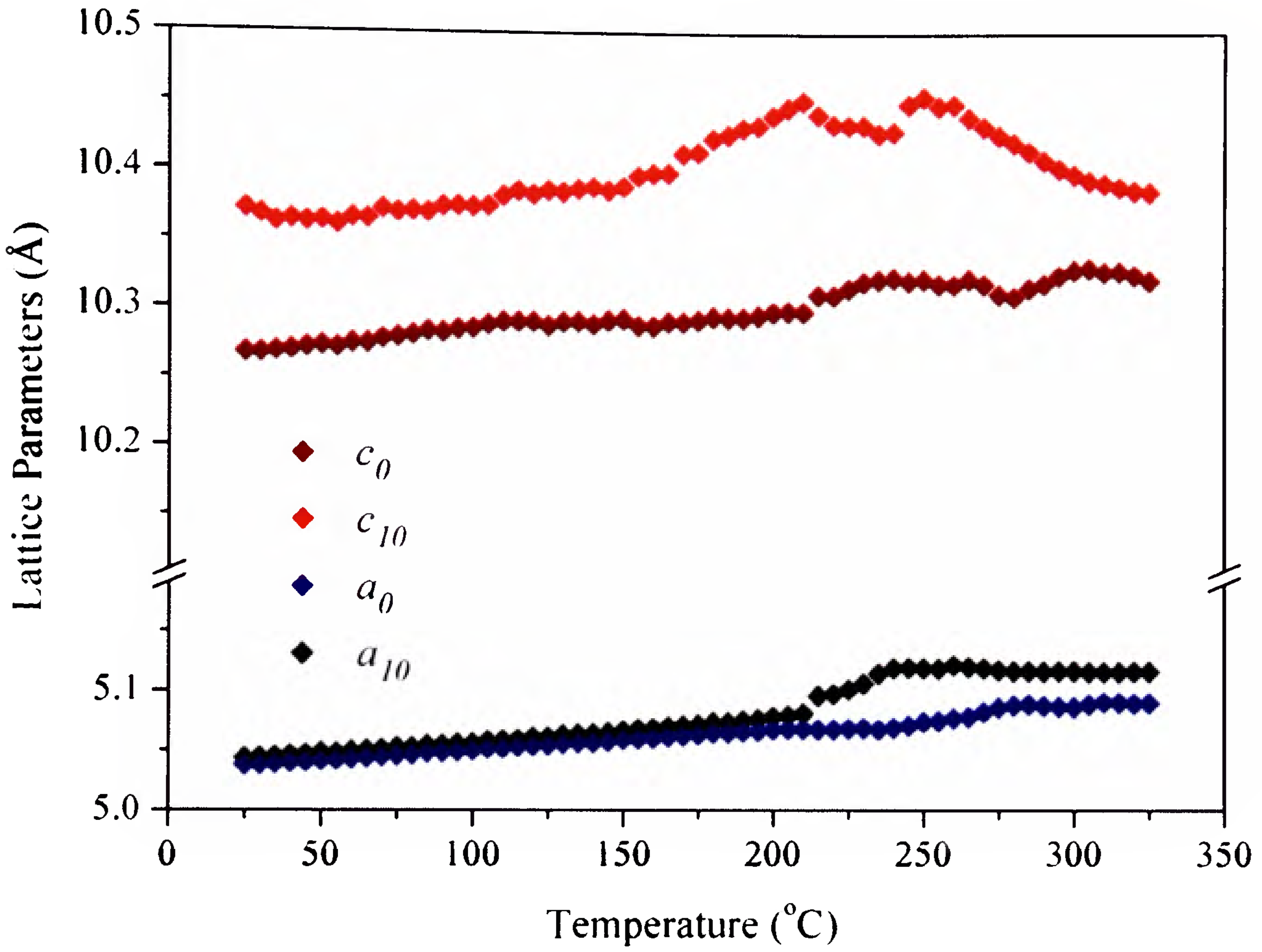

Figure 4.33b : Summary of calculated lattice parameters of $Li_{(1-z)}Na_zNH_2$ obtained from Rietveld analysis (*via* batch refinement) of the synchrotron diffraction data collected during the variable temperature study of $Li_{(1-z)}Na_zNH_2$ between room temperature and 325 °C. Mean errors a_o ± 0.00018, a_{10} ± 0.0002, c_o ± 0.0005 and c_{10} ± 0.0005. Error bars not shown as smaller than data markers.

The c_0 and c_{10} parameters increased linearly with temperature only up to 155 °C, at which point the c_{10} parameter began to increase at a much faster rate than previously observed, and the c_0 decreased in length slightly before continuing to increase linearly. These trends continued until the sample reached 215 °C, at which point a decrease was observed in c_{10} (up to 240 °C) and c_0 began to increase non-linearly with temperature.

The temperature dependant changes observed in a_0, a_{10}, c_0 and c_{10} up to 240 °C suggest that the $Li_{1-z}Na_zNH_2$ phases underwent thermal expansion during heating to 155 °C, after which point a complex structural transition occurred as the sample temperature increased to 240 °C.

As the temperature reached 250 °C, the $Li_{1-z}Na_zNH_2$ c_{10} parameter increased sharply, just as a decrease was observed the $Li_3Na(NH_2)_4$ phase fraction (Figure 4.33a). This is consistent with the formation of high-*z* $Li_{1-z}Na_zNH_2$ phases from the breakdown of $Li_3Na(NH_2)_4$. As the sample reached 280 °C, the values of a_0 and c_0 continued to increase with temperature and the values of a_{10} and c_{10} were observed to decrease. This suggests that a_0 was tending towards a_{10} and that c_0 was tending towards c_{10}, which is consistent with the formation of single composition $Li_{1-z}Na_zNH_2$, with $a_0 = a_{10}$ and $c_0 = c_{10}$.

The relative proportions of the different $Li_{1-z}Na_zNH_2$ phases were observed to vary as a function of temperature, as shown in Figure 4.33c.

The low *z* phases ($Li_{1-z}Na_zNH_2$_00 and 01) constituted the greatest proportion of the $Li_{1-z}Na_zNH_2$ present at low temperature. As the temperature of the sample increased above 170 °C, larger proportions of the more intermediate phases ($Li_{1-z}Na_zNH_2$_02, 03 and 04) were observed. Decomposition of the $Li_3Na(NH_2)_4$ impurity at 240 °C greatly increased the amount of mobile sodium in the system, resulting in an increased proportion of the $Li_{1-z}Na_zNH_2$ phases of high *z* ($Li_{1-z}Na_zNH_2$_09 and 10), at the expense of the low-*z* phases.

At the end of the experiment, the $Li_{1-z}Na_zNH_2$ present in the sample appeared to consist almost entirely of a single phase ($Li_{1-z}Na_zNH_2$_09). This suggests that heating the sample increased the Li and Na ion mobility of both $Li_{1-z}Na_zNH_2$ and $Li_3Na(NH_2)_4$, resulting in an even distribution of the Na ions throughout the material, and the formation of a single-phase Li – Na – N - H material of stoichiometry $Li_{0.982(9)}Na_{0.018(9)}NH_2$, with Li_2O impurity.

A full summary of the refined structural parameters is presented in Appendix A1.1.

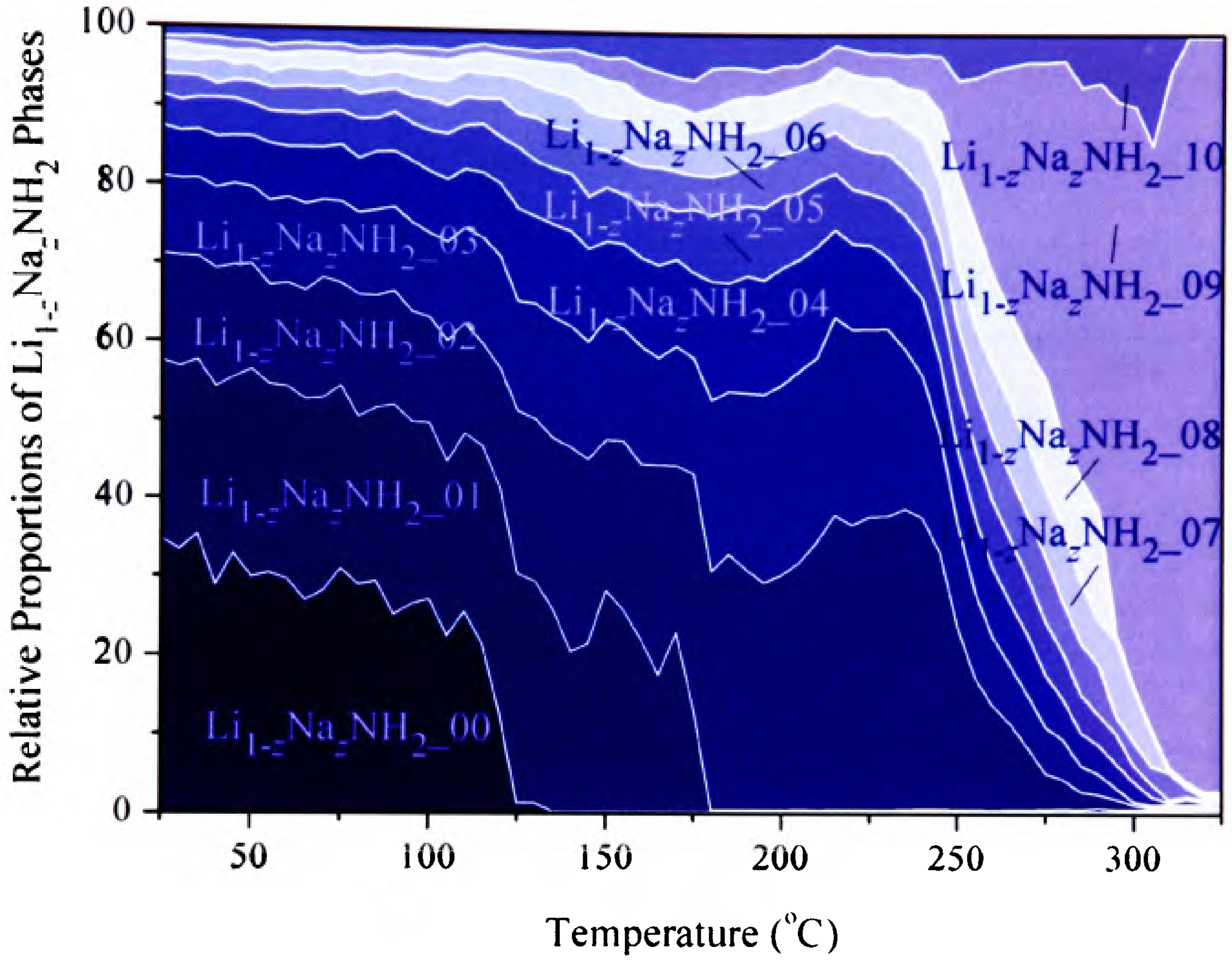

Figure 4.33c : Summary of relative proportions of various $Li_{(1-z)}Na_zNH_2$ phases obtained from Rietveld analysis (*via* batch refinement) of the synchrotron diffraction data collected during the variable temperature study of $Li_{(1-z)}Na_zNH_2$ between room temperature and 325 °C. $Li_{(1-z)}Na_zNH_2$ _00 corresponds to the composition of lowest *z* and $Li_{(1-z)}Na_zNH_2$ _10 that of highest *z*.

4.9.3 Neutron Diffraction Study of $Li_{1-z}Na_zND_2$

A sample of $Li_{1-z}Na_zND_2$ was synthesised for neutron diffraction studies in order to determine the atomic positions of deuterium within the crystal structure.

The $Li_{1-z}Na_zND_2$ sample was formed from the 95:5 reaction of $LiND_2$ (from $Li_3N + ND_3$, section 2.6.2.1) with $NaND_2$ (from $NaH + ND_3$, section 2.6.3.1) in a sealed evacuated tube at 200°C for 12 hours (section 2.6.5.3). The powdered sample was loaded into a vanadium can under inert conditions, and neutron diffraction data were collected for one hour using the GEM diffractometer at the ISIS pulsed neutron facility (section 2.1.3.1). The data collected from banks 4 and 5 underwent simultaneous Rietveld analysis[11] (section 2.1.4) using the TOPAS Academic software suite,[12] according to the general method outlined in section 2.1.4.1. The diffraction data and refined model are presented in Figure 4.34.

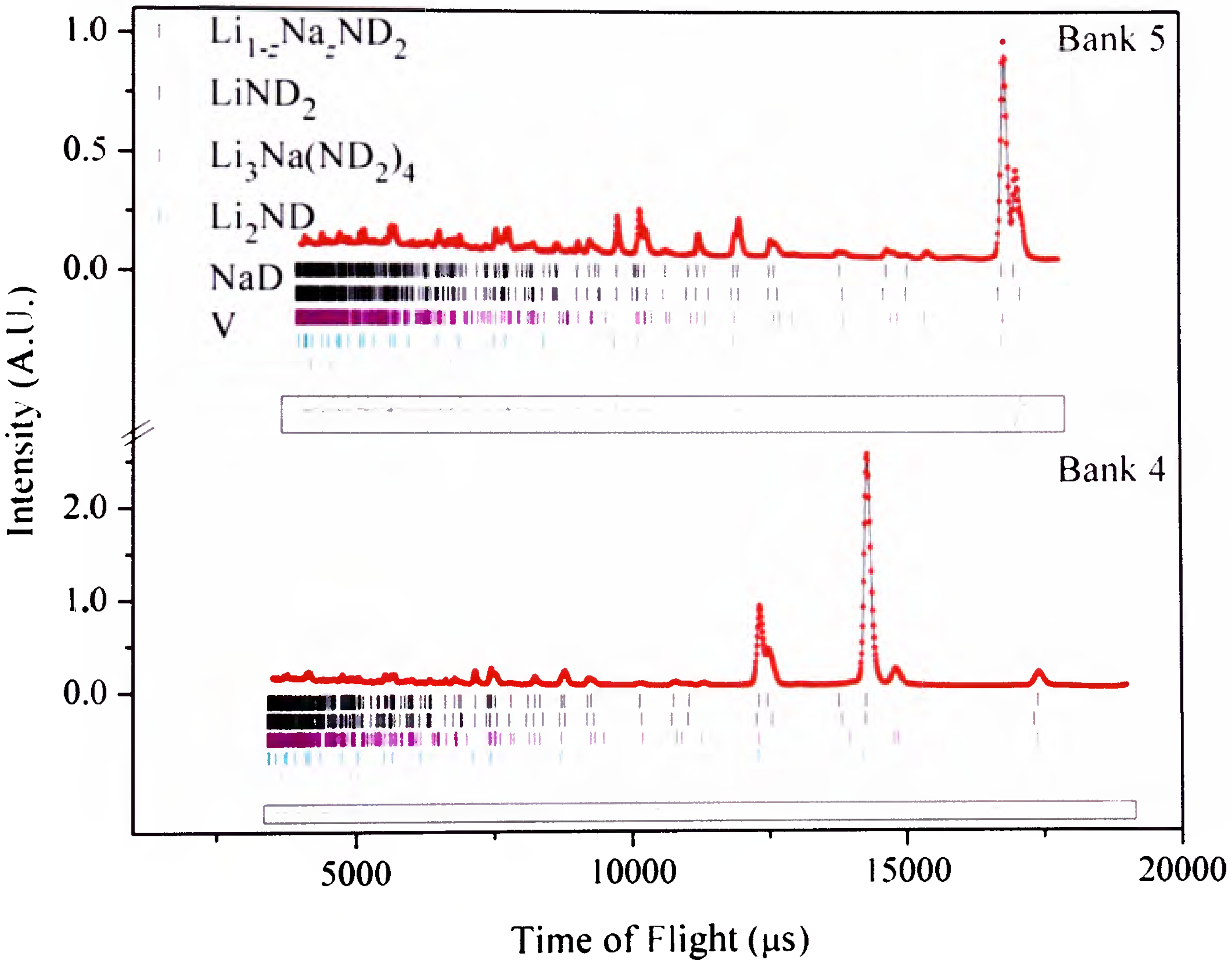

Figure 4.34 : Observed (solid lines), calculated (red dots), and difference plots (y_{obsd} - y_{calc}, solid lines in boxes) for the structure refinement of $Li_{1-z}Na_zND_2$, from neutron diffraction data collected at banks 4 and 5 of the GEM diffractometer at the ISIS pulsed neutron facility. The Bragg peak positions for $Li_{1-z}Na_zND_2$, $LiND_2$, $Li_3Na(ND_2)_4$, Li_2ND, NaD, and V are shown by the vertical tick marks. R_{wp} 3.443, R_{exp} 0.789, goodness of fit 4.363.

In addition to the parameters listed in section 2.1.4.1, the *x*, *y* and *z*-coordinates of the 8g (*x*,*y*,*z*) N position and the *z*-coordinate of the 4f (0,½,*z*) Li position were also refined. It was not possible to model the non-stoichiometry of $Li_{1-z}Na_zND_2$ from the data collected as the line-widths of the Bragg reflections were too large to effectively model any peak asymmetry. $Li_{1-z}Na_zND_2$ was therefore modelled as a line-phase material.

Having refined the coordinates of the 8g nitrogen position (N1), the atomic coordinates of the two D positions, D1 and D2, were refined. A rigid rotor model (with N1 as the fixed point) was used for the ND_2^- unit in order to ensure that the N1 – D1 and N1 – D2 bond distances remained equal. Using this model, the N – D bond lengths and the D1 – N1 – D2 bond angle were calculated to be 0.966(3) Å and 103.0(4)°, respectively. These values are very similar to those reported for $LiND_2$ (N – D bond length 0.967 Å and 0.978 Å, D – N – D angle 104.0°).[21]

The Li occupancies of the 2a, 4f and 2c lattice sites (p_{2a}, p_{4f}, p_{2c}, respectively) were allowed to refine, and the Na occupancy of each site (q_{2a}, q_{4f}, q_{2c}) was set at $1-p_{2a}$, p_{4f} and p_{2c} (respectively). Similarly, the deuterium occupancies of the 8g sites (o_D) were refined, and the hydrogen occupancy of the sites (o_H) was set equal to $1-o_D$. The structural parameters calculated for $Li_{1-z}Na_zND_2$ during these refinements are summarised in Table 4.12. The stoichiometry of the $Li_{1-z}Na_zND_2$ material was calculated to be $Li_{0.98(10)}Na_{0.02(10)}ND_2$. The lattice parameters and unit cell volume calculated from these refinements are in good agreement with the values reported for the hydrogenated material in section 4.9.1.

According to the Rietveld analysis[11] of the of $Li_{1-z}Na_zND_2$ neutron diffraction data, the preferred lattice site for Na substitution in this sample was the 2a (0,0,0) site. This contrasts with the hydrogenated sample studied by synchrotron diffraction (section

4.9.1), where the 2c (0,½,¼) lattice site was favoured. This discrepancy between the hydrogenated and deuterated materials can be understood through consideration of the initial state of the $LiNH_2$ and $LiND_2$ precursor materials.

$Li_{1-z}Na_zND_2$

Atom	Site	x	y	z	Occupancy	B_{iso} (Å^2)
Li1	2a	0.0	0.0	0.0	0.92(3)	1.2(1)
Na1	2a	0.0	0.0	0.0	0.08(3)	1.2(1)
Li2	2c	0.0	0.50	0.25	1.00(3)	1.2(1)
Na2	2c	0.0	0.50	0.25	0.00(3)	1.2(1)
Li3	4f	0.0	0.5	0.0042(7)	1.00(3)	1.2(1)
Na3	4f	0.0	0.5	0.0042(7)	0.00(3)	1.2(1)
N1	8g	0.2420(7)	0.2444(8)	0.1150(2)	1	1.61(6)
D1	8g	0.4049(7)	0.3354(8)	0.1357(2)	0.781(4)	1.61(6)
H1	8g	0.4049(7)	0.3354(8)	0.1357(2)	0.219(4)	1.61(6)
D2	8g	0.2091(7)	0.1403(8)	0.1925(2)	0.781(4)	1.61(6)
H2	8g	0.2091(7)	0.1403(8)	0.1925(2)	0.219(4)	1.61(6)

a = 5.0561(18) Å, c = 10.2439(4) Å

Table 4.12: Refined structural parameters and atomic positions for $Li_{1-z}Na_zND_2$ (space group $I\bar{4}$, number 82), calculated from Rietveld analysis of neutron diffraction data. A rigid rotor model was employed for the ND_2^- unit, which calculated a N – D bond length of 0.966 (3) Å, and a D – N – D bond angle of 103.0 (4)°

$LiNH_2$, as purchased, was shown to be a fully stoichiometric material, with an occupancy of 1 at each of the 2a, 4f and 2c lattice sites, and wholly vacant 2b, 2d and 4f sites (section 3.3.3). As such, the crystallographic layer containing the occupied 2c site was otherwise entirely unoccupied, and an easy pathway for Na-migration into the 2c site existed (*via* the vacant 2d and 4e sites).

In contrast, neutron diffraction studies of $LiND_2$ formed from Li_3N + ND_3 (section 3.5.1) indicated that the material was Li-rich with formula $Li_{1+y}ND_{2-y}$. The 2a (0,0,0) and 4f (0,½,z) lattice sites in the $LiND_2$ sample were fully occupied, and the 2c (0,½,¼), 2d (½,0,¼) and 4e (0,0,z) lattice sites were each partially occupied by Li ions, hindering Na migration into the 2c/2d/4e layer. This means that no clear pathway existed for Na migration in this material, making Na substitution at the 2c site much more difficult in $LiND_2$ than in $LiNH_2$. The only unoccupied lattice site in $LiND_2$ was the 2b (0,0,½) site, suggesting that Na ions may have migrated into the $LiND_2$ structure *via* the vacant 2b lattice sites, and from here, replaced Li ions at the 2a sites.

The composition of the sample was calculated from refined scale factors to be majority $Li_{1-z}Na_zND_2$ (60 wt%) with impurity phases $LiND_2$ (10 wt%) $Li_3Na(ND_2)_4$ (12 wt%) Li_2ND (7 wt%), Li_3N (4 wt%), NaD (4 wt%) and Li_2O (3 wt %), which arose from impurities in the $LiND_2$ and $NaND_2$ precursor materials.

4.9.4 Intelligent Gravimetric Analysis with Neutron Diffraction Study of $Li_{1-z}Na_zND_2$

The decomposition reaction of $Li_{1-z}Na_zND_2$ was further studied using intelligent gravimetric analysis combined with neutron diffraction (IGA^n).

The $Li_{1-z}Na_zND_2$ sample discussed in section 4.9.3 was loaded under inert conditions into a quartz bucket, which was then loaded into the IGA^n apparatus as outlined in section 2.2.2. The sample was heated to 270 °C at a rate of 3 °C per minute under dynamic vacuum, and this temperature was maintained until no further mass loss was observed in the thermogravimetric data.

Neutron diffraction data were collected at intervals of 2.52 minutes throughout the course of the experiment, and the sample mass, temperature and pressure were recorded every 5.7 seconds.

A surface plot (section 3.4) of the neutron diffraction data collected at bank 5 is presented, alongside the corresponding thermogravimetric data in Figure 4.35. The brightness of the lines in the surface plot is indicative of the relative intensities of the Bragg reflections, as outlined in section 3.6.4.

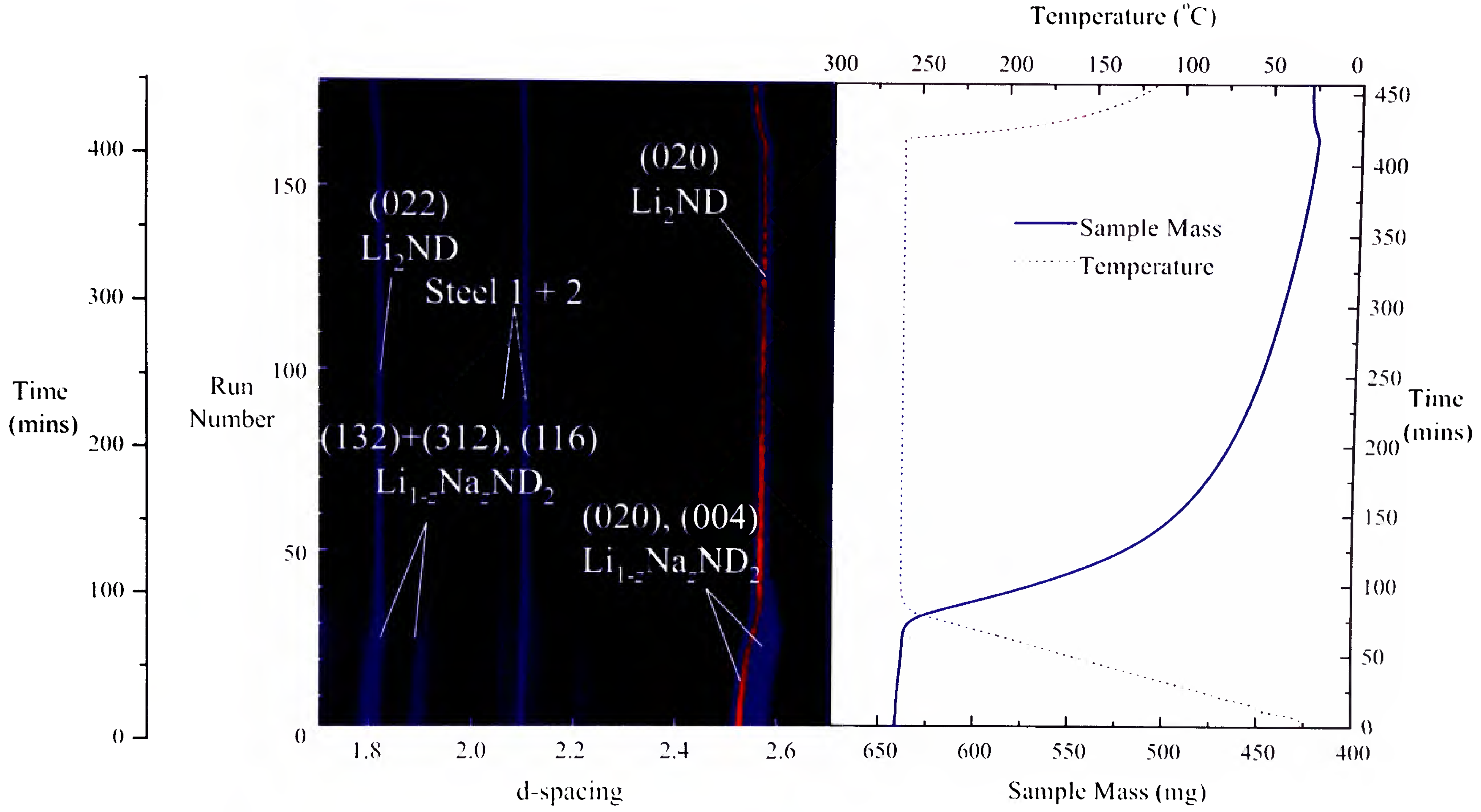

Figure 4.35 : Comparison of the surface plot of the neutron diffraction data (collected at bank 4) and the thermogravimetric data, collected during the decomposition of $Li_{1-z}Na_zND_2$in the IGA^n apparatus under dynamic vacuum. Bragg reflections for the various phases present are indexed.

The surface plot of the diffraction data closely resembles that obtained from the decomposition of the $LiND_2$ sample in section 3.6.4. The Bragg reflections observed between d-spacing 2.5 and 2.6 Å (indexed to the (020) and (004) reflections of $Li_{1-z}Na_zND_2$) coalesced to form one Bragg peak as the sample temperature increased above 190 °C. This is consistent with the transformation of a tetragonal material into a cubic material, which is what we would expect for the decomposition of $Li_{1-z}Na_zND_2$ to form Li_2ND.

The thermogravimetric data show that the mass of the sample decreased slowly by 0.6 mass% as the sample temperature increased from room temperature to 192 °C. Increasing the temperature above 192 °C resulted in a rapid mass loss of 34.0 mass%.

4.9.4.1 Rietveld Refinement of Diffraction Data Collected During the Decomposition of $Li_{1-z}Na_zND_2$.

Rietveld analysis[11] (section 2.1.4) of the diffraction data collected during this experiment was performed both using batch techniques (according to the method outlined in section 2.1.4.2) and by refining a number of data sets individually (according to the method outlined in section 2.1.4.1). Generally, the data collected during phase transformations were refined individually and that collected throughout the remainder of the experiment were refined using the batch facility of TOPAS Academic.[12]

The doping level of Na in the $Li_{1-z}Na_zND_2$ sample was so low that, due to the resolution of the diffraction data, modelling the occupancy of the Li lattice sites was not possible.

The refined scale factors and lattice parameters of $Li_{1-z}Na_zND_2$, $Li_3Na(ND_2)_4$ and Li_2ND are presented in Figures 4.36a and b, respectively.

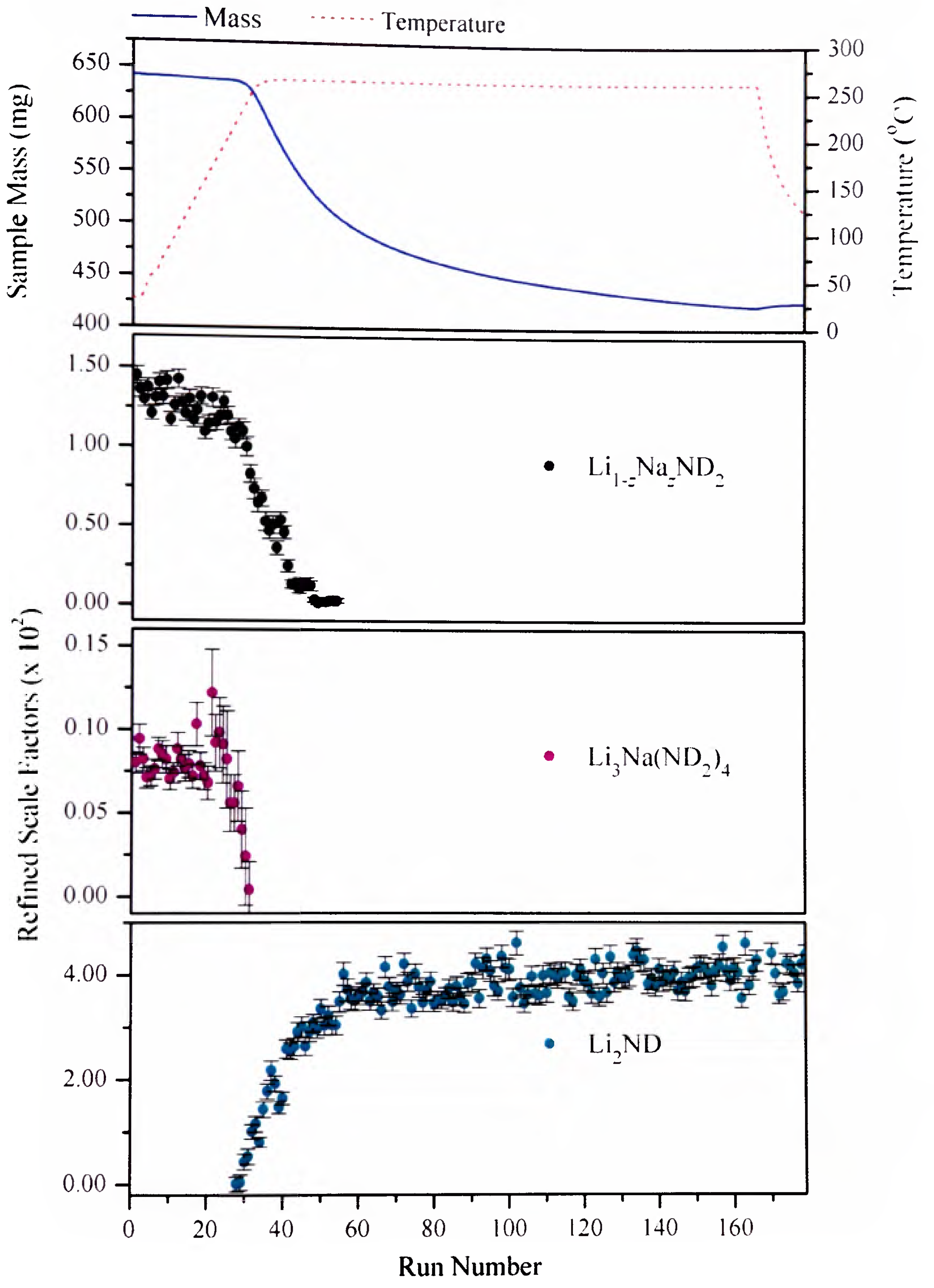

Figure 4.36a : Summary of refined scale factors, obtained from Rietveld analysis (*via* batch refinement) of the neutron diffraction data collected during $Li_{1-z}Na_zND_2$ decomposition in the IGA[n]. The thermogravimetric data are also presented for ease of comparison. Mean errors $Li_{1-z}Na_zND_2$ ± 0.0004, $Li_3Na(ND_2)_4$ ± 0.00017, Li_2ND ± 0.0018

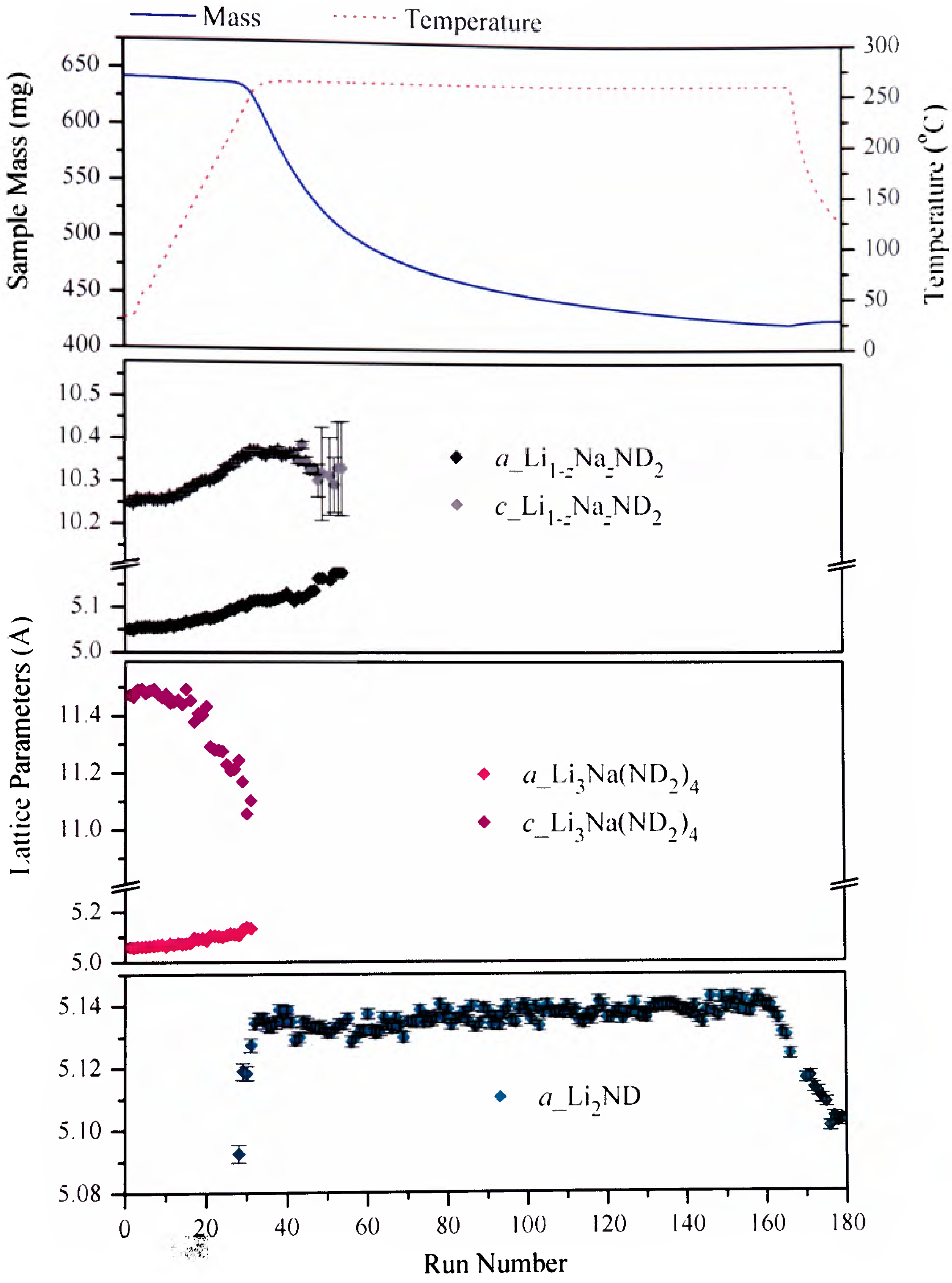

Figure 4.36b : Summary of the refined lattice parameters of $Li_{1-z}Na_zND_2$, $Li_3Na(ND_2)_4$ and Li_2ND, obtained from Rietveld analysis (*via* batch refinement) of the neutron diffraction data collected during the decomposition of the $Li_{1-z}Na_zND_2$ sample in the IGA^n apparatus. The mass and temperature traces are included for ease of comparison. Mean errors a_ $Li_{1-z}Na_zND_2$ ± 0.006, c_ $Li_{1-z}Na_zND_2$ ± 0.02, a_ $Li_3Na(ND_2)_4$ ± 0.003, c_ $Li_3Na(ND_2)_4$ ± 0.01 and a_Li_2ND *a* ± 0.0017. Error bars only presented if larger than data markers.

The scale factors of $Li_{1-z}Na_zND_2$, $Li_3Na(ND_2)_4$ (Figure 4.36a) were both observed to decrease with increasing temperature. The decrease in the $Li_3Na(ND_2)_4$ scale factor proceeded at a faster rate than that of $Li_{1-z}Na_zND_2$, with the $Li_3Na(ND_2)_4$ Bragg reflections disappearing completely from the diffraction data as the sample reached 237 °C.

Although the $Li_{1-z}Na_zND_2$ scale factor decreased slowly from the beginning of the experiment, rapid decrease was only observed after the $Li_3Na(ND_2)_4$ scale factor had reached zero. This is consistent with the formation of $Li_{1-z}Na_zND_2$ from $Li_3Na(ND_2)_4$ decomposition, as suggested in section 4.7.3.

The decrease observed in the $Li_{1-z}Na_zND_2$ scale factor above 237 °C coincided with an increase in the scale factor of Li_2ND, suggesting that the decomposition of $Li_{1-z}Na_zND_2$ resulted in the formation of Li_2ND.

The lattice parameters of $Li_{1-z}Na_zND_2$ (Figure 4.36b) increased linearly with temperature up to 250 °C, which is consistent with thermal expansion of the phase. As the temperature of the sample became constant, the *a* and *c* parameters remained constant until the $Li_{1-z}Na_zND_2$ scale factor decreased to zero. At this point, an increase was observed in the $Li_{1-z}Na_zND_2$ *a*-parameter and a decrease was observed in the *c*-parameter, resulting in a *c/a* ratio of ~ 2. As outlined in section 3.6.3, this is an artefact of the refinement, arising from the similarity of the $LiND_2$ and Li_2ND crystal structures.

The *a*-parameter of $Li_3Na(ND_2)_4$ showed a linear variation with temperature, indicating that thermal expansion of the phase took place. As observed in section 4.7.3, the decreasing sodium occupancy of $Li_3Na(ND_2)_4$ compensated for thermal expansion along the *c*-axis, resulting in a $Li_3Na(ND_2)_4$ *c*-parameter which remained virtually constant up to 210 °C. Above 210 °C, the *c*-parameter decreased quickly, presumably due to rapid Na migration out of the $Li_3Na(ND_2)_4$ structure.

The lattice parameter of Li_2ND was observed to vary linearly with temperature, indicating thermal expansion of the phase.

The mass loss anticipated from the decomposition of $Li_{0.98(1)}Na_{0.02(1)}ND_2$ *via* the release of ND_3 would be 39.5 mass %, which is in fairly good agreement with the experimental value of 34 mass%. The 5.5 mass% discrepancy between the calculated and experimental values may have resulted from decomposition of the $Li_3Na(ND_2)_4$ impurity or from the release of some D_2 from the sample.

To summarise, as the temperature of the system increased, $Li_{1-z}Na_zND_2$ appeared to decompose primarily with ammonia loss to form Li_2ND. The decomposition pathway of $Li_{1-z}Na_zND_2$ is suspected to mirror that of the structurally similar $Li_3Na(ND_2)_4$.

4.9.5 Thermogravimetric Study of $Li_{1-z}Na_zND_2$ Using Intelligent Gravimetric Analysis with Mass Spectrometry

The decomposition reaction of $Li_{1-z}Na_zNH_2$ was further studied using intelligent gravimetric analysis combined with mass spectroscopy (IGA-MS, section 2.2.1). A powdered sample of $Li_{1-z}Na_zNH_2$ was heated in the IGA under a flow of 1 bar He to 400 °C, at a rate of 2 °C/min, and maintained at this temperature for 12 hours. The outgoing gases were sampled by a dynamic sampling mass spectrometer (section 2.2.1), which was set in flow mode to detect 17, 2, 28, 23 and 39 atomic mass units AMU (corresponding to NH_3, H_2, N_2, Na and $NaNH_2$, respectively).

The thermogravimetric data collected during this experiment are presented in Figure 4.37, together with the partial pressures of released gases, recorded using *in-situ* mass spectrometry.

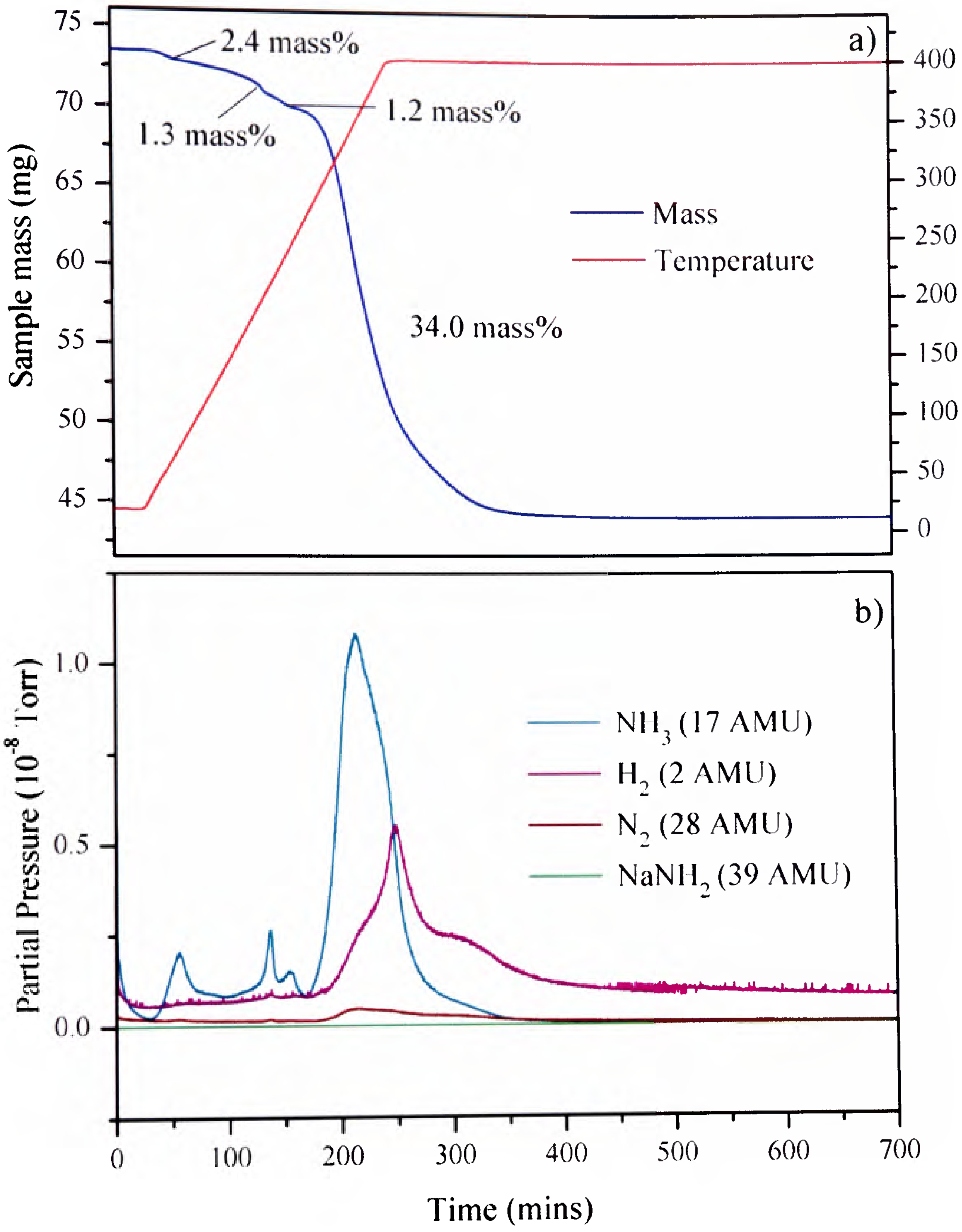

Figure 4.37a and b : a) Thermogravimetric data of high purity $Li_{1-z}Na_zNH_2$, collected using intelligent gravimetric analysis, with heating rate 2 °C/min and target temperature 400 °C. The red line represents the temperature of the sample and the blue line the sample mass. b) Partial pressures of H_2 (purple), NH_3 (turquoise), N_2 (dark red) and $NaNH_2$ (green), recorded during thermogravimetric study of $Li_{1-z}Na_zNH_2$using *in-situ* mass spectrometry.

Four mass losses were observed, as determined by the changes in gradient of the thermogravimetric data (the differential of the sample mass with respect to time is presented in Appendix).

Three small mass losses of 2.4 mass%, 1.3 mass% and 1.2 mass% were observed as the sample temperature was increased from room temperature up to 250 °C. A large mass loss of 34 mass% was observed as the temperature of the sample increased above 262 °C.

The three mass losses observed between room temperature and 250 °C (2.4 mass%, 1.3 mass% and 1.2 mass%, respectively) were accompanied by peaks in the partial pressure of NH_3 (17 AMU, Figure 4.37b), indicating that these mass changes arose from the desorption of physisorbed ammonia from the surface of the powder grains.

The major mass loss (34 mass%), observed as the sample temperature increased above 262 °C, was accompanied by peaks in the partial pressures of both NH_3 and H_2 (2 AMU) at temperatures of 344 °C and 353 °C, respectively.

Integration of the partial pressures of NH_3, H_2 and N_2 with respect to time indicated that the molar ratio of the gases released during the decomposition of $Li_{1-z}Na_zNH_2$ was 10 : 10 : 1, NH_3 : H_2 : N_2. These findings contrast with the 1:3 ratio of H_2 : NH_3 observed during the decomposition of pure $LiNH_2$ (section 3.2.1).

The pathway by which $Li_{1-z}Na_zNH_2$ decomposition released approximately equi-molar amounts of NH_3 and H_2 is not clear. The structural similarities between $Li_{1-z}Na_zNH_2$ and $Li_3Na(NH_2)_4$ suggest that the two materials may decompose *via* similar pathways. If this was indeed the case, separation of $Li_{1-z}Na_zNH_2$ towards $(1\text{-}z)LiNH_2$ + z $NaNH_2$ would be followed by the decomposition of $NaNH_2$ to form Na (or NaH), which would capture the NH_3 produced during the subsequent decomposition of $LiNH_2$, and release H_2 (section 4.7.6). The fact that a much greater proportion of NH_3 was released during $Li_{1-z}Na_zNH_2$ decomposition (compared to $Li_3Na(NH_2)_4$ decomposition) supports this theory, as the concentration of Na in $Li_{1-z}Na_zNH_2$ is much lower than in $Li_3Na(NH_2)_4$.

Nevertheless, the inclusion of only 5% $NaNH_2$ has had a significant impact on the decomposition properties of $LiNH_2$, reducing the amount of NH_3 released by half, and greatly increasing the proportion of H_2 released, compared to pure $LiNH_2$ (section 3.3.1).

4.10 Conclusions

The solid state reaction of $LiNH_2$ with $NaNH_2$ has been shown to form two mixed metal amides of formula $Li_3Na(NH_2)_4$ and $LiNa_2(NH_2)_3$.[13] The crystal structure of $LiNa_2(NH_2)_3$ was solved using a model based on $K_2Li(NH_2)_3$,[14] and the structure of $Li_3Na(NH_2)_4$ was shown to agree with that reported previously in the literature.[10] Unlike previous studies of the mixed Li / Na amides,[10] the formation of $Li_5Na(NH_2)_6$ was not observed.

If the reaction of $LiNH_2$ with $NaNH_2$ was performed in a sealed evacuated tube, the Bragg reflections arising from $Li_3Na(NH_2)_4$ and post-reaction $LiNH_2$ exhibited significant asymmetry. This arose from non-stoichiometry in $Li_3Na(NH_2)_4$ and $LiNH_2$, indicating that the phases would be better described as $Li_{3+y}Na_{1-y}(NH_2)_4$ and $Li_{1-z}Na_zNH_2$, respectively.

$NaNH_2$ was therefore shown to be soluble in $LiNH_2$ at the 2c (0,½,¼) lattice site, resulting in the formation of Li/Na amides with varying stoichiometries, all of which adopted the $I\bar{4}$ space group. Na was not observed at any of the other lattice sites, indicating that materials of composition $Li_{3-x}Na_{1+x}(NH_2)_4$ (with $x>0$) could not be formed. As such, compositions of $Li_{3+y}Na_{1-y}(NH_2)_4$ and $Li_{1-z}Na_zNH_2$ with $y = 0$ and $z = 0$ (stoichiometric $Li_3Na(NH_2)_4$ and $LiNH_2$, respectively) can be regarded as the two end-point compositions of a solid solution of $NaNH_2$ in $LiNH_2$.

The solubility of $NaNH_2$ in $LiNH_2$ arises due to the layered structure of $LiNH_2$, which is able to expand along the *c*-axis, increasing the size of the 2c lattice sites and allowing the substitution of larger Na^+ ions for smaller Li^+ ions at these sites. The non-stoichiometry observed between the two end-point compositions of the $LiNH_2$ / $NaNH_2$ solid solution is believed to arise due to cationic mobility within $LiNH_2$ and $Li_3Na(NH_2)_4$ at the reaction temperature.

$LiNa_2(NH_2)_3$, was shown to exist as a line phase material. The presence of non-stoichiometry in $Li_3Na(NH_2)_4$ and $LiNH_2$, and its absence in $LiNa_2(NH_2)_3$ was attributed to the different crystal structures of the materials, with particular regard to the relative sizes of the Li and Na lattice sites and potential for cationic mobility.

Of the three mixed Li / Na amides formed during the reaction of $LiNH_2$ with $NaNH_2$, only the sodium-rich mixed amide, $LiNa_2(NH_2)_3$, was formed during the reaction of Li_2NH with $NaNH_2$. This arose due to the full occupancy of all of the tetrahedral cation sites within the cubic anti-fluorite Li_2NH structure, which did not allow migration of Na into the material.

Heating stoichiometric combinations of $LiNH_2$ and $NaNH_2$ under flowing gas resulted in the formation of high purity $Li_3Na(NH_2)_4$ and $LiNa_2(NH_2)_3$. Slight deviations from exact 3:1 and 1:2 ratios of $LiNH_2$: $NaNH_2$ were found to produce materials of highest purity, presumably due to the relative purities of the starting materials. In contrast with the samples formed in sealed evacuated tubes, $Li_3Na(NH_2)_4$ formed under flowing Ar was shown to be a line-phase material.

$Li_3Na(NH_2)_4$ and $LiNa_2(NH_2)_3$ synthesised in this way were studied using a variety of techniques in order to increase understanding of their crystal chemistry and decomposition properties.

$Li_3Na(NH_2)_4$ was believed to decompose after melting, *via* partial separation towards its constituent amide phases, $NaNH_2$ and $LiNH_2$ (through $Li_{1-z}Na_zNH_2$). After separation, $NaNH_2$ was believed to decompose first, forming Na and releasing H_2 and N_2. It was postulated that $LiNH_2$ would then decompose, producing $Li_2NH + NH_3$, and that the NH_3 thus formed would be released (under vacuum) or captured by Na (under ambient pressures). H_2 would be released from the NH_3 capturing reaction at ambient pressures, and $NaNH_2$ would be reformed, only to decompose again, and capture ammonia once more; $NaNH_2$ would therefore decompose and be reformed a number of times throughout the decomposition, until all of the $LiNH_2$ present in the sample had been converted to Li_2NH.

The final product of $Li_3Na(NH_2)_4$ decomposition, both under vacuum and under flowing gas, was shown to be Li_2NH. No Na – containing material was visible in the diffraction data of the decomposed products, suggesting that Na was volatised from the samples. This will have presumably arisen due to the low vapour pressure of sodium.

An alternative decomposition pathway at ambient pressures is also possible, where the non-gaseous product of $NaNH_2$ decomposition is NaH. This pathway was believed to be less plausible than decomposition *via* Na formation due to the conditions necessary for NaH volatisation.

The crystal structure of $LiNa_2(NH_2)_3$ was solved and shown to be similar to that of $K_2Li(NH_2)_3$. $LiNa_2(NH_2)_3$ appeared to decompose after melting to release predominantly H_2, together with small quantities of NH_3 and N_2. The release of these gases appeared to precede the evaporation of some Na from the material.

Decomposition of $LiNa_2(ND_2)_3$ under vacuum resulted in the formation of a crystalline material, which was indexed to an *Immm* unit cell with lattice parameters a = 5.543(18) Å, b = 5.5426(3) Å and c = 3.9192(2) Å. This material was hypothesised to be some form of mixed Li / Na nitride or imide.

The synthesis of $Li_{1-z}Na_zNH_2$ was observed only in sealed evacuated tubes. A sample of $Li_{1-z}Na_zNH_2$ was studied by variable temperature synchrotron X-ray diffraction, and appeared to undergo a complex structural transformation during heating. The sample then annealed in the beam, transforming from a continuum of non-stoichiometric $Li_{1-z}Na_zNH_2$ phases with $Li_3Na(NH_2)_4$ impurity, into a material of composition $Li_{0.982(9)}Na_{0.018(9)}NH_2$.

$Li_{1-z}Na_zNH_2$ was shown to decompose to release equi-molar quantities of H_2 and NH_3, forming Li_2NH. This was believed to occur *via* a similar mechanism to that outlined for the decomposition of $Li_3Na(NH_2)_4$, due to the structural similarity of the materials. It is therefore likely that any sodium present in $Li_{1-z}Na_zNH_2$ was volatised during the decomposition reaction.

It is clear that the presence of Na in the Li – N – H system strongly encourages the production of H_2 during decomposition over the production of NH_3, with even a 5% doping level reducing the proportion of NH_3 released by half.

Loss of Na from all of the mixed Li / Na amides during decomposition means that the reversibility of such materials is limited under these conditions.

4.11 Suggestions for Further Work

Although the data presented during this work has given an indication of the decomposition processes of the mixed Li / Na amides, further study is required to unravel the complex decomposition mechanisms of these materials.

Further thermogravimetric study of each compound, using intelligent gravimetric analysis with mass spectrometry, would be valuable in the determination of the individual processes which occur during decomposition of the mixed Li / Na amides. The use of different ramp rates and maximum temperatures would potentially provide a greater understanding of the mechanisms by which gases are released, and may also present conditions under which sodium does not volatise from the materials. Quenching the decomposition reactions of the Li / Na amides after each desorption step may also provide great insight into their decomposition mechanisms, particularly if synchrotron diffraction data of the decomposition intermediates could be collected.

More in-depth crystallographic studies are necessary to identify the solid product formed from the decomposition of $LiNa_2(NH_2)_3$. Unfortunately, the Li_2O content of the material formed during the combined gravimetric analysis with neutron diffraction experiment was very high, and so alternative methods of synthesising the decomposition product would be useful, where the $LiNa_2(NH_2)_3$ does not come into contact with quartz.

The performance of further DSC studies using different heating rates would allow the determination the activation energies of the various transformations of the Li / Na amides. This could be accomplished using Kissinger's method, which utilises the shift in the peak temperature of a transformation with it's heating rate.[25]

Ionic mobility is thought to be responsible for the non-stoichiometry observed in $Li_{3+y}Na_{1-y}(NH_2)_4$ and $Li_{1-z}Na_zNH_2$, however, no data is currently available to support this theory. As such, ionic mobility studies using methods such as variable temperature solid state NMR and four-point probe conductivity analysis would be necessary to explore this possibility further.

Finally, the low vapour pressure of sodium (2.6×10^{-4} mbar at 200 °C)[18] leads to intrinsic problems for the mixed Li / Na amide materials in terms of reversibility. These problems may be negated, whilst maintaining the benefits of a mixed amide system, by using higher pressures of H_2 / Ar over the mixed Li / Na amides during decomposition. Alternatively, the formation of other mixed Li / metal amides, where the metal used has a higher vapour pressure than sodium may be found to have greater potential for reversibility. Potassium, for example, would be a promising candidate, as it has a vapour pressure of 9.3×10^{-3} mbar at 200 °C[18] and moreover, is known to form a number of mixed amides with Li.[14, 30]

4.12 References

1. Z. Xiong, J. Hua, G. Wu, P. Chen, W. Luob, K. Gross and L. Wang, *Journal of Alloys and Compounds*, 2005, **398**, 235-239.
2. W. F. Luo, *Journal of Alloys and Compounds*, 2004, **381**, 284-287.
3. W. F. Luo and S. Sickafoose, *Journal of Alloys and Compounds*, 2006, **407**, 274-281.
4. Y. Chen, C. Z. Wu, P. Wang and H. M. Cheng, *International Journal of Hydrogen Energy*, 2006, **31**, 1236-1240.
5. P. Chen, Z. Xiong, L. Yang, G. Wu and W. Luo, *Journal of Physical Chemistry B*, 2006, **110**, 14221 - 14225.
6. H. Y. Leng, T. Ichikawa, S. Hino, N. Hanada, S. Isobe and H. Fujii, *Journal of Physical Chemistry B*, 2004, **108**, 8763-8765.
7. H. Y. Leng, T. Ichikawa, S. Hino, T. Nakagawa and H. Fujii, *Journal of Physical Chemistry B*, 2005, **109**, 10744-10748.
8. Y. Nakamori, G. Kitahara, K. Miwa, N. Ohba, T. Noritake, S. Towata and S. Orimo, *Journal of Alloys and Compounds*, 2005, **404**, 396-398.
9. Y. Nakamori, G. Kitahara, K. Miwa, S. Towata and S. Orimo, *Applied Physics A - Materials Science & Processing*, 2005, **80**, 1-3.
10. H. Jacobs and B. Harbrecht, *Journal of the Less-Common Metals*, 1982, **85**, 87 - 95.
11. H. M. Rietveld, *Journal of Applied Crystallography*, 1969, 65-71.
12. A. Coelho, *TOPAS, General Profile and Structure Analysis Software for Powder Diffraction Data, version 4.0, Bruker AXS, Karlsruhe, Germany, 2004; http://members.optusnet.com.au/_alancoelho*, 1992-2004.
13. R. L. Lowton, M. O. Jones, W. I. F. David, M. Sommariva and P. P. Edwards, *Journal of Materials Chemistry*, 2008, **18**, 2355 - 2360.
14. F. Kraus and N. Korber, *Journal of Solid State Chemistry*, 2005, **178**, 1241-1246.
15. M. Nagib, H. Kristrup and H. Jacobs, *Atomkernenergie*, 1975, **26**, 87 - 90.
16. A. Zalkin and D. H. Templeton, *Journal of Physical Chemistry*, 1956, **60**, 821.
17. J. B. Yang, X. D. Zhou, Q. Cai, W. J. James and W. B. Yelon, *Applied Physics Letters*, 2006, **88**, 3.
18. http://www.veeco.com/images/library/VaporPress1B_large.jpg, Accessed 24.06.09.
19. K. Sakurazawa and R. Hara, *J. Soc. chem. Ind. (Japan) Suppl.*, 1937, **40**, 10.
20. R. Juza, *Angewandte Chemie-International Edition*, 1964, **3**, 471-481.
21. M. H. Sorby, Y. Nakamura, H. W. Brinks, T. Ichikawa, S. Hino, H. Fujii and B. C. Hauback, *Journal of Alloys and Compounds*, 2007, **428**, 297-301.
22. P. T. Cunningh and V. A. Maroni, *Journal of Chemical Physics*, 1972, **57**, 1415-&.

23. R. A. Forman, *Journal of Chemical Physics*, 1971, **55**, 1987-&.
24. M. P. Balogh, C. Y. Jones, J. F. Herbst, J. L. G. Hector and M. Kundrat, *Journal of Alloys and Compounds*, 2006, **420**, 326-336.
25. H. E. Kissinger, *Analytical Chemistry*, 1957, **29**, 1702 - 1706.
26. F. E. Pinkerton, *Journal of Alloys and Compounds*, 2005, **400**, 76 - 82.
27. X. Z. Ke and I. Tanaka, *Physical Review B*, 2005, **71**, 16.
28. J. P. O. Bohger, R. R. Essmann and H. Jacobs, *Journal of Molecular Structure*, 1995, **348**, 325-328.
29. S. J. Clark, M. D. Segall, C. J. Pickard, P. J. Hasnip, M. J. Probert, K. Refson and M. C. Payne, *Zeitschrift Kristall.*, 2005, **220**, 567-570.
30. H. Jacobs and B. Harbrecht, *Zeitschrift Fur Anorganische Und Allgemeine Chemie*, 1984, **518**, 87-100.

~ Chapter Five ~

Summary

5.1 Studies of the Li – N – H System

The results presented in Chapter Three gave an in-depth crystallographic and thermogravimetric insight into the hydrogen sorption reactions of the Li – N – H system.

Intelligent gravimetric analysis combined with mass spectrometry was performed on samples of $LiNH_2$ and 1:1 $LiNH_2$ + LiH. The results collected during these studies confirmed that $LiNH_2$ decomposes primarily with the release of ammonia in isolation,[1, 2] and with release of hydrogen in the presence of LiH.[3-7]

$LiND_2$ was synthesised from the reaction of Li_3N with ND_3, and was shown by analysis of thermogravimetric and neutron diffraction data, to be a lithium hyper-stoichiometric material, with formula $Li_{1.24(7)}ND_{1.770(9)}$. Rietveld analysis of the neutron diffraction data collected from this sample indicated that all of the tetrahedral sites except the 2b (0,0,½) site were at least partially occupied by Li-ions. The formation of $LiND_2$ from Li_3N + ND_3 therefore appeared to progress through a series of non-stoichiometric intermediate phases of formula $Li_{1+x}ND_{2-x}$, although the kinetics of D_2 uptake became very slow as x reached a limiting value (0.24(7)). It remains unclear whether or not the synthesis of $Li_{1.24(7)}ND_{1.770(9)}$ proceeded *via* the formation of Li_2ND.

Variable temperature synchrotron X-ray diffraction experiments were performed on samples of $LiNH_2$ and $LiND_2$ for temperatures between 25 °C – 350 °C. These studies indicated that the two materials behaved very differently upon heating. $LiNH_2$ underwent a first order transition in lattice parameters at 295 °C, and was not observed to decompose up to a temperature of 350 °C. Conversely, no structural transition was observed in the lattice parameters of $LiND_2$, and this material decomposed at 325 °C. forming Li_2ND.

The differences in the decomposition properties of $LiNH_2$ and $LiND_2$ were attributed to the relative degree of disorder within the samples. $LiNH_2$ (Aldrich, 95% purity) had been shown by synchrotron diffraction to be a highly stoichiometric, ordered phase, whereas the synthetic method used for $LiND_2$ (Li_3N + ND_3) was known (from neutron diffraction) to form a highly disordered Li – rich material.

The structural transition observed in $LiNH_2$ at 295 °C was therefore designated as an order-disorder transition. This conclusion was supported by the variation in the Li-site occupancies observed above 295 °C, which were thought to arise from the increased disorder of the Li^+ sub-lattice.

Further *in-situ* thermogravimetric and neutron diffraction studies using the IGA^n apparatus (section 2.2.2) implied that disorder of Li – N – D materials may also play a significant role during the re-hydrogenation of lithium imide.

Samples containing ball-milled (disordered) Li_2ND underwent smooth crystallographic transitions between Li_2ND and $LiND_2$ during D_2-cycling. This was not the case for un-milled Li_2ND, where deuteration caused a sudden, sharp decrease of the Li_2ND lattice parameter, prior to conversion of the phase into $LiND_2$. The presence of this unit cell contraction in the un-milled sample, but not in the milled samples, led to the conclusion that the ordered Li_2ND underwent an order-disorder transition prior to rearrangement into $LiND_2$.

The masses of the Li_2ND – LiD samples during these experiments were observed to increase prior to the crystallographic change of Li_2ND into $LiND_2$, which implied that D_2 absorption in Li_2ND may have progressed *via* a series of expanded cubic $Li_{2-x}ND_{1+x}$ phases. Re-ordering of these phases, from cubic $Li_{2-x}ND_{1+x}$ into tetragonal $Li_{1+y}ND_{2-y}$, would occur at a limiting value of x, with y tending towards zero as the absorption reaction reached completion.

The defect concentration in Li_2ND – LiD mixtures was also studied, but was shown to have little effect on the rate of deuterium sorption in the Li_2ND / LiD samples beyond the observations described above.

5.2 Studies of the Li – Na – N – H System

The research presented in Chapter Four was concerned with the solid state reaction of lithium amide with sodium amide. The reaction of the two compounds in sealed evacuated tubes was shown to produce two distinct mixed amide phases of formulae $Li_3Na(NH_2)_4$ ($a = b = 5.081$ (1) Å and $c = 11.511$ (5) Å) and $LiNa_2(NH_2)_3$ ($a = b = 6.2838$ (1) Å and $c = 11.1485$ (2) Å).[8] The crystal structure of $Li_3Na(NH_2)_4$ was shown to agree well with that reported previously in the literature[9] and the crystal structure of $LiNa_2(NH_2)_3$ was solved[8] using a model based on the structure of $K_2Li(NH_2)_3$.[10]

The phase space between $LiNH_2$ and $NaNH_2$ was investigated by synchrotron X-ray diffraction. The Bragg reflections arising from $Li_3Na(NH_2)_4$ and $LiNH_2$ exhibited significant two theta-dependent peak asymmetry, suggesting that these phases were non-stoichiometric; the $Li_3Na(NH_2)_4$ and $LiNH_2$ observed during this study could, therefore, be more accurately described as $Li_{3+y}Na_{1-y}(NH_2)_4$ and $Li_{1-z}Na_zNH_2$, respectively.[8] The non-stoichiometry exhibited by these materials demonstrated the solubility of Na in $LiNH_2$ at the 2c (0,½,¼) lattice site. Na-occupancy of the other lattice sites was not observed, suggesting that phases of formula $Li_{3-x}Na_{1+x}(NH_2)_4$ with

x>0 could not be formed. This indicated that $Li_3Na(NH_2)_4$ and $LiNH_2$ can be regarded as the two end-point compositions of a solid solution of $NaNH_2$ in $LiNH_2$.

$LiNa_2(NH_2)_3$, was shown to exist as a line phase material. The presence of non-stoichiometry in $Li_3Na(NH_2)_4$ and $LiNH_2$, and its absence in $LiNa_2(NH_2)_3$ was attributed to the different crystal structures of the materials. Both $LiNH_2$ and $Li_3Na(NH_2)_4$ adopted the $I\bar{4}$ space group, which consists of an almost ideal cubic close packed anion lattice (reminiscent of that of Li_2NH), with cations located in ½ of the tetrahedral interstices. The close resemblance of the crystal structures of these materials to the anti-fluorite structure[11, 12] suggested that at elevated temperatures, the cations may have displayed significant mobility between the close-packed layers of the nitrogen sub-lattice.[13] This cation mobility would allow interchange between the Li and Na ions at the large 2c (0,½,¼) lattice sites within the material, resulting in the formation of non-stoichiometric phases. Furthermore, the layered nature of $LiNH_2$ is such that expansion of the unit cell along the c-axis would not have a high energetic barrier, and the larger Na^+ cation could be easily accommodated in the 2c lattice sites.

$LiNa_2(NH_2)_3$ adopted the $P4_2/m$ space group. The structure of this material has an anionic sub-lattice vastly distorted from ideal cubic close-packing, due to the presence of a screw axis, which suggests that cationic mobility within $LiNa_2(NH_2)_3$ would be extremely low. Furthermore, the difference in size between the Li^+ and Na^+ lattice sites in the $LiNa_2(NH_2)_3$ structure would be too great to allow cross-occupation of these sites, meaning that $LiNa_2(NH_2)_3$ existed only as a stoichiometric, line phase material.

That $LiNa_2(NH_2)_3$ was the major phase formed from the reaction of $LiNH_2$ with $NaNH_2$ in sealed evacuated tubes at high Li-concentrations suggested that $LiNa_2(NH_2)_3$ formation is an irreversible process. The formation of $LiNa_2(NH_2)_3$ thus resulted in the trapping of the Na cations, limiting subsequent $Li_3Na(NH_2)_4$ formation. The formation of $Li_3Na(NH_2)_4$ is believed to be a reversible process due to the mobile nature of the cations within the layered structure, which suggests that $Li_3Na(NH_2)_4$ may have existed in an equilibrium with $3LiNH_2 + NaNH_2$ under these reaction conditions.

Synchrotron X-ray diffraction data of the samples formed from the reaction of Li_2NH with $NaNH_2$ indicated that the products consisted of a mixture of un-reacted starting materials and $LiNa_2(NH_2)_3$; no $Li_3Na(NH_2)_4$ was observed. This was not surprising, given the full Li-occupancy of all tetrahedral sites in Li_2NH.

The synthesis of high-purity samples of $Li_3Na(NH_2)_4$ and $LiNa_2(NH_2)_3$ was accomplished through the reaction of near stoichiometric mixtures of 3:1 and 1:2 $LiNH_2 + NaNH_2$ under flowing gas at 200 °C. Samples of $Li_3Na(N(H(D)_2)_4$ and $LiNa_2(N(H(D)_2)_3$ formed in this way were studied using synchrotron and neutron powder diffraction techniques. Rietveld analysis[14] of the data collected during these studies allowed the lattice parameters and atomic positions of the crystal structures to be determined.

The behaviour of $Li_3Na(NH(D)_2)_4$ during decomposition was studied using calorimetry and intelligent gravimetric analysis combined with either mass spectrometry or neutron diffraction. These experiments indicated that decomposition of $Li_3Na(NH_2)_4$ predominantly released hydrogen *via* a multi-step pathway involving the partial separation of $Li_3Na(NH_2)_4$ towards its constituent amide phases, $3LiNH_2$+$NaNH_2$ (probably *via* $Li_{1-z}Na_zNH_2$ formation). After separation, $NaNH_2$ was believed to decompose to form $Na + ½ N_2 + H_2$, and $LiNH_2$ to form $½Li_2NH$ and $½NH_3$. The Na present was thought to capture the evolved NH_3, resulting in the release of H_2 and the formation of $NaNH_2$. This $NaNH_2$ was subsequently decomposed and reformed a number of times, a process that continued until all of the $LiNH_2$ had been converted into

Li_2NH. As no Na–containing material was visible in the diffraction data of the final products, it was concluded that the remaining Na was volatized.

The decomposition pathway of $LiNa_2(NH(D)_2)_3$ was also studied using calorimetry and thermogravimetric analysis combined with mass spectrometry and neutron diffraction. Decomposition of $LiNa_2(NH_2)_3$ resulted predominantly in the release of H_2 from the sample, along with a small quantity of NH_3. The $LiNa_2(N(H(D)_2)_3$ samples were observed to melt prior to release of gas, and Na was volatised towards the end of the experiments. An unknown solid phase was observed after the decomposition, the Bragg reflections from which were indexed to a body centred orthorhombic structure with space group *Immm* and lattice parameters a = 5.543(18) Å, b = 5.5426(3) Å and c = 3.9192(2) Å.

$Li_{1-z}Na_zNH_2$ was only observed from reactions performed in sealed evacuated tubes, with optimal sample purity obtained using a ratio 95:5 $LiNH_2$ + $NaNH_2$. Variable temperature synchrotron X-ray diffraction studies of $Li_{1-z}Na_zNH_2$ revealed that the material underwent a structural transition and annealed upon heating, resulting in the formation of a material with single stoichiometry.

Thermogravimetric data, collected using intelligent gravimetric analysis with mass spectrometry, indicated that the decomposition of $Li_{1-z}Na_zNH_2$ released approximately equi-molar quantities of NH_3 and H_2.

Combined thermogravimetric and neutron diffraction studies suggested that $Li_{1-z}Na_zND_2$ decomposed to form Li_2ND. No Bragg reflections were observed for any Na-containing phase, suggesting that either such phases were amorphous, or that Na was volatized during the decomposition reaction. $Li_{1-z}Na_zNH_2$ decomposition was believed to occur *via* a similar mechanism to that outlined for $Li_3Na(NH_2)_4$ due to the structural similarity of the two materials.

These findings imply that only small amounts of Na-doping are necessary to significantly alter the chemistry of the Li – N – H system.

5.3 Conclusions

The work reported in this thesis can be broadly divided into two areas of research. The first provides new information regarding the transformations which occur during H_2-cycling of $LiNH_2$ and Li_2NH. The role of cation disorder has been explored, and crystallographic ordering of the Li^+ ions within the lithium amide and imide phases has been shown to significantly affect the sorption properties of the materials. Order-disorder transitions were observed both during hydrogen desorption from ordered $LiNH_2$ and during deuterium absorption on ordered Li_2ND. Such transitions were not observed in disordered materials. The intrinsic disorder and the stoichiometry of Li – N – H(D) materials was shown to depend strongly on the techniques used during their synthesis.

Secondly, the synthesis, crystal chemistry and decomposition properties of the mixed Li / Na amides were studied using a variety of techniques. The $Li_3Na(NH_2)_4$ and Na-doped $LiNH_2$ formed in sealed evacuated tubes were found to exhibit significant non-stoichiometry, whereas $LiNa_2(NH_2)_3$ was shown to exist as a line phase. The presence of sodium in these materials reduced the proportion of ammonia evolved during decomposition compared with pure $LiNH_2$. Na was volatized during the decomposition of the mixed Li / Na amides due to its low vapour pressure.

5.4 References

1. R. Juza, *Zeitschrift fur Anorganische und Allgemeine Chemie*, 1951, **266**, 325.
2. F. E. Pinkerton, *Journal of Alloys and Compounds*, 2005, **400**, 76 - 82.
3. P. Chen, Z. T. Xiong, J. Z. Luo, J. Y. Lin and K. L. Tan, *Nature*, 2002, **420**, 302-304.
4. P. Chen, Z. T. Xiong, J. Z. Luo, J. Y. Lin and K. L. Tan, *Journal of Physical Chemistry B*, 2003, **107**, 10967-10970.
5. Y. H. Hu and E. Ruckenstein, *Journal of Physical Chemistry A*, 2003, **107**, 9737-9739.

6. T. Ichikawa, N. Hanada, S. Isobe, H. Leng and H. Fujji, *Journal of Physical Chemistry B*, 2004, **108**, 7887 - 7892.
7. G. P. Meisner, F. E. Pinkerton, M. S. Meyer, M. P. Balogh and M. D. Kundrat, *Journal of Alloys and Compounds*, 2005, **404**, 24-26.
8. R. L. Lowton, M. O. Jones, W. I. F. David, M. Sommariva and P. P. Edwards, *Journal of Materials Chemistry*, 2008, **18**, 2355 - 2360.
9. H. Jacobs and B. Harbrecht, *Journal of the Less-Common Metals*, 1982, **85**, 87 - 95.
10. F. Kraus and N. Korber, *Journal of Solid State Chemistry*, 2005, **178**, 1241-1246.
11. T. W. D. Farley, W. Hayes, S. Hull, M. T. Hutchings and M. Vrtis, *Journal of Physics-Condensed Matter*, 1991, **3**, 4761-4781.
12. M. Hayoun, M. Meyer and A. Denieport, *Acta Materialia*, 2005, **53**, 2867-2874.
13. W. I. F. David, M. O. Jones, D. H. Gregory, C. M. Jewell, S. R. Johnson, A. Walton and P. P. Edwards, *Journal of the American Chemical Society*, 2007, **129**, 1594 – 1601
14. H. M. Rietveld, *Journal of Applied Crystallography*, 1969, 65-71.